

# **An Indole Trimer: Synthesis, Self-assembly and Applications**

Iris Coe

**Thesis submitted for the degree of Doctor of Philosophy**



School of Physics  
University of Edinburgh  
2013

## Abstract

The organic semiconductor, the indole-5-carboxylic acid asymmetric trimer (ICAT), was chemically synthesised using a new procedure. Self-assembly of ICAT in solution, produced narrowly dispersed discotic nanoparticles that are stable in solution and transferable between surfaces. Highly ordered ICAT bulk molecular and nanoparticle thin films were produced through controlled assembly of ICAT at the solution/solid interface, using glass substrates functionalised with a variety of self assembled monolayers (SAMs). Two films, in particular, on the hydroxyl and the amine-functionalised substrates had extremely well ordered microstructures, suitable for device application.

An immersion based deposition technique was developed, where gold and SAM-functionalised glass substrates were immersed in ICAT solutions made with solvents with a range of polarities. At short immersion times, bulk or particulate films were deposited, as a function of immersion solvent. Longer immersion times produced size tailored vertically aligned nanorod and nanowire arrays, as a function of immersion solvent. The immersion time also controlled both the rod density and rod orientation on the substrates. The results were interpreted in terms of heterogeneous nucleation and subsequent growth. Solvophobic forces induced homogeneous nucleation rather than heterogeneous nucleation, in the immersion systems with water and hydrocarbon based immersion solvents. Aligned nanorods and nanowires were assembled on gold and hydroxyl-functionalised glass substrates when polar aprotic immersion solvents were used. There was no obvious correlation between nanostructure dimensions and solvent polarity in these experiments. This is the first time vertically aligned nanorod arrays have been fabricated with small organic functional molecules, through a solution based technique (non-template).

Solution based deposition techniques developed here were used to deposit ICAT onto field effect transistors (FETs), resulting in devices with a range of ICAT film morphologies. Single crystal devices were also produced where the ICAT crystal bridged the active channel, defined as the gap between the source and drain electrodes. Several chips, with over 20 FETs on each chip, with each ICAT film morphology type, were fabricated. Selected chips had consistent, reproducible current/voltage (IV) outputs that varied within  $\ll$  one order of magnitude, when probed on all areas. The devices produced n and p-type unipolar activity and the onset of ambipolar activity in ambient conditions, at low voltage probing ranges. Carrier type was dependent on the film morphology. Device lifetime was dependent on film thickness.



# Declaration

This thesis has been composed by myself. The work reported here was performed by me unless otherwise stated. This work has not been submitted in any previous application for a degree.

Iris Coe

## Acknowledgements

I would like to thank Wilson Poon for his enthusiasm, patience and support. Also thank you to Andrew Mount for his assistance in chemistry. I am grateful to Nhan Pham for introducing me to nanopatterning and AFM. I would like to give a special thank you to Jane Patterson for her care throughout my time in Edinburgh.

I would like to thank the people in the office 2510 for a pleasant working environment. Thank you to Andrew Schofield and Manuel Reichert for coffee, a supply in biscuits and stimulating conversation. Many thanks to the Kings Buildings squash club, in particular Niek Hijnen, for getting me fit.

Thank you to my friends and family for their support, in particular Heidi Brotherton for her encouragement throughout my PhD.

# Contents

<b>1 Introduction</b>	<b>1</b>
1.1 Organic semiconductors. ....	2
1.2 Why marry nanomaterial and organic semiconductor science. ....	4
1.3 Thesis summary. ....	7
<b>2 Organic semiconductors</b>	<b>9</b>
2.1 Conducting Polymers. ....	10
2.2 Electronic and chemical structure. ....	11
2.3 Doping. ....	13
2.4 General properties. ....	17
2.5 Polyindoles. ....	19
2.5.1 Introduction to indoles. ....	19
2.5.2 The electropolymerisation of indoles. ....	20
2.5.3 The chemical polymerisation of indoles. ....	23
2.5.4 Indole properties and applications. ....	23
<b>3 One dimensional (1D) organic nanostructures</b>	<b>27</b>
3.1 Introduction. ....	28
3.2 Organic 1D nanostructure synthetic strategies. ....	29
3.3 Organic 1D nanostructure properties and applications. ....	32
3.4 Conclusion. ....	34
<b>4 The organic field effect transistor (OFET)</b>	<b>36</b>
4.1 Introduction. ....	37
4.2 The device. ....	38
4.3 Device configuration. ....	39
4.4 Current-Voltage (IV) Characteristics. ....	41

4.5 The organic thin film/metal interface. ....	42
4.6 The gate dielectric. ....	46
<b>5 Microscopy</b>	<b>48</b>
5.1 AFM .....	49
5.2 SEM. ....	54
<b>6 ICAT Part 1: Synthesis and characterisation</b>	<b>58</b>
6.1.1 Introduction. ....	59
6.1.2 Experimental method. ....	62
6.1.3 Results and discussion. ....	63
<b>6 ICAT part 2: Nanoparticles</b>	<b>72</b>
6.2.1 Introduction. ....	72
6.2.2 Experimental Method. ....	72
6.2.3 Results .....	73
6.2.4 Discussion .....	78
6.3 Conclusion. ....	80
<b>7 ICAT self-assembly on functionalised surfaces</b>	<b>82</b>
7.1 Introduction. ....	83
7.2 Experimental Method. ....	87
7.2.1 Substrate cleaning procedure. ....	87
7.2.2 Chemical modification of glass substrates .....	87
7.2.3 Activation of ICAT carboxylic acid side groups .....	88
7.2.4 Immersion coating. ....	88
7.2.5 Analysis. ....	88
7.3 Results 1: ICAT film morphology on hydroxyl terminated glass .....	89
7.4 Results 2: ICAT coating morphology on HMDS-functionalised glass. ....	92
7.5 Results 3: ICAT coating morphology on APS-functionalised glass. ....	96
7.6 Results 4: ICAT macroscopic film morphology .....	100

7.7 Discussion .....	101
7.7.1 ICAT assembly on OH-functionalised substrates .....	102
7.7.2 ICAT assembly on HMDS-functionalised substrates. ....	104
7.7.3 ICAT assembly on APS-functionalised substrates. ....	106
7.7.4 ICAT bulk film quality. ....	109
7.8 Conclusion. ....	111
 <b>8 Self-assembled ICAT 1D nanostructures</b>	 <b>112</b>
8.1 Introduction. ....	113
8.2 Experimental method. ....	114
8.2.1 ICAT thin film procedure .....	114
8.3 Results 1: Controlled ICAT 1D assembly as a function of solvent. ....	114
8.4 Results 2: Nanostructure evolution with immersion time. ....	123
8.4.1 Nanostructure evolution from ICAT/DMSO solution. ....	123
8.4.2 Nanostructure evolution from ICAT/methanol solution. ....	126
8.5 Results 3: 1D assembly on varied surfaces. ....	130
8.5.1 Self assembly on hydrophobic surfaces. ....	130
8.5.2 Self assembly on gold surfaces. ....	135
8.6 Discussion. ....	136
8.6.1 ICAT 1D assembly as a function of solvent. ....	137
8.6.2 1D assembly as a function of immersion time. . . . .	143
8.6.3 1D assembly as a function of substrate. ....	148
8.6.4 Result assessment. ....	151
8.7 Conclusion. ....	155
 <b>9 Self-assembly in organic electronics</b>	 <b>156</b>
9.1 Introduction. ....	157
9.2 Experimental method. ....	159
9.2.1 Device Configuration. ....	159
9.2.2 Substrate cleaning procedure. ....	160

9.2.3 ICAT solutions. . . . .	161
9.2.4 Micro-molding in capillaries (MIMIC) deposition. . . . .	161
9.2.5 Deposition system 1: Enhanced-MIMIC at 60 °C. . . . .	163
9.2.6 Deposition system 2: Enhanced-MIMIC with applied pressure . . . . .	163
9.2.7 Deposition system 3: Immersion coating. . . . .	164
9.2.8 Deposition system 4: Enhanced-drop casting. . . . .	164
9.3 MIMIC results and discussion. . . . .	164
9.3.1 Deposition system 1: MIMIC at 60 °C results. . . . .	164
9.3.2 Deposition system 2: MIMIC at room temperature results. . . . .	166
9.3.3 MIMIC deposition discussion. . . . .	168
9.4 Immersion coating and enhanced-drop casting results and discussion . . . . .	171
9.4.1 Deposition system 3: Immersion coating results. . . . .	171
9.4.2 Deposition system 4: Enhanced drop-casting results. . . . .	174
9.4.3 Film discussion. . . . .	175
9.5 Conclusion. . . . .	177
 <b>10 ICAT semiconducting properties</b>	 <b>178</b>
10.1 Introduction. . . . .	179
10.2 Experimental methodology. . . . .	180
10.2.1 Electronic characterisation of ICAT films. . . . .	180
10.3 Results 1: Electronic properties of films deposited with MIMIC at 60 °C . . . . .	181
10.3.1 Electronic behaviour in ambient conditions. . . . .	181
10.3.2 Electronic behaviour post heat treatment. . . . .	183
10.3.3 Electronic behaviour post ethanol treatment. . . . .	190
10.3.4 Summary . . . . .	191
10.4 Results 2: Electronic properties of films deposited with MIMIC at RT. . . . .	192
10.4.1 Electronic behaviour in ambient conditions. . . . .	192
10.4.2 Summary. . . . .	196
10.5 Results 3: Electronic properties of films deposited with immersion coating . . . . .	196



10.5.1 Electronic behaviour in ambient conditions. ....	196
10.5.2 Electronic behaviour post ethanol treatment . . . . .	199
10.5.3 Expanded probing range. ....	200
10.5.4 Summary. ....	201
10.6 Results 4: Electronic properties of films deposited with enhanced-drop casting. . .	201
10.6.1 Electronic behaviour in ambient conditions. ....	201
10.6.2 Expanded probing range. ....	204
10.6.3 Summary. ....	206
10.7 Discussion. ....	206
10.7.1 Common factors. ....	206
10.7.2 ICAT-based OFET properties . . . . .	210
10.8 Conclusion . . . . .	224
 <b>11 Conclusion</b>	 <b>227</b>
 <b>Bibliography</b>	 <b>232</b>

# **Chapter 1**

## **Introduction**

## 1.1 Organic semiconductors

Since the production of the highly conducting polyacetylene film in 1977,  $\pi$ -conjugated systems have been thoroughly investigated for development of the next generation of electronics, nominally organic electronics (Shirakawa et al. 1977). Conceptually, organic electronics is very different to that of inorganic electronics, as the structural versatility of organic semiconductors allows for the incorporation of functionality by molecular design, which leads to a new and exciting starting point for electronics design. To date, amazing advances have been made in the molecular design and synthesis of an impressive variety of  $\pi$ -conjugated molecules (including small functional molecules and polymers) (Heeger et al. 2001, MacDiarmid et al. 1987, MacDiarmid et al. 1980 and Richardson et al. 2000). There is now strong synthetic control and tunability of the band structure, optical, redox and electrochemical properties of organic semiconductors, at the molecular level (MacDiarmid et al. 2001, Pron et al. 2010, Roncali et al. 1997, Sirringhaus et al. 1998, Talbi et al. 1998a and Talbi et al. 1997). Organic electronics devices are being developed with the aim of cheap fabrication and enabling completely new device functionalities (e.g., mechanical flexibility, impact resistance, and optical transparency) that are difficult to achieve with silicon. Organic  $\pi$ -conjugated molecules have now been applied in a wide variety of applications in information, energy and sensors (Berdichevsky et al. 2006, Haberkorn et al. 2009, Jiang et al. 2011, Lee et al. 2007, Lim et al. 2009, Locklin et al. 2006, MacInnes Jr. et al. 1981, Pandey et al. 1998b and Piok et al. 2003).

Organic device performance is mainly determined by the chemical structure, the purity and the morphology of the organic semiconductor film. While, unprecedented progress has been made in molecular synthesis and functional design, much less attention has been given to the different hierarchies of organization, going from molecules to the devices, although this area is generally accepted to be the most critical issue. The current inability to deposit these molecules in a controlled manner onto devices, is severely holding back progress in the area. This young area of research still has other key

challenges to overcome, notably the poor stability and mobility of organic semiconductors and shortage of n-type semiconductors. Also there is a lack of knowledge regarding the structure/property relationship in semiconducting organic films applied in electronics devices, which is needed for understanding the charge transport of  $\pi$ -conjugated systems, and accordingly developing the device structure. Further exploration of structure/property relations can be realized through applying the semiconductor film to organic field effect transistors (OFET), a device consisting of an organic semiconducting layer, a gate insulator, and three terminals (drain, source and gate electrodes), which can provide an invaluable insight into the charge transport of  $\pi$ -conjugated systems.

Attention is therefore focused on controlling the assembly of the organic semiconductor in the devices. The future for organic thin film deposition is solution based, as vacuum deposition is extremely expensive and requires sophisticated instrumentation. However, current solution-based deposition techniques tend to produce films, with highly disordered morphologies and/or are limited to amphiphilic molecules (Langmuir-Blodgett deposition) or soluble semiconducting polymers, (spin coating) of which there few in number (Dimitrakopoulos et al. 2002, Dimitrakopoulos et al. 2001, Katz et al. 2000, Katz et al. 1999, Katz et al. 1998 and Laquindanum et al. 1998). Thus attention is shifting away from conducting polymers towards small functional molecules, as the molecular packing in polymers can be difficult to control, due to the complicated intermolecular interactions and polydispersity of the chains, while molecular building blocks with weaker interactions allow highly flexible structural tunability. Small  $\pi$ -conjugated molecules are much easier to process, can be purified relatively easily and have been demonstrated to form well ordered films with ordered interfacial alignments (Dimitrakopoulos et al. 2001, Garnier et al. 1996, Katz et al. 2004, Potzorov et al. 2003 and Shirota et al. 2007).

The small organic semiconductor, ICAT, was selected to work with here as it can establish multiple highly directional H-bonds with ICAT molecules, solvents and

surfaces, which have been used effectively in similar functional molecules, to control the assembly process (Ajayagosh et al. 2006, Aoki et al. 2002, Autwer et al. 1999, Duzho et al. 2006 and Gao et al. 2008). This highly processable molecule has 3 carboxylic acid side groups per molecule, which should greatly enhance solubility. The planar structure allows for potential liquid crystal formation and  $\pi$ - $\pi$  stacking in solution to form 1D assemblies. Also, the electron deficient, nitrogen containing, heterocyclic structure lends its self towards n-activity (Newman et al. 2004). ICAT also offers high redox activity, interesting fluorescent properties, excellent thermal stability and biological compatibility (Bartlett et al. 1992, Bieganski et al. 1995, Mackintosh et al. 1995, Mackintosh et al. 1994 and Mackintosh et al. 1994a).

## 1.2 Why marry nanomaterial and organic semiconductor science?

The colossal rise in nanoscience over the last two decades has been initiated by the advances in production and understanding of the properties of low dimensional nanostructures and nanomaterials, in which at least one of the dimensions falls within 1-100 nm (Alvisatos et al. 1996, Becerril et al. 2005, Ong et al. 2005 and Yin et al. 2004). Research has focused on low dimensional nanostructures due to their unique properties superior to those of the bulk material, attributed to their surface (Ball et al. 1992), quantum size (Goldstein et al. 1992) and macroscopic quantum tunneling effects (Reed et al. 1989). Highly developed synthetic procedures, with carefully controlled solid state properties, in inorganic semiconductor and metal nanomaterials, have resulted in a rich array of nanoscale devices with superior properties to those of conventional microelectronics and optoelectronics (Alvisatos et al. 1996, Shipway et al. 2000 and Yin et al. 2004). In the last decade, headway has also been made in organic macromolecule nanostructure (conducting polymer, semiconducting polymer and biopolymer) synthesis and property development (Becerril et al 2005, Hoeben et al. 2005, Jang et al. 2002 Kasai et al 1997, Nakanishi et al 1998 and Ong et al 2005).

Until recently there was little interest in nanomaterials composed of small organic conjugated molecules, as size dependent optical and electronic properties were not predicted, as the small exciton Bohr radius in organic semiconductors (relative to inorganic semiconductors) dictates that the nanoparticles could be no larger than a couple of nm, to present traditional quantum confinement properties (So et al. 1992). Also nanofabrication issues were anticipated, as they have lower melting temperatures, thermal instability, and poorer mechanical properties than their inorganic counterparts. Still research into these materials went ahead because of the wide structural diversity in organic molecules, facile tunability of their properties, cheap production methods, biocompatibility and easy hybridization with inorganic and metallic nanostructures (Fu et al. 2001, Gong et al. 2002, Latterni et al. 2006 and Winiarz et al. 1999).

Nanofabrication has made colossal progress, with a new nanofabrication approach, different to that of the inorganic nanomaterials, supramolecular assembly. Supramolecular assembly, defined as molecular assembly using noncovalent interactions, relying mainly on hydrogen bonds (H-bonds) and  $\pi$ - $\pi$  stacking, and to a lesser extent van der Waals and solvophobic interactions, has been successfully implemented to make an extensive range of nanostructures with well controlled sizes and shapes (Hartgerink et al. 2001, Hoebein et al. 2005, Jonkheijm et al. 2003, Kim et al. 2011). Organic nanostructures and their assemblies have now demonstrated novel and improved properties to those of the bulk materials and have been applied in a wide variety of opto-electronic and electronics devices (Cassagneau et al. 1998, Cui et al. 2008, Kasai et al. 1997, Fu et al. 2001, Piok et al. 2003, Winiarz et al. 1999, van Nostrum et al. 1995 and Zhao et al. 2008). Nanostructures have been assembled directly in the solid state, using liquid crystal organic semiconductors, and in solution using specific supramolecular interactions, commonly  $\pi$ - $\pi$ , hydrophobic and H-bonding interactions and then deposited on substrates (Cui et al. 2008 and Hoebein et al. 2005). Self-assembly at liquid/liquid and solid/solution interfaces has also been investigated (Kim et al. 2011). Self-assembly is still at the early stages. However, the combination of solution-based large scale synthesis of these molecules with self-assembly into



functional low dimensional nanostructures, nanodevices and nanosystems represents a viable approach to high volume affordable nanotechnologies.

Several novel, size-dependent optical and electronic properties have now been demonstrated with these materials, although the structure/property relationship in organic nanoparticles is as yet, far from understood (An et al. 2002, Kasai et al. 1997, Fu et al. 2001 and Zhao et al. 2008). For example, in selected cases, similar to inorganic particles, there is a correspondence between organic particle size and optical absorption (Fu et al. 2001). However, this effect may not originate from so-called quantum confinement due to the small radius of the organic exciton (Xiao et al. 2003). This change in optical absorption with particle size may be attributed to a surface effect (Fu et al. 2002) or an aggregate effect (Fu et al. 2001 and Xiao et al. 2003) or increased intermolecular interactions induced by lattice change (Kasai et al. 1997). Another fascinating new property, referred to as aggregation induced enhanced emission (AIEE), has presented in a few nanoparticles, where the nanoparticles present a substantial increase in the fluorescence emission intensity as compared with that of the bulk sample (An et al. 2002, Chen et al. 2004 and Lim et al. 2004). This is highly unusual as typically organic conjugated molecules are highly emissive in dilute solutions but when they aggregate and form films they become weakly luminescent. The AIEE effect is not yet resolved but has been linked to the molecular shapes, conformational flexibility, intramolecular movements, packing structure and organizational morphology (Bao et al. 2006, Dong et al. 2007, Li et al. 2004, Sun et al. 2007, Tong et al. 2007 and Tong et al. 2006). 1D organic nanomaterials, in particular, have displayed some novel luminescent behaviours, such as fluorescence narrowing with decreasing nanowire diameter (Zhao et al. 2006a, Zhao et al. 2007 and Zhao et al. 2008a). Finally, as the intermolecular interactions in organic materials are of the weak supramolecular type, the electronic and optical properties of these nanomaterials are significantly different to those of inorganic materials. There is massive potential with these nanomaterials, as the organic small semiconducting molecules have an extensive variety of molecules, which are readily functionalised to tune properties and assembly.

### 1.3 Thesis Summary

In this thesis, ICAT was self assembled in solution, and at several solution/solid interfaces, creating a range of low dimensional nanostructures with tailored shapes and sizes, which were assembled in thin films with a variety of morphologies. Bulk films were also deposited on varied substrates from molecularly dissolved ICAT solutions. The thin film morphologies and microstructures were analysed with AFM, SEM and optical microscopy. The basic aggregate properties in solution were analysed with NMR, fluorescence and UV-visible spectroscopy. The thin films were deposited on FET devices, to study the assembly/property relationship and assess the potential of this molecule in organic electronics.

Chapter one introduces the massive impact of organic semiconductor molecules and their nanomaterials in electronics and optoelectronics today. Chapter two follows with the history of the organic semiconductor and a review of indole based polymers and small molecules. Chapter three reviews organic 1D nanostructures. Chapter 4 provides a detailed introduction to the OFET device and chapter 5 an explanation of how the AFM and SEM work.

In chapter 6 the ICAT synthetic procedure is described and spectral analysis provided, which established that the pure ICAT molecule was synthesised. The experimental methodology is provided detailing NMR fluorescence, and UV-visible spectroscopy analysis of ICAT solutions at a range of concentrations, with a range of solvents. The spectroscopy results were interpreted as ICAT aggregates were assembled at raised concentrations, which displayed AIEE properties.

In chapter 7, the experimental methodology, describing the controlled assembly of ICAT at the solution/solid interface, using glass substrates functionalised with a variety of SAMs, is provided. The film morphologies were discussed with regards to understanding the assembly process and potential device application.

In chapter 8, an immersion based-deposition technique that produced vertically aligned ICAT 1D nanostructures on surfaces, as a function of immersion time, is detailed. The assembly process was followed as a function of immersion time and the results discussed in terms of heterogeneous nucleation and subsequent growth.

Chapter 9 provides the details of how solution based techniques were developed and used to deposit ICAT thin films onto FET devices. The resulting film morphologies were discussed in terms of application potential

The OFET devices fabricated in chapter 9, were tested in chapter 10. The testing conditions are detailed and the results discussed in terms of the ICAT film morphology/activity relationship and the application potential for the ICAT molecule and its assemblies.

Chapter 11 concludes the thesis.

## **Chapter 2**

# **Organic semiconductors**

## 2.1 Conducting polymers

Conducting polymers and small functional organic aromatic molecules have sparked interest in recent years due to their diverse applications in fields including coatings for electrostatic discharge protection (Soberanis et al. 2009), electrodes for metallization, batteries (Goto et al. 2008 and Pandey et al. 1988a), field effect transistors, (Shao et al 2011), diodes, (Cassagneau et al. 1998 and Tang et al. 1998), light emitting diodes (LEDs), (Piok et al. 2003 and Burroughes et al. 1990), all polymer electronic circuits, (Drury et al. 1998), information storage (van Nostrum et al. 1995), supports for pharmaceuticals (Chaubey et al. 2000), chemical and biological sensors (Bieganski et al. 2006 and Pandey et al. 1999) and artificial muscles (Baughman et al. 1996). An intrinsically conducting polymer, which is also commonly referred to as a synthetic metal, is defined as an organic polymer that possesses the electrical, electronic and optical properties of a metal whilst retaining attractive polymeric properties, such as flexibility and ease of processing. The basic prerequisite for a conducting polymer is a conjugated structure which is redox active. The two main genres in the field of conducting polymers are the polyenes and polyaromatics. In addition to the traditional conducting polymer,  $\pi$ -conjugated large molecules (referred to as  $\pi$ -conjugated oligomers) are becoming increasingly popular as they are structurally well defined with facile purification processes and can form highly ordered thin films through vacuum deposition (Martin et al. 1999).

As early as the 1930s, it had been postulated that an infinitely long chain joined by alternating single and double bonds would be electrically conducting. More specifically, it was expected that an infinitely long, one dimensional arrangement of  $\pi$ -electrons forms a half filled band, or the highest occupied and the lowest unoccupied  $\pi$ -electron bands merge with each other, thus creating metallic behaviour. Conducting polymers had been discovered at that time but were discarded as they were produced in the form of a black intractable powder which was insoluble and therefore unusable. The first step

towards scientific salvation was in the 1950s when Natta polymerised acetylene and produced a black intractable powder, which was pure enough to be properly characterised (Shirakawa et al. 2001). This polymer that Natta produced was semiconducting but unfortunately it was in a form that was totally unprocessable.

The real breakthrough came in 1967, when polyacetylene was synthesised directly in the form of a thin film by a fortuitous error (Ito et al. 1974). These films were far easier to characterise and much more applicable than the former powder form. These first films were composed of 20 nm fibrils and 2/3 void space. Unfortunately these polymer films were insulating and therefore not that attractive to industry. The ultimate discovery was made finally in 1976 when, through redox doping with bromine, these films were elevated from insulating or semiconducting to metallic conductivities (Shirakawa et al. 1977). This was realised with polyacetylene when it was demonstrated that the conductivity could be varied easily over twelve orders of magnitude. Since then a great deal of research has been dedicated to conducting polymers, as from that point onwards they were easily processable in their thin film form and their conductivity could be readily tailored to fit industrial requirements.

## 2.2 Electronic and chemical structure

A polymer may be defined simply as a macromolecule, which consists of a great number of more or less repeating units that are coupled to each other forming a chain. Conducting polymers are constructed in the same manner as other polymers but in addition they possess linear or aromatic carbon chains which have alternating double and single (conjugated) bonds.

The electronic structure of polyacetylene (PA), which is one of the most structurally simple conducting polymers is now considered. Three of the four valence electrons on each carbon in the polymer chain occupy a hybridized  $sp^2$ -orbital, which is a linear combination of the spherical s-orbital and two lobed p-orbitals. These  $sp^2$ -orbitals



consist of three lobes in a trigonal planar arrangement. Two of these lobes form sigma bonds with adjacent carbon atoms and the third bonds with a hydrogen atom. The fourth valence electron of each carbon atom resides in a  $p_z$ -orbital that is perpendicular to the plane of the  $sp^2$ -orbitals. The electronic wavefunctions of the  $p_z$ -orbitals on adjacent carbon atoms overlap and form the delocalised  $\pi$ -band. The electrons in the sigma bonds form the backbone of the chain and dominate the mechanical properties of the polymer and the delocalised  $\pi$ -electrons determine the electronic and optical properties of the polymer.

The sigma bonds form completely filled low lying energy bands that have a much larger ionisation potential than the  $\pi$ -electrons and thus do not significantly contribute to the electronic or optical properties at IR, visible and soft UV wavelengths. The  $\pi$ -bonds form an energy band in which each carbon contributes one electron and thus the band should be half filled due to spin degeneracy. Thus metallic behaviour would be predicted. In reality PA is a semiconductor rather than a metal due to the formation of a band gap, between the filled bonding states ( $\pi$ -bands) and the empty anti-bonding states ( $\pi^*$ -bands), lowering the energy of the filled states on account of Peierls instability (Heeger et al. 2001). The Peierls theorem states that a one dimensional system (the PA long carbon chain) with a half-filled band, distorts creating a gap at the Fermi level (Hoffmann et al. 1991). The semiconducting state is therefore energetically more favourable than the metallic one.

The band gap, which determines the optical and electrical properties in conjugated polymers ranges from 0.8 to 4 eV, spanning the entire range from infrared (IR) to UV and is dependent on the extent of  $\pi$ -delocalisation. Also interchain interactions,  $\pi$ - $\pi$  stacking and side groups play a major role in charge transport in conducting polymers. Typically as conducting polymer films are highly amorphous and full of defects, there is only weak overlap between the  $\pi$ -orbitals between neighbouring polymer chains, thus electrons and holes tend to be delocalised along individual chains although they may hop

between chains. Charge transport in conducting polymers is both complex and not well understood.

## 2.3 Doping

Typically when doped, a conducting polymer changes from an insulating or semiconducting state with a small conductivity of between  $10^{-10}$  to  $10^{-5}$   $\text{Scm}^{-1}$  to a metallic state with a conductivity range of between 1 and  $10^4$   $\text{Scm}^{-1}$ . In 2001, the conductivities attainable for electronic polymers reached a historic new level when superconductivity was demonstrated in regioregular poly(3-hexylthiophene) (Schon et al. 2001). Unfortunately this polymer only operated in the superconducting regime when in a thin film form in a field effect transistor configuration at a low temperature (ca. 2K).

Before the unique protonic acid doping of polyaniline, during which the number of electrons associated with the  $\pi$ -backbone remains constant, while the energy levels are rearranged (Chiang et al. 1977), the only doping method used for conducting polymers was redox doping. This involves partial removal (oxidation) or addition (reduction) of electrons from or to the  $\pi$ -backbone of the polymer. Doping is reversible and may be carried out chemically, electrochemically or by methods involving no dopant ions.

All conducting polymers, for example poly-(para-phenylene) (figure 2.1a), polypyrrole (figure 2.1b), polythiophene (figure 2.1c), polyfuran (figure 2.1d) and polyaniline (figure 2.1e) illustrated in figure 2.1 undergo either p and/or n-redox doping by electrochemical and/or chemical methods. Simple examples illustrating p and n-chemical doping follow.

The partial oxidation of a  $\pi$ -backbone (p-doping) was first discovered when *trans*-(CH)<sub>x</sub> was treated with iodine, as illustrated in equation 2.1 (Chiang et al. 1977):



where  $y \leq 0.07$ .

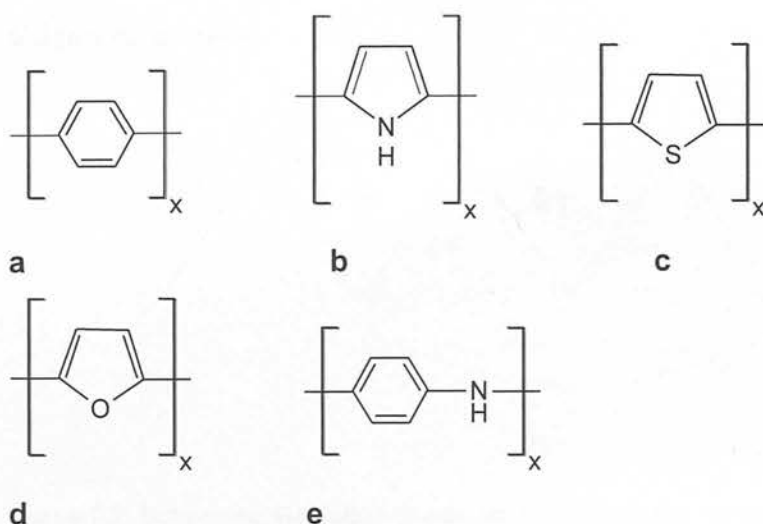


Figure 2.1: Selected examples of well researched conducting polymers, which are redox active, where figure 2.1.a is poly-(para-phenylene), figure 2.1b is polypyrrole, figure 2.1c is polythiophene (figure 2.1c), figure 2.1d is polyfuran and figure 2.1e is polyaniline (MacDiarmid et al 2001).

There was a conductivity increase from  $10^{-5} \text{ Scm}^{-1}$  to  $10^3 \text{ Scm}^{-1}$  that accompanied this reaction. Approximately 85% of the positive charge is delocalised over 15CH units (depicted in figure 2.3 for simplicity over 5 CH units) giving a positive soliton, schematically depicted in figure 2.2. A neutral soliton corresponds to an electronic state in the middle of the otherwise forbidden energy gap, and has a spin of a half but carries no charge. It can be created through a defect in the chain or through the doping process, where the added charge energetically prefers to reside in soliton states in the band gap. When the polymer is oxidized through doping, the single unpaired electron of the neutral soliton can be removed, thus creating a positive charged soliton. Since the original electron in the neutral soliton has been removed, the spin has been removed also. Thus the positively charged soliton has no spin.

p-Doping may be accomplished by electrochemical anodic oxidation by immersing a trans-(CH)<sub>x</sub> film in, for example, a solution of LiClO<sub>4</sub> dissolved in propylene carbonate and depositing it on the positive terminal of a direct current (DC) power source, while

the negative terminal is attached to an electrode and also immersed in the solution (Nigrey et al. 1979).

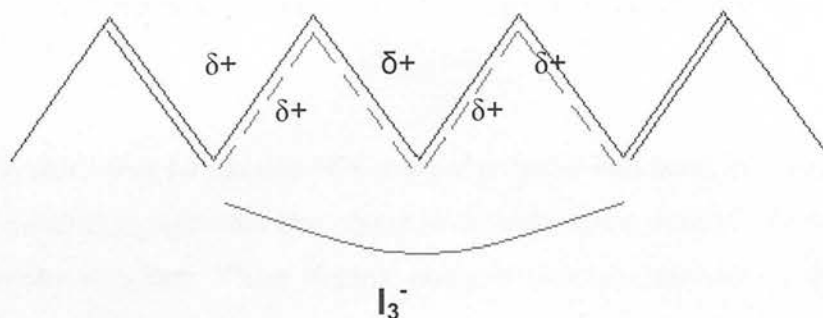
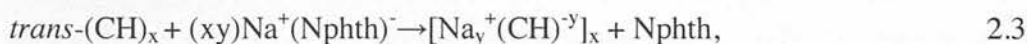


Figure 2.2: Schematic illustration of a positive soliton, taken from MacDiarmid et al 2001.

p-Doping may be accomplished by electrochemical anodic oxidation by immersing a  $\text{trans}-(\text{CH})_x$  film in, for example, a solution of  $\text{LiClO}_4$  dissolved in propylene carbonate and depositing it on the positive terminal of a direct current (DC) power source, while the negative terminal is attached to an electrode and also immersed in the solution (Nigrey et al. 1979).

The partial reduction of the polymer  $\pi$ -backbone, referred to as n-doping was also discovered using  $\text{trans}-(\text{CH})_x$  when it was treated with a reducing agent (Chiang et al. 1977). Equation 2.3 illustrates the n-doping process for this polymer with a sodium naphthalene reducing agent:

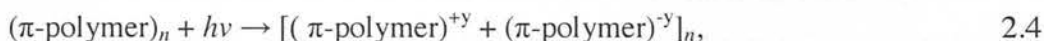


where  $y \leq 0.1$  and Nphth is naphthalene.

As a result of this reaction, the antibonding  $\pi$ -system becomes partially populated and there is a conductivity increase of about  $10^3 \text{ Scm}^{-1}$ . The n-doped polymers discovered here were more stable than the p-doped equivalents.

n-doping may be carried out using an electrochemical cathodic reduction (MacInnes Jr et al. 1981). For example, the *trans*-(CH)<sub>x</sub> film may be immersed in a solution of LiClO<sub>4</sub>, dissolved in tetrahydrofuran and attached to the negative terminal on a DC power source with the positive terminal attached to an electrode also immersed in the solution.

The doped systems thus far, consist of a charged polymer backbone with counter dopant ions. There are doping processes that do not involve the incorporation of counter doping ions in polymer structure. These doping methods produce transitory doped species, which have similar spectroscopic signatures to polymers containing dopant ions. Photo-doping is an example of such types of redox doping. During the photo-doping process the polymer becomes locally oxidized and (near by) reduced by photo-absorption and charge separation occurs (electron-hole creation and separation into free carriers) as shown in equation 2.4:



where  $y$  is the number of electron-hole pairs. Following photoexcitation from the ground state to the lowest energy state, recombination to the ground state can be either radiative (luminescence) or non-radiative. When the polymer is irradiated solitons are formed. However, when the radiation is discontinued the solitons disappear rapidly as the electrons and holes recombine. In the case of photo-excitation the doping is only transient and lasts until the excitations are either trapped or decay back to the ground state. Photoconductivity is observed when a potential is applied during irradiation and the electrons and holes separate. Charge-injection doping is the other doping method that does not involve counter dopant ions in the polymer structure and is discussed later as this method is utilised in this thesis.

## 2.4 General properties

Typically the magnitude of conductivity of conducting polymers is far inferior to that of metals. However, conducting polymers even with their inferior conductivities still have a great deal to offer in their unique blend of electronic, mechanical and processing properties. The ease of processability, in the form of melt and solution processing, is particularly attractive to industry. Their unique optical and electronic properties combined with other characteristics such as low density, plasticity and elasticity may revolutionise the optoelectronics industry. The low toxicity and non-energy intensive synthesis and processing satisfy a variety of increasingly important ecological targets. The fact that many of them are chemically inert and non-toxic (more research into long term degradation products is required) means they have great potential in biotechnology.

Unfortunately there are some undesirable properties, which are prevalent in many conducting polymers. Most of them are highly insoluble and are therefore extremely difficult to process. To combat this insolubility, several strategies have been researched including side chain or polar group attachment to the polymer backbone (Leclerc et al. 2004), oligomer production (Garnier et al. 1993), electrochemical processing (Goto et al. 2008) and in situ polymerisation (Jensen et al. 2004). One particularly popular approach is to use  $\pi$ -conjugated oligomers, which tend to be much more soluble and more readily purified than conducting polymers (Hoeben et al. 2005). Also the precise chemical structure and conjugation length of oligomers give rise to further attractive properties, including defined functional properties, enhanced control over supramolecular architecture and ordered thin film formation. This approach is adopted in this thesis.

Another major problem is that the doping process tends to produce undesirable side effects. Chemically doped conducting polymers are not stable in air nor are they thermally stable much above room temperature. The majority of chemicals used to dope the polymers are extremely toxic (e.g.  $\text{AsF}_5$ ,  $\text{I}_2$  and  $\text{Br}_2$ ). Another unattractive by-product of the chemical doping process is that after doping the polymers tend to become brittle



where they were previously flexible. There has been some success with alternative doping methods, such as electrochemical doping, photo-doping and charge-injection doping (discussed further in section 2.3). In particular, the electrochemically doped conducting polymers tend to be more stable in air than their chemically doped counterparts (Sun et al. 1989).

A lack of understanding of the assembly process and the fact that the majority of the conducting polymer structures have not been solved has certainly hindered progress. The fact that conducting polymers tend to be highly insoluble and poorly crystalline renders characterization extremely difficult. To date most structural data has been obtained through indirect methods (mainly optical spectroscopy), which is not ideal. Further research on the assembly process and conducting polymer structures should help us achieve the goal of ordered conducting polymer films with desired morphologies.

Unfortunately the majority of conducting polymers are unstable in ambient conditions, as they can be sensitive to both the moisture and oxygen in the air and sometimes light (Chen et al. 2004). This severely limits their applicability in the electronics industry as they cannot compete with their inorganic counterparts. However, measures have been implemented to counteract this problem, such as protective encapsulation on conducting polymer electronic devices and long term operational stability has now been realized.

To conclude further enhancement of conductivities, optical properties, environmental stability and development of organic systems requires innovative thin film processing, further understanding of properties and assembly processes and computer simulation to provide fundamental understanding of charge injection and transport. Still the future for conducting organic materials and their hybrids with further research is very promising.

## 2.5 Polyindoles

A review is now provided on the relatively new conducting polymer polyindole and its derivatives, as the work in the thesis is centred around poly(indole-5-carboxylic acid) and the indole-5-carboxylic acid asymmetric trimer.

### 2.5.1 Introduction to indoles

Indole, as illustrated in figure 2.3a, and its derivatives are highly fluorescent with interesting properties, such as particularly pronounced solvatochromism (Jennings et al. 1998, Lami et al. 1995, Mackintosh et al. 1995, Mackintosh et al. 1994 and Steen et al. 1974). The sensitivity of the indole emission originates from the near degeneracy of two low lying electronic states, labelled  $^1L_a$  and  $^1L_b$  (Callis et al. 1991). Several mechanisms have been proposed to account for this large Stokes shift, including  $^1L$  level inversion (Lami et al. 1996), formation of a solvent-solution exciplex (Walker et al. 1967) and relaxation of the solvent dipoles around the increased dipole moment of the excited state relative to that of the ground state (Mataga et al. 1956). It has been proposed that in non polar media, emission arises from the  $^1L_b$  level, which lies at lower energy than the  $^1L_a$  state. While the  $^1L_a$  state becomes the fluorescent state in polar environments because it is more strongly stabilised by solute-solvent relaxation due to a greater dipole moment than the  $^1L_b$  level resulting in  $^1L_a$  and  $^1L_b$  level inversion.

It is of particular interest, as it is the fluorescent chromophore of the amino acid tryptophan (figure 2.3b) and therefore it could potentially probe the structure and dynamics of both proteins and peptides (Chen et al. 1990 and Tilstra et al. 1990).

Indoles were polymerised electrochemically for the first time by Touillon and coworkers in 1982 (Touillon et al. 1982). The resultant electropolymerised film deposited on the electrode surface was found to be semiconducting. This new example of a conjugated

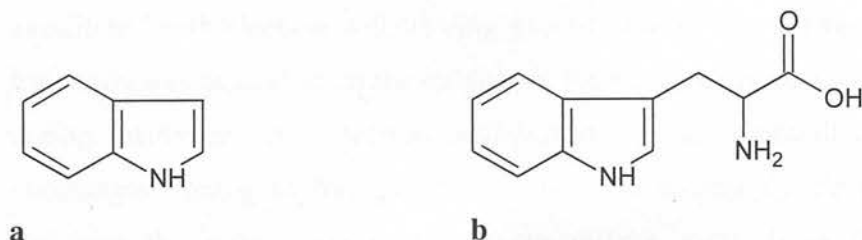


Figure 2.3: The structure of the indole molecule (figure 2.4a) and the amino acid tryptophan (figure 2.4b).

organic semiconductor sparked a great deal of interest from researchers, which eventually in 1994 led to the demonstration of a fluorescent emission from these films (Mackintosh et al. 1994). The majority of research into indole electropolymers has been dedicated to resolving the structure, electrochemistry and establishing the photophysics.

## 2.5.2 The electropolymerisation of indoles

Ever since it was first demonstrated that indoles could be electropolymerised to form conducting polymer films, there has been considerable debate over the molecular structure of the film and polymerisation mechanism. Initially it was proposed that indoles would polymerise in a similar fashion to other heterocycles such as pyrroles, to give a linear polymer. A number of conflicting structures and mechanisms were proposed by researchers (Lewis et al. 1997, Talbi et al. 1997, Waltman et al. 1984 and Zotti et al. 1984). In all the cases it was assumed that the structure consisted of a linear chain of monomers linked through two sites.

The 5-substituted indole electropolymerisation is of particular relevance here as 5-substituted indoles are researched in this thesis. Waltman and co-workers analysed the 5-substituted indole electropolymerisation and suggested the capacity to form a conducting film was a function of electronic effects rather than due steric effects (Waltman et al. 1984). This proposal was attributed to the fact that bulky substituents, such as bromine, did not inhibit film formation while smaller substituents such as hydroxyl did. Waltman actually found that the highest quality films were produced using indole monomers

substituted with electron withdrawing groups. It was thus suggested that the polymer formation was dependent on the stability of the monomer radical cation, which is formed during oxidation. An electron withdrawing group destabilises a cation, which encourages linking to form a polymer whereas a strongly electron donating group stabilises the cation, allowing them to diffuse away from the electrode before polymerisation can occur.

Then research commenced into solving the molecular structure of these films. Talbi and co-workers studied the electrochemical oxidation of both 5-cyanoindole (Talbi et al. 1997) and 5-nitroindole (Talbi et al. 1998) and performed a theoretical analysis of indole polymerisation using Hartree-Fock calculations (Talbi et al. 1998a). Talbi proposed a 1,1-3,3 bonding mechanism, which was in direct conflict to the structural proposals of Mount and co-workers (Jennings et al. 1997 and Mackintosh et al. 1995).

Mount and co-workers carried out substantial work into resolving the structure of the 5-substituted indole electropolymerised films. Initially research was centred around indole-5-carboxylic acid and 5-cyanoindole because they were potentially useful in fast response pH sensors (Bartlett et al. 1992). It was found that in both indole derivatives, the films consisted of two chemical species that were separated by their different solubility in dimethylformamide (DMF). Characterisation of these species was performed using mass, UV-visible, fluorescence, IR and NMR spectroscopy, and it was suggested that the DMF-soluble product was an asymmetric trimer structure (indole-5-carboxylic acid asymmetric trimer), as illustrated in figure 2.4 and that the other DMF-insoluble species was a polymer consisting of linked trimers (Mackintosh et al. 1994).

This trimer consisted of three monomers, linked through their two and three positions, which is consistent with the research of Zotti (Zotti et al. 1994) and Talbi who also proposed binding through positions two and three (Talbi et al. 1998, Talbi et al 1998a and Talbi et al. 1997). In addition, there was evidence to suggest that the trimers linked through two of the one positions on each trimer, which accounts for the decrease in

intensity of the N-H stretch in the IR spectrum upon polymerisation, reported by Waltman and Tourillon (Tourillon et al. 1982 and Waltman et al.1984).

The proposed mechanism for the 5-substituted trimer formation and polymer growth electrochemically is described in equations 2.8 and 2.9:



where In,  $\text{In}_3^+$  and  $[(\text{In})_3^+]_n$  represents the 5-substituted monomer, oxidised trimer and oxidised polymer species respectively (Jennings et al. 1997).

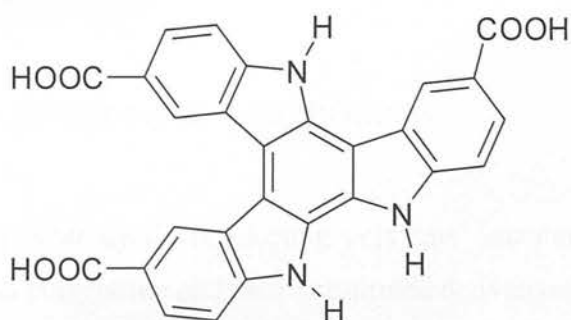


Figure 2.4: Structure of the electrochemically oxidised, 5-substituted indole trimer, as proposed by Mount et al. (Mackintosh et al. 1994).

Equation 2.8 illustrates the first step of the polymerisation, where the monomer oxidation occurs in the diffusion layer near the electrode thus producing a trimer film on electrode surface. The film acts as a surface on which further adsorption and oxidation of the monomer can occur, followed by further radical cation linkage and trimer formation, resulting in film growth. Once deposited, the second part of the process is initiated and the reaction, illustrated in equation 2.9, occurs where the trimers may undergo further oxidation and react with neighbouring trimers to form a polymeric

chain. It was found that the first step was kinetically favoured over the second step, hence controlling the monomer supply to the electrode allows some control over the polymer and trimer content of the film. Research involving a wider range of 5-substituted indoles confirmed this proposed mechanism (Jennings et al. 1997).

### **2.5.3 The chemical polymerisation of indoles**

There have been a few attempts to chemically polymerise indoles, which resulted in a complex mixture of products including various dimers, trimers and tetramers (Billaud et al. 1995, Bocchi et al. 1986, Ishii et al. 1988 and Ishii et al. 1988a). Unfortunately these chemical methods to date have been complex with very low yields and have produced a polymer with a much lower conductivity (several orders of magnitude) than the electrochemical films.

### **2.5.4 Indole properties and applications**

The studies of heterocyclic conducting polymers containing nitrogen atoms, such as polypyrrole and polyaniline and their substituted derivatives, have attracted considerable attention (MacDiarmid et al. 2001). Indole based polymers are structurally similar to the aforementioned conducting polymers but have scarcely been investigated. Recently polyindole has gained significant attention due to high thermal stability and interesting fluorescence and electrochemical properties (Jennings et al. 1997, Mackintosh et al. 1994 and Tourillon et al. 1982).

Thus far all of the indole polymer based films have been produced electrochemically. The electrochemically synthesised polyindole films have the advantages of fairly good thermal stability (Pandey et al. 1998a), high redox activity and stability (Jennings et al. 1997, Mackintosh et al. 1994 and Tourillon et al. 1982) and slow degradation rate in comparison with polyaniline and polypyrrole (Abthagir et al. 1998). However, the

electrodeposited polyindole films tend to exhibit poor mechanical properties and are difficult to characterize structurally due to their poor quality (Pandey et al. 1998, Talbi et al. 1998b and Tourillon et al. 1982). Studies of the morphology of electropolymerised polyindole and poly(indole-5-carboxylic acid) films revealed structurally poor films with highly irregular morphologies (Sivakkumar et al. 2005 and Tourillon et al. 1982).

The electroactive capacity for pure polyindole is reported as much lower (several orders of magnitude) than other commonly used polymers, such as polypyrrole and polythiophene (Tourillon et al. 1982). Research into enhancing the conductivity of indole based polymers has focused on self-doping electrochemical poly(indole-5-carboxylic acid) films (Mackintosh et al. 1994, Mackintosh et al. 1994a and Mackintosh et al. 1995). The anionic dopant ion  $\text{COO}^-$  covalently attached to the polymer backbone forces predominant cation movement during the doping/dedoping process. Self doped polymers offer the advantages of fast redox kinetics due to the absence of the need for the diffusion of an external dopant into the polymer matrix and enhanced stability. The conductivity of the electrochemically synthesised, self-doped poly(indole-5-carboxylic acid) films was found to be  $3.1 \times 10^{-3} \text{ Scm}^{-1}$  by Sivakkumar and co-workers (Sivakkumar et al. 2005). Abthagir and co-workers also established the conductivity of this film as within the  $10^{-3} \text{ Scm}^{-1}$  range at room temperature with a maximum conductivity of  $4.5 \times 10^{-2} \text{ Scm}^{-1}$  at 399K (Abthagir et al. 2004). Another successful approach to enhance electrochemical activity of the indole polymer was through electrochemically copolymerizing pyrrole and indole (Wan et al. 2001).

Currently polyindole films have only been used in very limited biological and electronic applications as indole science is relatively young compared with other conducting polymers. Polyindoles have been successfully applied in various batteries (Pandey et al. 1998a, Sivakkumar et al. 2005 and Zhijiang et al. 2005). Polyindoles have also been applied in the biotechnology field. Pandey and co-workers have constructed highly sensitive potassium and copper ion sensors using indole polymer modified electrodes which have great potential in analytical, biological and clinical fields (Pandey et al. 1999



and Pandey et al. 1998b). The suitability of poly(indole-5-carboxylic acid) to be used as a polymer matrix for one step enzyme immobilization was researched for potential application in biosensors. This molecule was selected because the carboxylic acid groups allow facile one step covalent binding of enzymes. Bieganski and co-workers successfully immobilized the enzyme tyrosinase onto the electrochemically formed poly(indole-5-carboxylic acid) film through the carboxylic acid group and demonstrated that the enzyme remained biologically active after the attachment to the polymer surface (Bieganski et al. 2005). However, when compared to other conducting polymer based sensors, where tyrosinase was trapped in polymer matrix, such as polypyrrole and polythiophene, much lower values of sensitivity were obtained.

Currently all of these applications are based on electrochemically synthesised polyindole and derivatives. There is however, an interesting line of research based on the oligomeric products of indole-3-carbonol (found in Brassica vegetables) following ingestion. These oligomeric products are under study as tumour preventative agents for several organs (Grose et al. 1992 and Riby et al. 2000). A major oligomeric product produced when indole-3-carbonol reacts with gastric fluids is a cyclic indole trimer (5,6,11,12,17,18 hexahydrocyclona[1,2-*b*:4,5-*b'*:7,8-*b''*]triindole).

Riby and co-workers researched this molecule and found that it was a strong agonist of the estrogen receptor signalling pathway and helped prevent activation and proliferation of estrogen dependent cultured breast tumour cells (Riby et al. 2000). Conformationally this molecule fits into the estrogen binding site of the estrogen receptor signalling pathways. The indole trimeric product here resembles the indole trimeric products formed as part of a polymer/trimer mixture in electrochemical synthesis of the indole monomer (Mackintosh et al. 1994). It would therefore be interesting to research this indole trimer product as a potential cancer preventative agent.

In conclusion polyindole is well worth researching as it has good thermal stability, a high redox activity, interesting fluorescence properties and is thought to be biologically



compatible. The fact that polyindoles do not polymerise in a linear fashion like other nitrogen containing conducting polymers may lead to new properties and supramolecular structures. The structure of the electrochemically produced poly(indole-5-carboxylic acid) is finally resolved and is potentially applicable in the electronic and biotechnology industry. In addition to self-doping the poly(indole-5-carboxylic acid) offers the advantages of enhanced solubility and has carboxylic acid groups available for enzyme immobilisation and may covalently anchor or weakly attach (through hydrogen bonds) the molecule to surfaces. The carboxylic acid group could potentially allow enhanced control of the assembly process in film formation.

Alas currently polyindole can only be made electrochemically or through complex chemical synthesis, both of which result in low, inhomogeneous yields. Polyindole thus far has very poor solubility and is virtually impossible to process. In fact the only way that films have been produced has been through electrochemical means. These electrochemically deposited polyindole films have highly irregular morphologies and exhibit poor mechanical properties. The most notable disadvantage is that the conductivity of pure polyindole, doped polyindole and self-doped poly(indole-5-carboxylic acid) is much lower (several orders of magnitude) than other commonly used polymers. In order to compete with other conducting polymers the lack of solubility, very difficult processing, low conductivity, poor (film) structural quality and inefficient synthesis of polyindole must be dealt with.

## **Chapter 3**

# **One dimensional (1D) organic nanostructures**

### 3.1 Introduction

Organic conjugated molecules are widely applied in the optoelectronics and electronics fields due to facile synthetic procedures, readily tailored properties through polyfunctionalisation and the potential for low-cost fabrication of flexible and/or large area devices. However, very recently the research focus has shifted from bulk molecular properties towards the self-assembly and synthesis of conjugated organic solid materials with low dimensional structures, which have distinct properties from those observed from the bulk materials (Cui et al. 2008 and Zhao et al. 2008). These novel properties include improved physical and chemical properties that are desirable for potential electronic and optoelectronic applications in areas such as solar energy conversion (Chen et al. 2011), information storage (Yang et al. 2005c), flat screens and displays (Takazawa et al. 2005), chemical sensors (Garjonyte et al. 2000) and device miniaturization (Zang et al. 2008b).

Since the discovery of carbon nanotubes in 1991, 1D inorganic and metallic nanostructures including wires, tubes, fibres, rods and belts have attracted a great deal of attention due to applications in the fabrication of electronic (Briseno et al. 2007), optoelectronic (Cui et al. 2012), electrochemical and electromechanical (Kim et al. 2011 and Xia et al. 2003) nanoscale devices as interconnects and functional units. It is generally believed that 1D nanostructures should provide a good system to investigate the electrical, thermal or mechanical property dependence on dimensionality and size reduction. Organic macromolecular 1D nanostructures composed of graphene (Geim et al. 2007), conducting polymers and biomolecules (Cui et al. 2008, Hartgerink et al. 2001 and Zang et al. 2008b) have also been under the spotlight in the last decade. Functional small planar conjugated organic molecule, (referred to as small organic molecules from this point onwards), based nanomaterials have however, attracted more attention recently than their inorganic and macromolecular counterparts. Three major factors lie behind the lack of research in this area. Firstly the fabrication methods for small organic molecule based nanomaterials are very limited as compared to that of inorganic

nanomaterials because of their comparatively low melting points, thermal instability and inferior mechanical properties. Secondly, there has been considerable difficulty in controlling the assembly of the organic nanostructures into aligned ordered arrays, which is essential for practical applications (Briseno et al. 2007, Leclerc et al. 2004, Tang et al. 2006, Zang et al. 2008b and Zhao et al. 2008). Again the commonly used, well developed fabrication methods for metal and oxide 1D nanostructure film preparation, such as chemical vapour deposition, thus far are not transferable to organic conjugated materials (Chen et al. 2001a and Ren et al. 1998). Finally, until recently, size dependent properties were not anticipated in organic nanomaterials because unlike the case of Wannier excitons in inorganic and metallic crystals, the optoelectronic properties of organic crystals are determined by charge transfer excitons and Frenkel excitons with a smaller radius (detailed in section 3.1). However, with a superior understanding of organic materials, progress has recently been made in these areas resulting in the construction of a few small organic molecule 1D nanostructures, which display novel optical and electrical properties (Cui et al. 2008).

The following section reviews 1D organic small molecule nanostructures, including preparation, properties and applications with a particular emphasis on nanorod preparation and electronic properties as they feature in this thesis.

### **3.2 Organic 1D nanostructure synthetic strategies**

The current lack of construction methodologies in this area has drawn researchers to focus on the development of facile, widely applicable fabrication methods to prepare small organic molecule 1D nanostructures. To date, there are limited 1D small organic molecule nanostructure fabrication techniques, as the well established inorganic 1D synthetic approaches tend not to be transferable to these materials. Several strategies including vapour, template (Fu et al. 2003) and molecular self-assembly (Takazawa et al. 2005) have been developed to prepare 1D structures from small organic molecules (Cui et al. 2008, Liu et al. 2003a and Wang et al. 2007).

Initially vapour deposition and template based fabrication methods were explored as both techniques had successfully produced inorganic and polymeric 1D nanostructures (Cui et al. 2008 and Xia et al. 2003). However, template based fabrication techniques tend to be arduous and involve multistep preparations with complex chemistry (Becceril et al. 2005, Berry et al. 1996, Fu et al. 2003, Kim et al. 2003 and Minelli et al. 2005). Thus far only surfactant micelle based soft templates have been successfully applied in the production 1D nanostructures from small organic molecules (Fu et al. 2003). A couple of researchers have successfully applied hard template methods to fabricate 1D small organic molecule nanostructures (Lee et al. 2002 and Zhao et al. 2005a). Nevertheless, a protocol to release the delicate organic nanostructures from the hard template without damage is needed before the hard template fabrication method may be widely applied.

The vapour deposition method delivers well defined 1D inorganic and polymeric materials but results in extremely polydisperse particle yields, when applied to small organic molecules. Limited success in this area has been achieved through complicated technique developments designed to control the local supersaturation level, including adding templates and introducing solid-phase reactions (Lee et al. 2002 and Liu et al. 2003).

So in recent years research into organic 1D nanostructure fabrication has centred on facile single-step self-assembly in the liquid phase. Supramolecular assembly is the key to self assembled nanostructure fabrication (Elemans et al. 2003 and Hartgerink et al. 2001). Non-covalent interactions, such as hydrogen bonding and  $\pi$ -stacking interactions, have been used in the construction of elaborate organic nanoarchitectures (An et al. 2004, Schoonbeek et al. 1999, Wang et al. 2007 and Zhao et al. 2005). Hydrogen bonding, in particular, has attracted much attention due to its specificity and high degree of directionality (Liu et al. 2004 and Wang et al. 2007). The principal flaw in the molecular self-assembly fabrication methodologies thus far, is the lack of control over the resultant nanostructure size and shape and therefore function (Djurisic et al. 2008).

However, a few researchers have recently demonstrated noteworthy morphology control and have produced a wide array of nanostructures, using self-assembly based fabrication techniques (Balakrishnan et al. 2006a and Wang et al. 2007).

Control over the assembly process has been achieved through substituting varied functional groups at varied positions on the organic functional molecule (Balakrishnan et al. 2006a and Wang et al. 2007). Limited control over the self-assembly of the organic material in the solvent (organic dispersion) and consequently the size and shape of the organic 1D nanostructures has been demonstrated through solvent selection, temperature and sonication of the organic dispersion (Takazawa et al. 2005, Zang et al. 2008b and Zhao et al. 2005). Rapid dispersion of these organic molecules from a good solvent, in which the molecule dissolves, into a poor solvent where the molecule has limited solubility, is used to form self assembled 1D aggregates through  $\pi$ - $\pi$  stacking, and has successfully produced nanofibres of a well controlled length and size (Tian et al. 2004, Zang et al. 2008 and Zhao et al. 2005). Yao and co-workers applied this method to prepare more sophisticated 1D structures with a comparatively high monodispersity, with the formation of single-crystalline nano and sub-micrometer tubes, by inducing the self-assembly in liquid of 2,4,5 triphenylimidazole in water at different temperatures (Zhao et al. 2005). This method has limited applications, as when there are strong lateral interactions from planar molecules through side chains or functional groups (e.g., hydrogen bonding or hydrophobic interactions), the crystallization (precipitation) proceeds too quickly when the molecule is dispersed in the poor solvent thus producing very large agglomerates. Also, there is very little control over the nanostructure orientation and subsequent film morphology when depositing them on bulk surfaces.

When the strength of the  $\pi$ - $\pi$  stacking and the side chain interactions of the organic molecules are not well matched and consequently the self-assembly of the organic molecules is difficult to control by simple solution-based processing, gelation can be used as an alternative (An et al. 2004, Balakrishnan et al. 2006, Dautel et al. 2008, Schoonbeek et al. 1999 and Zang et al. 2008). Entangled nanofibrils tend to form

through the gelation of small organic planar molecules typically with long alkyl chains or steroid groups as they become highly organized, with optimal  $\pi$ - $\pi$  stacking in cooperation with side-chain association (Abdallah et al. 2000 and Balakrishnan et al. 2006).

Finally the self-assembly of these organic molecules on bulk surfaces may also be induced through solvent evaporation of the organic molecular solutions, although the size, morphology and uniformity of the aggregates are notoriously difficult to control (Datar et al. 2006 and Zhao et al. 2006). Nevertheless, Yao and co-workers have achieved well controlled 1D assembly of 2,4,5-triphenylimidazole (TPI) on glass and quartz substrates with this technique by suspending the substrates in vials of TPI solution and sonicating the solution during the solvent evaporation process (Zhao et al. 2006).

### **3.3 Organic 1D nanostructure properties and applications**

Nanoscale 1D organic small molecule structures have drawn attention in recent years because of efficient charge transport in devices due to favourable molecular packing and interface alignment, surface and interface effects, resulting in novel physical and chemical properties and anisotropic charge transport possibilities. Organic low dimensional nanostructure properties are highly dependent on the particle chemical structure, morphology, size, dimensions and assembly (Zhao et al. 2008). The desired chemical structure is achieved effectively through molecular design. However, controlling the morphology, size and assembly of the organic 1D nanostructures is extremely difficult. Interestingly while controlling the different hierarchies of organization going from the molecular stage to the actual device is acknowledged as the most critical issue in this field, it has been addressed to a much lesser extent than the molecular design. Consequently there are very few studies of organic 1D nanostructure properties and their applications.



Organic semiconducting nanoparticles in general have drawn interest in the optics field due to the combination of optical tunability, high luminescence efficiency and optical properties that are fundamentally different from those of inorganic particles (detailed in section 3.1). However, 1D organic crystalline materials in particular have displayed some novel luminescent behaviours, such as fluorescence narrowing with decreasing nanowire diameter (Zhao et al. 2006a, Zhao et al. 2007 and Zhao et al. 2008a).

In recent years small organic molecule 1D nanostructures have been reported to display attractive optoelectronic and electronic properties for applications, such as organic solar cells, optical waveguides and lasers (Briseno et al. 2007, Pramanik et al. 2007, Takazawa et al. 2005, Tang et al. 2006, Yang et al. 2005c, Zang et al. 2008 and Zhao et al. 2008a). 1D organic small molecule nanostructures predominantly self assemble along the  $\pi$ - $\pi$  stacking direction which favours high charge-carrier mobilities as a result of the strong intermolecular coupling between the packed molecules according to theoretical modelling and calculations (Curtis et al. 2004, Lemaire et al. 2004 and Rocherfort et al. 2002). Thus far there is very little experimental evidence to verify this theory. However, more recently Che and co-workers demonstrated effective long-range  $\pi$ -delocalisation within a N,N'-di(propoxyethyl)perylene-3,4,9,10-tetracarboxylic diimide nanobelt (PTCDI) and Dautel and co-workers demonstrated charge delocalization in amorphous organic oligomeric oligo(phenylenethienylene) derivative nanorods over several micrometers (Che et al. 2007a and Dautel et al. 2008). Che then went on to demonstrate enhanced electrical conductivity through surface doping of the PTCDI nanobelt which was enabled through the long-range  $\pi$ -electron delocalisation.

In the electronics field, FETs are currently one of the promising applications for organic small molecule 1D nanostructures, (as the active semiconducting layer), for the following reasons. Device output from FETs with conducting polymer based active layers tends to be unsatisfactory due to poor charge transport within the active layer. While optimization of the electrical conductivity in these devices may be achieved through a single crystalline phase, these large scale crystals are very difficult to



synthesize, are fragile to handle and moreover it is very challenging to direct the molecular orientation of the molecular stacking within the crystal when aligning it with the electronic device, where directional control over transport is desirable. Thus organic small molecule 1D nanostructures which are easy to handle and have molecular packing which favours efficient directional charge transport and facile alignment with device interfaces are currently under investigation as the active layer in FET devices. Favourable carrier mobilities have recently been obtained with organic 1D nanostructure functionalised FET devices (Briseno et al. 2007, Moon et al. 2004, Tang et al. 2006 and Xiao et al. 2007).

Well Controlled assembly of 1D organic small molecule nanostructures into ordered arrays is absolutely crucial for device performance and unfortunately the majority of nanostructure deposition methods used today do not fulfil this requirement (chapter 4). Thus far the active semiconducting layers in these FET devices are composed of random assemblies and/or sparse coverage of 1D nanostructures, which tend to have poor contact with the device (Briseno et al. 2007, Shea et al. 2007 and Tang et al. 2006). In fact the electronic properties range from non operational to extremely favourable within a single device and therefore a considerable amount of work is required here before these devices are fit for industry (Briseno et al. 2007 and Tang et al. 2006). To date, detailed 1D nanostructure film morphology/property relationship studies in these devices have not been possible due to the random nature of the 1D nanostructure assemblies in the FETs. Limited progress however, has been made in similar organic FET devices that use either conducting polymer or organometallic small molecule 1D nanostructure films as the active semiconducting layer (Kline et al. 2005, Shea et al. 2007 and Yang et al. 2005d).

### 3.4 Conclusion

To conclude organic small molecule 1D nanostructures have attracted a great deal of attention, as they have many potential applications in diverse areas of the electronics

industry but a considerable amount of work still remains here as research in this area is still in its infancy. Several areas need to be addressed but particular attention is required in the development of fabrication methodologies for organic 1D nanostructures with desired morphologies and structures, understanding the optoelectronic properties of these structures and finally the production of well ordered thin films and patterns of these organic nanostructures on solid substrates.

## Chapter 4

### The organic field-effect transistor

#### (OFET)

## **Chapter 4**

# **The organic field-effect transistor (OFET)**

## 4.1 Introduction

Field-effect behavior was demonstrated in small organic molecules as early as 1964, (Heilmeier et al. 1964 missing) and in polymers in 1983 (Ebisawa et al. 1983) but until recently OFETs failed to have any major optoelectronic industrial impact, as their properties were far inferior to that of amorphous silicon thin film devices. OFETs could not compete with traditional inorganic amorphous silicon thin film transistors with field effect mobilities of  $0.5\text{--}1\text{ cm}^2\text{V}^{-1}\text{s}^{-1}$  and on/off ratios  $10^6\text{--}10^8$ . The field effect mobility quantifies the average charge carrier drift velocity per unit electric field and the on/off ratio is defined as the drain current ratio between the on and off states. Recently, however, field effect mobilities in OFETs, have overtaken inorganic transistor mobilities and OFETs based on vacuum-deposited small molecules have achieved mobilities of up to a staggering  $5\text{ cm}^2\text{V}^{-1}\text{s}^{-1}$  (Baude et al. 2003). Modern OFETs offer a viable alternative to traditional inorganic field effect transistors, in the form of easy, cheap and low temperature solution-processing (Sirringhaus et al. 2005). These processing properties make OFETs ideally suited for low-cost, large area electronic functions on flexible substrates OFET applications, include switching devices for active matrix flat panel displays based on liquid crystals, electronic paper displays (Wisnieff 1998), cost effective, simple, radiofrequency identification tags (Clemens et al. 2004) and sensing devices (Crone et al. 2001).

Charge mobility tends to be limited by the organic thin film morphology. The deposition of the organic semiconducting layer is the determining step of OFET fabrication, as the rest of the process is controlled by well established, conventional techniques. Solution based deposition techniques are preferred as vacuum sublimation requires sophisticated instrumentation and is expensive and have produced homogeneous films with excellent control over thickness and over large areas in limited cases (Bao et al. 1999a, Bao et al. 1996, Katz et al. 2000, Katz et al. 1999 and Meijer et al. 2003a). Unfortunately the most commonly applied solution deposition techniques spin coating and drop casting typically

produce films with variable thickness, morphology and electrical properties. The other popular solution deposition technique Langmuir-Blodgett can only be applied to amphiphilic molecules. Another major disadvantage of solution processing is that soluble polymers are required.

Currently the emphasis on OFET development is in establishing OFETs with high mobilities that are stable in ambient conditions (air, moisture and light exposure). So far the majority of research has focussed on organic semiconductor p-type conductivity (Brown et al. 1995, Chang et al. 2004, Kline et al. 2003, Laquindanum et al. 1997, Sirringhaus et al. 1999, Sirringhaus et al. 1998 and Veres et al. 20004) but recently there has been a drive to understand n-type and ambipolar organic semiconductors for use in complementary metal oxide semiconductor (CMOS) type circuits, p-n junctions and light emitting field effect transistors (Bao et al. 1998, Haddon et al. 1995, Horlet et al. 2011 and Newman et al. 2004) The primary reason for n-type OFETs lack of progress is the inherent instability of the anions, in particular carbanions that react with oxygen and water under ambient conditions. FET devices also provide a valuable insight into charge-transport and charge-injection physics of organic semiconductors and their structure property relationships, through their ability to control charge carrier concentration electrostatically rather than chemically. Other fundamental considerations for organic electronic devices include understanding the electronic structure of organic semiconductors, and their behaviour at the interface with the dielectric, and how the organic film microstructure, which can be quite complex, control their electrical characteristics.

## **4.2 The device**

The basic OFET operating principles and how the interactions between the materials used in the OFET substrate and the organic films being tested will affect the device output are introduced here. An OFET may be described as a capacitor (defined as a

device that can store energy in an electric field between a pair of conducting plates), where one plate is a conducting channel between two ohmic contacts, the source and the drain electrodes. The term ohmic means that the contacts have been designed to produce linear and symmetrical current-voltage characteristics. The charge carrier density in the channel is modulated through applied voltage on the gate electrode, which acts as the second plate in the capacitor. Depending on the gate bias, an OFET may be in an off or an on state. The OFET is in the off state if there are limited free charge carriers in the transistor channel between the source and the drain and it is in the on state if the free charge carriers enter the channel from the source and flow to the drain. In the on state, the charge carriers in the transistor channel are capacitively paired with the gate, thus forming a parallel plate capacitor with the transistor channel. The drain current is controlled by the gate to channel voltage, which modulates the charge carrier concentration in the transistor channel.

### 4.3 Device configuration

There are several different FET structures available but the most common is the MOSFET which stands for metal oxide semiconductor OFET, consisting of a gate insulated with a  $\text{SiO}_2$  layer with a metal or doped silicon substrate and can adopt the configuration, as used in this thesis, illustrated in figure 4.1. This structure is well adapted for low conductivity materials and is currently used in amorphous silicon transistors. The source and drain electrodes form direct ohmic contacts with the conduction channel. Low off currents are only possible with a low conductivity semiconductor. This OFET operates in the accumulation regime (defined in detail further on).

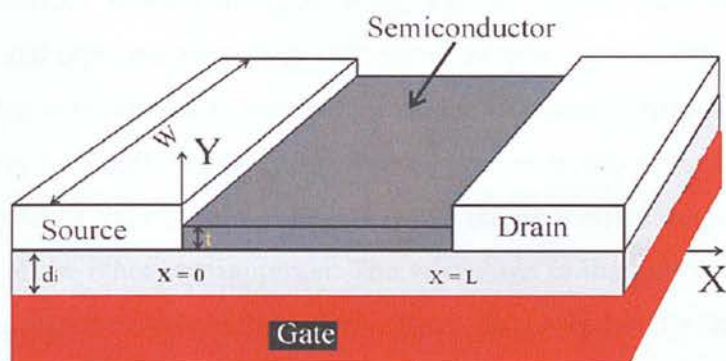


Figure 4.1: Schematic illustration of an OFET where  $d_i$  is the dielectric thickness,  $t$  is the semiconductor thickness,  $W$  is the channel width and  $L$  is the channel length.

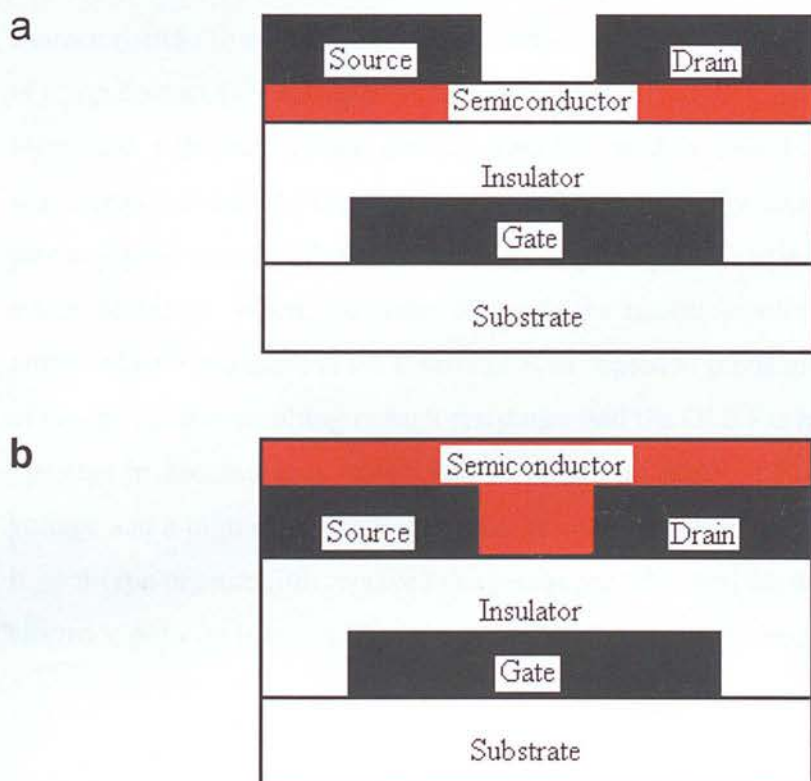


Figure 4.2: Schematic illustration of OFET device configurations, where (a) is a top contact device and (b) is a bottom contact device.

The top contact configuration, as illustrated in figure 4.2a, and bottom contact configuration, as seen in figure 4.2b, are the most widely used configurations. The source and drain electrodes are evaporated onto the organic film through a shadow mask in the top contact OFET device. In contrast, the organic film is deposited onto the gate dielectric with prefabricated source and drain electrodes in the bottom contact structure. The appeal of the top contact device is that the field effect mobilities tend to be superior to that of the other configuration. The advantage of the bottom contact configuration is that moisture exposure to the organic film is minimised in the OFET production process, as the organic film is the final step of the configuration process.

#### 4.4 Current-Voltage (IV) Characteristics

A polycrystalline pentacene based OFET is now used to demonstrate typical OFET IV characteristics (Dimitrakopoulos et al. 2002). Figure 4.3 illustrates the IV characteristics of a top contact OFET (figure 4.2a), with a polycrystalline pentacene film as the active layer, and a thermal silicon dioxide modified with a 1-diethoxy-1-silacyclopent-3-ene self assembled monolayer, as the gate insulator, a heavily doped n-type Si wafer as the gate and gold source and drain electrodes. This IV plot may be used to calculate the field effect mobility. When the gate electrode is biased positively with respect to the grounded source electrode the transistor is in depletion mode and the channel is depleted of charge carriers resulting in high resistance and the OFET is in the off state. The OFET operates in accumulation mode and is in the on state when there is a negative gate voltage and a high concentration of charge carriers accumulate in the transistor channel. If an n-type organic film replaced the pentacene film then for the transistor operation the electrode polarity is reversed as the majority of carriers are electrons rather than holes.



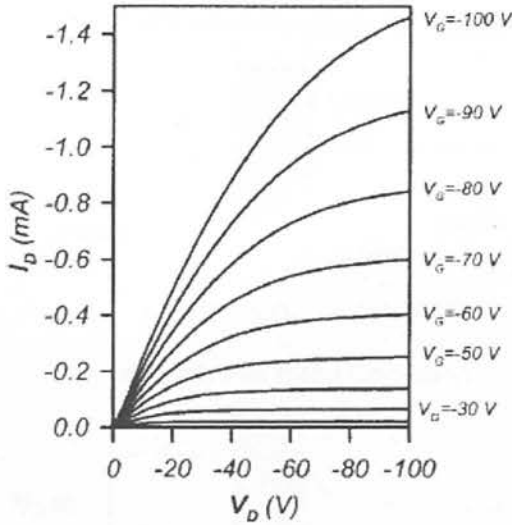


Figure 4.3: A plot of a drain current  $I_D$  versus drain voltage  $V_D$  at various gate voltages from a top contact OFET with a polycrystalline pentacene film as the active layer and a thermal silicon dioxide modified with a 1-diethoxy-1-silacyclopent-3-ene self assembled monolayer as the gate insulator, a heavily doped n-type Si wafer as the gate and gold source and drain electrodes (taken from Dimitrakopoulos et al. 2002).

#### 4.5 The organic thin film/metal interface

The next major consideration is what happens at the organic film/ metal interface. At the metal/organic film interface, there is energy level alignment, which is connected with charge transfer across the interface, which results in band bending in the semiconductor and interfacial dipole formation (Peisert et al. 2002 and Richardson et al. 2000). This concept is now explained in the context of a p-type OFET, using an energy band diagram for an OFET with an active 2,2,7,7-tetrakis-(diphenylamino)-9,9-spirobifluorene layer shown in figure 4.4 (Saragi et al. 2004).

Figure 4.4a illustrates the flat band condition when the gate bias is zero and there is no charge transfer between the metal and the organic active material. Here the work function difference is regarded as zero. When a negative charge is applied to gate electrode the valence band (HOMO) bends upwards, as depicted in Figure 4.4b.

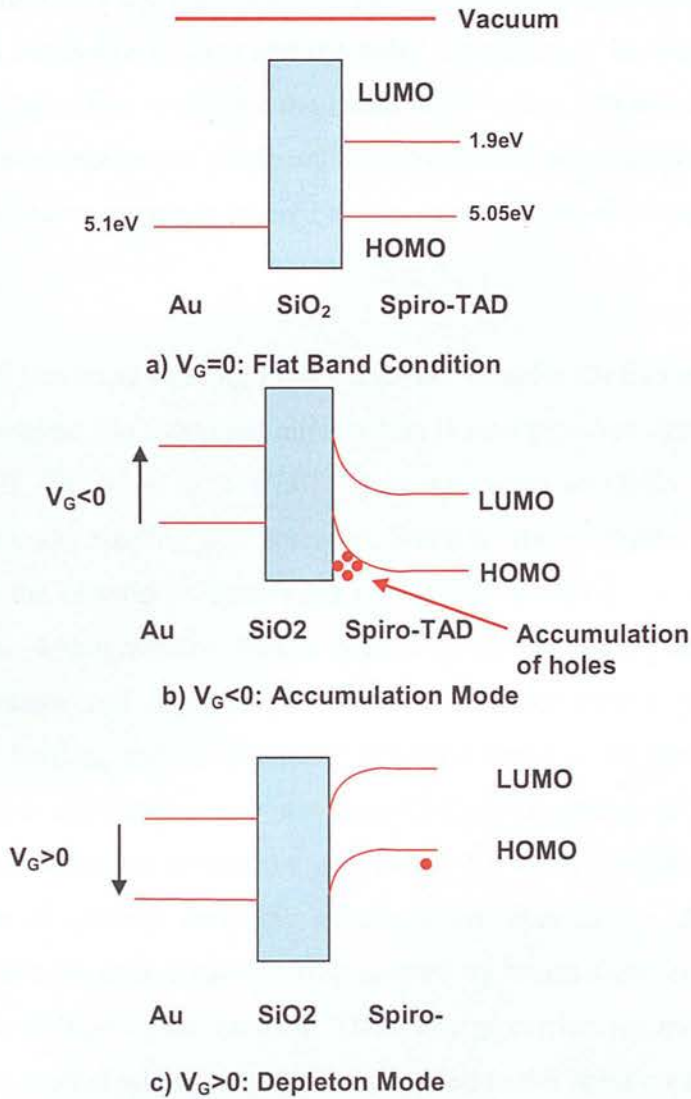


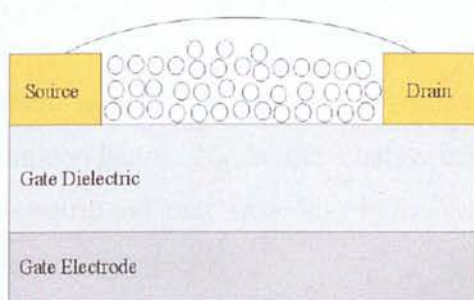
Figure 4.4: Energy band diagram for an OFET with a p-type organic active layer where a) represents flat band condition when  $V_G=0$ , b) depicts accumulation mode where  $V_G<0$  and c) represents depletion mode when  $V_G>0$ .

As the charge carrier density is exponentially dependent on the energy difference between the valence and conduction band (LUMO), the band bending initiates a hole accumulation near the semiconductor/insulator interface. This is what happens in the OFET when it is in accumulation mode.

Figure 4.4c illustrates the depletion case, when a positive bias is applied to the gate the valence band bends downwards and the holes are depleted. In inorganic FETs, when a larger positive gate bias is applied the bands bend further in a downwards direction and the intrinsic level (defined as the Fermi level in the absence of doping) crosses the Fermi level. The inversion regime is entered at this point and the electron density exceeds the hole density.

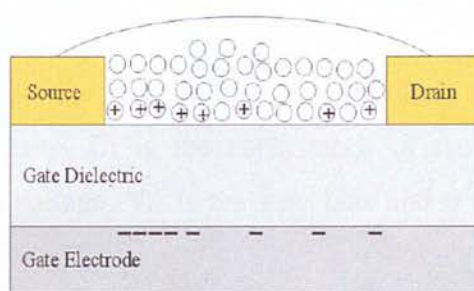
Unfortunately this band bending model does not hold for OFETs as they do not possess an inversion regime. So a detailed introduction is now provided discussing specifically a p-active OFET (Brown et al. 1987a). Figure 4.5 shows an OFET with a p-type active organic layer under varying gate potential. When all the electrodes are held at zero bias (figure 4.5a) the channel is dominated by neutral molecules (represented by circles). Then in figure 4.5b a negative bias is applied to the gate ( $V_G$ ), and the potential drops over the insulator and organic film near the insulator/organic film interface, which induces band bending and an accumulation region forms in the transistor channel. If the dielectric has a capacitance per unit area  $C_i$  then, assuming the charge carriers are uniformly distributed, the charge per unit area is  $V_G C_i$ . So radical cations, (represented by plus signs in circles), form the accumulation layer in the channel and an equal quantity of opposite charge carriers (represented by minus signs in circles) is formed in the gate at the dielectric/gate interface. These charge carriers are mobilised and carry the current in the channel when a small bias is applied to the drain contact, as seen in figure 4.5c. Then if a positive gate bias is applied band bending in the opposite direction at the semiconductor /insulator interface occurs, and charge carriers are depleted in the active channel (figure 4.5e). The following equation (equation 4.12) gives the depletion layer of width  $W_d$  in the organic semiconducting film (Meijer et al. 2003):

$$V_S = V_D = V_G = 0$$



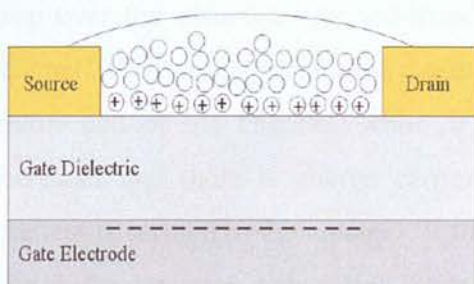
(a)

$$V_S = 0, V_D < 0, V_G < V_D < 0$$



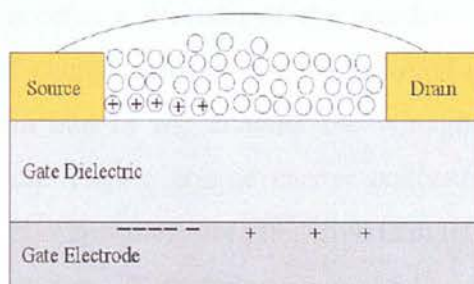
(c)

$$V_S = V_D = 0, V_G < 0$$



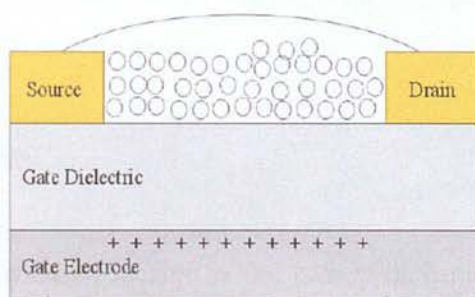
(b)

$$V_S = 0, V_D < 0, V_D < V_G < 0$$



(d)

$$V_S = V_D = 0, V_G > 0$$



(e)

Figure 4.5: Schematic diagram of an OTFT, where the circles represent neutral molecules, the circles containing a plus sign represent radical cations and the circles containing a minus sign represent anions (taken from Saragi et al. 2004).

$$W_d = \frac{\epsilon_0 \epsilon_{semi}}{C_i} \left[ \sqrt{1 + \frac{2C_i^2 (V_G - V_{SO})}{qN_B \epsilon_0 \epsilon_{semi}}} - 1 \right], \quad (4.1)$$

where  $\epsilon_0$  is the permittivity of vacuum,  $\epsilon_{semi}$  is the relative dielectric constant of the semiconductor,  $N_B$  is the charge carrier density,  $C_i$  is the capacitance of the gate dielectric per unit area,  $V_{SO}$  is the switch-on voltage,  $V_G$  is the gate bias and  $q$  is the elementary charge.

At low drain and large negative gate potentials there is a uniform distribution of charge carriers in the channel. However, as the drain bias becomes more negative the voltage drop over the insulator and semiconductor becomes a function of the position in the channel. The voltage drop and the number of charge carriers remains constant at the source end of the channel, while at the drain end of the channel the voltage drop decreases and there is charge carrier depletion. Thus a charge carrier concentration gradient is formed in the channel. If the drain bias becomes more negative than the gate bias then a depletion zone forms around the drain area, as shown by figure 4.5d.

This OFET may also be used to establish the conductivity of the organic thin film through plotting the drain voltage versus current with zero gate potential or with a gate bias lower than the switch on voltage  $V_{SO}$ .

## 4.6 The gate dielectric

The final consideration in OFET design is the gate, which plays a major role in OFET output. The dielectric can influence carrier transport and mobility in several ways (Veres et al. 2004). Primarily the orientation and morphology of the organic semiconductor layer is influenced by the dielectric interaction. The interface roughness may be influenced by the dielectric and deposition conditions.

Gate voltage dependent mobility and variation in  $V_T$  behavior may be attributed to dielectric interface effects. One theory is that the carrier concentration induced by the insulator modulates the mobility itself by changing the occupation level in the interface density of states. As this is happening the gate field may drive the carriers to the interface in a 2D manner rather than allowing them to travel through a more efficient 3D path through the bulk. Variable  $V_T$ s may be attributed to built-in charge and may be an indication of threshold states (undesirable chemical groups on the insulator or on impurities) that result in carrier trapping. The polarity of the dielectric interface can dictate OFET properties, through influencing local morphology and electronic states distribution in the organic semiconductor.

## **Chapter 5**

# **Microscopy**



The atomic force microscope (AFM) and scanning electron microscope (SEM) were used to resolve the various ICAT film morphologies. The basic principles of operation for these two techniques are detailed in this section.

## 5.1 AFM

The AFM was developed to resolve the atomic surface structure of insulating materials (Bining et al. 1986). It combines the principles of the scanning tunnelling microscope and the stylus profilometer and incorporates a probe that does not damage the surface. The AFM consists of a cantilever with a sharp tip to scan the specimen surface, as illustrated in figures 5.1 and 5.2. AFM images are obtained through measuring the force on a sharp tip created by the proximity of the sample surface. The force causes a deflection of the cantilever, according to Hooke's law, which was measured in the first AFM with an STM (Bining et al. 1986). The back of the cantilever was metalized and a tunnelling tip was brought close to it to measure the deflection. Whilst the tunnelling effect is very sensitive to distance, the numerous drawbacks associated with this deflection detection method has led to other optical (optical interferometry) and electrical (capacitive sensing and piezoresistive AFM cantilevers) deflection detection methods developments. The bouncing beam detection method is most commonly used where the deflection is measured with a laser spot reflected from the top surface of the cantilever into an array of photodiodes, as illustrated in figure 5.2.

The force is maintained at a constant small level with a feedback mechanism (figure 5.2). When the tip is moves sideways it will follow the surface contours (trace B, figure 5.1). Traditionally the sample is mounted using a piezoelectric tube that can move in the z direction to maintain a constant force and the x and y directions for scanning the sample. In modern designs, the tip is mounted on a vertical piezo scanner while the sample is scanned x and y using another piezo block.



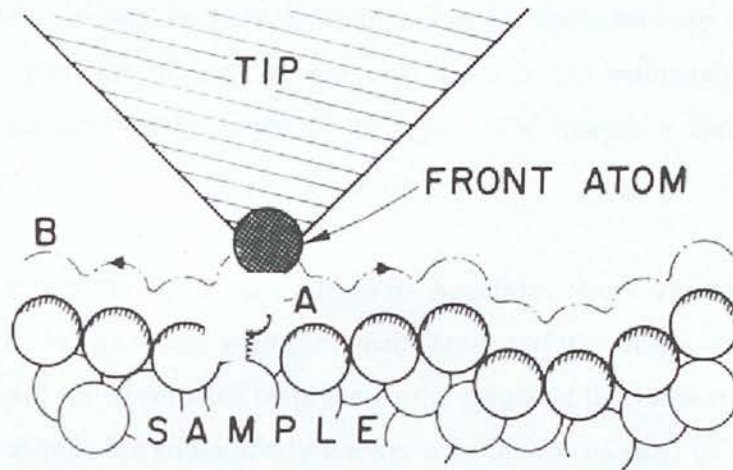


Figure 5.1: Description of the principle of operation of AFM (taken from Binnig et al. 1986). The tip follows contour B to maintain constant force between the tip and the sample.

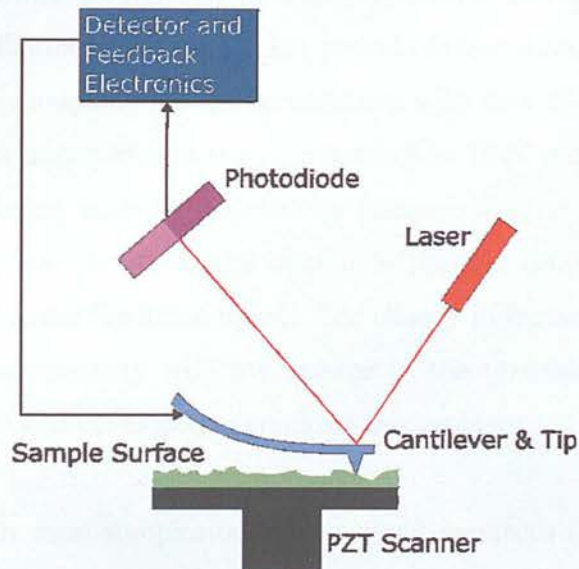


Figure 5.2: Schematic illustration of AFM (bouncing beam mode).

The AFM imaging can be operated in different modes, depending on the application. Generally imaging modes fall under contact mode or non contact modes where the cantilever is vibrated. In contact mode the static tip deflection is used as a feedback signal. Static mode AFM requires the cantilever to be much softer than the bonds between the bulk atoms in the tip and sample. Static mode AFM is operated where the overall force is repulsive as close to the surface the attractive forces can be strong

forcing the tip to snap into the surface. In this mode the force between the tip and the surface is kept constant during the scanning process by maintaining a constant deflection. The physical interpretation of the static AFM images is simple where the image is a map of  $z$ .

In non contact mode the tip hovers 50 - 150 Angstrom above the sample surface. Attractive Van der Waals forces acting between the tip and the sample are detected and topographic images are constructed by scanning the tip above the surface. The attractive forces from the sample are substantially weaker than the forces used by contact mode. Therefore the tip must be given a small oscillation, so that the small forces between the tip and the sample can be detected, by measuring the change in amplitude, phase, or frequency of the oscillating cantilever in response to force gradients from the sample. Changes in the oscillation frequency, which provide information about the tip-sample interaction (frequency modulation) can be measured with very high sensitivity and this was the first AFM technique to gain atomic resolution in UHV (Giessibl et al. 2003). In the amplitude modulation mode (AM mode) the actuator is driven by a fixed amplitude at a fixed frequency and the phase and amplitude changes caused by the tip sample interactions are used as the feedback signal. The change in the amplitude in AM mode does not occur instantaneously with the change in the tip-sample interaction. Thus frequency modulation was developed to eradicate this problem.

In ambient conditions most samples develop a liquid meniscus (condensed water and environmental contaminants) that can be several nanometers thick. In the non contact mode it is extremely difficult to keep the probe tip close enough to the sample to detect short range forces, whilst preventing the tip from sticking to the surface in ambient conditions. Tapping mode was developed to overcome this problem (Zhong et al. 1993). The amplitude of cantilever oscillation in tapping mode is typically of the order of a few tens of nms which ensures that the tip does not get stuck in liquid layer. Tapping mode is now the most frequently used operating AFM mode as it overcomes problems associated with friction, adhesion, electrostatic forces, and other difficulties that plague

conventional AFM scanning methods, by alternately placing the tip in contact with the surface to provide high resolution and then lifting the tip off the surface to avoid dragging the tip across the surface (Zhong et al. 1993). It may be applied to soft surfaces and tends to be much more effective than non contact mode for scanning large areas, which may include large variations in sample topography.

In this work images were taken using tapping mode. The principles of operation for tapping mode are as follows. A small piezoelectric element mounted in the AFM tip holder drives the cantilever to oscillate up and down near its resonant frequency. The amplitude of the oscillation is greater than 10 nm, typically 100 to 200 nm. The oscillating tip is then moved toward the surface until it begins to lightly tap the surface. During scanning, the vertically oscillating tip alternately contacts the surface and lifts off, generally at a frequency of 50,000 to 500,000 cycles per second. The interaction of the forces (dipole-dipole interaction, electrostatic etc) acting on the cantilever as the tip approaches the surface cause the amplitude of this oscillation to decrease. An electronic servo uses the piezoelectric actuator to control the height of the cantilever above the sample. This servo adjusts the height to maintain a set cantilever oscillation amplitude as the cantilever is scanned over the surface. A tapping mode image is produced by imaging the force of the oscillating contacts of the tip with the sample surface. The reason why tapping mode prevents the tip from sticking to the surface and causing damage during the scanning process is that when the tip contacts the surface, the high frequency (50k - 500k Hz) makes the surfaces stiff (viscoelastic) thus reducing the tip-sample adhesion forces.

There is however, a major resolution limitation experienced in all operating modes of AFM. The steric hindrance of the tip prevents access to all the structural elements of a surface, unless the surface is rough at an atomic scale. Prominent steric artefacts occur when the characteristic dimensions and angles of the tip are comparable to those of the surface topography (Castle et al. 1997). The image arises from a convolution of surface topography and tip shape, and is dependent on the interaction. Deconvolution is possible

to calculate, in principle, with accurate knowledge of two out of the three elements (tip, surface and interaction). In practise, the prerequisite information is a rarely obtainable. Procedures for tip shape surface convolution are discussed where appropriate in the experimental chapter.

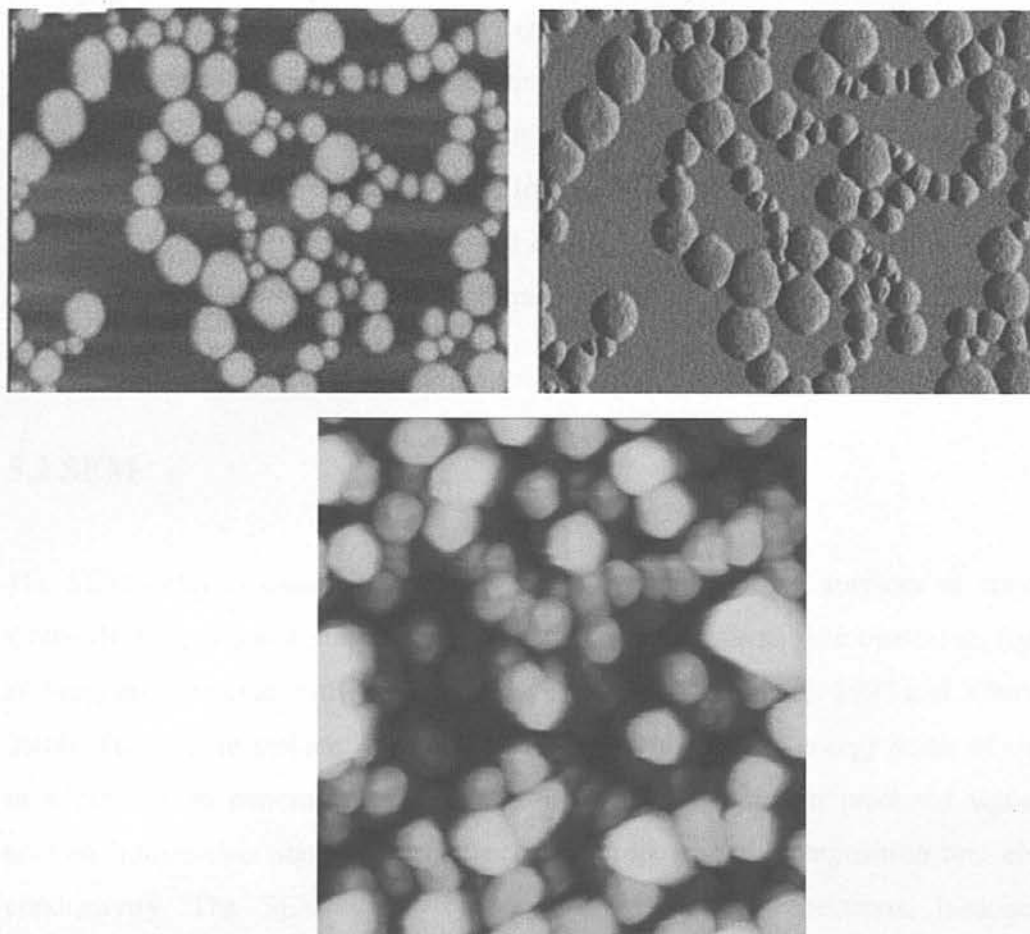


Figure 5.3: Topographical (a) and amplitude (b) AFM images of Langmuir-Blodgett polystyrene-graft-poly(ethylene oxide) copolymer films, where the image width is  $1.5\ \mu\text{m}$  (taken from Njikang et al. 2008). Image (c) is a topographical image of ZnO rods, where the image width is  $5\ \mu\text{m}$  (taken from Schlenker et al. 2007).

Surfaces are most frequently displayed using topographical (height) images, as illustrated in figure 5.3(a). The images are presented as a map of different coloured pixels, with a colour bar relating the colour shade to the height (here the lighter colour represents the thicker film domains of maximum  $15\ \text{nm}$ ). Both lateral and height

measurements can be made from these images. However, a major drawback is that some images can look very different from the actual optical appearance. Thus feature shapes may not be immediately recognisable to the casual observer. This point is well represented using figure 5.3(c), where an ensemble of ZnO nanorods is not readily discernible using topographical imaging. Commonly a 3D image is fabricated using the height data to alleviate this problem (Duzhko et al. 2008). Amplitude images often display the shape of the sample more accurately but the z-scale is meaningless in terms of sample structure. The fine details can be seen more clearly in amplitude images as compared with those of topographical images, as exemplified in figure 5.3 using (a) topographical and (b) amplitude images of a copolymer film. Thus some surfaces are best represented using the usual topographical images combined with the 3D and/or amplitude images.

## 5.2 SEM

The SEM today is capable of subnanometer resolution of the surfaces of conducting materials directly and insulating materials with appropriate surface treatments (typically surfaces are sputtered with an ultra-thin gold layer) (Castle et al. 1997 and Young et al. 2008). The sample surface is imaged by scanning with a high energy beam of electrons in a raster scan pattern. The sample atom/electron interaction produces signals that contain information about the sample surface topography, composition and electrical conductivity. The SEM signal types include secondary electrons, back-scattered electrons, characteristic X-rays, light, specimen current and transmitted electrons. Secondary electron imaging is the most common detection mode. This mode was used for the work in this thesis and is therefore introduced in much greater detail than the other operational modes.

The primary operation systems of the SEM are schematically depicted in figure 5.4 (Chescoe et al. 1990 and Dunlap et al. 1997). Typically an electron beam is thermionically emitted from an electron gun fitted with a tungsten filament cathode at



the top of the microscope column. The grid (Wehnelt cylinder) controls the electron flow with a positively charged anode plate that attracts and accelerates the electrons down the column to the sample.

Electrons in motion are controlled in the electron column by magnetic fields. Vacuum is necessary as the electrons will rapidly disperse or scatter due to collisions with other molecules. These fields are used to form electron microscope electromagnetic lenses by passing electric current through a copper wire. The electron beam (standard energy range from few hundred eV to 40keV) is focussed by these condenser lenses to a spot 0.4-5 nm diameter. Magnetic lenses developed to correct astigmatism and alignment are typically applied to the SEM. As the beam passes through the final condenser lens, two sets of magnetic radially opposing scanning coils (raster coils) allow the beam to move in x and y directions.

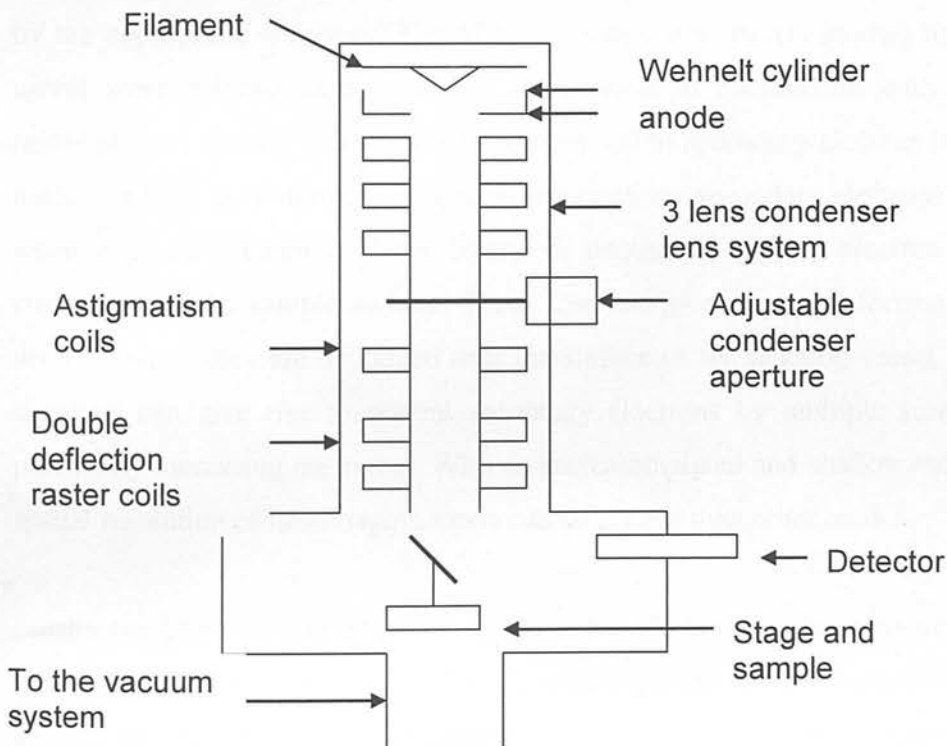


Figure 5.4: Schematic illustration of experimental SEM setup (taken from Dunlap et al. 1997).

Magnification in a SEM can be controlled over a range up to six orders of magnitude, from about 10 to 500000 times, and results from the ratio of dimensions of the raster of the specimen and the raster on the display device. Assuming that the display screen has a fixed size, higher magnification results from reducing the size of the raster on the specimen and vice versa. Magnification is controlled by the current supplied to the x, y scanning coils, or the voltage supplied to the x, y deflector plates.

The electrons lose energy when the electron beam interacts with the sample, through repeated random scattering and absorption within a teardrop-shaped volume that ranges between 100 nm-5  $\mu$ m into the surface. The volume size is dependent on the electrons' landing energy, the atomic number of the specimen and the sample density. The energy exchange between the electron beam and the sample results in the reflection of high-energy electrons by elastic scattering, emission of secondary electrons by inelastic scattering and the emission of electromagnetic radiation, each of which can be detected by the appropriate detectors. The SEM can operate in backscattering mode, which is useful when relative atomic density information in conjunction with topographical information is desired. The SEM can be operated in secondary electron mode, which is useful for high resolution topographical information. Secondary electrons are generated when a primary electron (from beam) or another secondary electron dislodges an electron from the sample surface. These low energy secondary electrons can only be detected when they are dislodged near the surface of the reaction vessel. The primary electrons can give rise to several secondary electrons by multiple scattering events, potentially increasing the signal. With an increased signal and shallow escape depth the spatial resolution of this imaging mode can be greater than other modes.

Finally the beam current absorbed by the specimen can also be measured and used to create images of the distribution of the specimen current. Electron amplifiers are used to amplify the signals which are displayed as variations in brightness in a cathode ray tube (CRT). The raster scanning of the CRT display is synchronised with that of the beam on



the sample. Thus the raster scanning of the image is a distribution map of the signal intensity from the scanned area of the sample.

## Chapter 6

### ICAT-Part B Synthesis

#### characterisation

## **Chapter 6**

# **ICAT Part 1: Synthesis and characterisation**

### 6.1.1 Introduction

Current chemical indole polymerization methods tend to be arduous and result in poor yields of complex mixtures of products, including various dimers, trimers, tetramers and polymers (Billaud et al. 1995, Bocchi et al. 1986, Ishii et al. 1988, Ishii et al. 1988a and Kaneko et al. 1981). Polyindoles are virtually impossible to process due to their poor solubility and the molecular packing is difficult to control due to complicated intermolecular interactions and chain/sheet polydispersity. In fact the only way that polyindole films have been produced has been through electrochemical means, which resulted in films with poor mechanical properties that proved difficult to characterize structurally due to their poor quality (Pandey et al. 1998, Talbi et al. 1998b and Tourillon et al. 1982).

Polyindoles with various functional groups have been synthesised to enhance solubility and direct the assembly process (Bartlett et al. 1999, Jennings et al. 1998 and Sivakkumar et al. 2005). Poly(indole-5-carboxylic acid) and ICAT offer numerous attractive properties, as detailed in the following chapter. Unfortunately, poly(indole-5-carboxylic acid) is still highly insoluble and consequently difficult to process, and the electropolymerised poly(indole-5-carboxylic acid) films are structurally poor in quality, with highly irregular morphologies (Sivakkumar et al. 2005). Thus a viable synthetic and processing route is highly sought after. The molecule ICAT was selected as the weaker intermolecular interactions in small functional molecules, as compared with those of polymers, tend to allow highly flexible structural tunability, offer enhanced solubility and consequently more efficient thin film processing. ICAT in particular, can establish multiple highly directional H-bonding interactions with ICAT molecules, the solvent and surfaces which have been used effectively in similar functional molecules, to control the assembly process (Ajayagosh et al. 2006, Aoki et al. 2002, Autwer et al. 1999, Duzho et al. 2006 and Gao et al. 2008).

An ICAT/polymer mixture has been synthesised previously in house, which is not suitable for device applications, due to very limited control over the assembly process during film processing. In fact, this mixture was synthesised here initially and proved impossible to process through solution based deposition methods. However, pure oligomeric materials are suitable for device applications, in particular organic electronics, as they are much easier to process and form films with ordered interfacial alignments and bulk assemblies (Dimitrakopoulos et al. 2001, Garnier et al. 1996, Katz et al. 2004, Potzorro et al. 2003 and Shirota et al. 2007). Finally pure ICAT, rather than a charge transfer complex as produced by Maeda, is favoured for semiconductor applications (Maeda et al. 2009).

To date, ICAT thin films have not been produced. Thus far electrochemically synthesised, substituted indole trimers have insufficient cycle characteristics, disordered film microstructures, have only been produced on a very small scale and are not applicable to industrial production (Billaud et al. 2003 and Jennings et al. 1997). Thus a chemical synthetic route was investigated.

Kaneko produced a complex mixture of products, through chemical synthesis that included the asymmetric indole trimer (Kaneko et al. 1981). Billaud and co-workers chemically polymerised indole, through adding an indole solution drop wise to an oxidant solution, producing a polymer containing indole as a repeat unit, with no mention however, of an indole trimer (Billaud et al. 1995). The synthesis was sensitive to solvent type, concentration of the reacting agents, temperature and the redox potential of the oxidant. Ferric chloride in acetonitrile solution was demonstrated to be an effective oxidant. Since I completed the synthesis here, Maeda and co-workers published a patent, using the Billaud methodology applied to an indole -5-carboxylic acid monomer, producing a charged ICAT complex. There was no mention, however, of the polymer, but they described overoxidation of the trimer degrading the product. An oxidant solution with water, was dripped into an indole-5-carboxylic acid monomer solution, where the preferred solvent is acetonitrile, and one of several oxidants from a

list, which included ferric chloride anhydrate and ferric chloride hexahydrate were added. The molecule was doped during the oxidation process, but was then further doped with an acidic solution. The reaction was sensitive to the monomer/oxidant ratio, pH, temperature, reaction time and water content in the reaction mixture. Billaud and co-workers poured a ferric chloride-water solution into a mixture containing indole and water, with a small amount of acetonitrile necessary to solubilise the indole monomer, to produce the indole polymer. Billaud also produced the polymer though performing the reaction just in acetonitrile, and added water after the reaction was completed, for precipitation purposes. Billaud demonstrated that the polymer synthesis was independent of the water content in the reaction mixture. It is interesting that Maeda always used a water/solvent mixture to dissolve the monomer, and claimed that if the water content was low the trimer may be overoxidised, and the trimer may be inefficiently doped and that the oxidation reaction may not proceed well if the water content was too high.

Initially a solid phase reaction through dry grinding the monomer with oxidant iron chloride was investigated here, but resulted in a mixture of unreacted monomer and polymer, which was highly insoluble and difficult to process. I applied the Billaud synthesis, (originally applied to an indole monomer), to the indole -5-carboxylic acid monomer (prior to Maeda), and produced an ICAT/ poly(indole-5-carboxylic acid) mixture. Unfortunately this product proved difficult to process, using solution based film deposition methods, and produced very poor quality films.

This synthesis was refined to try to produce ICAT rather than the ICAT/polymer mixture. It was observed here that the polymer/ICAT product ratio was sensitive the oxidant/monomer ratio, and the optimal ratio was then selected for ICAT production. Mackintosh and co-workers electropolymerized indole-5-carboxylic acid producing a mixture of ICAT and a polymeric species, consisting of linked trimer units, poly(indole-5-carboxylic acid), which were roughly separated by their differential solubility in N, N-dimethylformamide (DMF) (Mackintosh et al 1994a). This differential solubility method was applied here and the polymer filtrate discarded. This method was not effective here

as the solute still had polymer in. Selective precipitation of the polymer, through solvent mixing with a range of good solvent: poor solvent ratios, was then applied. Again the product had polymer in, so required further treatment. Finally gel permeation chromatography was used and the pure ICAT molecule isolated.

### 6.1.2 Experimental method

All the reactions were carried out at room temperature. All chemicals used were analytical grade and purchased from Aldrich, unless otherwise stated. The molar ratio of monomer (indole-5-carboxylic acid), (A) to oxidant (anhydrous iron chloride), (B) [(A):(B)] applied, was in the range of [1:1] to [1:3], with the optimal ratio of [1:2] to induce neutral ICAT production. This is the stoichiometric ratio required for ICAT formation. Indole-5-carboxylic acid (4.0g) was dissolved in acetonitrile (800ml), in a three neck flask. Anhydrous iron chloride (8.1 g) was dissolved in acetonitrile (1200 ml), and added drop wise (to ensure homogeneous oxidation) to the monomer solution, and stirred vigorously for 6 hours. Water was then added for precipitation purposes, and a fine dark green powder suspended in a brown liquid was produced. The reaction liquid was filtered under vacuum through a perforated funnel and the filtrate washed with water, acetonitrile and methanol, in turn. DMF was then added to the product, and the mixture stirred for 30 minutes and the insoluble portion of the product filtered off. Ethanol was mixed with the solution, at a ratio (range 10:1 to 5:1) 5:1 of ethanol: solution, and stirred overnight. The mixture was centrifuged and the solid discarded. The solvent was removed through evaporation and the product washed with ethanol and dried. The product was then subjected to gel permeation chromatography, by separation with lyophilic Sephadex LH20 (Amersham). The fraction containing the trimer, (as confirmed by mass spectrometry and NMR), was then suction filtered through a perforated filter, washed and dried.

The products were characterised as follows. NMR measurements were taken using a 360 MHz NMR spectrometer (Brückner), with anhydrous D6-dimethyl sulphoxide as the

solvent. UV-visible spectrometer measurements were made using a Shimadzu UV-160A and fluorescence experiments were carried out using an LS-5 luminescence spectrometer (Perkin-Elmer). IR measurements were collected on a Bio-Rad FTS-7 FTIR spectrometer, using the KBr method.

The conductivity measurement was made on an early synthetic product (the DMF soluble product, prior to purification with solvent mixing and gel permeation chromatography). The product was pressure molded with a tablet molding machine. The conductivity was measured on compressed pellets, using the van der Pauw method, and the mean value was  $2.5 \times 10^{-6} \text{ Scm}^{-1}$  (Van der Pauw 1958). This is consistent with the conductivity of a neutral ICAT molecule.

### 6.1.3 Results and discussion

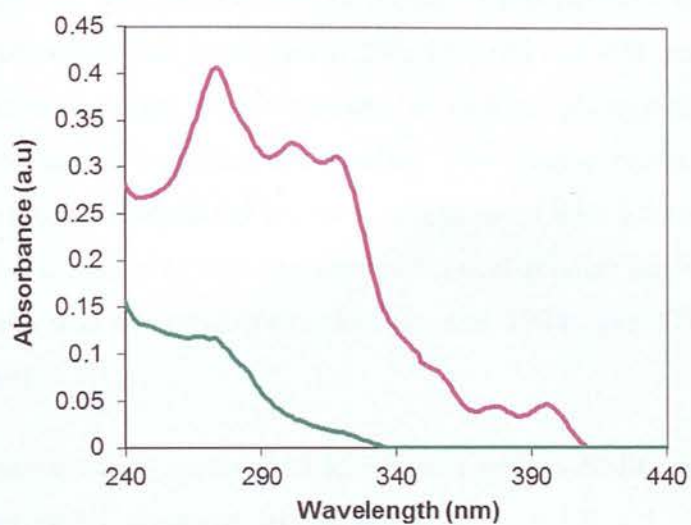
#### The ICAT molecule

The electrochemically synthesised ICAT and polymeric species were characterised spectroscopically, by Mount and co-workers (Mackintosh et al 1994). The UV-visible and fluorescence spectra were extremely similar for both species, which indicated that both species have the same chromophore. However, there were differences in the NMR between the species.

Evidence that the ICAT molecule and/or polymer were synthesised here is provided in the UV-visible (a) and fluorescence spectroscopy (b) results in figure 6.1. The UV-visible spectrum for the monomer has a single absorption peak, with a maximum at 280 nm. The electrochemically synthesised ICAT molecule and polymer presented this peak, in addition to peaks of comparable intensity with maxima at 305 nm and 320 nm and peaks of weaker intensity at 380 nm and 400 nm. The UV-visible spectrum here matches (within instrumental error) that of the ICAT molecule and polymer.



a



b

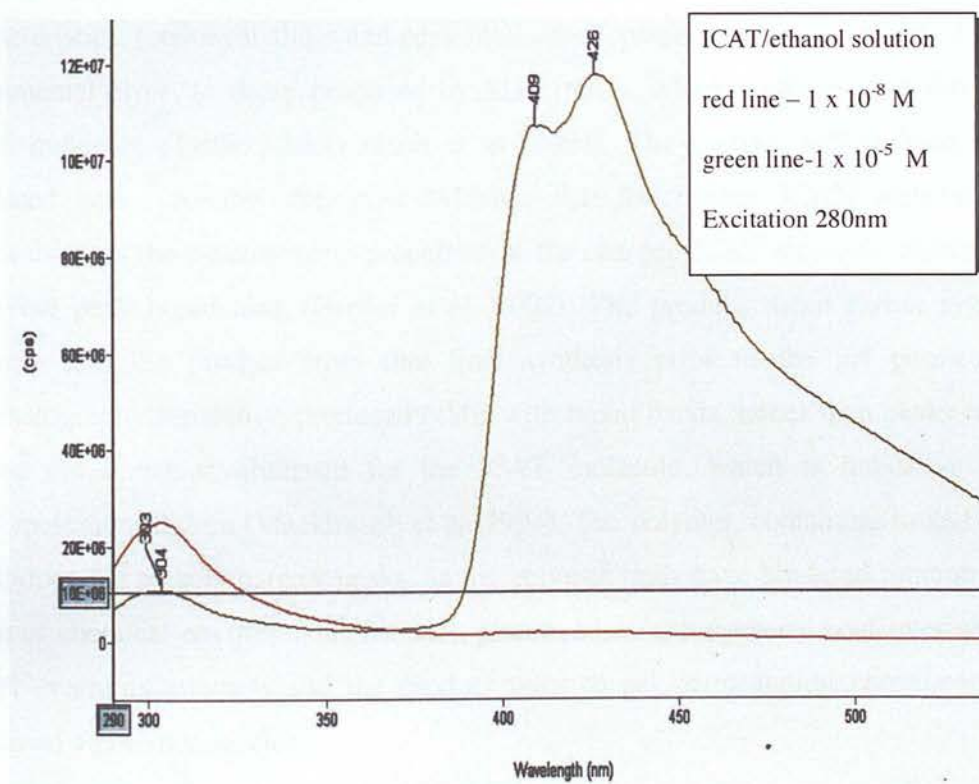


Figure 6.1: (a) UV-visible spectra of ICAT in ethanol at concentrations  $1 \times 10^{-5}$  M (series 1) and  $1 \times 10^{-6}$  M (series 2) and (b) fluorescence emission spectra of ICAT in ethanol at concentrations  $1 \times 10^{-5}$  M and  $1 \times 10^{-8}$  M.

The fluorescence emission spectra, from the electrochemically synthesised ICAT and polymer species, had two maxima of roughly equal intensity at 420 nm and 435 nm, while the monomer had 4 maxima at 280, 320, 380 and 400 nm. The species here also had two peaks of roughly equal intensity but with a slight hypsochromic shift relative to the electrochemically synthesised product. The hypsochromic shift, relative to the electrochemically synthesised product, is associated with a lesser degree of electronic delocalisation, indicating that the electrochemical product contains more polymer and/or aggregates than this product (Mackintosh et al. 1994). The 303 nm peak is the solvent Raman band.

The electrochemically synthesised ICAT presented an NMR spectrum with a series of overlapping peaks, clustered around  $\delta$  8.0,  $\delta$  9.5,  $\delta$  11.8 and  $\delta$  12.5 (Mackintosh et al. 1994). A typical NMR spectrum of the final product is provided in figure 6.2. The NMR characteristics, (chemical shifts and peak intensities), presented here are identical within instrumental error, to those produced by Mackintosh, which confirms that this is the ICAT molecule (Table 1, Mackintosh et al. 1994). The narrow well defined peaks, produced here, provides definitive evidence that the neutral ICAT molecule was synthesised, as the paramagnetic properties of the charged ICAT molecule would result in severe peak broadening (Bertini et al. 2002). The products from earlier synthesis attempts and the product from this final synthesis prior to the gel permeation chromatography separation produced NMR with broad bands, rather than peaks centred around the  $\delta$  values observed for the ICAT molecule, which is indicative of an ICAT/polymer mixture (Mackintosh et al. 1994). The polymer, containing linked trimer units, does not present narrow peaks, as the polymer units have hindered rotation and a range of chemical environments for each proton. Mass spectrometry confirmed that the earlier synthesis attempts and the product prior to gel permeation chromatography contained a polymer species.

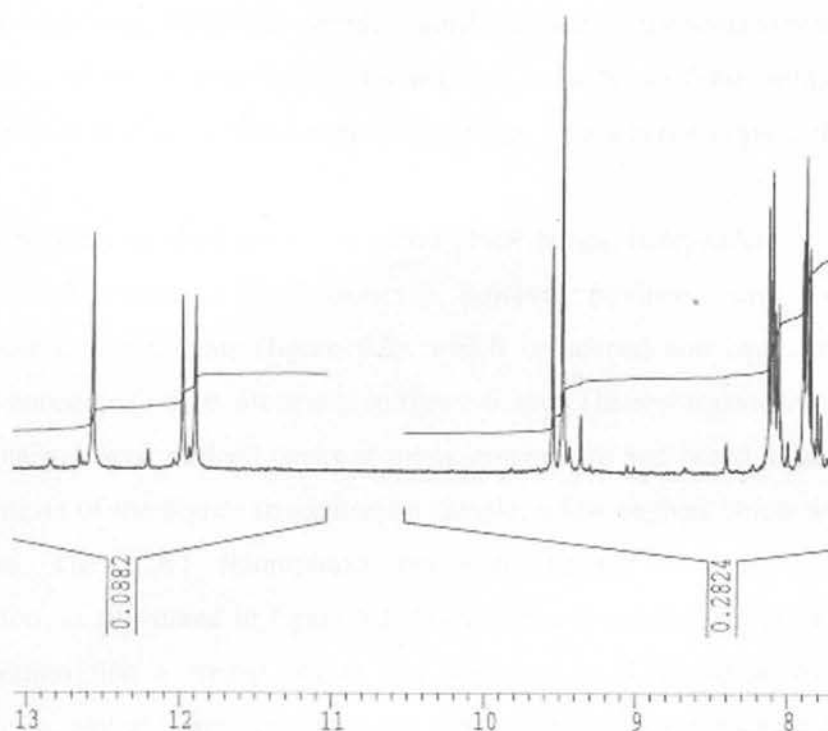


Figure 6.2: A typical NMR spectrum for the final synthetic product, the neutral ICAT molecule.

The product mean conductivity was, (semiconducting regime),  $2.5 \times 10^{-6} \text{ Scm}^{-1}$ . Maede's doped ICAT product conductivity was  $0.41 \text{ Scm}^{-1}$  and Billaud's product conductivity ranged from  $\sigma = 10^{-2}$ - $10^{-6} \text{ Scm}^{-1}$ , depending on the synthetic conditions. This low conductivity is actually preferable to Maeda's charge transfer complex, as for semiconductor applications the uncharged version is desirable so that the conductivity function can be switched on and off in the device.

### ICAT self-assembly in solution

The UV-visible and fluorescence spectra were reviewed to determine if ICAT self-assembled in solution as a function of concentration. Solution solvents were selected that had favourable properties (detailed in the following chapters), that ICAT is expected to be relatively soluble in and that were compatible with the spectrometers. Pre- and post-

aggregation solution concentration ranges of similarly structured dye molecules were selected to work with. This study should contribute towards the understanding of ICAT self-assembly, of which very little is known, and towards the fundamental science of self-assembly of small functional organic molecules, which is not as yet well developed.

The ICAT/polymer mixture presented broad NMR bands, independent of the solution concentration. The isolated ICAT molecule, however, produced narrow well defined peaks at low concentrations (figure 6.2), which broadened and loss definition with increasing concentration, as illustrated in figure 6.3(a). The lower concentration sample presented narrow well defined peaks at room temperature and broad ill defined peaks, similar to those of the higher concentration sample, a few degrees below average room temperature. The ICAT fluorescence emission changed form as a function of concentration, as illustrated in figure 6.3. Quantitative measurements were initiated by the observation that a strong purple hue appeared in ICAT solutions at elevated concentrations, and at lower concentrations the purple emission presented as a function of cooling the ICAT solution.

The following investigations of ICAT fluorescence properties were performed on the product prior to the final purification step, though gel permeation chromatography, and so still contained traces of polymer. The marked difference between the UV-visible spectra for ICAT in ethanol at  $1 \times 10^{-5}$  M and  $1 \times 10^{-6}$  M concentrations is illustrated in figure 6.1. The  $1 \times 10^{-6}$  M solution presents a very intense high energy absorption band, with a well defined peak around 202 nm (not seen on this figure) and a broad peak of lower intensity centred around 266 nm. At the raised concentration the high energy absorption band dropped substantially in intensity and broadened, while the 266 nm peak bathochromically shifted, increased in intensity and split into 3 sharper peaks. New low intensity absorption peaks of comparable intensity, were also formed centred around 376 nm and 395 nm.

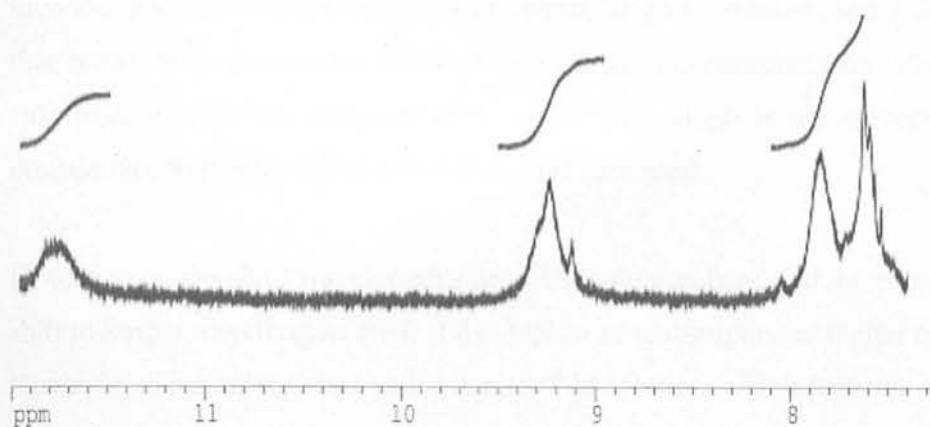
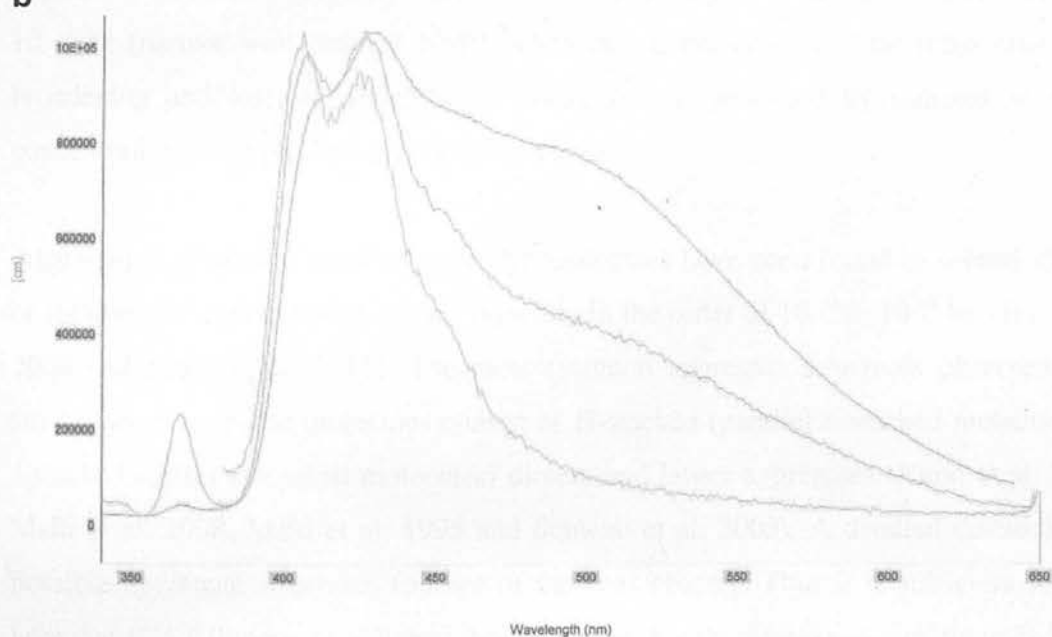
**a****b**

Figure 6.3: (a) a typical NMR spectrum of mM ICAT/DMSO solution and (b) fluorescence emission spectra (excitation 330 nm) of concentrations between  $1 \times 10^{-5}$  M and  $1 \times 10^{-3}$  M (blue trace) ICAT in an ethanol/DMSO mixture (5% DMSO).

Figure 6.3(b) illustrates the emission changes as the concentration is increased above  $1 \times 10^{-5}$  M ICAT in an ethanol/DMSO mixture (5% DMSO). DMSO is necessary here or

ICAT rapidly crashed out of ethanol at concentrations  $>1 \times 10^{-5}$  M. Primarily there is a narrow double peak of equal high intensity, and as the concentration increases the peak broadens and becomes a single peak and shifts bathochromically, and a shoulder appears that broadens and increases in intensity on increased concentration. The low intensity side peak ca 370 nm observed at  $1 \times 10^{-5}$  M, which is the solvent Raman band, disappears completely as the concentration is increased.

Distortion on the short wavelength side of the emission band and the emission maximum shift to longer wavelengths are features typical of reabsorption at higher concentrations. However, the shoulder observed in  $1 \times 10^{-5}$  M solution, which bathochromically shifted and broadened as the concentration was further increased, is typical of aggregate formation. The aggregation theory is further substantiated with the NMR data. ICAT appears to be molecularly dissolved in ethanol and DMSO at concentrations below  $1 \times 10^{-5}$  M (narrow well defined NMR below this concentration). The substantial peak broadening and loss of definition in NMR spectra produced by samples at raised concentrations, is typical of aggregate formation.

Aggregation of similar small organic dye molecules have been found in several classes of solvents for concentration ranges typically in the order of  $10^{-6}$  to  $10^{-4}$  M. (Bao et al. 2006 and Sauer et al. 2011). The most common aggregate structures observed with similar small aromatic molecules consist of H-stacked (parallel  $\pi$ -stacked molecule), or J-stacked (offset  $\pi$ -stacked molecules) dimers and larger aggregates (Kano et al. 2000, Malti et al. 1998, Malti et al. 1995 and Schwab et al. 2003). A detailed discussion of possible aggregate structures follows in the next chapter. Thus it is sufficient to state here that ICAT dimers, established though strong, highly directional quadruple H-bonds through the COOH functional groups, are the primary aggregate structures predicted, which can further H-bond with other dimers and solvent molecules and  $\pi$ -stack (either J-stack or H-stack), forming complex higher aggregates (Jonkheijm et al. 2006, Nguyen et al. 2004, Prins et al. 2001 and Wurthner et al. 2011).



The bathochromic shifts in absorption and emission peaks, relative to the monomer, observed here are characteristics, which are typical of J-aggregates (Kano et al. 2000, Schwab et al. 2003 and Wang et al. 2005). H-stacked aggregates of similar molecules produce absorption and emission peaks that are hypsochromically shifted (Kasha et al. 1963 and Malti et al. 1998). The bathochromic shift is associated with increased electron delocalisation associated with  $\pi$ -stacking (in particular J –stacking) (Bao et al. 2006, Jennings et al. 1997 and Mackintosh et al. 1994).

The emission band width, at  $1 \times 10^{-5}$  M in the solvent mixture, is actually relatively narrow as compared with similar J-stacked molecules, which points to a narrow particle size distribution and/or narrow range of particle structures. The complex peak structural changes at concentrations  $> 1 \times 10^{-5}$  M in the solvent mixture is indicative of aggregate structural changes, as illustrated in figure 6.3. The decrease in spectral fine structure and increase in emission shoulder size with increasing concentration, is associated with less ordered structures and/or increase in particle dispersity (Li et al. 2004, Xiao et al. 2004 and Xiao et al. 2003). The increasing red shift with concentrations  $> 1 \times 10^{-5}$  M is commonly associated with increased electron delocalisation as the aggregate size increases. It would be interesting to resolve the emission peaks with fluorescence lifetime studies. These emission properties could be attributed to kinetically limited aggregation, where molecules at increased concentrations have less time to form the most thermodynamically favourable structure, which would account for the broader less defined spectra at elevated concentrations.

Most organic dye molecules show fluorescence quenching in their aggregate state, and solids, owing to the formation of delocalised excitons or excimers, which can cause enhanced nonradiative deactivation of the excited state. In general when two or more molecules are interacting in an aggregate structure, two or more excitonic transitions with high transition moments are observed, and the original absorption bands are split into two or more components. According to the exciton theory of Kasha et al., only transitions to the low energy states of the exciton band are allowed in J-aggregates, and



consequently J-aggregates exhibit high fluorescence quantum yields (Kasha et al. 1965). While after exciting the higher energy states of the H exciton band, a rapid downwards energy relaxation occurs to the lower exciton states that exhibit vanishingly small transition dipole moments, thus suppressing fluorescence in H-aggregates.

It is interesting to note that the samples are still highly fluorescent at raised concentrations, where there is an increasingly high concentration of aggregates in the sample (although there is also an increase in molecular concentration too) and that ICAT films and crystals were also highly fluorescent. This behaviour is unusual and could be indicative of aggregation induced emission enhancement (AIEE), (increased fluorescence emission intensity from the aggregate as compared with that of the monomer) but further work would be required to substantiate this claim (study of emission spectra through selective excitation of just the aggregate). The AIEE effect is not as yet understood, but is linked to the molecular shapes, conformational flexibility, intramolecular movements, packing structure and organizational morphology (Bao et al. 2006, Dong et al. 2007, Li et al. 2004, Liu et al. 2003, Sun et al. 2007, Tong et al. 2007 and Tong et al. 2006). It would be worthwhile investigating the AIEE claim and relating it to the aggregate structure. Also investigating the correlation between the solid-state fluorescent properties in the ICAT crystals and molecular packing based on X-ray crystal structures would be insightful. Particularly, as there are numerous supramolecular interactions possibilities here, including intermolecular H-bonding and  $\pi$ -stacking with aromatic cores, which should have a strong influence over the emission.

## 6 ICAT part 2: Nanoparticles

### 6.2.1 Introduction

Further work was carried out to confirm the phase change as a function of solution concentration, investigate the aggregate structure, contribute towards the fundamental understanding of the self-assembly process and finally to determine if the aggregates could be harvested in a controlled fashion for applications. The aggregation was investigated through combining a rapid deposition technique, (with a very short deposition time scale and a rapid drying procedure), and careful substrate selection to minimise secondary aggregation on the surface (Kiriry et al. 2003, Schwab et al. 2003, Surin et al. 2006 and Wang et al. 2005). This deposition method is commonly used to analyse the dimensions and geometry of aggregates pre-formed in solution/suspension (Li et al. 2003a, Templeton et al. 1999, Wang et al. 2005 and Yang et al. 2005). DMSO was selected to work with here as it was more polar than ethanol and thus the strong solvent-ICAT interaction should allow more control over the assembly process and this solvent was used throughout the rest of the thesis.

### 6.2.2 Experimental Method

ICAT/DMSO solutions  $\geq 1 \times 10^{-4}$  M (higher than previous systems as ICAT is more soluble in DMSO than in ethanol) were made, aged a few hours, and 1 ml aliquots of the solutions were placed on a glass substrate, (cleaned with piranha solution, as detailed in the following paragraph), for five minutes and excess solution was removed by touching a small piece of filter paper on the edge of the substrate and then placed under nitrogen at room temperature, followed by 5 minutes in the oven at 115°C. The experiment was repeated with a pre-aged ICAT/DMSO solution (three months old) and identical particles were deposited. The deposition protocol was also applied to ICAT monolayer-functionalised glass substrates, (substrate functionalisation procedure provided in chapter 7), for adhesion purposes.

Glass microscope slides were rinsed in ethanol (analytical grade, Aldrich) and dried under nitrogen. They were then immersed in piranha solution (70%  $\text{H}_2\text{SO}_4$ , 30%  $\text{H}_2\text{O}_2$ ) for an hour, rinsed very thoroughly in distilled water and dried on a hotplate under nitrogen. The glass slides were used immediately post treatment.

The samples were analysed immediately after the films were deposited using a Molecular Imaging AFM. Topographical and amplitude AFM images were collected under ambient conditions, using tapping mode. Etched silicon tips of nominal radius 10 nm, with a typical spring constant of range 2.5-8.5 N/m and resonant frequency range 150-170 kHz were used. The measurements were repeated on several films, and in each film multiple micron scans were taken in different regions to ensure a good sampling of the film morphology. Solvent only immersion depositions were performed for comparison purposes.

### 6.2.3 Results

Identical particles were deposited on both surfaces but the ICAT monolayer-functionalised surface yielded a higher particle coverage density (where the particle coverage densities were compared on surfaces by counting the number of aggregates on several typical  $25\text{ }\mu\text{m}^2$  scanned areas on each surface). ICAT/DMSO solutions of  $1 \times 10^{-3}\text{ M}$  and  $1 \times 10^{-6}\text{ M}$  were also deposited on glass substrates using a different procedure (immersion coating as detailed in the following chapter) and identical particles (same dimensions within error) were deposited with  $1 \times 10^{-3}\text{ M}$  solutions.

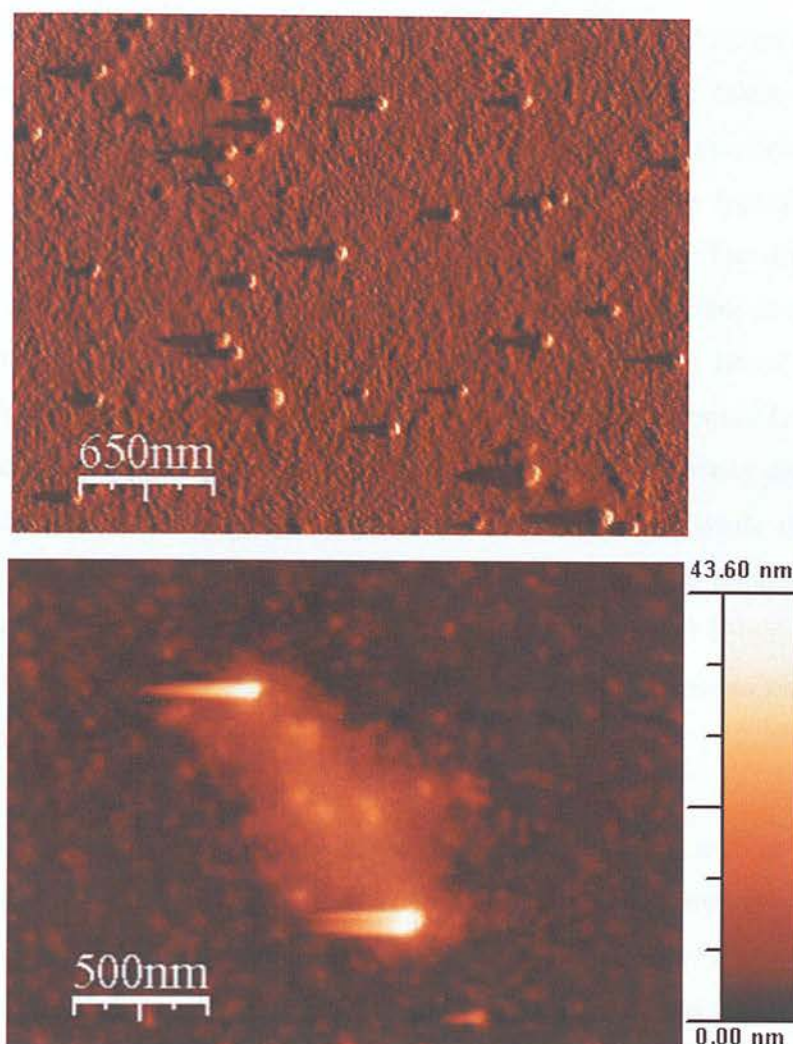


Figure 6.4: (a) Amplitude and (b) topographical AFM images of film morphology ( $1 \times 10^{-3}$  M ICAT/DMSO solution) deposited on a glass.

Figure 6.4a illustrates a typical nanoparticle assembly on a glass substrate. A sparse coverage of randomly positioned, single-bodied, discotic nanoparticles with a face-on orientation was observed. The tail adjacent to the particle is an AFM artifact, as established through scanning the sample in different directions. In conjunction with the particles there are also expansive thin deposits (islands) randomly shaped and positioned, as illustrated in figure 6.4b. These islands of growth have a regular thickness of 10-12 nm with an extremely broad distribution of lateral dimensions from 100 nm-1.4  $\mu\text{m}$  (very roughly taking the diameter as the longest straight line between two island edges).

Particle dimensions were measured from readily distinguishable individual particles from multiple AFM images from multiple samples. Particles were taken from an incomplete particle layer deposited on a rough bulk (non particulate) type layer, where the baseline for the particles, marked as zero on the z-scale of the typical particle profiles illustrated in 6.5a, is the mean height (5 nm) of the bulk layer. The dimensions of one hundred particles were measured and the (b) diameter and (c) height distributions are illustrated in figure 6.5. The diameter is defined as the maximal lateral (x axis) distance between the two outer points and the height as the peak maximum (z-axis) on the particle contour plots. Both particle heights and diameters are narrowly distributed. However, the diameters have two populations of preferred diameters while the height distribution consists of a single population. The two preferred diameter populations are roughly equal in proportion. The mean particle diameter 101 nm and height 19.3 nm combined with the round particle shape observed in the topographic images proves that these particles are discotic in shape.

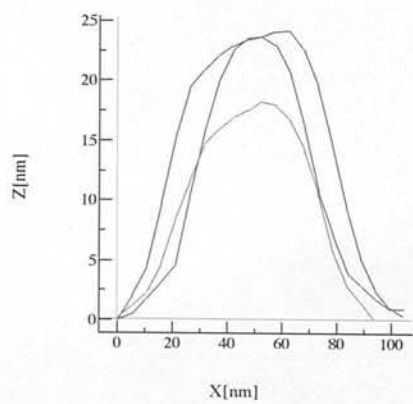
The deposition was repeated with a more concentrated ICAT solution and the resultant film morphology is illustrated in figure 6.6. There was a positive correlation between nanoparticle density of coverage and concentration. A clear increase in both the number of individual particles and the number of larger aggregates was observed with increasing concentration.

The larger aggregates that featured at increased concentration are highlighted in figure 6.7. These aggregates consisted of clusters of smaller discotic particles, where the smaller particles still maintain their identity rather than amalgamate to form one body. Most of these aggregate groups consisted of 2 to 3 smaller particles grouped together with heights consistent with 2 to 3 particles stacked in a face-on configuration on top of these particles.

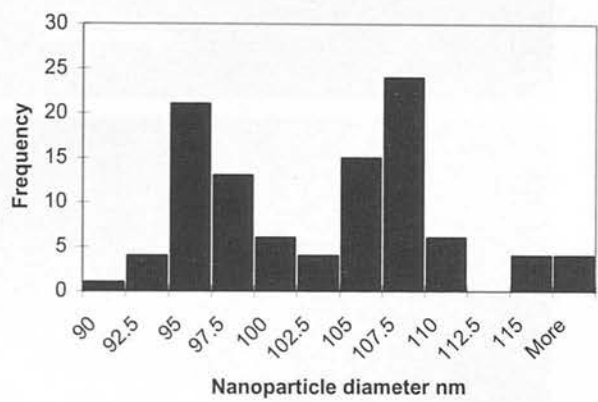
Finally, the number of thin randomly sized islands decreased with increasing concentration.



a



b



c

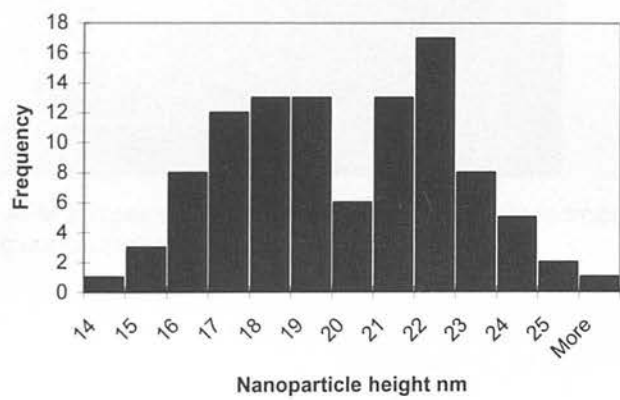


Figure 6.5 (a) typical particle diameter profiles taken from the AFM topographic images of nanoparticles, from ICAT/DMSO solution deposited onto glass substrates. Figure 6.5(b) diameter and (c) height distributions of the ICAT nanoparticles. The bin with the lowest dimension value in each figure ranges from 0 to the labelled value. The following bin values range from the lower value neighbour bin value +0.1 to the labelled value as the maximum.

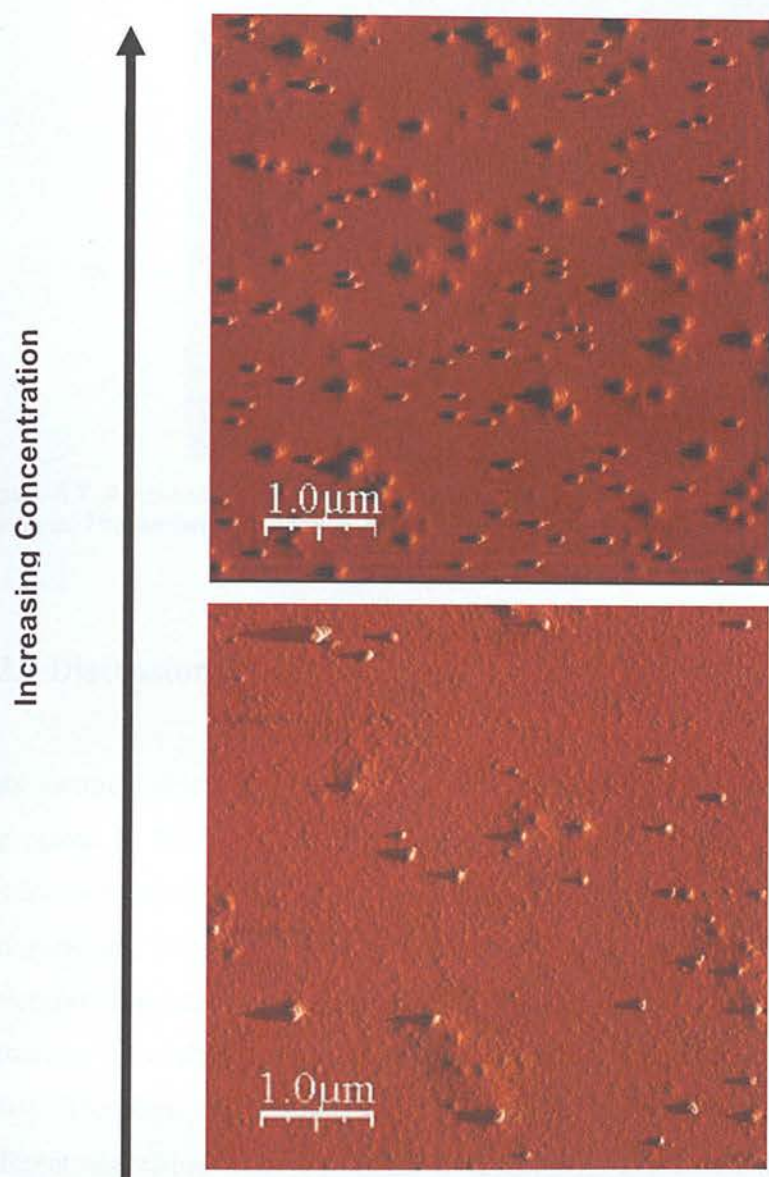


Figure 6.6 Amplitude AFM images of morphology development with increasing ICAT concentration (starting concentration  $1 \times 10^{-4}\text{M}$ ).



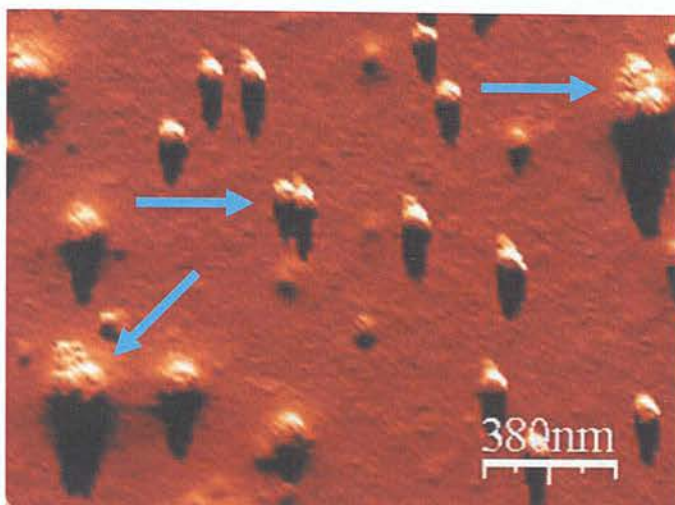


Figure 6.7 Amplitude AFM image of ICAT nanoparticles deposited with high concentration solutions. The arrows highlight the clusters of discotic particles.

#### 6.2.4 Discussion

Here identical discotic nanoparticles were deposited, which is typical of pre-established aggregates in solution, rather than molecularly dissolved species aggregating on the substrate (Jonkheijm et al. 2003 and Miao et al. 2009). In conjunction with the discrete nanoparticles, large polydisperse islands of ICAT growth, typical of a rapid bulk molecular deposition were deposited, which reduced in number as a function of increasing concentration (Duzhko et al. 2006, Jonkheijm et al. 2003 and Surin et al. 2004). The fact that identical particles were deposited on different surfaces with different deposition techniques, including one with aggressive drying, implies that these are the actual particles in solution. The evidence is suggestive of a mixture of phases including pre-established aggregates and a molecularly dissolved phase. The solution particle concentration increased and molecularly dissolved portion decreased as a function of concentration.

Spontaneous aggregate formation at raised concentrations, as a function of solvent parameters, has been observed frequently in solutions of similarly structured molecules

(Belleney et al. 2004, Duzhko et al. 2006, Jonkheijm et al. 2003, Nguyen et al. 2004, Snitka et al. 2005 and Yang et al. 2008). Assuming the particles here are pre-established in solution, the consistent narrow particle dispersity is suggestive of thermodynamic equilibrium between solute aggregates this size and the surrounding solvent molecules. These nanoparticles appear to be soluble in these solutions as when the solutions were aged >two years there was no precipitation. The aggregate solubility in DMSO can be related to DMSO's favourable KT parameters (table 8.1 chapter 8, (Garcie-Tellado et al. 1990) which is discussed at length in chapter 8.

The regular particle shape and dimensions, and the fact that the particles are transferable between surfaces throughout the range of (some particularly aggressive) experimental conditions reflects a high particle mechanical integrity and stability. This stability and regularity in shape is rare in aggregates self assembled in solution with similar molecules using supramolecular interactions, but has been observed in aggregates assembled with stronger supramolecular interactions, in particular multiple highly directional H-bonds (Jonkheijm et al. 2003 and Wang et al. 2007). The particle shape in solution could be slightly different to the shape of the particles deposited here as soft particles can be flattened through solvent removal and the local force applied by the AFM tip, although these effects are more prevalent in hollow particles (Avyppanpillai et al. 2006 and Yang et al. 2005).

The spectroscopic data was consistent with J-type stacking in the aggregates. It is interesting to note that H-type aggregates are usually narrow 1D nanowires while J-type stacking in aggregates tend to result in broader 1D aggregate shapes, but also results in roughly spherical and platelet aggregates, which is consistent with the discotic aggregates produced here (Balakrishnan et al. 2006, Balakrishnan et al. 2005, Leclere et al. 2004, Nguyen et al. 2004, Schwab et al. 2003, Tanaka et al. 2005, Wang et al. 2005, Yao et al. 2003 and Zhang et al. 2008). Note that J-type stacking is predicted with this molecule, as discussed in detail in the following chapters.

### 6.3 Conclusion

A pure crystalline ICAT product containing no polymer or unreacted monomer was successfully synthesised through the new chemical procedure. It had slightly different optical properties to Mount's product and vastly different conductivity to Kaneko's charge transfer product.

The combined NMR, UV-visible and fluorescence spectroscopy evidence pointed to a molecularly dissolved ICAT solution at lower concentrations and a phase change accompanied by a purple emission at elevated concentrations, in selected polar solvents.

The spectra properties at raised solution concentrations are characteristic of aggregate formation, which has been observed in similar molecules dissolved in several solvent classes at the same concentration range (Bao et al. 2006, Fu et al. 2001 and Sauer et al. 2011). The fluorescence spectral fine structure is characteristic of J-aggregate formation. The emission properties are typical of aggregates of colloidal dimensions with a narrow particle size distribution and/or narrow range of particle structures at  $1 \times 10^{-5}$  M concentrations in both solvent systems. As the concentrations were increased  $> 1 \times 10^{-5}$  M in the solvent mixture, the emission changes signified less ordered structures and/or increase in particle dispersity and increased electron delocalisation in the aggregates.

The AFM results confirmed that ICAT was molecularly dissolved at lower concentrations and aggregated as a function of concentration in ICAT/DMSO solutions. Narrowly dispersed discotic nanoparticles were deposited on the substrates and the deposition results implied that these were the actual particles pre-established in solution.

The particles were dissolved in the solution. The narrow particle dispersity is suggestive of thermodynamic equilibrium between solute aggregates this size and the surrounding solvent molecules. The consistency in particle shape and dimensions is rare but has been observed in similar systems involving self-assembly through multiple highly directional

H-bonds. The particle shape has been observed in J-stacked aggregates but not in H-stacked aggregates.

The AFM data was in agreement with the spectroscopic data that pointed to aggregation at raised concentrations. The narrow particle dispersity and highly regular structures will contribute towards narrow bands and detailed fine structure in the emission spectra.

We have developed a simple synthesis of nanoparticles that are transferable between surfaces, stable in solution and possess a high mechanical integrity. These properties are unusual and highly sought after in organic semiconductor aggregates, making them ideal candidates for electronic application purposes.

## **Chapter 7**

### **7 ICAT self-assembly on functionalised surfaces**

## 7.1 Introduction

Research into organic semiconducting small functional molecular thin films and nanoparticles is fuelled by a multitude of novel and enhanced properties as compared to those of conventional inorganic semiconductors, which have found diverse applications in electronics, (Cassagneau et al. 1998, Chen et al. 2004, Usta et al. 2011 and van Nostrum et al. 1995) optoelectronics (An et al. 2009, Chen et al. 2011 and Piok et al. 2003), biological sensors (Garjonyte et al. 2000 and Zhao et al. 2009) and data storage (Mustroph et al. 2006). Controlled assembly of these molecules is essential in tailoring and expanding device properties, fitting particular devices and connections, device miniaturization and exploring the fundamental science in the organic semiconducting area, which is as yet not well established. To date the overwhelming majority of organic semiconducting molecules are p-active (Balakrishnan et al. 2006, Balakrishnan et al. 2005 and Dimitrakopoulous et al. 2002). One reason behind the ICAT selection is that its structure lends itself towards n-activity (detailed in chapter 9) and electronic devices require both p and n-type organic materials and the n-type film structure-property relationship should provide an invaluable insight into fundamental organic semiconducting science and organic material based devices (Wen et al. 2010).

The self-organisation of organic semiconductor building blocks in solution and on surfaces is of interest as electronic device performance is strongly dependent on the interplay between electronic structure and molecular arrangement and could be the starting point for molecular electronics or even circuits with nanometer sized objects (De Cupere et al. 2006, Dimitrakopoulous et al. 2002, Kumaran et al. 2010, Lim et al. 2009, Lockilin et al. 2005 and Simson et al. 2004). There is an initiative to replace the current multi-stepped arduous solution-based deposition techniques, ineffective electrochemical techniques and expensive complex vacuum sublimation with facile, single-step, cost effective, large-scale solution based methods (Jin et al. 2008). Unfortunately it is notoriously difficult to control the assembly of organic semiconducting molecules and their aggregates using solution-based deposition techniques (Balakrishnan et al. 2006,



Duzhko et al. 2006, Jonkheijm et al. 2003, Shea et al. 2007, Shea et al. 2006, Snitka et al. 2005 and Surin et al. 2006). One of the foremost reasons for the attention shift from conducting polymers towards small functional molecules is that the molecular packing in polymers can be difficult to control due to the complicated intermolecular interactions and polydispersity of the chains, while molecular building blocks with weaker interactions allow highly flexible structural tunability. Several solution based deposition techniques, including direct chemical oxidation, dip-coating, drop-casting, immersion-coating and spin-coating were investigated using ICAT, ICAT polymer and ICAT salt solutions. Electrochemical ICAT deposition resulted in highly disordered assemblies of an ICAT molecule/polymer mixture (Mackintosh et al. 1994, Sivakumar et al. 1993 and Tourillon et al. 1992). The ICAT polymer was insoluble in most solvents and the ICAT salt resulted in highly disordered films, therefore the ICAT molecule was used throughout the thesis.

One of the most highly influential factors on film morphology is the solvent evaporation rate, which affects the solvent dewetting, which can interfere with the self-assembly of the molecule (Chang et al. 2004, Hoeben et al. 2005, Mas-Torrent et al. 2004, Samori et al. 2001). Two frequently used deposition methods, involving very different evaporation rates, were investigated here. Spin coating resulted in very poor coverage and dropcasting produced mixed phase, randomly sized and positioned deposits. Immersion coating coupled with a rigorous washing and rapid drying procedure typically resulted in continuous homogeneous films and therefore was used throughout this thesis. Relatively long immersion times with low concentration solutions were selected so as to allow the ICAT molecule to adopt the most thermodynamically favourable configuration in the film (Duzhko et al. 2006, Jonkheijm et al. 2003 and Surin et al. 2004). Also elevated concentration solutions (mMol) of similar molecules formed pre-established aggregates in solution, which can prove difficult to assemble on surfaces in a controlled fashion (Jonkheijm et al. 2003, Duzhko et al. 2006, Surin et al. 2004 and Yang et al. 2008). Therefore low concentration solutions with highly polar protic/aprotic solvents, in which ICAT should be highly soluble, were used with the intent of bulk molecular film



deposition. Post-immersion treatments were investigated including rinsing in the solution solvent to remove dissolved and poorly adhered ICAT molecules, followed by drying under nitrogen at room temperature with a short spell in an oven to remove any residual solvent.

Typically, assembly of small functional molecules using supramolecular interactions is highly unpredictable and difficult to control, resulting in extremely disordered films that are unsuitable for device application and provide a very poor starting point for scientific insight into the assembly process and structure-property relations (Ajayagosh et al. 2006, Balakrishnan et al. 2006, Ingrosso et al. 2009, Jonkheijm et al. 2003, Kiriya et al. 2003, Shea et al. 2007, Shea et al. 2006, Snitka et al. 2005 and Yip et al. 2008). The ICAT structure allows  $\pi$ - $\pi$  and multiple possible lateral H-bonding intermolecular interactions. Assembly of similar molecules using these intermolecular interactions is highly complex but has produced well-defined aggregates in a range of shapes and sizes in solution and/or at interfaces depending on the nature, position and number of functional groups, solvent environment and substrate chemistry (Ajayagosh et al. 2006, Aoki et al. 2002, Autwer et al. 1999, Duzho et al. 2006, Gao et al. 2008, Garcie-Tellado et al. 1990, Hoebe et al. 2005, Lahiri et al. 2000, Leclerc et al. 2004, Milic et al. 2002, Nguyen et al. 2004, Shirakawa et al. 2003, Tanaka et al. 2005 and Wang et al. 2007). A range of well-defined interfacial aggregate assemblies should be possible using these interactions.

The electron-deficient nitrogen-containing heterocycle ICAT allows for potential ambipolar activity (Newman et al. 2004). ICAT also offers high redox-activity, interesting fluorescent properties, excellent thermal stability and biological compatibility (Bartlett et al. 1992, Bieganski et al. 1995, Mackintosh et al. 1995, Mackintosh et al. 1994 and Mackintosh et al. 1994a). This highly processable molecule lends itself to potential liquid crystal formation and the 3 carboxylic acid side-groups per molecule should greatly enhance solubility. The chemical properties are readily tailored through facile functionalisation of the carboxylic acid groups and can be easily activated to form strong covalent attachments to surfaces. The asymmetric trimer molecule was selected

over the symmetric isomer as the extra intermolecular and ICAT-substrate H-bonding possibilities (through two carboxylic acid groups, as opposed to one from the symmetric isomer) should allow for much greater control over the assembly process and stronger adhesion to substrates (Jonkheijm et al. 2006 and Prins et al. 2001).

The experimental objectives were as follows. Firstly, to develop a facile cost-effective solution-based method to produce reproducible high quality ICAT thin films with a range of morphologies. Functional SAMs were selected to try to control the interfacial ICAT orientation, aggregation and coverage and consequently bulk morphology using supramolecular interactions, in particular multiple H-bonds. Functional SAMs were used here that are applicable in organic electronics and, in particular, enhance performance in devices functionalized with n-active organic semiconductors (Chau et al. 2005, Kobayashi et al. 2004, Shao et al. 2011, Sirringhaus et al. 1998, Sun et al. 2010 and Wen et al. 2010). Glass substrates were used as they are easy to functionalise and are structurally very similar to  $\text{SiO}_2$  dielectric surfaces, thus the film morphologies should be an accurate representation of those deposited in organic based electronic devices.

The ICAT carboxylic acid groups were activated to establish extremely strong, highly directional, interfacial ICAT-APS amide covalent bonds with the intent of inducing highly ordered interfacial assemblies and consequently a high quality microstructure on a functional surface, suitable for both electronic and bioelectronic applications. Through ICAT carboxylic acid activation, strong highly directional novel inter-ICAT covalent interactions were also induced with the aim of increasing control over the bulk assembly process (as compared to assembly using weaker supramolecular interactions) and produce novel assemblies.

The AFM film morphology analysis, interpreted using molecular modelling and supramolecular chemistry, should provide an invaluable insight into the assembly process and indeed into ICAT chemistry, of which little is known at present. SEM was

utilised to image the macroscopic film morphology and to determine which films were electrically conducting and potentially applicable in organic electronics. The ultimate goal here is to apply the newly gained understanding of the ICAT assembly process and novel range of ICAT film morphologies, in the production of a range of ordered tailored assemblies to control and expand organic electronics properties.

## **7.2 Experimental Method**

### **7.2.1 Substrate cleaning procedure**

Glass microscope slides were rinsed in ethanol (analytical grade, Aldrich) and dried under nitrogen. They were then immersed in piranha solution (70%  $\text{H}_2\text{SO}_4$ , 30%  $\text{H}_2\text{O}_2$ ) for an hour, rinsed very thoroughly in distilled water and dried on a hotplate under nitrogen. The glass slides were used immediately post treatment.

### **7.2.2 Chemical modification of glass substrates**

The piranha cleaning process hydroxylates the glass surface. 1,1,1,3,3,3-hexamethyldisilazane (HMDS) was attached to the glass, rendering them hydrophobic, with vapour phase treatment of the cleaned glass substrate with HMDS (Aldrich). Glass substrates were attached to the lid of a closed glass vessel (coated with HMDS) facing 0.5 ml of HMDS, placed at the base of the vessel, which was heated for at least 2 hours at 100°C. The glass substrates were allowed to cool before rinsing with distilled water and ethanol to remove residual HMDS.

Amino-terminated glass substrates were generated by immersing the glass slides in a 1% solution of 3-aminopropyl-triethoxysilane, (APS, Aldrich) in 95% ethanol for 2 hours in a sealed container (Zhang et al. 2004). Unreacted silane was removed by rinsing in distilled water and ethanol, before placing the slides in the oven for 5 minutes at 115°C. The slides were then rinsed again in ethanol and dried under nitrogen.

### 7.2.3 Activation of ICAT carboxylic acid side groups

The carboxylic acid side groups were coupled to the amino group of the APS terminated glass substrate, by reacting 0.3 mMol ICAT with 0.4 mMol of 1,3-diisopropylcarbodiimide (DIC, Aldrich) and 0.6 mMol hydroxybenzotriazole hydrate (HOBT, Aldrich) in the presence of 10 ml of dry N,N- dimethylformamide, (DMF, Aldrich) (Duan et al. 1995 and March et al. 1992). The reaction was performed overnight and the following morning the slides were rinsed thoroughly and dried under a gentle stream of nitrogen.

### 7.2.4 Immersion coating

The substrates were coated immediately after chemical modification (7.2.2). The functionalised substrates were immersion coated in freshly made filtered 0.001 mM ICAT/DMF solution overnight. The substrates were then washed thoroughly in DMF, followed by ethanol and dried under nitrogen and finished in the oven (100°C). Selected amino-terminated slides were placed in the carboxylic acid activation reaction overnight, as described in 7.2.3.

### 7.2.5 Analysis

The substrates were analysed immediately after immersion coating, using a Molecular Imaging AFM and with a SEM under vacuum operated at 2kV. Elemental analysis was performed on the films. For each immersion experiment the measurements were repeated on several films, and in each film multiple micron scans were taken in different regions to ensure a good sampling of the film morphology. Solvent-only immersion depositions were performed for comparison purposes.

Topographical and amplitude AFM images were collected under ambient conditions, using tapping mode. Tapping mode was used to minimise sample deformation although

limited sample deformation can occur still in this mode (Garcia-Parajo et al. 1997). Etched silicon tips of nominal radius 10 nm, with a typical spring constant of range 2.5-8.5 N/m and resonant frequency range 150-170 kHz were used.

In order to minimise scanning artefacts and contamination, each sample was scanned in opposite directions with a range of cantilever resonant frequencies and tip spring constants and shapes, with regularly changed tips, which were withdrawn and vibrated between scans. When collecting sample measurements the vertical resolution is outstanding, limited to 0.1 nm because of electronic noise from the detection system and cantilever thermal fluctuations (Garcia et al. 1997). The lateral resolution however is broadened by tip dilation.

### **7.3 Results 1: ICAT film morphology on hydroxyl terminated glass**

A continuous extremely smooth ICAT film was deposited on the hydroxyl (OH)-terminated substrate, as illustrated in the AFM images of two different samples in figure 7.1. The high quality and continuous nature of the film on a larger scale, is illustrated in the SEM images in section 7.6.

A film produced from a shorter immersion time with incomplete coverage was selected to observe the film growth, as seen in figure 7.2. The morphology consists of a continuous film with medium-sized approximately oval shaped ruptures (of length range 100-500 nm and width range 50-150 nm) in parallel alignment, with clusters of substantially smaller holes surrounding them. The rupture depth is discussed further following the next figure.



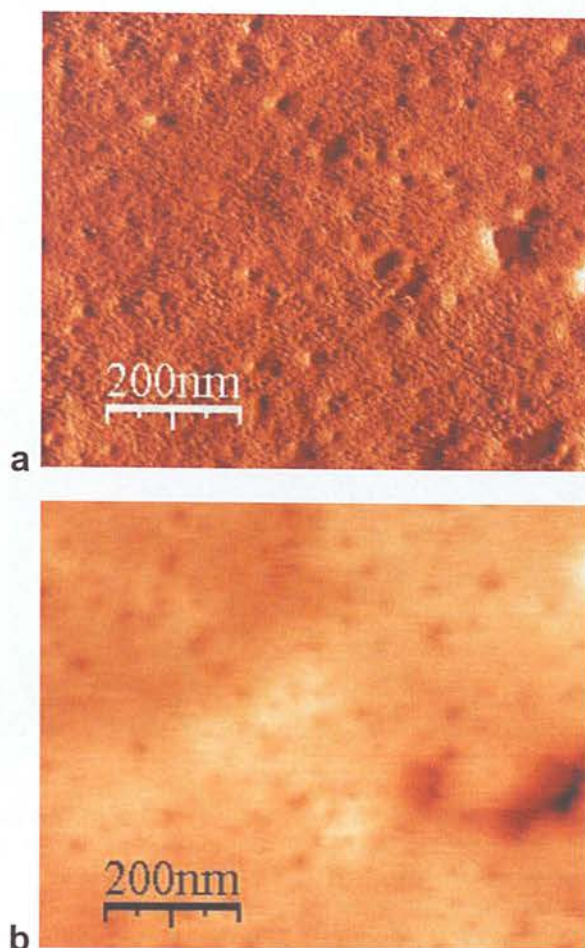


Figure 7.1: Amplitude (a) and topographical (b) AFM images illustrating ICAT morphology on the OH-terminated glass substrate from 48 hour immersion coating in ICAT/DMF solution.

The ruptures had raised features at the edges (edge features), as illustrated in the cross sectional profile in figure 7.3.

The step heights between the base of the ruptures and the film surface (excluding the edge features) were analyzed and the results are presented in figure 7.4. The most frequently encountered hole depth (the peak with the blue arrow) was subtracted from the most frequently encountered film height (the peak with the red arrow) to determine the step height. The step height was found to be  $1.5 \pm 0.2$  nm. (0.2 nm is the standard error on the mean). The very small peak labeled with the black arrow is the product of the edge features. Interestingly, many of the edge features were 1.5 nm in height and tended to increase in factors of 1.5 nm (figure 7.3).

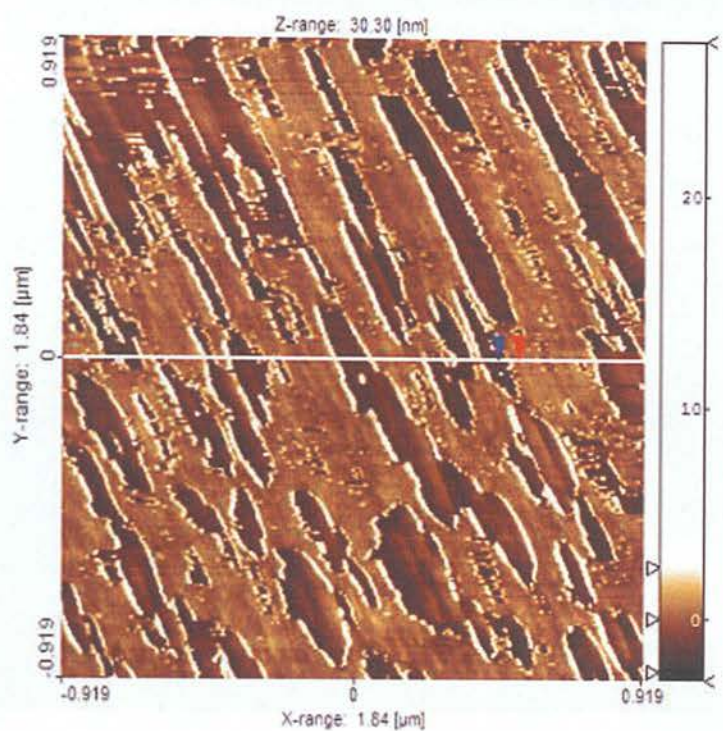


Figure 7.2: Topographical AFM image, illustrating ICAT morphology on the OH-terminated glass substrate from immersion coating overnight in ICAT/DMF solution. The line marks the location of the cross sectional profile illustrated in figure 7.3. The area marked with a red and blue arrow is an example of a step, defined as the height difference between the hole base and film edge (excluding the raised edge features), as marked with a blue box on the profile.

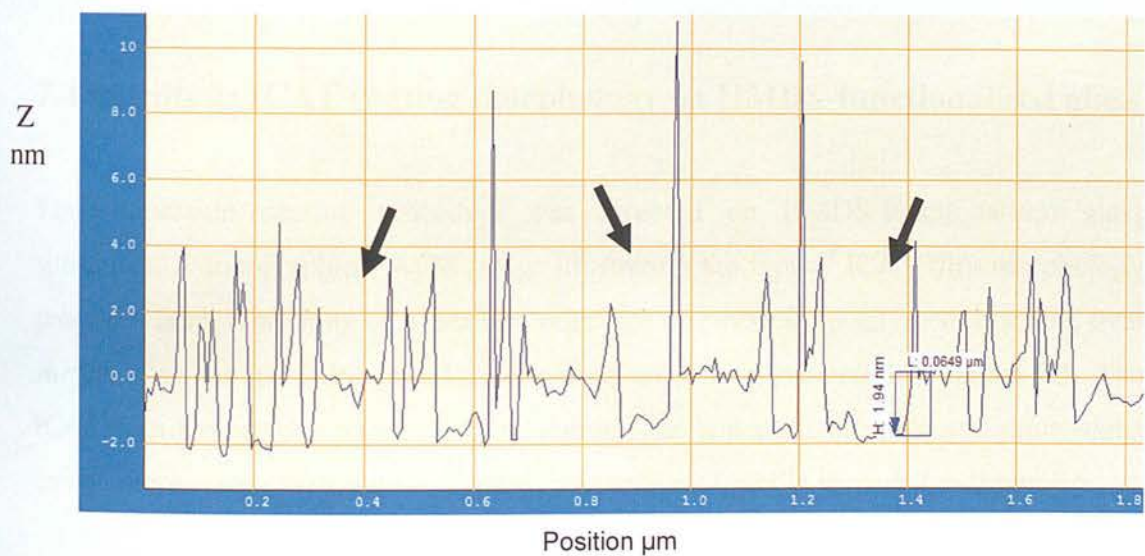


Figure 7.3: Typical cross sectional profile of the ICAT immersion coated film on the OH-terminated glass substrate. The black arrows highlight examples of 1.5 nm edge features.



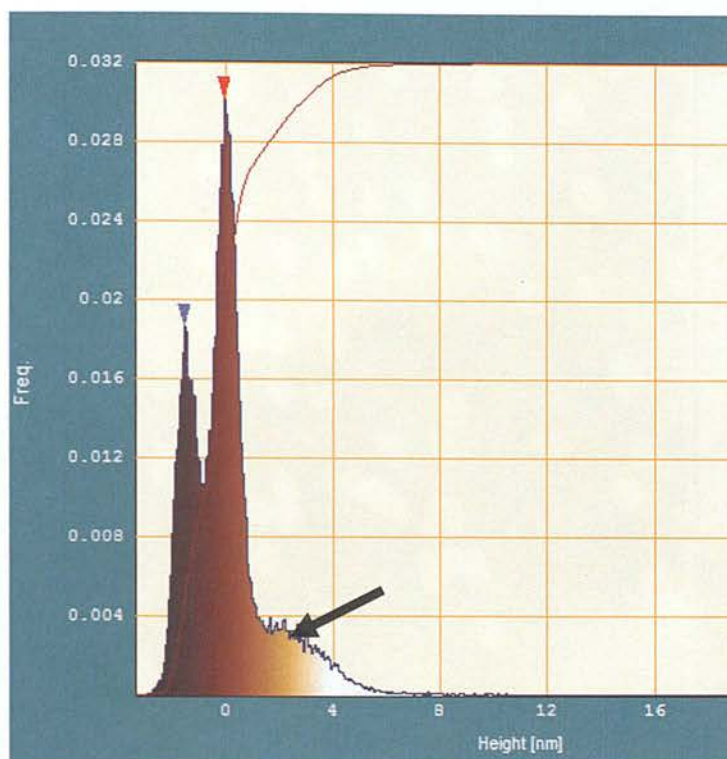


Figure 7.4: Step height analysis of immersion coated ICAT on the OH-terminated glass substrate. The peak labelled with the blue arrow represents the hole depth and the peak labelled with the red arrow represents the step height. The small peak labelled with the black arrow represents the edge features.

## 7.4 Results 2: ICAT coating morphology on HMDS-functionalised glass

The immersion coating procedure was repeated on HMDS-functionalised glass substrates. A topographical AFM image illustrating the typical ICAT film morphology produced here, consisting of a medium coverage of randomly positioned, discrete, oval shaped, flat nanoparticles in a face-down orientation is presented in figure 7.5. The ICAT film topography was highly undulating. The nanoparticle shape and dimensions can be more clearly distinguished in the cross sectional profile provided in figure 7.6.

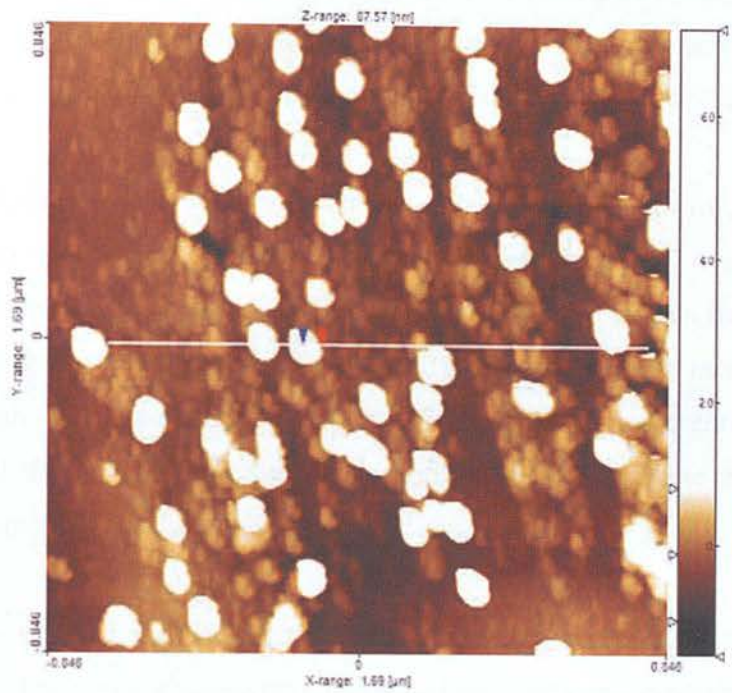


Figure 7.5: Topographical AFM image, illustrating ICAT morphology on the HMDS-functionalised glass substrate from immersion coating overnight in ICAT/DMF solution. The line marks the location of the cross sectional profile, provided in figure 6.6. The red and blue arrows on the particle provide an example of where particle heights were taken from, defined as the height difference between the particle maximum and the base, as marked with the blue box on the profile.

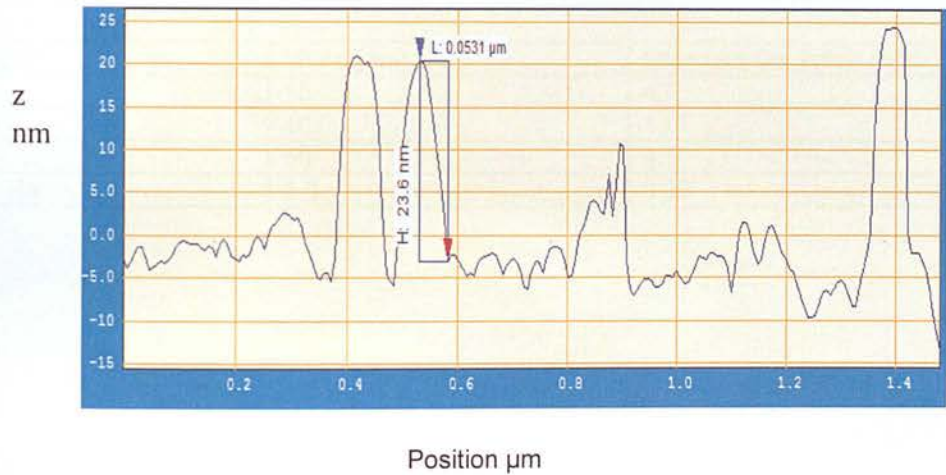


Figure 7.6: Typical cross sectional profile of the ICAT immersion coated film on the HMDS-functionalised glass substrate. The baseline is taken using AFM software as -5nm on the z scale.

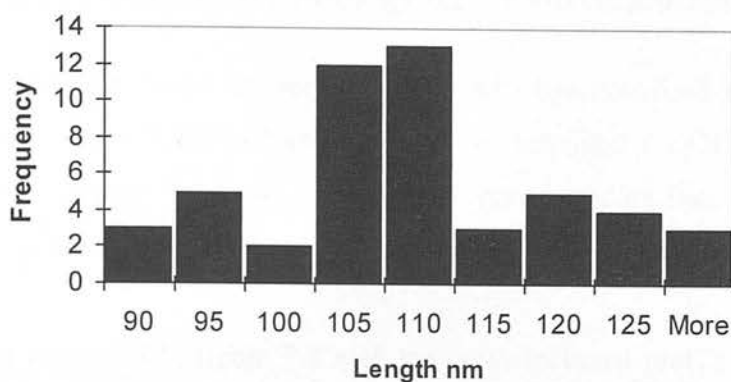
The film morphology consisted of a rolling continuous (non particulate) layer with an incomplete nanoparticle layer on top. The dimensions were measured from readily distinguishable individual particles from multiple AFM images from multiple samples.

Then a dimensional analysis was undertaken and the particle length (a), width (b) and height (c) mean values and distributions are illustrated in table 7.1 and figure 7.7 respectively. Cluster length is defined as the maximal distance between two points on an outer cluster contour and cluster width is defined as the cluster area inclusive of holes divided by length. The nanoparticle height is defined as the mean height of the particle contour. Lateral distortion is not significant here as the nanoparticle dimensions are substantially larger than the tip radius.

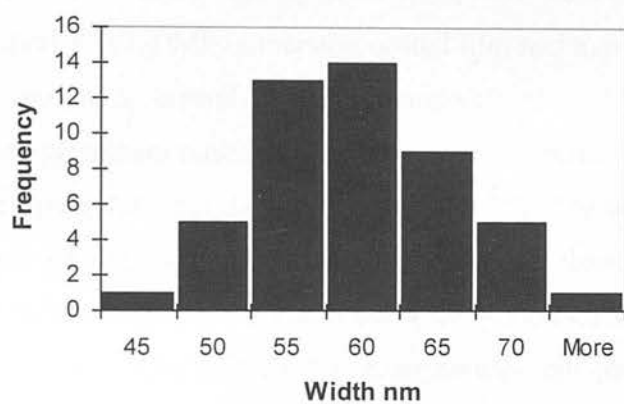
The particle aspect ratio, defined as particle length/width, mean value is 2.0 (standard deviation 0.33). The particle aspect ratio combined with the particle height illustrate that the particles are nanobar shaped. The particle distributions and standard deviations reveal the particle dimensions to be narrowly distributed centring around one clear dominant peak signifying a single population of preferred particle lengths, widths and heights respectively.

Table 7.1: Nanoparticle dimensions

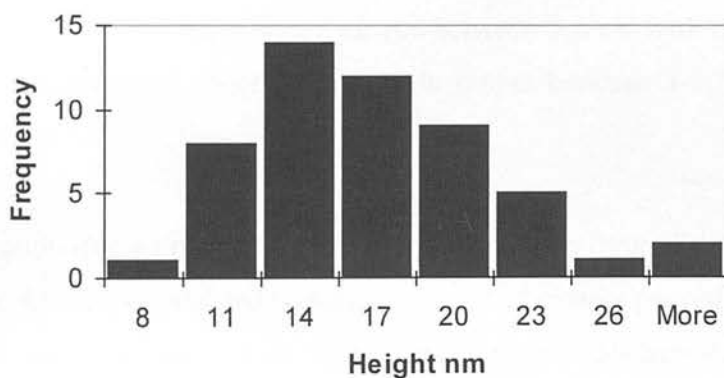
Parameter	Mean (nm)	Standard Deviation (nm)
Height	15	4.5
Length	107	10.7
Width	56	9.7
Aspect Ratio	2.0	0.33



a



b



c

Figure 7.7: Distribution taken from AFM topographic images of particle (a) length, (b) width and (c) height of the ICAT immersion coated film on the HMDS-functionalised glass substrate. The bin with the lowest dimension value in each figure ranges from 0 to the labelled value. The following bin values range from the previous bin number (neighbouring bin to the left of the bin) +0.1 to the labelled value as the maximum.



### 7.5 Results 3: ICAT coating morphology on APS-functionalised glass

The immersion-coating procedure was repeated on an APS-functionalised glass substrate with both the standard ICAT/DMF solution and an activated COOH ICAT/DMF solution (detailed in sections 7.2.2 and 7.2.3) and the corresponding film morphologies are illustrated in figures 7.8 and 7.10.

The AFM images presented in figure 7.8 with the cross-sectional profile illustrated in figure 7.9, highlight the morphological differences between these two films on the APS-functionalised surfaces. Both immersion systems produced continuous coatings. However, only the standard ICAT/DMF immersion-coated film had a medium coverage of large, polydisperse (spanning several 100 nm), randomly shaped and positioned surface indentations, with prominent raised features at the edges (examples of which are marked with arrows on figure 7.8a and the profile in figure 7.9). The activated COOH system had a much more rolling topography and rougher surface than that of the non activated film. Several micron areas were scanned using the WsxM4.0 software and the activated COOH system consistently had greater mean heights and root mean square (rms) deviation of the surface values (measurement of the standard deviation of surface heights which is a measurement of surface roughness) than those of the non activated system. The activated system mean height ranged between 5-6 nm with rms values 2.3-2.7 nm and the non activated system mean height ranges between 3-3.7 nm with rms values of 1.3-1.8 nm.

Higher magnification images of the two films, as illustrated in figure 7.10, revealed that both films on the APS-functionalised surfaces consisted of closely packed nanoparticles. An accurate assessment of nanoparticle dimensions is not possible here due to the close packed nature of the assemblies. Therefore cross-sectional profiles were taken from 15 carefully selected, discrete nanoparticles from both systems to provide a rough approximation of dimensions for comparison purposes.

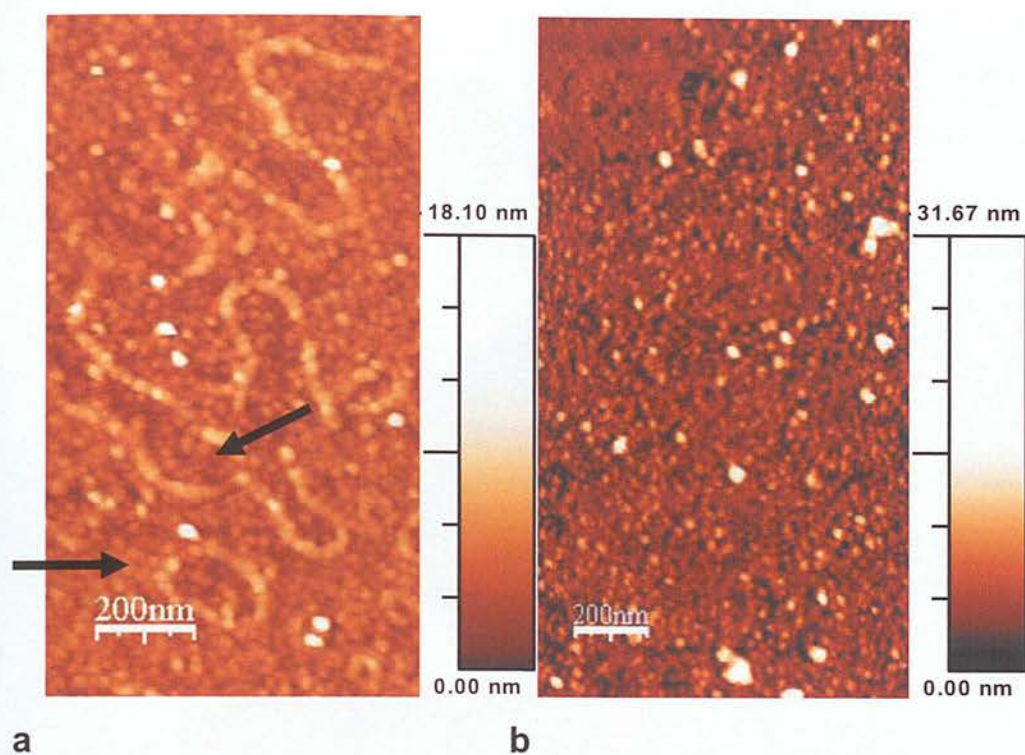


Figure 7.8: Immersion coated (overnight) ICAT morphology on APS-functionalised glass substrates with standard ICAT/DMF solutions, as illustrated by the topographical AFM image (a) and the activated COOH ICAT/DMF solution (detailed section 7.2.2), as illustrated by the amplitude image (b). The arrows denote examples of the surface ruptures on the non activated surface.

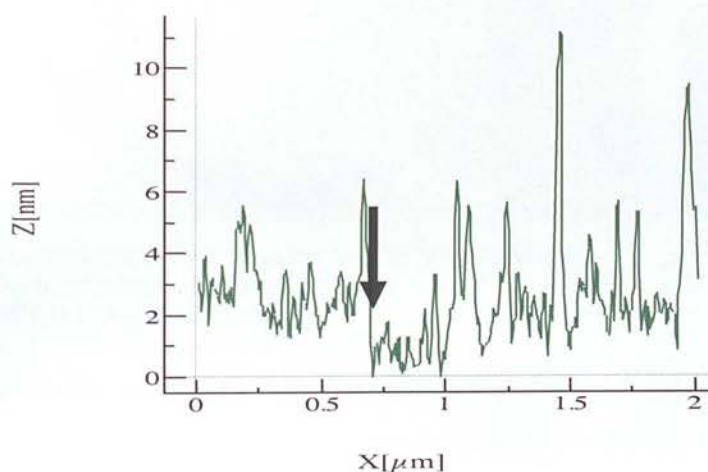


Figure 7.9: Typical cross sectional profiles from immersion coated films in the standard ICAT/DMF solution on APS-functionalised surfaces. The arrow denotes an example of the surface indentations, labelled with arrows on the topographical image.

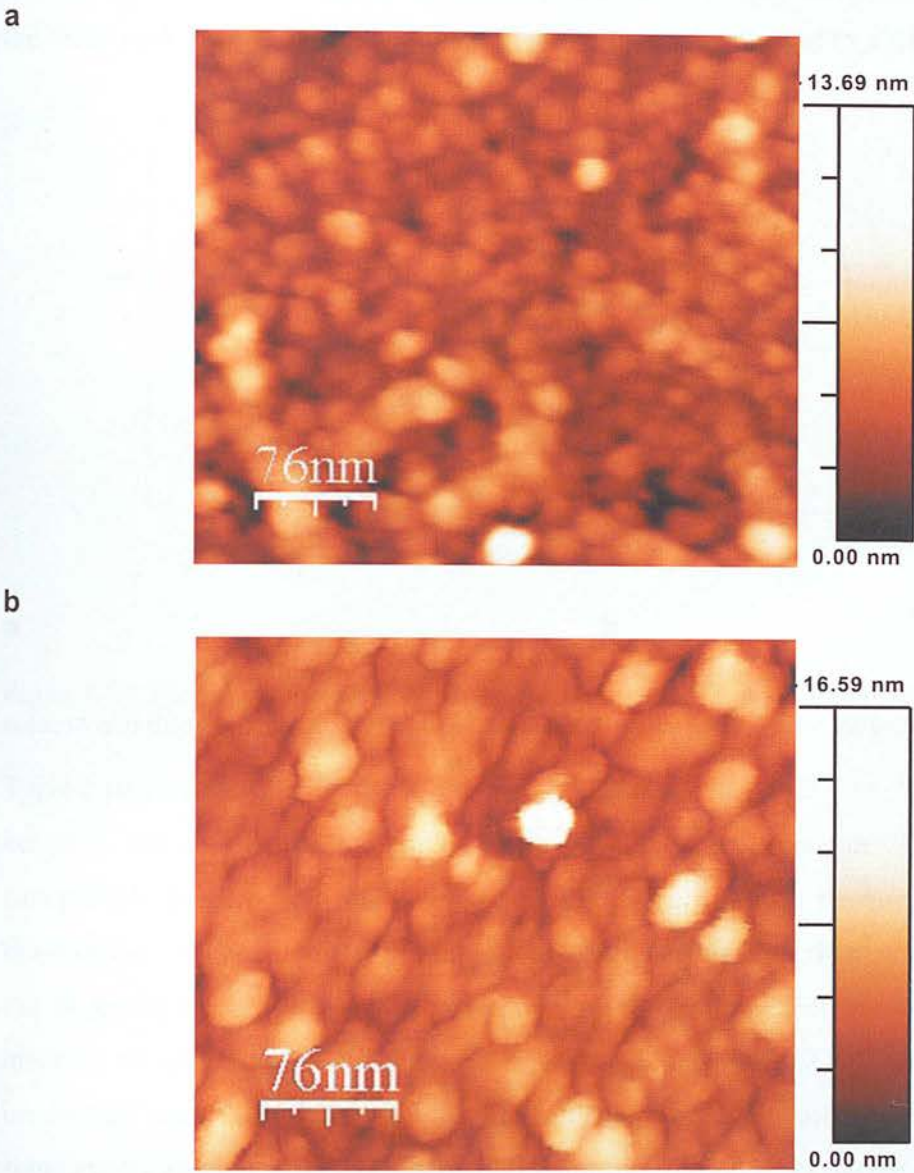


Figure 7.10: Topographical AFM images illustrating granular ICAT morphology from immersion coating on APS-functionalised glass substrates with (a) a standard ICAT/DMF solution and (b) an activated COOH ICAT/DMF solution.

Discrete particles were selected (baseline at 1nm) from mid range in the topography z-scale ( $> 2$  nm in height) so as to avoid measuring the close-packed particles in the lowest layer, but  $< 7$  nm so as to avoid the distorted particles (tip interaction) in the highest layer in the activated COOH system. Discrete particles were selected (baseline at 1nm)



from mid range in the topography z-scale ( $> 2.5$  nm in height) so as to avoid measuring the close packed particles in the lowest layer in the non- activated COOH system.

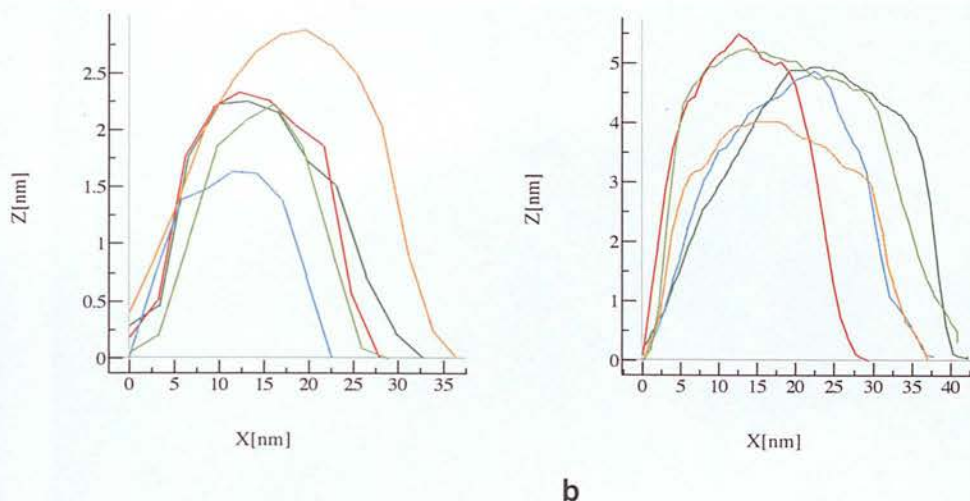


Figure 7.11: Typical particle profiles from immersion coated films in (a) the standard ICAT/DMF solution and (b) an activated COOH ICAT/DMF solution, on APS-functionalised surfaces.

Typical particle profiles for both systems are illustrated in figure 7.11. The nanoparticle height is defined as the maximum height of the particle contour. The majority of nanoparticle heights from the activated COOH system ranged between 5-6 nm while those of the standard immersion ranged between 1.5-3 nm. The diameters were taken as the maximal lateral distance between two points on the outer particle profile. The majority of nanoparticle diameters from both the activated COOH and the standard immersion films ranged between 22-33 nm. The actual nanoparticle diameters will be significantly smaller (approximately 10-15 nm over actual size) due to tip convolution effects, which are prominent when the nanostructure lateral dimensions approach that of the tip radius (tip radius 10 nm) (Ayyappanpillai et al. 2006 and Samori et al. 1998). These particle dimensions (allowing for lateral distortion) demonstrate that the activated COOH system nanoparticle is approximately spherical in shape and that of the standard immersion experiment is disc shaped.

## 7.6 Results 4: ICAT macroscopic film morphology

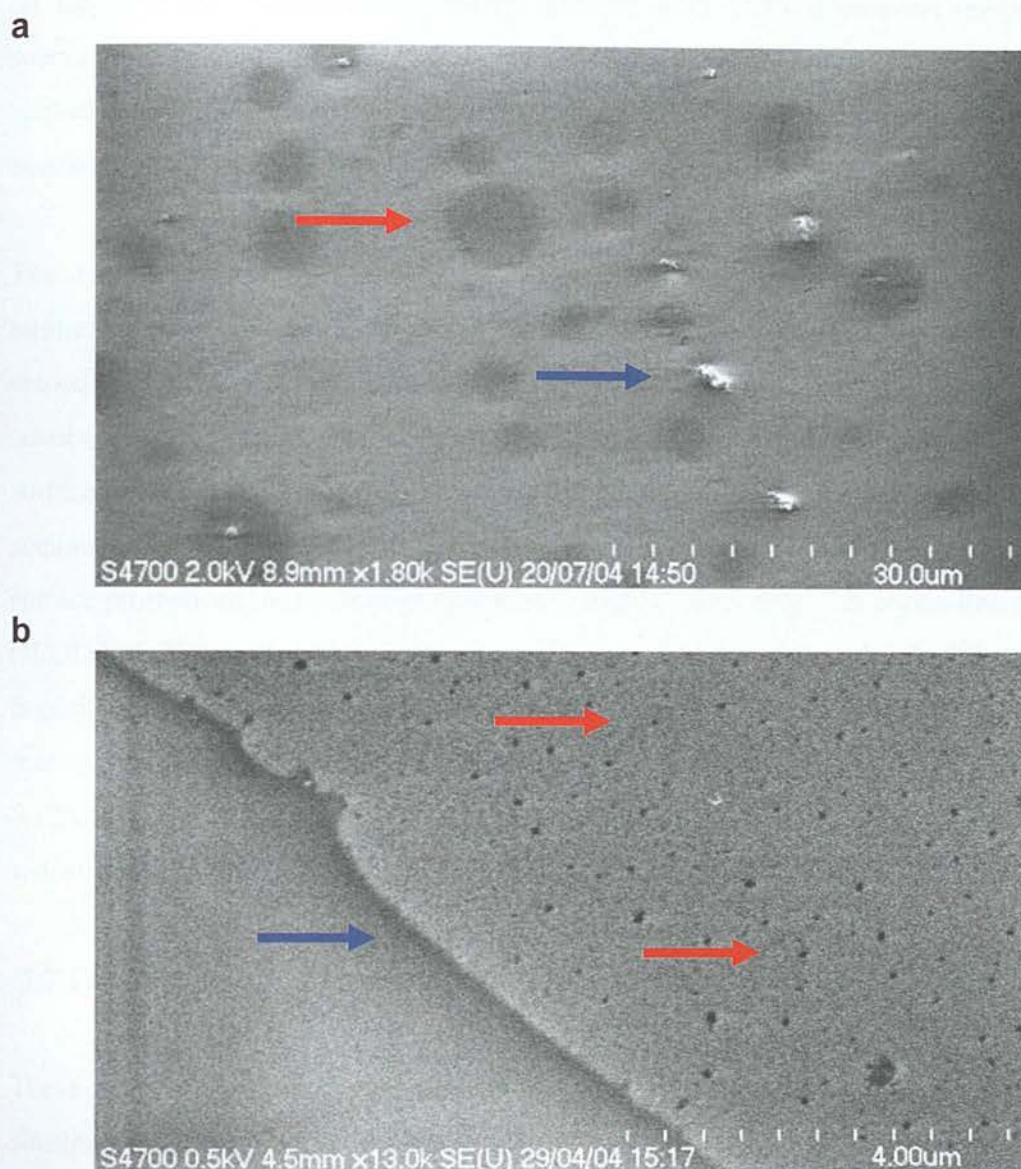


Figure 7.12: SEM images illustrating macroscopic ICAT morphology from immersion coating with (a) activated COOH ICAT/DMF solution on the APS-functionalised surface and (b) standard ICAT/DMF solution on the OH-terminated surface. The total length of the scale bar is given underneath the bar. The red arrow marks a typical example of the large surface indentations and the blue arrows denotes an example of what appeared to be a crystalline domain on figure (a). The blue arrow marks the edge of the sample where the film is to the right of the sample edge and the red arrows point examples of pinhole indentations on figure (b).

The sample is required to be electrically conducting for SEM to image it. It was not possible to image the uncoated glass substrate and the standard immersion-coated films on the APS and HMDS-functionalised surfaces with SEM. However, images were successfully taken of the immersion-coated film on the OH-terminated surface and the activated COOH immersion-coated film on the APS-functionalised surface (with conducting paint around sample rims).

The typical macroscopic activated COOH ICAT film morphology on the APS-terminated substrate, as illustrated in figure 7.12a, consists of a continuous, relatively smooth covering with a sparse coverage of what appears to be randomly positioned, small crystalline domains and a medium coverage of polydisperse, randomly positioned surface indentations. These pits may be a SEM artefact (edge effect) resulting from the accumulation of large quantities of secondary electrons generated at the edges of the surface protrusions, as the topography here is highly undulating with crystalline domains (JEOL Ltd. 2006). The film is homogeneous apart from a sparse quantity of crystalline deposits on the surface, although more work is required here to confirm this. A typical macroscopic ICAT film morphology on the OH-terminated substrate is given in figure 7.12b, showing a continuous, homogeneous, smooth coating with randomly positioned, sparsely distributed, pinhole-type indentations.

## 7.7 Discussion

These experiments established that the film morphology was dependent on both the substrate surface chemistry and the ICAT carboxylic acid activation. The complex interplay between the ICAT-ICAT molecules and the solvent medium in the solution, and the substrate in the film is considered here. The highly polar aprotic immersion solvent DMF has a high affinity for the ICAT molecule and all the surfaces here except for the HMDS-functionalised substrate. The ICAT-solvent interaction is discussed in further detail in the next chapter. The ICAT-ICAT and ICAT-substrate interactions are discussed as appropriate in each subsection.



### 7.7.1 ICAT assembly on OH-functionalised substrates

Microscopically, a smooth continuous homogeneous ICAT film with very few surface indentations was deposited on the OH-terminated substrate (figure 7.1). Macroscopically, the film was homogeneous with continuous coverage and therefore suitable for device application (figure 7.12b). The quality of these films at both the microscopic and macroscopic level is far superior to that of other solution deposited films with organic semiconducting molecules ((Leclere et al. 2004, Kumaram et al. 2010, Monti et al. 2004, Murphy et al. 2005, Sivakumar et al. 1993 and Sun et al. 1989). The mean film height of 1.5 nm was consistent with a monolayer of ICAT molecules in an edge-on configuration with their aromatic core perpendicular to the substrate, as schematically depicted in figure 7.13a (McDougal et al. unpublished data). In this configuration two of the ICAT carboxylic acid side groups can H-bond with the OH surface groups, as demonstrated in figure 7.13b, and the aromatic planes can overlap thus maximizing  $\pi$ - $\pi$  interactions.

Thus the assembly process is interpreted as follows. Firstly free ICAT molecules rather than pre-established aggregates in solution, H-bond with the substrate in an edge-on configuration and then it appears that other ICAT molecules H-bond in a parallel formation on top of the interfacial layer (the thicker edge features in the film increase in factors of 1.5 nm). It is possible there are small soluble aggregates consisting  $\pi$ -stacked ICAT molecules in a parallel formation (H-stacking) in solution as well as the molecules that would stack in the same edge-on orientation as the free molecules forming a layer of height 1.5 nm. However, H-stacks seem unlikely as there are multiple inter-ICAT H-bonding possibilities including quadrupole H-bonding interactions between ICAT molecules inducing dimer formation that are stronger than  $\pi$ - $\pi$  interactions. The fact that the film grows in molecular monolayers is indicative of molecularly dissolved ICAT, which is realised through the low concentration of ICAT molecules and strong multiple H-bonding ICAT interactions with the dipolar aprotic solvent DMF.

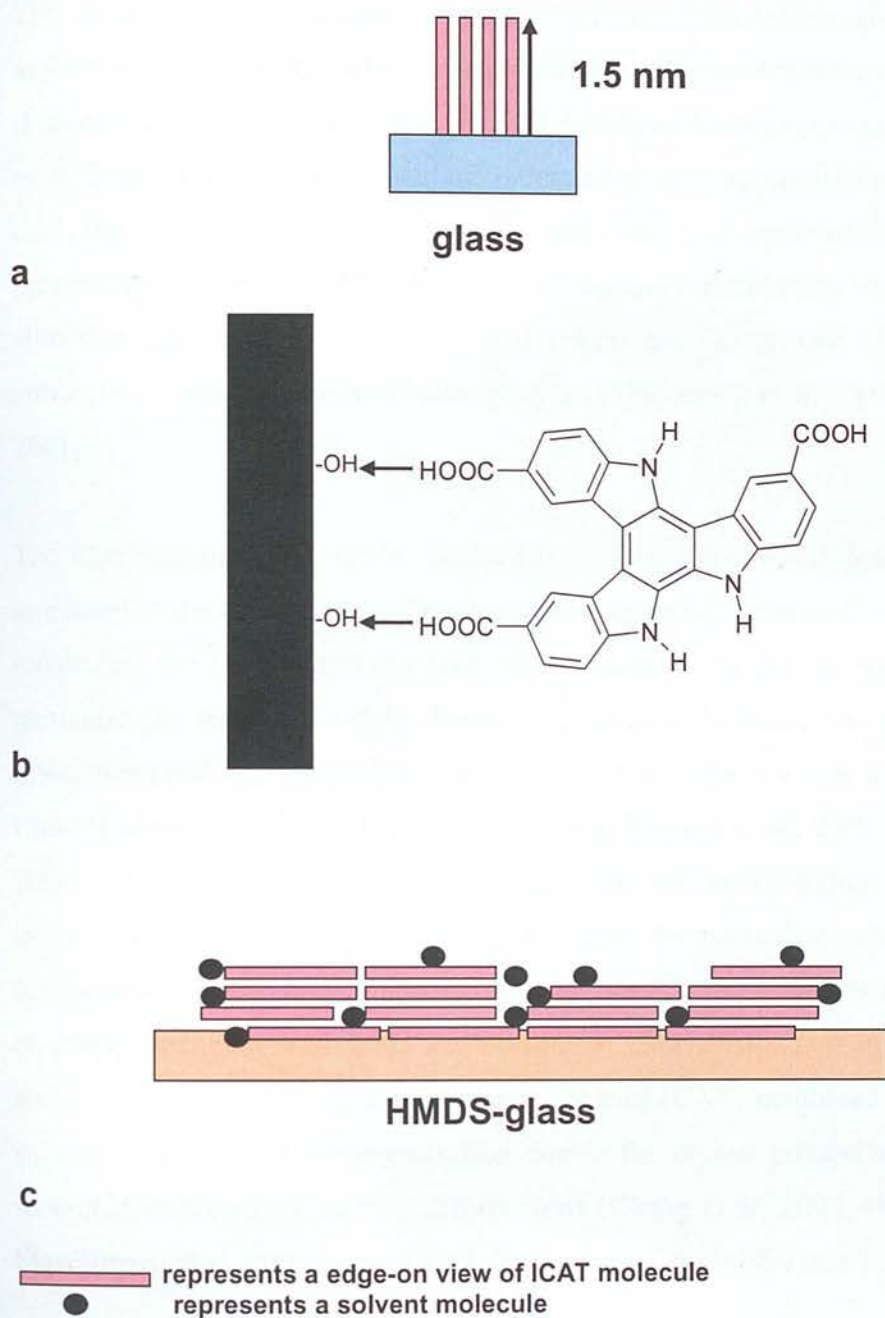


Figure 7.13: Schematic depiction of ICAT interfacial assembly (a) and molecular orientation (b) on glass and interfacial assembly on (c) HMDS-functionalised glass.

The strong highly directional double ICAT COOH-substrate H-bonds dictate the molecular alignment here which is stabilised through the intermolecular  $\pi$ - $\pi$  interactions (Fraxedas et al. 1999, Fraxedas et al. 1998, Gonzalez-Rodriguez et al. 2011 and Hoeben et al. 2005). Finally the film surface indentations with aggregated material around the rims, typically associated with the coffee stain effect, are established during the drying process (Deegan et al. 1997). The random indentation positioning and size is associated with thermally activated nucleation of dry spots and can also be triggered by defects, atmospheric contaminants and heterogeneities (Macdonald et al. 2003 and Seeman et al. 2001).

The high film quality is rarely obtained through solution based deposition and can be attributed to the combination of the favourable interplay between ICAT and other ICAT molecules, the solvent and the substrate combined with the deposition conditions. In particular the multiple, highly directional, selective H-bonds and  $\pi$ - $\pi$  intermolecular interactions and strong interfacial ordering will contribute towards the order in the bulk film (Hoeben et al. 2005, Leclere et al. 2004, Nguyen et al. 2007 and Nguyen et al. 2004). The deposition conditions, including the low concentration solution and long immersion times, should allow ICAT to adopt the most favourable thermodynamic configuration, which should again contribute towards the high film quality (Duzhko et al. 2006, Jonkheijm et al. 2003 and Surin et al. 2004). Also post immersion rinsing in solvent to remove dissolved and poorly adhered ICAT, combined with rapid drying should disfavour ICAT reorganisation during the drying process and help minimise solvent dewetting type surface deformations (Chang et al. 2004, Hoeben et al. 2005, Mas-Torrent et al. 2004, Samori et al. 2001, Samori et al. 1998 and Yan et al. 2008).

### **7.7.2 ICAT assembly on HMDS-functionalised substrates**

The ICAT film on the HMDS-functionalised substrate was highly undulating with a medium coverage of randomly positioned discrete nanobars in a face-down orientation

(figures 7.5 and 7.6). This ICAT film was established as insulating, as the SEM was unable to image it due to surface charging problems.

According to the laws of supramolecular chemistry, ICAT has a much higher affinity for other ICAT molecules through multiple strong intermolecular H-bonding and  $\pi$ - $\pi$  interactions than for the substrate  $\text{CH}_3$  groups (detailed in next chapter) (Gonzalez-Rodriguez et al. 2010 and Hoebe et al. 2005). DMF also has a substantially higher affinity for ICAT through H-bonding than for the substrate, through which it can only establish weak van der Waals interactions (Reichardt et al. 2003). DMF always contains water, which will dewet the hydrophobic substrate (water contact angle  $> 90^\circ$  on HMDS-functionalised substrates) (Padmaker et al. 1998).

These results are consistent with a self assembly process of the following kind. The cluster dimensions did not correspond to a monolayer of ICAT molecules in any conformation. An edge-on ICAT configuration where the ICAT molecule just interacts through the polar carboxylic acid groups with the hydrophobic surface  $\text{CH}_3$  groups is disfavoured and therefore a face-on interfacial orientation, physisorbing with the substrate is preferred (March 1992). The different bulk morphology on HMDS-functionalised glass, as compared to that on the OH-terminated glass, could be partially attributed to the different interfacial orientations in the two systems (Lecelere et al. 2004, Nguyen et al. 2002 and Surin et al. 2004). As explained in the previous paragraph, ICAT has a greater affinity for other ICAT molecules than for the substrate. This would instigate free ICAT molecules in the solution to aggregate at the interface rather than adhere to the substrate thus discrete piles of ICAT molecules develop at the interface, rather than a continuous monolayer. These interfacial assemblies will also be influenced the HMDS SAM quality (coverage, roughness etc) (Park et al. 2007). The nanobars formed here are expected to consist of disordered  $\pi$ -stacked piles of face-on orientated ICAT molecules, H-bonding laterally with each other as schematically depicted in figure 7.13c (Gonzalez-Rodriguez et al. 2010). These relatively large structures are likely to also contain DMF and water molecules H-bonding with the ICAT molecules, as both



solvents also have a higher affinity for ICAT than for the substrate (Nguyen et al. 2004). The nanobar shape is commonly associated with J-aggregated piles of similar small aromatic molecules (Okada et al. 2003). The nanobar shape (2.05 aspect ratio) is likely to be the result of piles of J-stacked (off set  $\pi$ -stacked) ICAT dimers (Jonkheijm et al. 2006, Prins et al. 2001 and Sibjesma et al. 2003). The ICAT dimer is very stable, reinforced with multiple H-bonds (details in next chapter) that even the highly polar solvent DMF is unlikely to interfere with (Sibjesma et al. 2003). The partial surface coverage could also be attributed to easy removal of ICAT, which is only weakly physisorbed to substrate, during the washing process. This surface differs from the other surfaces, in that it is only partially wettable (polar/hydrophobic interaction), and so is subject to spinodal dewetting during the drying stages, which will also contribute towards ICAT aggregation on the substrate (Padmaker et al. 1998 and Seeman et al. 2001).

### 7.7.3 ICAT assembly on APS-functionalised substrates

Both the standard immersion and activated COOH coatings on the APS-functionalised substrates produced continuous relatively smooth films, consisting of closely packed nanoparticles (figures 7.9 and 7.10). However, there were slight differences in the nanoparticle shape and size (figure 7.11), with more pronounced differences between the nanoparticle assembly between the two systems. SEM revealed high quality, macroscopic, activated COOH ICAT film morphologies on the APS-functionalised substrate, consisting of homogeneous continuous films with no ruptures suitable for device application (figure 7.12a). In both films the favourable interplay between ICAT, the solvent and the substrate, combined with the deposition conditions will again contribute towards the assembly order and continuous coverage (similar to that described on the OH- terminated surface in section 7.7.1). The morphology differences are attributed to the variation in the ICAT-substrate chemistry and intermolecular interactions between the two systems, described as follows.

## Standard immersion

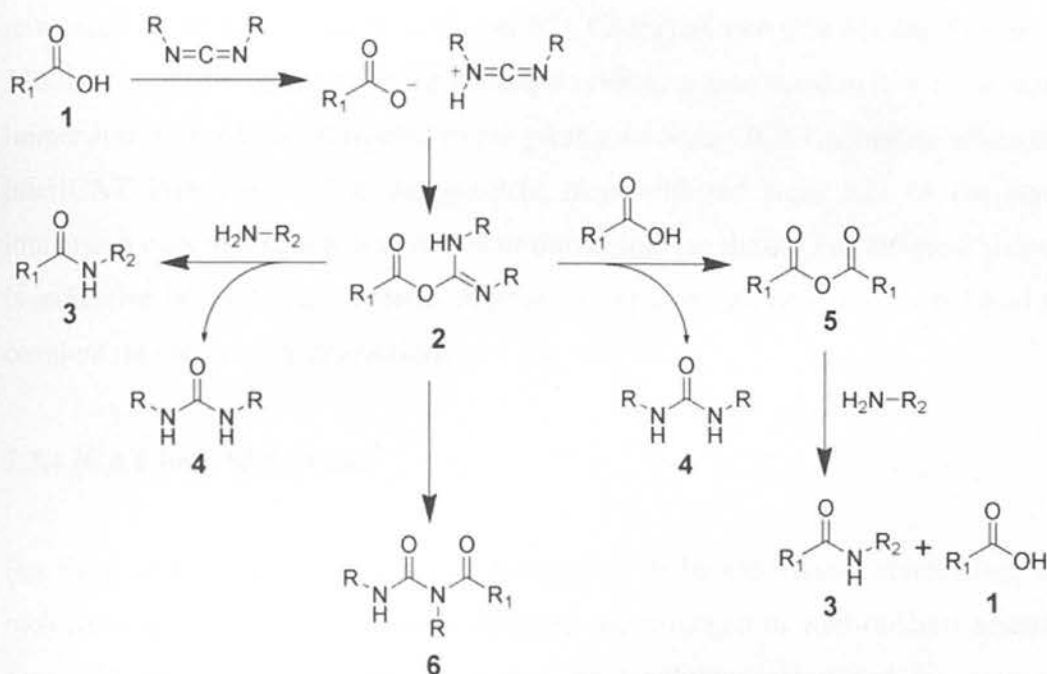
The standard interICAT and ICAT-DMF interactions in the solution and favourable DMF-substrate interactions apply, as described earlier for the standard immersion coating on APS-functionalised glass (similar to that of the OH-functionalised glass immersion experiment). There are strong multiple ICAT-substrate H-bonding possibilities in this system, including H-bonding to the amine functionalised substrate through the ICAT carboxylic acid side groups and  $\pi$ -H-bonds with the ICAT aromatic ring (March et al. 1992). An edge-on ICAT interfacial orientation, similar to that on the OH-terminated substrate, is possible here but we were not able to measure this here.

The particulate morphology (rather than smooth bulk layer, as on OH-terminated surfaces) may be partially attributed to the quality of the APS SAM (Park et al. 2007). This APS deposition procedure typically produces relatively smooth monolayers on glass substrates, but it has been established that the APS amine groups H-bond with surface hydroxyl groups and/or other OH groups on the silane molecules thus reducing the number of amino groups available on the surface to H-bond with the ICAT molecule (Metwalli et al. 2006). Thus the APS layer properties will influence whether the ICAT COOH groups will form single or multiple H-bonds with the substrate and interfacial layer ordering both of which can affect bulk morphology (Lecelere et al. 2004, Nguyen et al. 2002, Park et al. 2007 and Surin et al. 2004).

The clear dewetting pattern and undulating film topography is indicative of weak interICAT interactions in the particulate film and possibly weak ICAT-APS interfacial interactions, allowing ICAT to be removed during washing and mobile in the dewetting process (figures 7.8a and 7.9). The discotic particle shape observed here recurs frequently throughout the thesis.

### Activated COOH immersion

The carboxylic acid activation affects both the intermolecular and ICAT-substrate chemistry. The carbodiimide DIC catalyses the formation of a covalent amide bond between a carboxylic acid on the ICAT and amine surface group on the substrate as follows:



(Duan et al. 1995 and March et al. 1992). The acid (1) reacts with the carbodiimide to form the intermediate an o-acylurea (2) which can be regarded as a carboxylic ester with an activated leaving group. The intermediate can either be attacked directly by the amine to form the amide (3) and urea (4), or it can be attacked by a second carboxylate to give a carboxylic anhydride (5) which can react further to give the desired amide and urea. The major undesired reaction pathway is the rearrangement of the unstable o-acylurea to the stable N-acylurea (6). Therefore, in the activated system ICAT will be anchored covalently to the substrate via an amide bond. Also ICAT will react with other ICAT molecules to form an anhydride (5).

The activated system had significantly smaller surface indentations with less prominent edge effects as compared to those of the standard immersion experiment (figures 7.7 and 7.8). This is attributed to the extremely strong covalent intermolecular and ICAT-substrate interactions (considerably stronger than the supramolecular interactions in the standard experiment), hindering ICAT mobility on the substrate during solvent dewetting and removal during washing. It is possible that the interfacial ordering will be reinforced by double covalent bonds per ICAT between two COOHs and the substrate. The increased film thickness in the activated system, as compared to that of the standard immersion film, will be attributed to the greatly enhanced ICAT-substrate adhesion and interICAT interactions. The nanoparticle shape differed from that of the standard immersion experiment and does not recur throughout the thesis. The different shape here is indicative of a different internal structure in the two particles and is attributed to the covalent intermolecular interactions.

#### **7.7.4 ICAT bulk film quality**

For SEM imaging purposes the film is required to be electrically conducting, so the molecules in the film need to be conducting and arranged in well-ordered assemblies. Typically organic semiconductors in ambient conditions are doped by atmospheric contaminants and ICAT can self-dope so it should be possible to image these films with the SEM (Abdou et al. 1997, Bao et al. 1999a, Dimitrakopoulos et al. 2002, Sivakkumar et al. 2005 and Tagmouti et al. 1997). However, poorly ordered film microstructures usually limits charge transport in solution processed organic semiconductor films (Chesterfield et al. 2004, Lim et al. 2009 and Ling et al. 2004, Shirota et al. 2007 and Sirringhaus et al. 1999).

Therefore SEM was used to determine which films were suitable for device application, through assessing the film microstructure and establishing which films were electrically conducting. Despite occasional charging problems images were successfully obtained of the ICAT film on the OH-terminated substrate and the activated COOH ICAT film on

the APS-functionalised substrate, with the aid of conductive paint surrounding the sample rims. It was not possible to image the standard immersion ICAT films on the HMDS and APS functionalised substrates with the SEM.

The SEM revealed the films on the OH-terminated substrate and the activated COOH ICAT films on the APS-functionalised substrate to have a high quality microstructure (continuous coverage, relatively smooth topography), and are suitable for application purposes (figure 7.12). The film was homogeneous on the OH-terminated substrate, but the activated COOH ICAT films on the APS-functionalised substrate had a small quantity of crystalline domains interspersed with the bulk.

The fact that it was not possible to image the standard immersion ICAT films on the HMDS and APS functionalised substrates with the SEM indicates that these films are not yet suitable for device application. The surface charging problems when imaging the ICAT film on the HMDS-functionalised surface are likely to originate from the large irregular voids between the nanoparticles, acting as traps and allowing access to trapping atmospheric contaminants (figure 7.5) (Chesterfield et al. 2004 and Yang et al. 2005b).

It is interesting that the non-activated film on the amine-terminated surface was insulating, despite having a similar morphology to that of the activated film on that substrate (figures 7.8 and 7.10). The differences between the particle structure and subtle differences in size, shape and packing between the two systems will affect charge transport (Bredas et al. 2002, Dimitrakopoulos et al. 2002, Sirringhaus et al. 2004 and Sirringhaus et al. 1999). The charging issues of the non activated film are most likely attributed to the far greater number and size of surface indentations in the film and the thinner coverage than that of the activated film (Chesterfield et al. 2004). Also the non-activated system does not have the strong interfacial molecular alignment reinforced by covalent bonding like the activated system, which contributes towards the conducting properties of the activated film. Finally another plausible explanation for the insulating film properties in the standard system, is that as the particle size is smaller (only slightly

smaller however,) than that of the activated system and consequently the interparticle spacing is smaller and thus the film is less susceptible to atmospheric doping and therefore there are less charge carriers in the film (Bao et al. 1998 and Katz et al. 2000a).

## 7.8 Conclusion

This is the first time highly ordered assemblies have been produced with the ICAT molecule. Two films in particular, on the OH and (activated COOH) the APS-functionalised surfaces demonstrated very well ordered microstructures, suitable for device application. The well ordered range of assemblies delivered here using a solution based deposition method, particularly with an ambipolar molecule (demonstrated in chapter 9) is an extremely rare and sought after result. The results suggest that ICAT is molecularly dissolved, rather than pre-aggregated in solution, and that aggregation takes place at substrate/solution interface. ICAT assembly was well controlled using SAM chemistry. The combined multiple, strong, highly selective and directional H-bonds and  $\pi$ - $\pi$  interactions in the immersion systems were successfully applied to produce a continuous well ordered bulk molecular film and closely packed particulate films. Film quality was improved on the amine terminated substrate through introducing interICAT and substrate-ICAT covalent bonding. Specifically the particle size, shape and assembly, and the film thickness were altered using the covalent interactions.



## **Chapter 8**

# **Self-assembled ICAT 1D nanostructures**

## 8.1 Introduction

Organic semiconducting 1D nanostructures, (in particular nanorods and nanowires), and their assembly have attracted a great deal of attention recently due to their extensive application potential in many areas of research including optoelectronics (Haberkorn et al. 2009 and Lee et al. 2007), electronics (Jiang et al. 2011), data storage, device miniaturisation, sensing, artificial actuators (Berdichevsky et al. 2006) and surfaces exhibiting special wetting properties (Liu et al. 2003 and Shea et al. 2006). However, despite their unique properties and diverse applications, only a limited number of researchers have synthesised 1D organic semiconducting nanostructures and even fewer researchers have successfully transferred them between substrates or deposited the nanostructures in well ordered assemblies (Balakrishnan et al. 2006, Huang et al. 2009, Jonkheijm et al. 2003, Lecelere et al. 2004, Schwab et al. 2003 and Singh et al. 2006).

To incorporate 1D ICAT nanostructures into useful nanoscale devices and to establish the fundamental science behind the nanostructure formation and assembly, their organization and stability on different surfaces must be evaluated. It is essential to determine whether the 1D nanostructures, and if so in ordered assemblies, are transferable to metallic electrode surfaces, such as gold, applicable in devices. Also a comparison of ICAT assembly on a hydrophilic, a hydrophobic and an inert gold surface should contribute greatly towards understanding and controlling ICAT nanostructure formation and assembly.

In this work supramolecular interactions between ICAT and a range of substrates and polar solvents are used to control ICAT nanoscale assembly to form a variety of 1D nanostructures. Size-tailored, monodisperse, closely packed, vertically aligned ICAT nanorod assemblies were deposited on various substrates through a facile solution based method developed in chapter seven. Nanowire arrays were also produced with this method. This is the first time a well ordered nanorod array has been deposited on a substrate, with a small functional organic molecule, using a solution based deposition

method. A seeded based mechanism as applied previously on frequent occasions to inorganic oxide 1D orientated growth (Aizenberg et al. 1999 and Sounart et al. 2006) and once to a conducting polymer 1D system (Liu et al. 2003) was applied to rationalise ICAT nanostructural development in these experiments.

## **8.2 Experimental method**

### **8.2.1 ICAT thin film procedure**

The glass substrates were cleaned and selected slides were functionalised with HMDS, using the protocol and chemicals described in the previous chapter. Gold substrates (glass substrates sputter coated with gold) were also immersion coated with ICAT/DMSO solution. The substrates were immersed immediately in freshly made 0.8 mM ICAT solutions, (and selected solutions were aged up to 1 year before immersion) ICAT/DMSO (solutions aged 4 months), post cleaning using a range of solvents with different properties for a set time. The substrates were then rinsed in the immersion solution solvent, followed by ethanol, dried under nitrogen and placed in the oven. Solvent-only films were prepared under the same conditions and the features were very different to all the films presented here. The samples were analysed using the AFM procedure, detailed in the previous chapter. In particular, a cantilever resonant frequency of 168 kHz was optimal for rod imaging. All the results were reproducible.

## **8.3 Results 1: Controlled ICAT 1D assembly as a function of solvent**

A novel facile solution based 1D nanostructure production method was developed (detailed in 8.2) here, which resulted in controlled growth of 1D ICAT nanostructure arrays on glass substrates. 1D ICAT arrays were not deposited when water and non-polar organic hydrocarbon based immersion solvents were used (rapid precipitation). However, when glass substrates were immersed in ICAT solutions with immersion

solvents methanol, DMF and DMSO 1D nanostructures were deposited on the substrate, as illustrated in figure 8.1.

Shorter immersion times were used to obtain less densely packed nanorod assemblies, so that individual nanorods could be selected, for the purposes of assessing nanorod dimensions. Figure 8.1a depicts the 1D ICAT nanostructures deposited on glass substrates, as a result of immersion coating in ICAT/DMSO solutions. The topographical images reveal the nanoparticles to be closely packed, single bodied and nanorod shaped. The AFM amplitude image of the assembly produced after a very brief immersion in figure 8.9b provides further clarification of the single-bodied, nanorod shaped structures in this system. These nanorods tended to form continuous closely packed layers. The long axis of the nanorods appeared to be aligned perpendicularly (or approaching perpendicular) to the substrate so that the nanorods were parallel to each other and vertically orientated with respect to the substrate. The broadening in the upper body of the nanorods on the topographical image is an AFM tip artefact (mushroom distortion), which has been previously observed in similar vertically aligned nanorod systems (Shea et al. 2006 and Schlenker et al. 2007). This broadening is only observed when the nanorods are/or approach vertical alignment and not when the rods are lying flat on the substrate surface (Schwab et al. 2003 and Shea et al 2007). Figure 8.13 provides a clear depiction of the nanorod vertical alignment through showing the topographic image of rods with the mushroom effect with the accompanying 3D image.

Again closely packed, single bodied nanorods with their long axis aligned perpendicular to the substrate were obtained from ICAT/methanol solutions, as illustrated in figure 8.1b. The topographical image depicts a continuous layer of closely packed nanorods, with some randomly positioned single nanorods on top of the layer. Again the mushroom distortion effect associated with vertical aligned nanorods with respect to the substrate is observed. In the immersion experiments in ICAT/DMSO and ICAT/methanol the nanorod assembly appeared to be attached strongly to the surface, as the AFM did not move material around the surface during the scanning procedure.

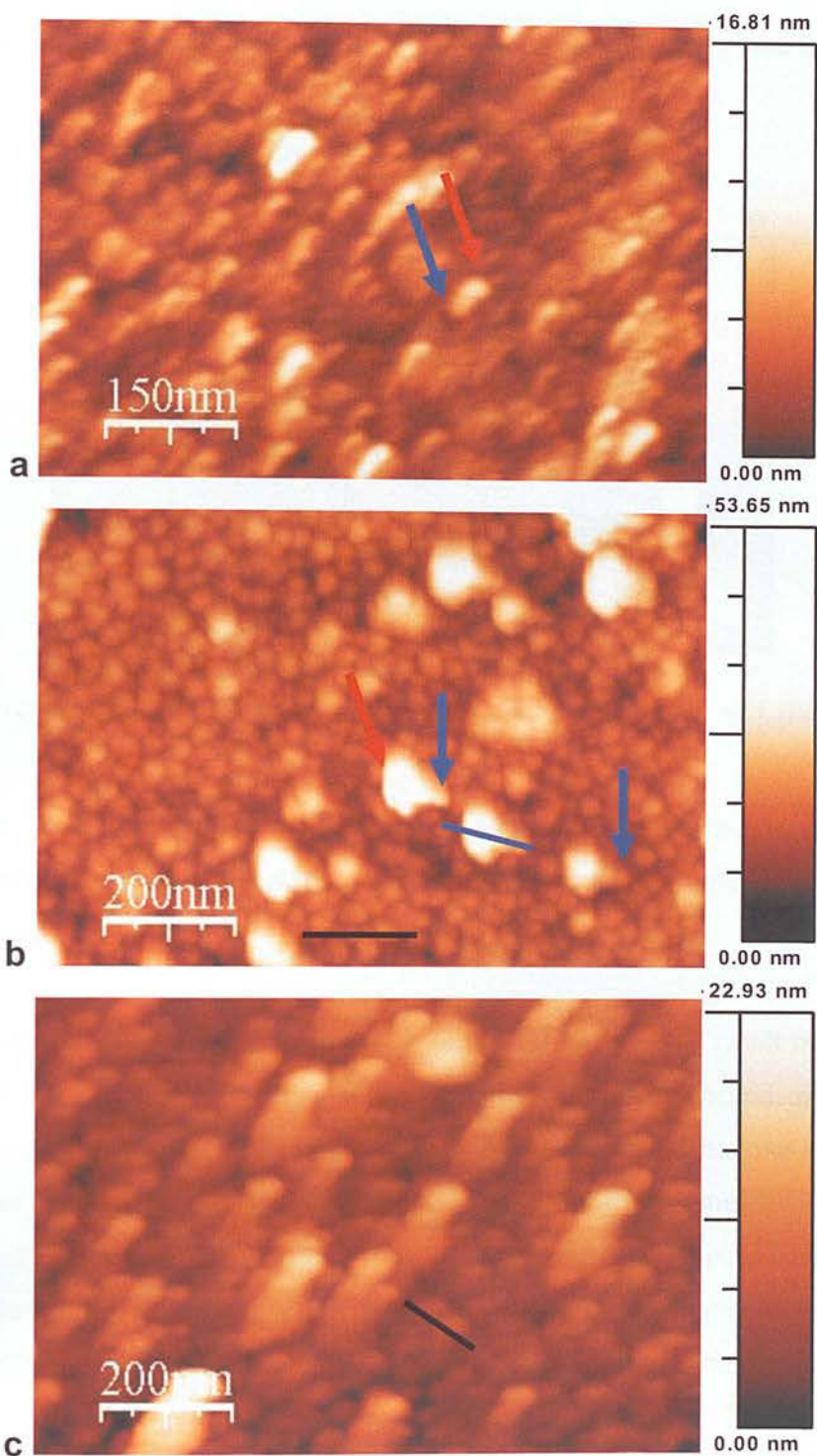


Figure 8.1: Topographic AFM images with ICAT 1D growth on OH-glass with (a) DMSO, (b) methanol and (c) DMF immersion solvents. Rod diameter profiles were taken typically from areas marked with the black line and the blue line marks the position where typical nanorod length profiles were taken from methanol. Diameters were taken from the head profiles taken from the closely packed particles in the lower layers as denoted by the black line in the DMF



image. The blue arrows highlight examples of nanorods where the entire span of the structure may be observed. The red arrows point to the mushroom distortion on one end of the nanorod.

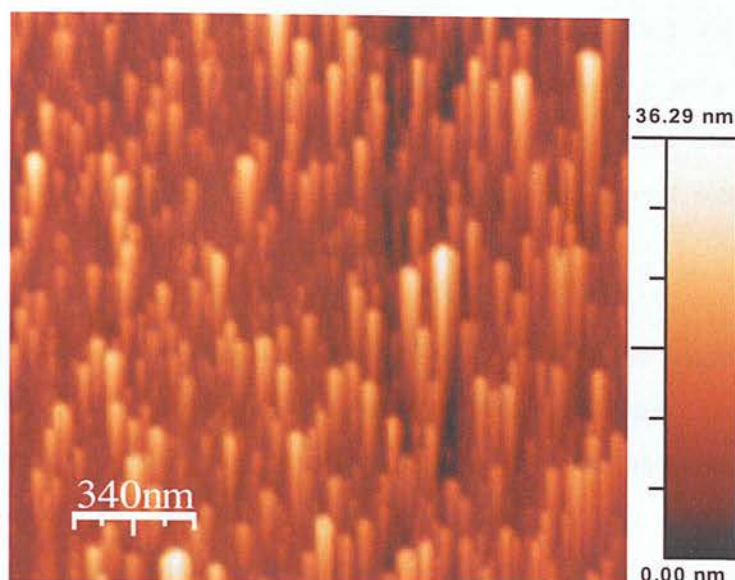


Figure 8.2: Topographic AFM image with ICAT 1D growth on OH-glass with DMF immersion solvent.

Furthermore these organic assemblies showed remarkable mechanical stability when shaken vigorously in several solvents and dried under nitrogen these 1D structures remained intact.

Figure 8.1c is the topographical AFM image of the 1D growth as a result of immersion in ICAT/DMF solution. There was a continuous layer of closely packed, single-bodied 1D nanoparticles in parallel alignment with each other. However, the long axis of these 1D nanostructures appears to be almost parallel to the surface (no mushroom distortion observed here, which is associated with vertically aligned nanorods). These 1D nanoparticles appear to be attached at one end to the substrate, with the opposite end (head) slightly raised with respect to the substrate. The shape of these particles appears to be different from that of the nanorods formed in the other systems. The base of the 1D nanoparticles on the top layer could not be distinguished from the heads of the 1D layer underneath, unlike that of the methanol and DMSO nanorods, where these features were easily differentiated (denoted with the blue arrows in figure 8.1a and b). So this image is



best interpreted as a nanowire array with a small number of randomly positioned nanowires distinctly longer than the majority. Figure 8.2 illustrates more clearly that these 1D structures are much longer than those produced in DMSO and methanol. Care must be taken with this image as there is a slight tip interaction with the head of the nanostructures under these scanning conditions. Again these structures showed remarkable mechanical stability, when rinsed intensely in several solvents and dried under nitrogen, these 1D structures remained intact.

A detailed analysis of the dimensions of the nanorods in the assemblies from the ICAT/DMSO immersion experiment was performed, as individual nanorods could be clearly depicted for measurement purposes. Readily distinguishable nanorods from an incomplete layer of rods, (baseline taken as 1 nm on topography z scale), were taken. As the nanorods were orientated at an angle with respect to the substrate, (AFM deflected nanorods during scanning procedure), dimension measurements and an error assessment were difficult. Profiles following the long axis of individual nanorods were taken between the point of attachment (0 nm on z-scale) to the highest point (maximum z value on the contour plot), as illustrated in figure 8.3. The nanorod length here is defined as the length of this profile slope.

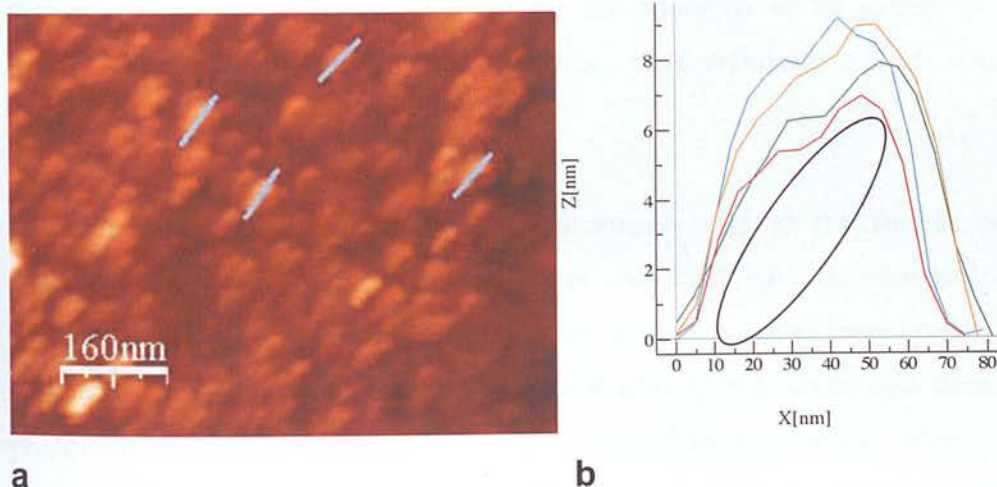


Figure 8.3: Topographical (a) AFM image of DMSO/ICAT immersion coated films on glass substrates. The lines mark the positions where typical nanorod length profiles were taken from and are displayed in profile (b) with an accompanying nanorod sketch demonstrating the orientation with respect to the substrate (x-axis).

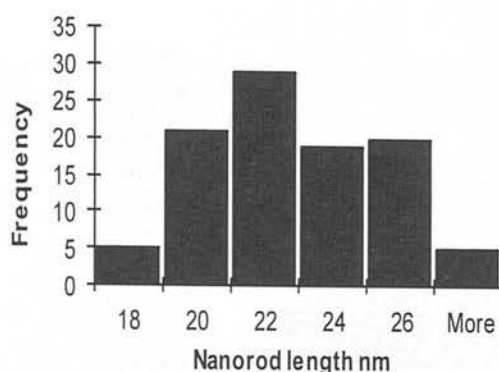


Figure 8.4: Length distribution taken from nanorods deposited on glass substrates from ICAT/DMSO immersion (allowing for tip convolution errors). The bin with the lowest value ranges from 0 to the labelled value. The following bin values range from the previous neighbour bin value +0.1 to the labelled value as the maximum.

The dimensions of over one hundred nanorods were measured and the length distribution is displayed in figure 8.4. The exact tip convolution value error is difficult to assess here as the rods are not lying flat on the surface, and the flat lying position is a prerequisite of the geometric model for broadening of the image due to the tip radius (Ayyappanpillai et al. 2006 and Samori et al. 1998). However, the error will lie within the range of 10-15 nm here, so 12.5 nm was deducted from the each nanorod length taken. The mean length was 21.9 nm with a standard deviation of 2.5 nm. The length distribution and standard deviation reveal the nanorods to be extremely narrowly distributed, centering around one clear dominant peak, signifying a single population of preferred nanorod lengths.

The rod diameters cannot be assessed accurately due to the further broadening associated with vertically aligned nanorods combined with the standard distortion associated with lateral measurements of an extremely small magnitude. However, randomly orientated nanorods were deposited after shorter immersion times, a small proportion of which, with their long axis parallel to the surface, were selected to measure. The heights of fifteen readily distinguishable, flat lying nanorods were taken to provide an accurate diameter.

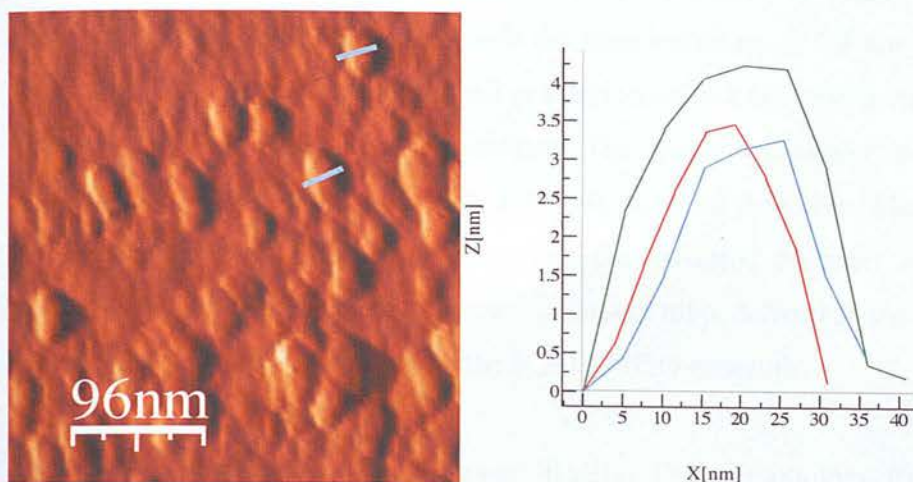


Figure 8.5: Amplitude (a) AFM image of a DMSO/ICAT immersion coated film on a glass substrate. The lines mark the typical positions where the nanorod profiles (b) were taken to provide nanorod diameters.

The nanorod diameter is defined here as maximum height taken from the nanorod profile cutting the long axis of a flat lying nanorod, as illustrated in figure 8.5. Profiles were taken from an incomplete layer of nanorods, where the baseline was taken at 1 nm on the topography z scale (0 nm on profile z-scale). The nanorod diameter ranged between 3.5-6 nm with a mean value of 5.0 nm. Note there is some lateral distortion in this image.

Fifteen methanol/ICAT nanorod profiles were measured for comparison purposes. The lengths of the individual nanorods, lying on top of the continuous nanorod (baseline taken as 8nm on topography z scale) layer, as illustrated by the blue line on figure 8.1b were measured. The lengths of which, were obtained from the length of the slope of the profiles scanning along the rod long axis, as defined for the DMSO rod lengths (figure 8.3). Lateral distortion is not significant here as the nanostructure length is substantially larger than the tip size. The length range was again narrowly distributed with a mean of 120nm (standard deviation 6 nm). The nanorod diameter proved difficult to measure, as there were no nanorods with their long axis parallel to the substrate available, so profiles scanning the heads of closely packed continuous vertically aligned nanorods were taken from the topography images as marked with the black line on figure 8.1b. The diameters



were taken from the profiles scanning across the centre of readily distinguishable nanorod heads  $\geq 5$  nm on z-scale, with the baseline taken as 2.4 nm, as illustrated in figure 8.6. The diameters were defined as the point where nanorod profile width (lateral distance on the x-scale) became constant. The nanorod diameter mean is 17.8 nm (allowing tip convolution error) with a 4.1 nm standard deviation. There will be some error with this methodology for estimating the nanorod diameter but was the best available method with this morphology. The aspect ratio, defined as the nanorod length / nanorod diameter, is 6.7 and 4.4 for the ICAT/DMSO nanorods.

The DMF nanostructures were assessed finally. The methodology for estimating the nanorod diameter, including the same diameter definition for the ICAT/methanol nanorods was applied here. There was some distortion with the most protruding particle heads (in the upper topography z-scale) therefore nanostructure profiles, as illustrated in figure 8.7, were taken from the continuous lower layer, as marked in the topography image figure 8.1(c). The baseline was taken from 1.2-1.4 nm on the z-scale and nanostructure profiles were taken of easily depicted structures with a maximum height 5-7 nm on the z-scale. The mean diameter was 62.9 nm (standard deviation 6.6) (lateral distortion does not make a significant contribution to errors here). The lengths of these structures were not readily measurable in this formation. However, the partial lengths, as seen in figure 8.2, show that some of the nanostructures are  $> 400$  nm in length.

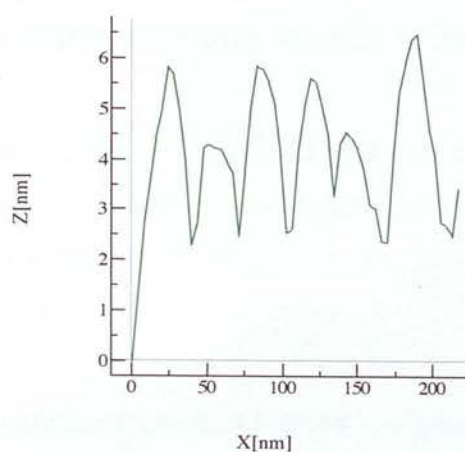


Figure 8.6: Typical cross section taken from the methanol/ICAT immersion coated films on glass substrates. This is taken from the close packed continuous nanorod layer, as marked with a black line on the topography image figure 8.1(b).

As these nanostructures were nanowires rather nanorods, despite the fact that the length of the wires was not measured, it may be assumed that the aspect ratio here is considerably higher than those of the nanorods produced in the other two solvents.

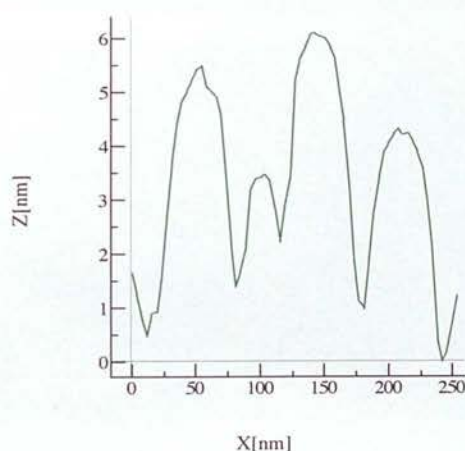


Figure 8.7: Typical cross section taken from the ICAT/DMF immersion coated films on glass substrates. The cross sections are taken from the close packed continuous nanostructure layer, one of which is marked with a black line on the topography image figure 8.1(c).

## 8.4 Results 2: Nanostructure evolution with immersion time

A study of the 1D nanostructural assembly was undertaken of the ICAT films produced through immersion for a range of times in solutions made with solvents with the lowest (methanol) and highest (DMSO)  $\pi^*$  values ( $\pi^*$  is a measure of the combination of polarity and polarizability).

### 8.4.1 Nanostructure evolution from ICAT/DMSO solution

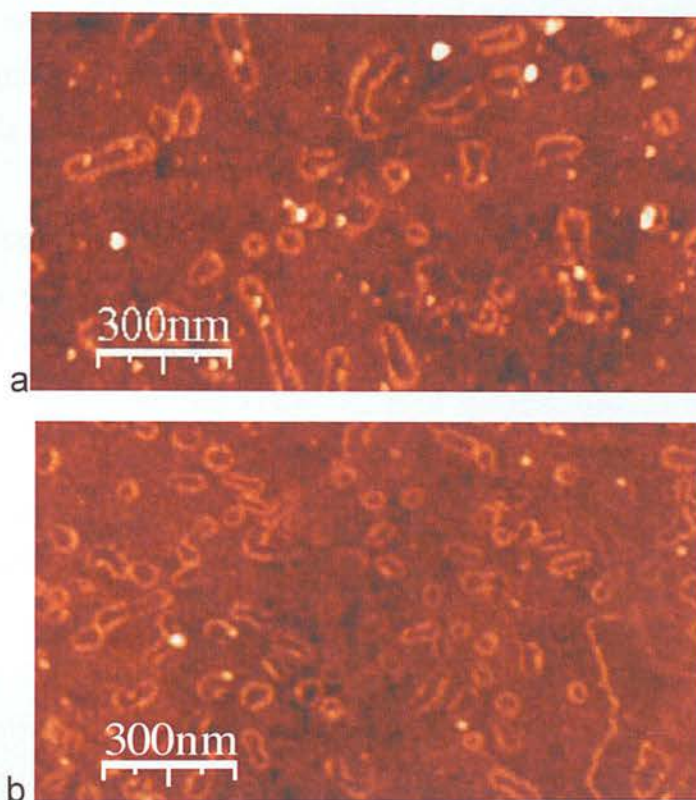


Figure 8.8: Topographic AFM images illustrating film morphology is independent of pre-immersion solution age where the film morphologies are the same when immersion coated in (a) freshly made and (b) 1 year old ICAT/DMSO immersion solution (1 day immersion).

The pre-immersion age of the solution was varied in order to establish whether the film morphology was dependent on the age of the solution. The film morphology was independent of the pre-immersion age solution (of age range 1 minute-1 year), as



illustrated in figure 8.8 (1 day immersion time). This experiment was repeated on a HMDS-functionalised glass substrate (pre-immersion solution age range 1 minutes-2 months) and again the film morphology was independent of the solution age.

The immersion time was increased and the corresponding ICAT morphologies are illustrated in figure 8.9. Initially (1 day immersion time) the film morphology consists of a relatively smooth continuous ICAT film with a granular texture, a medium coverage of randomly positioned nanorings and randomly positioned nanoparticles extremely sparsely dispersed throughout. The mean height of the features was 1.5 nm, which is consistent with an edge-on orientated ICAT molecule (chapter 7). The ring features as highlighted on image 8.9(a), are most likely solvent rings of solvent molecules formed during the drying procedure as were also observed in the solvent only films.

As the immersion time increases (3 days) a small coverage of randomly positioned single nanorods and lines of nanorods, (denoted with the blue arrow), appear (figure 8.9b). There is a clear increase in rod density observed as the immersion time is increased further (figure 8.9c) and a closely packed nanorod layer is established.

The nanorod orientation appears to be dependent on the immersion time also (figure 8.9b and c). After the longest immersion the nanorods appeared to be in parallel alignment with each other and are all orientated with their long axis normal to the substrate (figure 8.9c) (detailed description provided with figure 8.1). The nanorods do not appear to vertically orientated after 3 days (little or no mushroom distortion appeared which is typically associated with vertical alignment) but rather appear to be orientated with their long axis parallel to the substrate, or at a shallow angle ( $\ll 90^\circ$ ) from the point of attachment (figure 8.9b). More work is required to establish the exact orientation angle but it can be stated that the orientation angle is different in the two images.

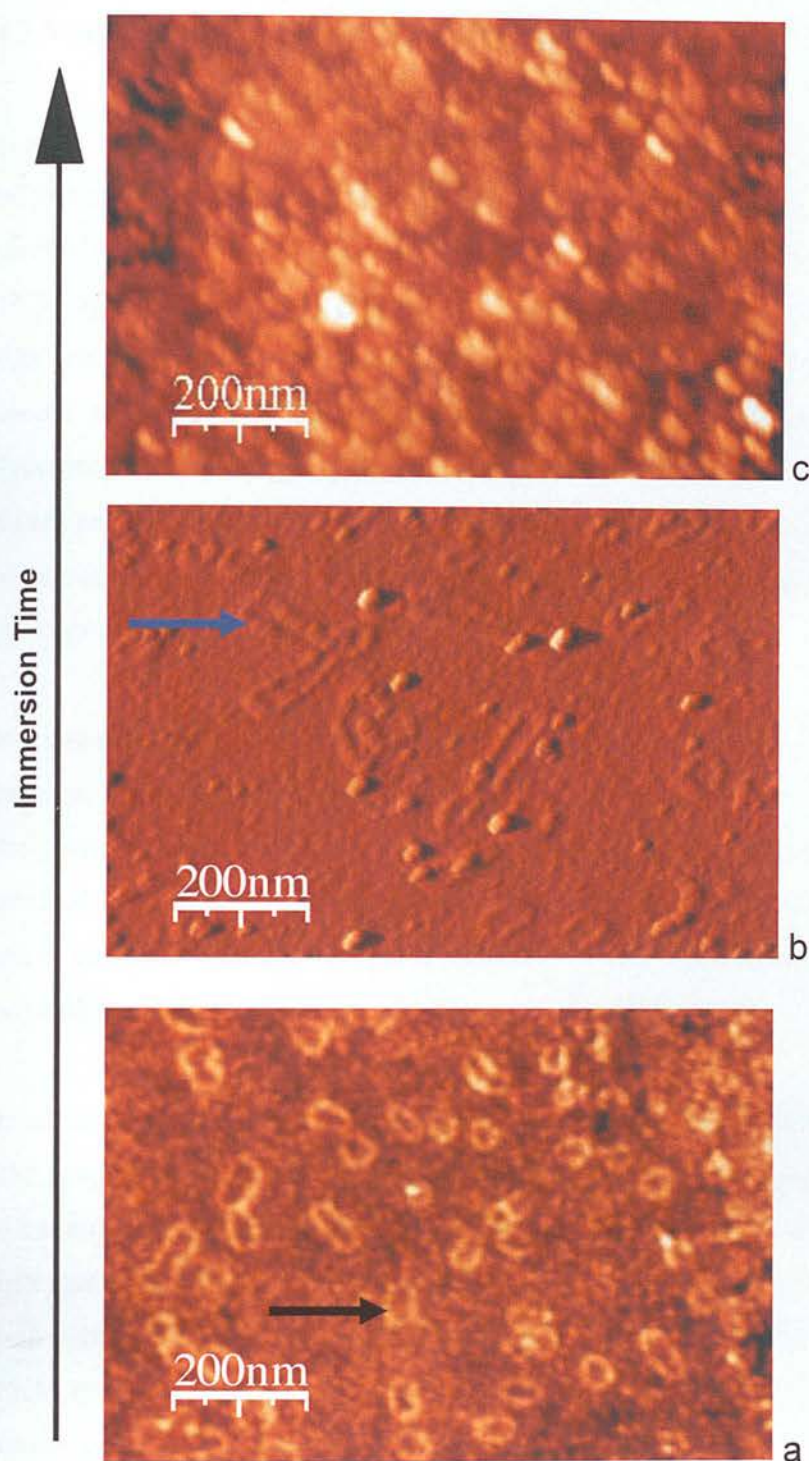


Figure 8.9: Topographic AFM images illustrating ICAT 1D nanostructural evolution on a glass substrate with immersion time in an ICAT/DMSO solution for (a) 1 day, (b) 3 days and (c) 4 days. The black arrow highlights a solvent ring and the blue arrow points to a line of nanorods.

#### 8.4.2 Nanostructure evolution from ICAT/methanol solution

The immersion time was increased in ICAT/methanol solution and the corresponding film morphologies are illustrated in figures 8.10 and 8.13. Figure 8.10 illustrates the typical film ICAT morphology on glass substrates, resulting from three day immersion in ICAT/methanol solutions. The majority of areas scanned were similar to that of image 8.10b, where the morphology consisted of a medium to dense coverage of discrete flat ellipsoid particles in a non-edge on (face-on) orientation. Sparsely distributed larger polydisperse globular aggregates and elongated 1D aggregates were also present in all scanned areas (figure 8.10a and b). A small number of very large ICAT deposits were also present (figure 8.10c). These islands appeared to consist of layered 1D vertically aligned growth of varied lengths.

The dimensions of one hundred readily distinguishable, flat lying particles were measured. The diameters were taken as the maximal distance between two points on the outer particle profile, spanning the shorter axis (width) of the face of the particles, as illustrated in figure 8.11. The particle height is defined as the maximum height of the particle profile. The particle profile baseline (0 nm z-scale) is taken at 1 nm on the topography scale.

The lateral distortion here can be estimated using a geometric model, commonly applied to flat lying rectangular and spherical particles (spherical tip) (Ayyappanpillai et al. 2006 and Samori et al. 1998). Using the equation provided by Samori, where both the particle height and the tip radius 10 nm are required, the effective broadening can be calculated (mean value 16.2 nm). The mean particle height was 4.2 (standard deviation 0.6). The particle diameter distribution, as illustrated in figure 8.12, is narrow with a single diameter population, peaking between 8.1 and 9 nm. The diameter mean value was 9.2 nm (standard deviation 1.7).



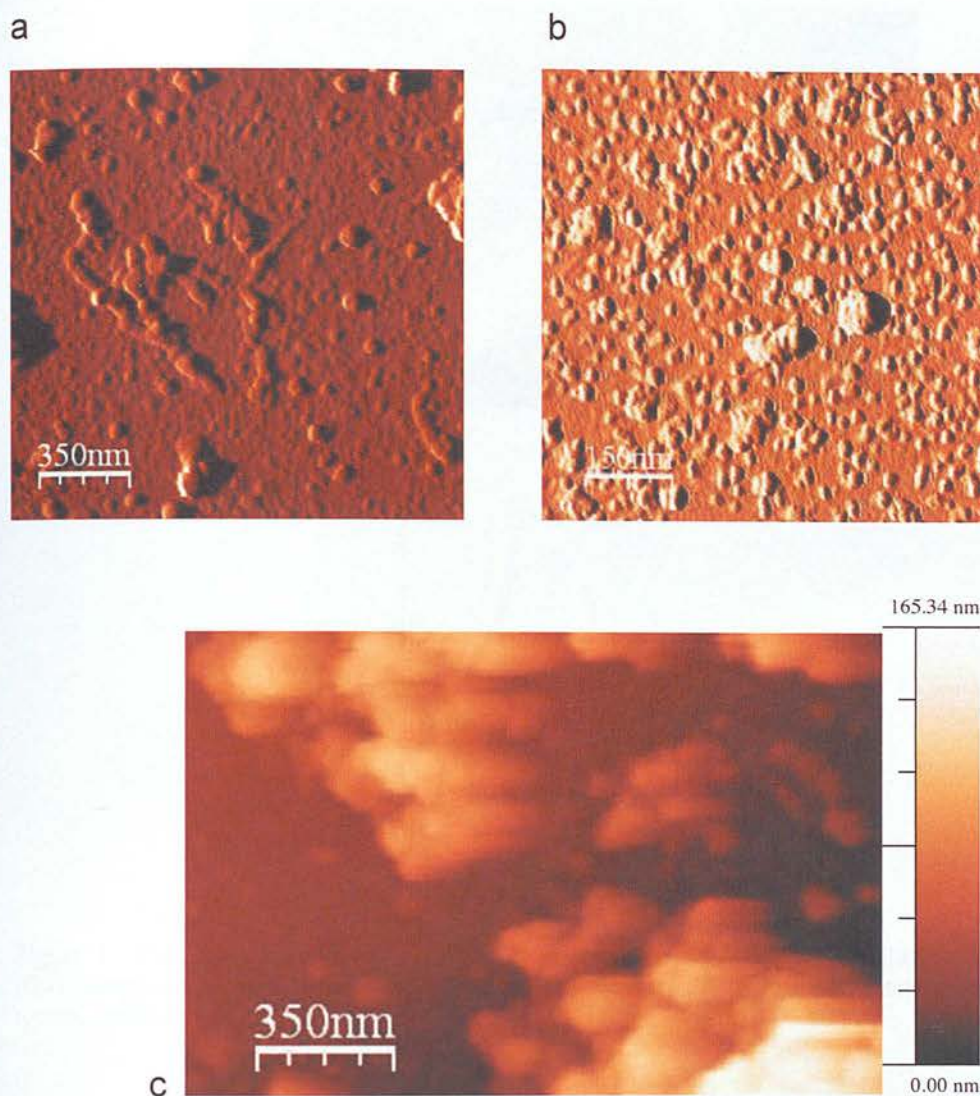


Figure 8.10: Amplitude (a) and b) and topographical (c) AFM images illustrating ICAT morphology on a glass substrate after a 3 day immersion in an ICAT/methanol solution.

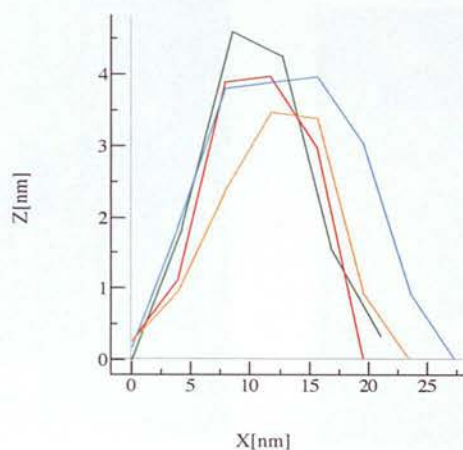
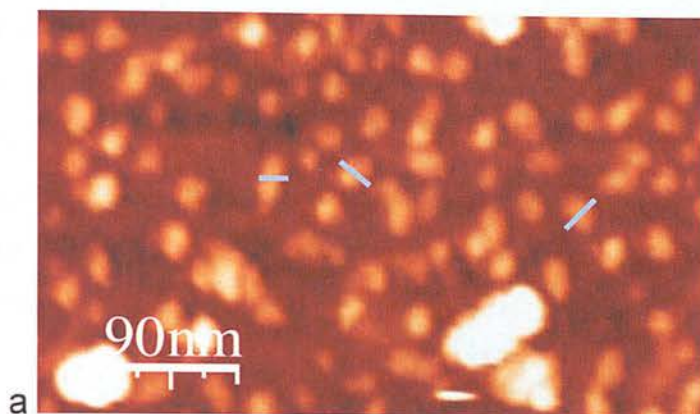


Figure 8.11(a) Topographical AFM image of immersion coated films on glass substrates with ICAT/methanol solution (3 day immersion). The lines mark the particles selected to illustrate typical particle profiles (b).

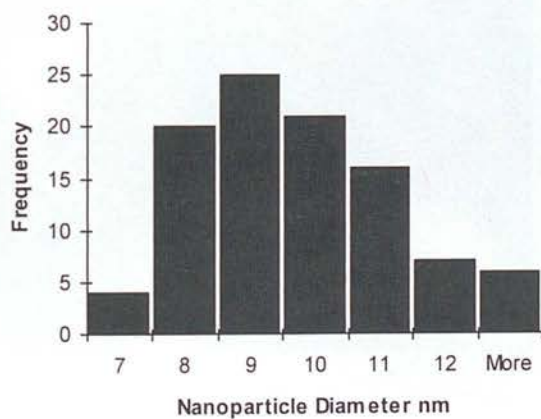


Figure 8.12: Diameter distribution of ICAT particles from ICAT/ methanol solution deposited onto glass substrates. The bin values are labeled as with previous distributions.

The film morphology develops with immersion time, as illustrated in figure 8.13 (20 days immersion time). The three dimensional representation (figure 8.13a) of topographical image (8.13c) is provided, as the 1D assembly can be seen more clearly than in the topographical image. The film morphology now consists of multiple layers of nanorods, as seen in figure 8.13b. All scanned areas yield continuous layered growth of closely packed, vertically aligned nanorods.

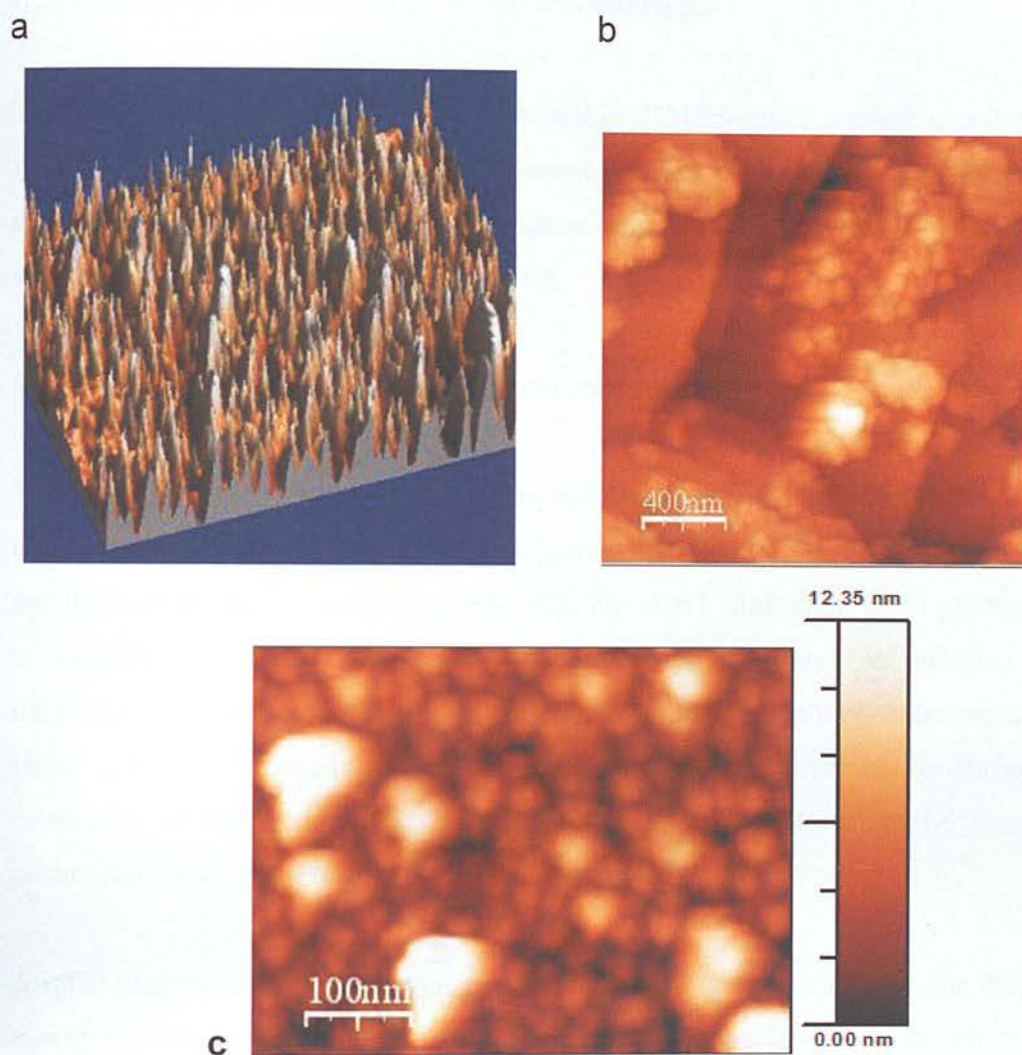


Figure 8.13: a) 3D representation of (c) and (b) and (c) topographical AFM images illustrating ICAT morphology on a glass substrate after a 20 day immersion in an ICAT/methanol solution. The height scale on image (b) was 188.7 nm and on (c) was 23.9 nm.



One model proposes that with increasing immersion time the small flat particles, (as observed at 1 day immersion time), stack on top of one another and fuse together to form the nanorods (orientated aggregation). This theory is substantiated by the fact that the small particle diameter is the same as the nanorod diameter, within error (lateral distortion).

### **8.5 Results 3: 1D assembly on varied surfaces**

The experiments were repeated on hydrophobic (HMDS-functionalised glass) and inert metal (gold) substrates. The results presented here are for the ICAT/DMSO immersion experiments. The ICAT morphology appeared to be identical when DMF and DMSO were used to make the immersion solutions.

#### **8.5.1 Self-assembly on hydrophobic surfaces**

The topographical AFM images, presented in figure 8.14, illustrate the distinct differences in the film morphology deposited on the hydrophilic substrate (figure 8.14a) and the hydrophobic substrate (figure 8.14b). The ICAT film on the hydrophobic surface is substantially rougher than that of the hydrophilic surface, as reflected by the difference in height scale. The 1D nanostructures on the hydrophobic substrate are much larger and more sparsely distributed than those on the hydrophilic surface. The orientation of the hydrophobic 1D nanostructures with respect to the substrate is commented on in detail further on in the section.

A small proportion of the 1D aggregates were considerably smaller than the majority of nanostructures. Some of these smaller aggregates are marked with arrows on figure 8.14b and magnified in figure 8.15a.

The dimensions of the 1D nanostructures were compared. A 3D representation of the ICAT film in conjunction with its accompanying 2D topographical image is provided in

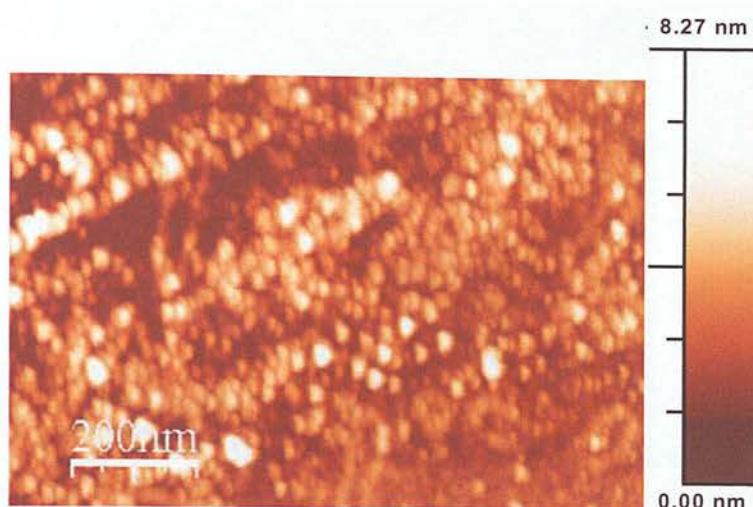
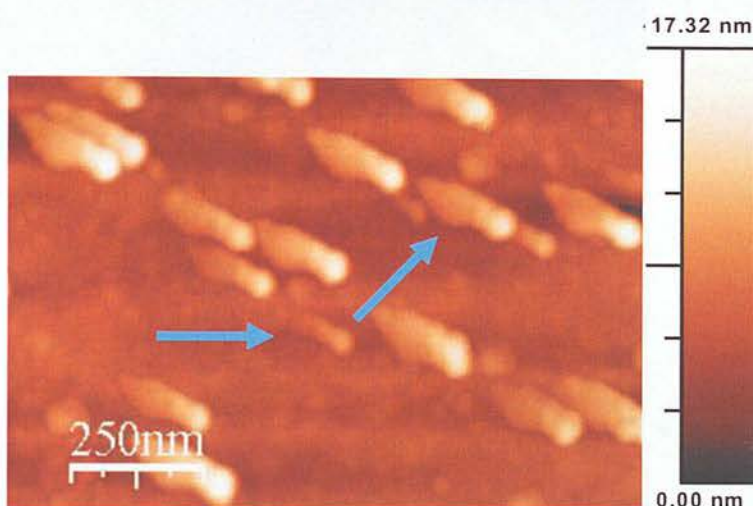
**a****b**

Figure 8.14: Topographical AFM images demonstrating the difference between ICAT film morphology from a three day immersion coating in ICAT/DMSO solution on (a) a glass substrate and (b) a HMDS-functionalised glass substrate. The arrows highlight examples of the smaller aggregates.

figure 8.15b and c. Profiles of the nanostructures on hydrophobic surfaces are given in figure 8.16.

Profiles spanning the length and width of fifteen readily distinguishable large and small 1D aggregates were taken, (baseline 0.5 nm on topography scale is zero nm on profile z scale), as marked on a nanostructure in figure 8.15a. Only a sample of the length profiles

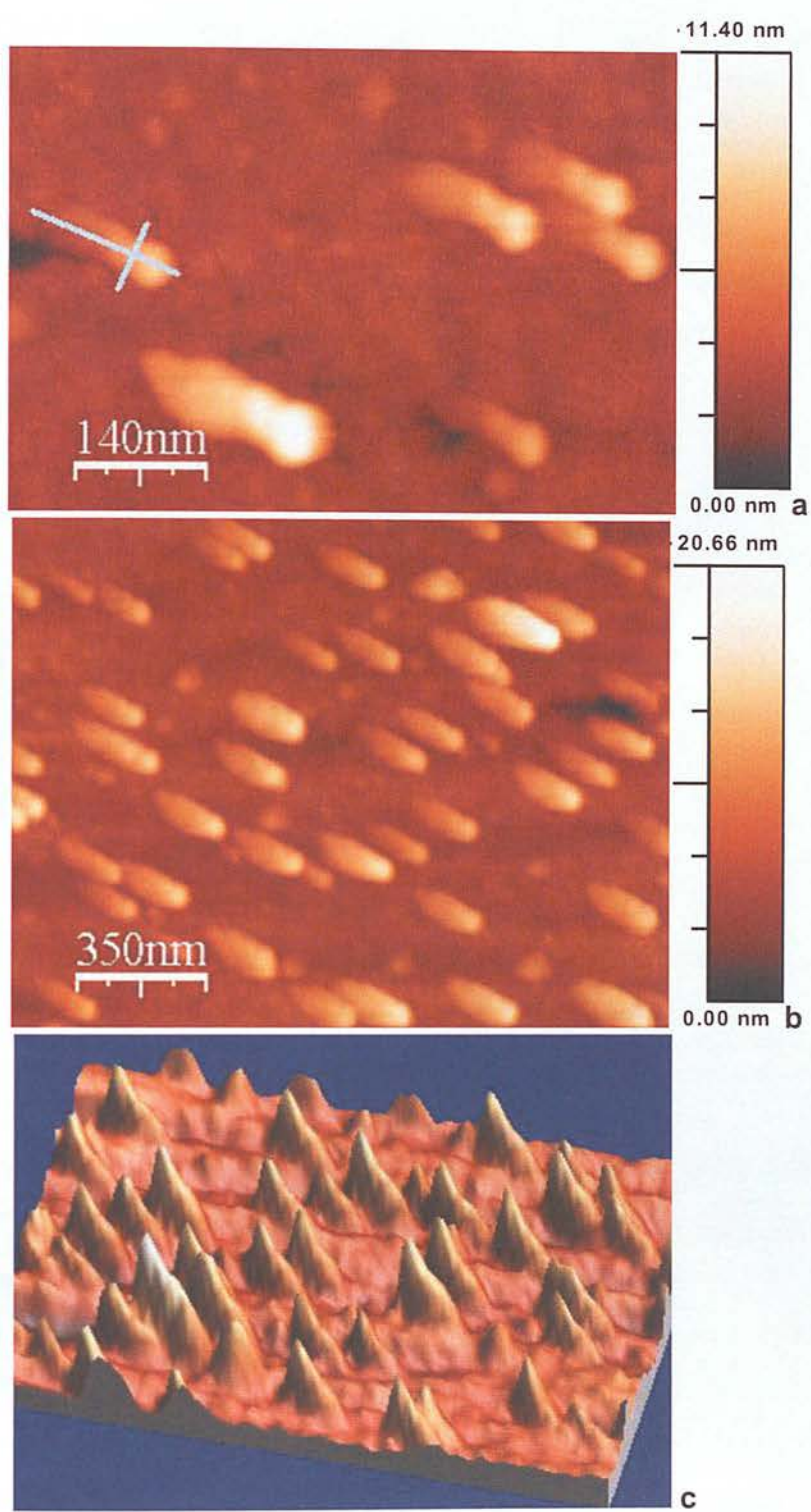


Figure 8.15: (a) and (b) topographical AFM images and (c) 3D representation of (b) showing growth on the hydrophobic substrate (3 day immersion). The shorter blue line on the nanostructure in (a) marks the position where a typical width profile was taken from and the longer line marks the position where a typical length profile was taken from.



of the (a) smaller and (b) larger nanostructures are given in figure 8.16, as they provide a greater insight into the nanostructure morphology than the width profiles do.

The aggregate length is defined as the maximal lateral (x axis) distance between zero and the highest point on the z-axis on the 1D aggregate length contour plot, as illustrated in figure 8.16 (as orientated close to flat). The aggregate width is defined as maximal distance between two points on an outer width cluster contour. The dimensions as measured from the contour plots are provided in table 8.1.

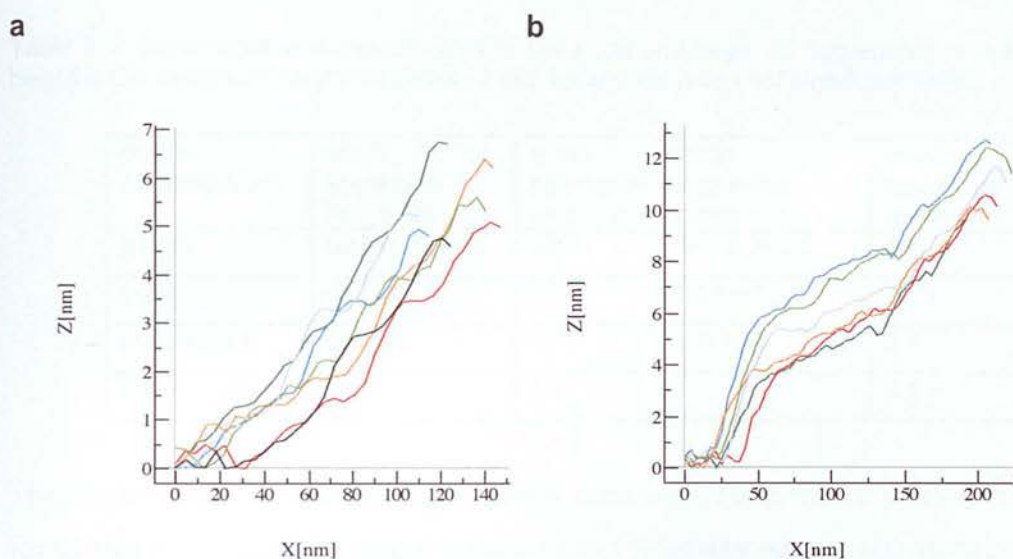


Figure 8.16: Typical length profiles of the (a) small and (b) large 1D nanostructures on the hydrophobic substrates. The profiles span the length of the 1D aggregate as illustrated with the longer line in figure 8.14a.

Care must be taken with the profile height scale (z-scale). When the substrates were scanned in different directions, the maximum height of the aggregates changed. Scanning parallel to the aggregate length profile, resulted in the profile peaks being about 2 nm higher than those produced when scanned perpendicular to the aggregate long axis. Therefore the extra 2nm in the profile peak maybe an AFM artifact attributed to a tip interaction. Also care was taken selecting the width location along the nanorods, as to avoid this artifact.

The aggregate length profiles are extremely similar, with an undulating profile at a very shallow incline, following the long axis of the aggregate (figure 8.16). The fact that the profiles are not smooth may indicate that the aggregates are not single entities. Indeed the topographical 2D and 3D images (figure 8.15) of the 1D aggregates appear to have >1 peak along the long axis. These 1D nanostructures appear to consist of smaller aggregates fused together. This is discussed further at the end of this section. It appears that the long axis of 1D aggregates are orientated at an extremely shallow incline from the point of attachment to the substrate (even accounting for the scanning artifact).

Table 8.1: Dimensions and aspect ratios of the small and large 1D aggregates where the max height is the maximum height on profile- 2 nm. Lateral distortion not significant here.

profile measurement	small aggregate range nm	small aggregate mean nm	large aggregate range nm	large aggregate mean nm
length	89.9-125.1	109.2	167.8-205.3	183.4
width	45.0-59.1	51.6	67.5-83.5	75.6
max height	3.3-4.8	3.9	6.0-10.2	8.4
aspect ratio		2.1		2.4

The similar shape (figure 8.16) and narrow dimension range of the profiles (table 8.1) reveal that both sized 1D nanostructures have a relatively narrow size distribution and are all nanobar shaped (flat with a low aspect ratio). The 1D nanostructures have mean lengths of 109.2 nm and 183.4 nm. Note the larger aggregate maximum height is approximately twice that of the smaller aggregate. The increasing aspect ratio with aggregate size infers that for the larger aggregates there is a proportionally greater length increase than width increase. More data is needed here to confirm the increasing aspect ratio with aggregate size, as there is slight overlap with standard deviations with the aspect ratios (small aggregate aspect ratio standard deviation 0.27 and large aggregate 0.28).

These nanobar dimensions (3 day immersion) were compared with those deposited from one day immersion (chapter 7). The small 3 day nanobar lengths and widths were



roughly the same size as those deposited after 1 day immersion (length range 111-137 nm and width range 55-65 nm) (chapter 7). Note there is a considerable aggregate height decrease in the nanostructures with increasing immersion time (1 day immersion time nanostructure height range 14-27 nm). The nanostructure developments with immersion time are interpreted as follows. The ICAT stacks (deposited 1 day immersion time) assemble into lines of 2 and 3 stacks (orientated aggregation) with increasing immersion time. More ICAT preferentially adsorbs on these lines of ICAT stacks rather than the hydrophobic surface and eventually the stacks collapse and the ICAT molecules fuse to form flatter nanobar shaped objects.

This theory is supported by the following facts. Even after 1 day immersion time the ICAT stacks are observed aligning into pairs and lines of three, but they still remain as separate entities at this point (chapter 7 figure 7.4). The larger nanobar dimensions (3 day immersion) could feasibly be two or three smaller ICAT stacks that have merged. The idea of lines of ICAT stacks collapsing is not only supported by the decreased height of the nanobars as compared to the ICAT stacks, but also the fact that the nanobars are slightly wider and longer than 2 clusters aligned side by side. The fact that the 3 day immersion larger nanobars were much higher than the smaller nanobars, (same immersion time), illustrates the fact that ICAT preferentially adsorbs on top of ICAT rather than the substrate. Finally from close inspection of the 3D and 2D topographical AFM images, combined with the undulating topographical length profile of the aggregates, the nanobars did appear to be formed from fused smaller particles.

### **8.5.2 Self-assembly on gold surfaces**

The standard ICAT/DMSO immersion experiment was repeated using gold substrates. SEM was used to image these films, as it useful to image a soft film with more than one microscopy technique and gold is an ideal substrate for this technique as it is highly conductive. A SEM image of the typical ICAT film on a gold surface is provided in figure 8.17.

This should be an accurate representation of the surface, as no sputtering with a conductive coating was required to image it, which tends to deform soft films. Single bodied, closely packed nanorods formed a continuous layer on the gold surfaces. The long axes of the nanorods were aligned parallel to each other.

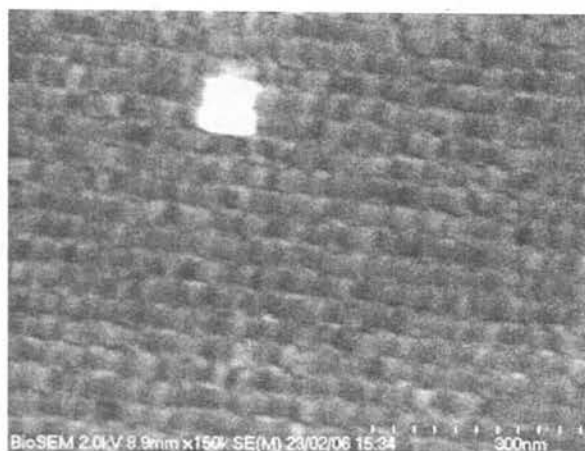


Figure 8.17: SEM micrograph of self-assembled ICAT nanorods on a gold surface (3 day immersion coating)

Note that the morphology here is extremely similar to that of the film deposited on glass from ICAT/DMSO solution, as imaged with the AFM (figure 8.1a). The validity of the nanorods is supported by the fact that both SEM and AFM imaged them. The nanorod length could not be measured with any high degree of accuracy from the SEM images, due to charging effects associated with the SEM but the nanorod length appeared comparable to that of the nanorods deposited on glass substrates (figure 8.4). To conclude, the nanorods were successfully transferable to a gold substrate in an ordered assembly.

## 8.6 Discussion

This is the first time well ordered vertically aligned 1D nanostructures have been produced with a small functional organic molecule, through solution deposition (non-template deposition). In fact to date only two organic small functional molecules and

their derivatives (perylene and porphyrin) have produced nanostructures (including 1D nanostructures) on substrates in highly disordered arrangements through solution based techniques (non-template) (Huang et al. 2009, Milic et al. 2002, Monti et al. 2004, Schwab et al. 2003 and Snitka et al. 2005).

The nanostructure formation, in this section, is discussed in terms of supramolecular assembly. When polar protic and aprotic organic immersion solvents, which are capable of hydrogen bonding (H-bonding) were used 1D ICAT arrays were successfully deposited on the substrates. The balance between the ICAT molecule's affinity for itself and for the solvent medium in the solution and for its substrate in a film is considered here.

#### **8.6.1 ICAT 1D assembly as a function of solvent**

The aspect ratio and size of the 1D nanostructures were dependent on the immersion solution solvent (figure 8.1). Both ICAT and the solvents, which produced 1D arrays (DMSO, DMF and methanol) have a high affinity for the substrate (OH-functionalised glass). The substrates were all the same in this section, therefore differences in the assembly are attributed to the solvent properties in each system.

The aggregation process is a result of more favourable ICAT-ICAT interactions over ICAT-solvent interactions. The first part of this section discusses how the ICAT-ICAT supramolecular interactions, featuring highly directional hydrogen bonds, could consistently produce 1D nanostructures and compares these intermolecular interactions with similar small planar molecules functionalised with hydrogen bond acceptor/donor (HBA and HBD) groups that commonly assemble into 1D nanostructures. The second half of the section relates the assembly differences to the solvent properties for each immersion system.

The strongest intermolecular ICAT interactions are highly directional H-bonds, which are dependent on the solvent environment and the number and sequence of the hydrogen bonds in the system and the weaker (less understood)  $\pi$ - $\pi$  interactions, which vary greatly depending on the structure and functional groups attached to the molecule and its solvent environment (Gallant et al. 1991, Gao et al. 2008, Garcia-Teelado et al. 1990, Hoebein et al. 2005, Jorgensen et al. 1990, Lahiri et al. 2000 Leclere et al. 2004, Milic et al. 2002, Murray et al. 1992, Nguyen 2004 and Prins et al. 2001). The strongest intermolecular interaction is a lateral quadruple H-bonding interaction, between the two carboxylic acid groups on one side of each of two ICAT molecules, as labelled with red arrows on figure 8.18, thus forming a stable ICAT dimer (Jonkheijm et al. 2006 and Prins et al. 2001). The single carboxylic acid group, on the opposite side of the ICAT molecule, as labelled with a black arrow on figure 8.18, can form 2-fold H-bonds with another ICAT molecule, which will also be a strong interaction.

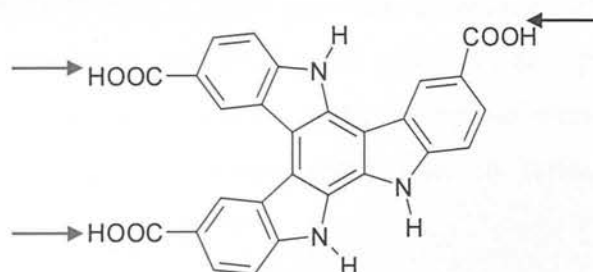


Figure 8.18: Schematic diagram of the ICAT molecular structure where the red arrows denote the carboxylic acid groups that can together form quadrupole hydrogen bonds with the same carboxylic acid groups on another ICAT molecule and the black arrow denotes the carboxylic acid group that can form double hydrogen bonds with carboxylic acid groups on another ICAT molecule.

Finally the carboxylic acid groups can H-bond with NH groups on the ring and H-bonding is possible with the  $\pi$ -system (Philip et al. 1996). Thus the assembly process here is quite a complex but will involve  $\pi$ -stacks of groups of ICAT molecules laterally H-bonding with each other and the solvent.

Small, planar, discotic,  $\pi$ -conjugated molecules functionalised with HBD and HBA groups self assembled through hydrogen bonds and/or  $\pi$ -stacking, commonly form simple rod structures, fibres and fibre networks (Aoki et al. 2002, Jonkheijm et al. 2003, Nguyen et al. 2004 and Tanaka et al. 2005). The most typical molecular arrangements, within these broader 1D nanostructures, as opposed to molecular wires, which usually consist of H-stacked molecules with no lateral H-bonding interactions (Chaudhuri et al. 2011), tend to be piles of J-stacked molecules (Okada et al. 2003 and Schwab et al. 2003),  $\pi$ -stacked columns of individual molecules with strong lateral intermolecular interactions between the columns, and/or strong solvent-molecule interactions (Nguyen et al. 2004) and  $\pi$ -stacking interactions between chains of molecules that form intermolecular head to tail H-bonds with each other (Aoki et al. 2000 and Aoki et al. 2002). In accordance with supramolecular chemistry, piles of J-stacked ICAT dimers H-bonding with other dimers, ICAT molecules and the solvents is the most probable molecular arrangement in these broader 1D nanostructures (Jonkheijm et al. 2006, Okada et al. 2003, Prins et al. 2001 and Sibjesma et al. 2003).  $\pi$ -stacked chains of ICAT molecules, H-bonding through head to tail carboxylic acid groups is another possibility. ICAT has the propensity to J-stack, as J-stacking has already been observed in ICAT aggregates (aggregates in solution rather than on surfaces), as confirmed by the spectroscopy results in chapter 6.

The next stage in the discussion is to determine the structure/solvent property relationship. Solvent polarity in similar systems (drop and spin cast) has been used to control self-assembly on surfaces (Balakrishnan et al. 2006, Duzhko et al. 2006, Huang et al. 2009, Surin et al. 2004 and Yang et al. 2008). Kamlet-Taft solvent parameters were selected here, as and they have been correlated previously with the nanostructure aspect ratio in similar systems involving H-bonding interactions (Aoki et al. 2002 and Tanaka et al. 2005). The basic empirical Kamlet-Taft parameters used here are  $\pi^*$ ,  $\alpha$  and  $\beta$ . The  $\alpha$ -scale quantifies the solvent hydrogen bond donor (HBD) acidity, the  $\beta$  scale quantifies the solvent hydrogen bond acceptor (HBA) basicity, and  $\pi^*$  is a measure of the



combination of polarity and polarizability. These solvent parameters, provided in table 8.2, determine how effectively the solvent can solvate ICAT.

Table 8.2: Empirical Kamlet-Taft parameters (Reichardt et al. 2003).

Solvent	$\pi^*$	$\alpha$	$\beta$
DMSO	1.00	0.00	0.76
DMF	0.88	0.00	0.69
methanol	0.60	0.98	0.66
water	1.09	1.17	0.47

Solvophobic forces also play a role in ICAT assembly in the immersion experiments and are discussed where appropriate. DMSO and DMF are aprotic solvents, which are not hydrogen bond donors ( $\alpha = 0$ ), while methanol is a protic solvent and can donate a hydrogen bond with ease (high value  $\alpha = 0.98$ ). The  $\beta$  values show that DMSO has a strong tendency to accept hydrogen bonds ( $\beta = 0.76$ ) and DMF and methanol are weaker hydrogen bond acceptors (methanol  $\beta = 0.66$ , DMF = 0.69).  $\pi^*$  assesses the dipole attraction in the solute-solvent interactions. High  $\pi^*$  values equate to the ability to form strong hydrogen bonds in this context. Both DMSO and water are highly polar solvents ( $\pi^* = 1.00$  and 1.09 for DMSO and water respectively). DMF is regarded as very polar still ( $\pi^* = 0.88$ ) and methanol is of intermediate polarity ( $\pi^* = 0.6$ ). The  $\pi^*$  here reflects the ability of the solvent to interfere with ICAT intermolecular H-bonding interactions and solvate ICAT. DMSO, for example, with the extremely high  $\pi^*$  value, has even on rare occasions been able to solvate supramolecular complexes held together through quadruple H-bonding interactions (Garcie-Tellado et al. 1990).

1D nanostructures were not assembled on the substrate, but rather ICAT precipitated out when water and non polar hydrocarbon (HC) immersion solvents were used. This effect was attributed to the poor ICAT solubility at room temperature in these solvents. The non-polar HC based solvents had very low  $\pi^*$  values, while highly polar water has a very high  $\pi^*$  value and is a very strong hydrogen bond donor and good hydrogen bond acceptor. So the rapid precipitation in the ICAT/water immersion experiment proceeded

despite the favourable Kamlet-Taft parameters. The aggregation in these two immersion experiments is attributed to solvophobic effects. In water the  $\pi$ -stacking of aromatic molecules is driven mainly by the solvophobic effect (Marmur et al. 2000). Water molecules solvating the aromatic surface have higher energy than bulk water molecules, which results in the stacking of the molecules to reduce the total surface exposure to water. In the non polar hydrocarbon based aggregation and rapid precipitation would be expected to be driven by solvophobic forces too. The polar ICAT functional groups would be expected to form intermolecular hydrogen bonds to minimise contact with the non polar HC solvent and lower the free energy. The self-assembly process is dominated by the solvophobic forces in these systems and is independent of Kamlet-Taft parameters. However, in polar protic and aprotic organic solvents, where solvophobic forces were not dominant, ordered assemblies of 1D nanostructures were deposited on the substrate.

Similar studies involving small aromatic molecules functionalised with HBD and HBA groups have discussed assembly in terms of solvent polarity (Aoki et al. 2002 and Duzho et al. 2006). However, this is quite a complex system and there is no obvious nanostructure aspect ratio or size correlation with  $\pi^*$  here (although a wider selection of solvents might be required). A direct comparison may be made between the nanostructure dimensions produced from immersion in ICAT/DMSO and ICAT/DMF solutions, as both are highly polar solvents with high  $\beta$  values and zero  $\alpha$  values. Both solvents can accept H-bonds from the NH groups on the ICAT ring system and COOH functional groups. The slightly less polar DMF, which has weaker H-bond interactions than those of DMSO tends to produce nanostructures with a greater aspect ratio and larger size (nanowires) than DMSO (nanorods) (figure 8.1). Despite the fact that it was not possible to calculate the exact DMF nanowire aspect ratio, it is assumed that it is greater than that of the two other solvent systems, as nanowires were produced in DMF and nanorods were produced in DMSO and methanol.

Here the ability of DMSO to solvate ICAT more effectively than DMF, (as reflected by the higher  $\pi^*$  and  $\beta$  values than DMF), may be correlated to the nanostructure smaller aspect ratio and size in the DMSO immersion system (Garcie-Tellado et al. 1990). Specifically, the superior ability of DMSO, as compared with DMF, to interfere with the multiple lateral intermolecular H-bonding interactions, which are the strongest intermolecular interactions here will limit ICAT aggregation. For example, DMSO can interfere with extremely strong quadrupole H-bonds, which are expected to be the dominant interaction in the aggregation process here, while DMF is not capable of this. Particle aspect ratio and size were inversely proportional to the solvent  $\pi^*$ ,  $\alpha$  and  $\beta$  values in solution based depositions, with similar molecules functionalised with HBD/HBA groups (Aoki et al. 2002 and Garcie-Tellado et al. 1990).

DMF, with a higher  $\pi^*$  value and extremely similar  $\beta$  value to that of methanol, deposited larger aspect ratio and sized 1D aggregates than methanol did (figure 8.1(b) and (c)). However, methanol has a substantial  $\alpha$  value, while DMF has a zero  $\alpha$  value, indicating that the ability to donate a H-bond could lead to more effective ICAT solvation, producing smaller aspect ratio and sized 1D nanostructures (similar line of reasoning used in previous paragraph). However, it was observed that ICAT is less soluble in methanol than DMF and the  $\pi^*$  difference is held accountable for this difference. So the line of argument suggested above seems unlikely and is discussed further in the next section.

Finally, the similar aspect ratio in the 1D nanostructures produced by methanol and DMSO may infer a similar structure. The nanowires deposited from ICAT/DMF would be expected to have a different structural arrangement. This would be interesting to resolve, as the DMF nanowires might have quite different fluorescent properties as compared with those of the nanorods.

To conclude, much was learnt about ICAT self-assembly, of which very little is known. Solvophobic forces were demonstrated to induce precipitation rather than controlled 1D

growth in the immersion experiments with water and HC based immersion solvents. It was established that organic polar aprotic solvents are required for orientated 1D growth on the substrate. (However, a solvent with zero  $\beta$  value and a high  $\alpha$  value was not tested, so a polar protic solvent immersion experiment should be performed). There is not a simple correlation between nanostructure dimensions and  $\pi^*$  in this system. Thus it appears that 1D nanostructure growth is also influenced by the other Kamlet-Taft parameters, but further studies are required to determine the exact nature of the Kamlet-Taft influence.

### 8.6.2 1D assembly as a function of immersion time

The assembly process was followed as a function of immersion time in order to understand and potentially control the assembly process. Two immersion systems, using the same substrate and immersion solvents with extreme  $\pi^*$  (and  $\alpha$  values), (methanol and DMSO) were selected. The assembly process was successfully controlled with immersion time, producing bulk, particulate or well ordered nanorod film morphologies (section 8.4). The ICAT/DMSO immersion film morphology developed from a continuous, smooth bulk molecular film to an array of vertically aligned nanorods with increasing immersion time (figure 8.9). The immersion time also controlled both the rod density and rod orientation (figure 8.9(b) and (c)). The film morphology was found to be independent of the pre-immersion age of the ICAT/DMSO solution (figure 8.8). The ICAT/methanol immersion film morphology transformed from particulate (flattened ellipsoid particles) (figure 8.10(b)) to a vertically aligned nanorod array, with increasing immersion time (figure 8.13).

To date (non-template) solution based small organic functional molecule depositions produce randomly orientated, randomly positioned and/or clustered polydisperse 1D nanostructures (Balakrishnan et al. 2006, Huang et al. 2009, Jonkheijm et al. 2003, Schawb et al. 2003, Shea et al. 2006, Shea et al. 2007, Snitka et al. 2005, Surin et al. 2006 and Uscowitz et al. 2011). However, similar vertically aligned nanorod assemblies

on surfaces from solution deposition have been observed in inorganic (metal oxide) seeded nanostructure growth (Sounart et al. 2006 and Wang et al. 2004), dry colloidal sediments (Maeda et al. 1996) and lyotropic liquid crystals (Seo et al. 2006). The assembly in the two immersion experiments is discussed in terms of ICAT solubility in each immersion solvent in turn, and how this affects the ICAT/substrate interfacial morphology and the subsequent nanorod growth on the substrate.

The nanorods were not assembled directly in the ICAT/DMSO solution but on the substrate as a function of immersion time (figures 8.8 and 8.9). The evidence points towards a molecularly dissolved solution (possibly with small soluble aggregates), (which is consistent with the favourable DMSO  $KT$  parameters) for the following reasons. The assembly was independent of the pre-immersion age of the solution (solution aged for up to one year) (figure 8.8). The solution presented narrow, well defined NMR spectra at this concentration (chapter 6). Short immersion times produced an ICAT monolayer, where the film thickness was consistent with an edge on ICAT configuration (figure 8.9(a), film thickness measurements in chapter 7). The growth process consists of ICAT molecules forming a monolayer at the interface initially, and then further ICAT molecules assembling on this layer with increased immersion time, and arranging to form nanorod arrays.

It was also established that the nanorods were not assembled directly in the ICAT/methanol solution, but on the substrate as a function of immersion time (figures 8.10 and 8.13). However, this time the evidence pointed to ICAT aggregating in the solution (consistent with the intermediate polarity ( $\pi^* = 0.6$ ), as short immersion times produced particulate films (with particles of regular shapes and size) (figure 8.10(b)) and precipitation occurred when the solution was aged (1 day). The assembly process here appeared to consist of face-on assembly of ICAT particles at the interface and then further ICAT particles assembling on top of these particles to form 1D arrays (section 8.4.2).



These assembly processes are now discussed. The ID arrays assemble here, from what appears to be heterogeneous nucleation (nucleation on a surface) and subsequent growth, and has been applied frequently in metal oxide systems when a functionalised substrate is immersed in a metal oxide solution (under a narrow range of conditions) and once in a conducting polymer orientated growth system (Aizenberg et al. 1999, Liu et al. 2003, and Sounart et al. 2006). Nanorods are not deposited in these two immersion systems without the substrate. Heterogeneous nucleation can be promoted by functionalising the surface with surface active SAMs or seeding the substrate in particles of the same material (Aizenberg et al. 1999 and Sounart et al. 2006). The heterogeneous nucleation here is promoted by the substrate functionalisation with a complete layer of surface active OH groups, which can H-bond twice with each ICAT molecule reducing the substrate/ICAT interfacial free energy.

There is a narrow window of orientated growth for these systems, as demonstrated by the following example. Figure 8.19 is a schematic plot of the number of nuclei ( $N$ ), as a function of the degree of supersaturation ( $S$ ), showing that there is a narrow window where nucleation is favoured for orientated nanostructures.

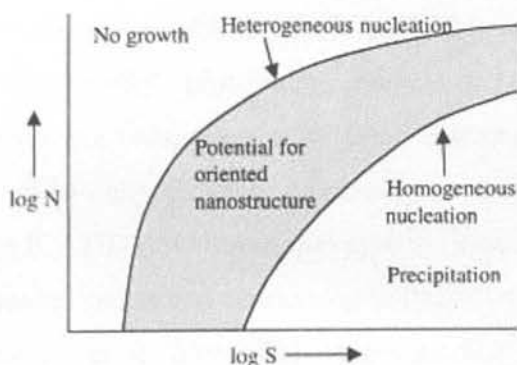


Figure 8.19: Schematic diagram for idealized nucleation and growth (taken from Liu et al. 2003).

In particular controlling the degree of supersaturation in the solution is a common problem. This point is well illustrated by the fact that particular care had to be taken with the ICAT/methanol concentration as uncontrolled precipitation and/or highly disordered

films with no 1D nanostructures occurred on several attempts. Temperature variation and solvent mixing techniques were also used to try and control the degree of saturation in methanol and water immersion systems, but were not successful. When immersion solvents water and HC based solvents were used rapid precipitation occurred and no orientated nanostructure growth was observed. The solvophobic driven ICAT aggregation would be expected to dramatically increase the degree of supersaturation in the system. The degree of supersaturation was reduced by using organic solvents with intermediate and high  $\pi^*$  values that will not induce solvophobically driven aggregation. The combination of OH-functionalised substrates with low concentration ICAT solutions, with solvents with intermediate and high  $\pi^*$  values, provided favourable growth conditions for orientated 1D nanostructures.

The differences between the 2 systems, nominally the larger size and aspect ratio of the ICAT/methanol nanostructures, as compared to those of the ICAT/DMSO immersion, are attributed to the different interfacial ICAT/substrate assemblies (molecular monolayer and particulate on the substrates in DMSO and in methanol respectively) and the larger aggregate building blocks in methanol as the opposed to the molecular building blocks in the molecularly dissolved ICAT/DMSO solution. Similar behaviour has been observed previously where the interfacial assembly on the substrate (seeding layer) has controlled the density, positioning, orientation, size and shape of the nanostructures in oxide systems (Aizenburg et al. 1999, Hirano et al. 2004 and Sounnart et al. 2006). The change in nanostructure orientation in the early growth stages to vertical alignment in the ICAT/DMSO immersion system (figure 8.9) has been observed previously in both in seeded oxide and conducting polymer orientated growth systems (Liu et al. 2003 and Sounart et al. 2006). This behaviour was attributed to the kinetic limitations of randomly orientated growth. The growth of the randomly orientated nanorods formed in the initial stages becomes retarded when the nanostructures begin to overlap with each other and only nanostructures orientated normal to the substrate can grow freely.

The ICAT/DMF immersion experiment produced larger and greater aspect ratio 1D nanostructures (nanowires) than those of the ICAT/methanol system (nanorods) (figure 8.1(b) and (c)). This is now discussed using a possible seeding based mechanism. The nanostructure morphology can be influenced by both the aggregation state of ICAT in solution and the interfacial assembly. An edge-on ICAT interfacial molecular layer, similar to that of DMSO, (chapter 7, figure 7.1) is deposited from ICAT/DMF immersion, which differed from the particulate interfacial layer from ICAT/methanol immersion (figure 8.10(b)). It has been observed that ICAT is less soluble in methanol than DMF and the  $\pi^*$  difference is held accountable for this difference. The much greater nanostructure aspect ratio associated with the ICAT/DMF immersion experiment as compared to the ICAT/methanol immersion experiment, may be determined by the kinetics of aggregate formation in solution. More organised packing and growth along the long axis of the 1D nanostructure may be associated with the expected slower ICAT aggregate formation in ICAT/DMF solution (higher  $\pi^*$  value). The rate of crystallization has been demonstrated to affect the 1D aggregate length in perylene based solution deposition previously, where the slower crystallization rate produced longer nanorods (Huang et al. 2009). If  $\pi^*$  is too low and the molecules aggregate too quickly due to stronger ICAT-ICAT association leading to the formation of more seeding particles, then there will be no free molecules for the later stage growth into the nanowire thus forming shorter nanorods. A similar mechanism based on the speed of aggregation, which was dependent on solvent polarity produced different 1D nanostructure lengths was suggested by Che and co-workers (Che et al. 2007).

To conclude immersion time and solvent selection have allowed the production of bulk, particulate, size tailored vertically orientated nanorods and nanowire arrays and provided greatly needed insight into the assembly process. This is the first time vertically orientated nanorod arrays with an organic small functional molecule have been produced (solution based, non-template deposition).

### 8.6.3 1D assembly as a function of substrate

1D assembly was studied here on a hydrophobic (HMDS-functionalised glass), hydrophilic (OH-functionalised glass) and an inert (gold) substrate. This experiment established that the 1D nanostructures and their assemblies are sensitive to the substrate chemistry. Similar highly ordered nanorod assemblies were deposited on the hydrophilic glass and inert gold surfaces (figures 8.1(a) and 8.17). While 1D nanostructures were also deposited on the hydrophobic surface, their assembly, dimensions and aspect ratio (the ICAT/DMSO nanorod aspect ratio is 4.4 on OH-terminated glass and 2.1-2.4 on HMDS-terminated glass) were completely different to those deposited on glass and gold surfaces (figures 8.14 and 8.16). The ICAT morphology on the hydrophobic substrate was identical with two different immersion solvents DMSO and DMF. Finally, it was established that the samples remained unchanged after intense washing in a selection of solvents, which reflected that these nanostructures had a high mechanical integrity. There are two major points of interest here. The formation and assembly of the 1D nanostructures on the hydrophobic and gold surfaces, including a detailed comparison with the 1D growth on hydrophilic glass, is addressed in turn.

The 1D nanostructures on the hydrophobic substrate were considerably larger and more sparsely distributed than those of the hydrophilic surface (figure 8.14). The 1D aggregates on both substrates were randomly positioned (same immersion time). The ICAT morphology was the same on the hydrophobic substrates when two different immersion solution solvents (DMSO and DMF) were used, but was different on the hydrophilic substrate with these two immersion solution solvents.

Bulk film morphologies are commonly sensitive to interfacial layering and two different ICAT interfacial orientations were observed on the hydrophobic and hydrophilic surfaces (an edge-on ICAT orientation at the hydrophilic interface and a face-on orientation at the hydrophobic surface were observed in chapter 7) (Leclerc et al. 2004, Nguyen et al. 2002 and Surin et al. 2004). The lesser coverage on the hydrophobic

surface may be attributed to the weaker ICAT-substrate interaction at the hydrophobic interface, leading to ICAT clustering at the interface (demonstrated in chapter 7) and possible removal of ICAT during the washing process. The increased roughness of the HMDS-functionalised surface, as compared to the glass surface, would be expected to have a strong influence over the ICAT morphology. The 1D nanostructure dimension differences, between the hydrophobic and hydrophilic surfaces, maybe associated with the different solvent interactions with the substrates (Nguyen et al. 2004). The fact that DMSO has a much greater affinity for ICAT than the hydrophobic substrate, (which is not the case for the hydrophilic substrate), could lead to DMSO clustering with the ICAT nanostructures on the hydrophobic substrate. Again the hydrophobic substrate ICAT nanobar shape is commonly associated with J-aggregated piles of small aromatic molecules (Okada et al. 2003).

The consistent ICAT morphology on the hydrophobic substrate with DMF and DMSO immersion solutions is interesting. Previously these immersion solutions had produced different shaped nanostructures on the hydrophilic substrate (figure 8.1a and b). So despite the  $\pi^*$  difference in these solvents affecting the ICAT solubility, the substrate-HMDS functionalisation is the determining factor in the nanobar deposition. The hydrophobic HMDS interaction with the ICAT and polar solvent molecules appears to dominate the assembly process here.

The aspect ratio of the nanostructures on the hydrophobic surface was dependent on immersion time. Short immersion times at low concentrations of ICAT/DMSO solution resulted in clusters forming on the hydrophobic surface (chapter 7), and as the immersion time was increased the aspect ratio of the clusters changed and nanobars were deposited on the surface (figure 8.15). The nanoparticles had a relatively large length increase and height decrease with increasing immersion time. The (brief immersion) submonolayer clusters (aspect ratio 2) (chapter 7) were interpreted as face-on piles of  $\pi$ -stacked ICAT dimers. The AFM images (figure 8.15(b) and (c)) and accompanying nanostructure profiles (figure 8.16) in this chapter (prolonged immersion times)



indicated that the nanobars were not single bodies but rather made from fused smaller clusters.

The theory here, based on a comparison of these AFM results with those in chapter 7, is that the piles of  $\pi$ -stacking face down ICAT dimers (chapter 7) assemble into twos and threes in a line formation (orientated aggregation) and fuse (strong ICAT-ICAT interactions), with increasing immersion time. The orientated aggregation of the stacks is most probably driven by the highly directional intermolecular H-bonding between molecules in the stacks. The height decrease of particles with immersion time maybe attributable to the lines of clusters growing higher, as more ICAT molecules preferentially adsorb on the ICAT clusters, rather than on the hydrophobic surface with immersion time, and eventually collapsing to form slightly broader and longer but very much flatter nanobars. The fact that longer nanobars are higher than the shorter nanobars (table 8.1) reflects that the ICAT molecules preferentially adsorbs on top of ICAT clusters, rather than on the HMDS-functionalised surface. Irregular packing of the  $\pi$ -stacked ICAT piles, complicated by DMSO interactions and hydrogen bonding between neighbouring ICAT molecules would be expected to contribute towards the stacks collapsing and wide nanobar shape (Nguyen et al. 2004).

To conclude, immersion time can be used to control the aspect ratio and size of 1D nanostructures on hydrophobic surfaces. Surface functionalisation can be utilized to control 1D nanostructure shape (nanobar on hydrophobic surface and nanorod on hydrophilic surface). It was demonstrated that the HMDS-functionalised glass surface was the determining factor in the ICAT assembly process in the hydrophobic immersion experiment.

A continuous layer of single bodied, closely packed nanorods of similar size to those deposited on glass, with their long axis aligned parallel to each other (figure 8.1a) was deposited on the gold surfaces (figure 8.17). Gold is a noble metal and has low chemical activity (low surface free energy) and is regarded as an inert surface in this context. The

interfacial ICAT/gold orientation of ICAT has not been confirmed yet. However, with this inert surface, unlike the other two surfaces a definite preferred ICAT orientation at the interface is not expected. The weak dispersion based interaction between similar small aromatic planar molecules and gold has resulted in both face and edge-on interfacial orientations (Barth et al. 2003, Miao et al. 2009 and Tautz et al. 2007). Typically aromatic and aliphatic carboxylic acids only physisorb to gold surfaces and consequently do not adhere well to gold substrates (Han et al. 2000). Certainly the fully protonated carboxylic acid groups here would not be expected to chemisorb to the gold surface. So the ICAT-ICAT interaction is far stronger than the ICAT-gold interaction, which would be expected to favour an edge-on interface orientation thus maximising the ICAT-ICAT  $\pi$ - $\pi$  interaction (Miao et al. 2009 and Tautz et al. 2007).

It is interesting here that the ICAT morphology is extremely similar on the inert gold substrate and the hydrophilic substrate. Both surfaces are smooth with DMSO favourably wetting both. As explained in the previous paragraph, a similar ICAT interfacial assembly is anticipated here as at the ICAT/glass interface, which could contribute towards the similar bulk ICAT assemblies (Leclerc et al. 2004, Nguyen et al. 2002 and Surin et al. 2004). The recurrent nanorod shape could be favoured as the ICAT-ICAT interactions comprise of relatively strong, highly directional hydrogen bonding as well as the  $\pi$ -interactions. Finally the well ordered nature of both assemblies can partially be attributed to the relatively smooth gold and glass surfaces (Yokoyama et al. 2001).

#### 8.6.4 Result assessment

This section assesses how useful these achievements are to science today. It commences with a brief review of why research is focusing on 1D small functional organic molecular nanostructures and solution based fabrication, with an in depth commentary of how my results fit the specific requirements in this area. It closes with an assessment of the fundamental science learnt here.

Reproducible, mechanically stable nanowire arrays, particulate films and size-tailored vertically aligned monodisperse nanorods were deposited on substrates as a function of immersion solvent and immersion time (section 8.3). 1D organic nanostructures are of fundamental importance in modern electronics and opto-electronics (detailed in introduction). The variety of shapes and sizes of the 1D nanostructures produced here is essential in expanding device properties, fitting particular devices and connections, device miniaturization and exploring the science in the organic semiconducting area, which is as yet not well established. Organic nanowire arrays are still a rarity despite organic nanowire electronic applications such as optical waveguides, chemical sensors and FETs (Briseno et al. 2007, Zhao et al. 2010 and Zhao et al. 2009). The vertically aligned nanorods produced here are particularly interesting, as electroactive and chemically active, orientated, open structures are highly desirable for applications in chemical and biological sensing and diagnosis, microelectronic devices and interconnects, energy conversion and storage. The high surface area and high porosity associated with open nanostructures, as well as their favourable orientations, usually translate into high capacity and high efficiency for the devices.

Thus far most organic 1D nanostructures have been fabricated with conducting polymers (Tran et al. 2009), while organic small functional molecule 1D nanostructures have only been produced with perylene and porphyrin derivatives (solution deposition, non-template methods) (Huang et al. 2009, Milic et al. 2002, Monti et al. 2004, Schwab et al. 2003 and Snitka et al. 2005). However superior control over the assembly process is shifting research away from polymers towards organic small functional molecule. Electronic devices require both p and n-type organic materials but to date the overwhelming majority of 1D nanostructures are produced with p-active small functional organic molecules, with the exception of n-active perylene tetracarboxylic diimide derivative nanobelts (Balakrishnan et al. 2006 and Balakrishnan et al. 2005). This is the first time organic small molecule 1D nanostructures have been produced with an ambipolar molecule (activity demonstrated in chapter 10).

Very limited success has been achieved in 1D organic nanostructure synthesis and assembly with complicated, arduous, multi-step, expensive template and vapour deposition based production methods (Haberkorn et al. 2009, Lee et al. 2002 and Liu et al. 2003). Thus the current research drive is centred on developing large scale, facile, single step, cost effective self-assembly in the liquid phase. 1D nanostructure shape, aspect ratio, size, substrate coverage and orientation were controlled through solvent selection and immersion time. The immersion coating based procedure used here is single step, incredibly facile and cost effective.

It is notoriously difficult to assemble organic aggregates into regular arrays with solution based deposition techniques. Typically in solution cast films (dip coating, drop casting and spin casting) there is no control over where the particles are deposited on the substrate (randomly sized and situated deposits, rings shaped deposits (coffee stain effect), they tend to aggregate further on surface into irregular piles or bundles and tend to have no organization with respect to the substrate or each other (Balakrishnan et al. 2006a, Jonkheijm et al. 2003, Schenning et al. 2006, Schwab et al. 2003, Shea et al. 2006, Shea et al. 2007, Snitka et al. 2005 and Surin et al. 2006). Here we have one step self-assembly and alignment of organic semiconductor nanorods and nanowires on varied surfaces. This is the first time that small functional organic molecule based-aligned nanorod arrays have been produced, and well ordered nanowire arrays have only been reported by two other researchers (Liu et al. 2009 and Wang et al. 2011), with solution based deposition methods (non template method).

Unfortunately solution based deposition methods for organic small functional molecular 1D aggregates tend to result in very polydisperse yields (Huang et al. 2009 and Schwab et al. 2003). A typical example is provided by Schwab and co-workers, who deposited porphyrin based nanorods on substrates through immersion coating with lengths between 130 nm and 2.3  $\mu\text{m}$  (Schwab et al. 2003). Thus the nanoparticle dispersities produced here are much narrower than those of typical nanostructures in this field.

To incorporate nanostructures into useful nanoscale devices, their organization and stability on different surfaces must be evaluated. To date only a handful of researchers have successfully transferred 1D aggregates between surfaces, and the activity has been limited by different nanorod assemblies on different surfaces in the electronic devices, such as FETs (Balakrishnan et al. 2006, Huang et al. 2009 and Schwab et al. 2003, Shea et al. 2006, Singh et al. 2006 and Zhang et al. 2008). Similar highly ordered ICAT nanorod assemblies were deposited on the hydrophilic glass and inert gold surfaces. Thus the well ordered nanorod assemblies produced here on both gold and glass (which is structurally very similar to silicon dioxide used in electronics) is a valuable result.

Primarily the synthesis of these structures is particularly challenging due to the weak intermolecular interactions between organic semiconductors, complexities of the self-assembly process, and difficulties to control molecular packing. Thus any insight into the ICAT assembly process provided by the experiments here will be invaluable to development in this area. Firstly ICAT has a propensity to assemble into 1D nanostructures, particularly nanorods on varied surfaces. The consistency of the structure shape is associated with the supramolecular assembly, involving relatively strong, highly directional hydrogen bonding and the  $\pi$ -stacking intermolecular interactions.

Substrate functionalisation can be used to control the 1D shape and assembly on surfaces. It appears that ICAT interfacial assembly dictates the bulk morphology on the substrate. When the glass substrate was functionalised with hydrophobic HMDS, the shape and size of the 1D nanostructures (nanobar) was consistent with different immersion solvents (DMF and DMSO). When these immersion solvents were used in the hydrophilic glass substrate immersion experiment two different 1D shapes were deposited. This indicates that the substrate chemistry is the determining factor in the ICAT assembly on the hydrophobic HMDS-substrate.



Solvent properties can be used to control both the size and shape of the 1D nanostructures. There is no obvious correlation between nanostructure dimensions and  $\pi^*$ . Both solvophobic forces and solvent HBD and HBA properties appear to play an integral role in this assembly process. Polar organic solvents with high Kamlet-Taft parameters are required for 1D growth.

Two assembly mechanisms, based on the film morphology developments with increasing immersion time, for immersion in ICAT/DMSO and ICAT/methanol were proposed.

## 8.7 Conclusion

This immersion based method produced a variety of ICAT 1D nanostructure shapes and sizes on varied substrates. This is the first time 1D nanostructures have been fabricated with an ambipolar and second time n-active organic small molecule. This is also the first time vertically orientated nanorod arrays have been fabricated with small organic functional molecules, through a solution based technique (non-template). The facile, single step, cost effective deposition procedure developed here fulfils the requirements that research and industry require in this field today. Finally this appears to be the first example of seeded 1D vertically orientated nanorod growth in an organic small molecule system.

## **Chapter 9**

# **Self-assembly in organic electronics**

## 9.1 Introduction

Modern OFETs offer a viable alternative to traditional inorganic FETs in the form of easy, cheap and low temperature solution-processing, good compatibility with a wide number of substrates and excellent opportunities for structural modification, making them suitable for low-cost large area electronic functions (Sirringhaus et al. 2005). FET devices also provide a valuable insight into charge-transport and charge-injection physics of organic semiconductors and their structure property relationships, through their ability to control charge carrier concentration electrostatically rather than chemically.

Despite these attractive properties, currently OFETs have slow responses and a limited lifetime as compared to silicon based technology. Nevertheless, research into organic semiconductors is still relatively young and hopefully as the scientific understanding grows the properties should improve. The current research drive is focussed on the realisation of air-stable materials with respectable electron and/or ambipolar carrier-transport capabilities which are rare and still require a great deal of work (Anthopoulos et al. 2004 and Newman et al. 2004). To date a very limited number of single component ambipolar OFETs have now been developed, but they only operate under vacuum (or nitrogen) and strongly favour either electron or hole mobility (Boer et al. 2005, Seo et al. 2006 and Zaumseil et al. 2006).

The other major centre of interest focuses on the deposition of the organic semiconducting film, which is the determining step of OFET fabrication (Dimitrakopoulos et al. 2001). OFET performance is strongly dependent on many factors, such as the semiconductor film microstructure and texture, molecular orbital energy alignment/shift with contacts and film morphology, which in turn is strongly dependent on the film growth mechanism and interfacial interactions with the gate. Device instability in ambient conditions, charge carrier type and mobility are closely linked to the organic film morphology. The future for organic thin film deposition is

solution based, as vacuum deposition is extremely expensive and requires sophisticated instrumentation. Langmuir-Blodgett deposition is restricted to amphiphilic molecules. Spin-coating is generally not suitable for oligomers and is limited to soluble conducting polymers, which are few in number. Unfortunately, the common solution based deposition techniques typically yield films that are non-uniform in thickness, morphology (including non-uniform patterns of rings, mixed phase growth and unconnected deposits) and consequently have wildly varied electrical properties (Dimitrakopoulos et al. 2002, Dimitrakopoulos et al. 2001, Katz et al. 2000, Katz et al. 1999, Katz et al. 1998 and Laquindanum et al. 1998). Thus much work is needed in this area.

ICAT despite its high redox activity, good solubility, interesting fluorescence properties, excellent thermal stability and biological compatibility has not yet been realised in any applications and its properties are not well understood due to previous poor quality synthesis (Mackintosh et al. 1994a). Notably, the structural properties (electron deficient-nitrogen containing heterocycle) of this molecule favour n-type transport, which is ideal for general OFET purposes and ambipolar OFET applications (Newman et al. 2004).

In this thesis, chemical synthesis produced the pure neutral ICAT molecule and well ordered ICAT assemblies were deposited on varied substrates, using solution based methods. Thus this molecule and its thin films are now suitable for deposition onto FET substrates to establish if the highly ordered range of assemblies could be transferred to devices and eventually test structure/property relations.

Spin, dip and drop coating were tried initially and produced extremely poor quality films. So solution based deposition techniques with original advancements, (some of which were developed in earlier chapters), were applied. The enhanced solution based deposition methods were applied to deposit ICAT onto FET substrates, in order to direct film growth into the active channel, (as defined in figure 9.3), and ultimately achieve

smooth, continuous, homogeneous coatings. Through using several different deposition techniques, a range of ICAT morphologies should be attainable, which is desirable as the organic film structure/device activity relationship is not as yet understood and there are specific advantages associated with different phases. For example, amorphous organic devices tend to have good ON/OFF ratios, good air stability and are readily applicable, while single crystal and polycrystalline devices typically have superior mobilities (Katz et al. 2004, Podzorov et al. 2003 and Saragi et al. 2005). Film thickness and interfacial ordering strongly affect charge transport in these devices. Thus the control over interfacial assembly on SiO<sub>2</sub> and HMDS-functionalised substrates, as demonstrated in chapters 7 and 8, was applied here. Also HMDS is commonly attached to these devices to alleviate n-activity shielding, commonly associated with SiO<sub>2</sub> dielectrics (Chau et al. 2005, Guillaud et al. 1998 and Olthgius et al. 1992). Films of varied thickness were produced. Ultimately through controlling the organic semiconductor film morphology, interfacial assembly and film thickness, it should be possible to control and gain much needed insight into the device properties.

## **9.2 Experimental method**

ICAT films, using varied deposition methods, were deposited on top of a pre-fabricated FET substrate, which had a conventional metal-oxide-semiconductor field-effect transistor structure.

### **9.2.1 Device Configuration**

The field-effect transistor substrate was produced in a back-gated, bottom contact configuration, schematically depicted in figure 9.1.



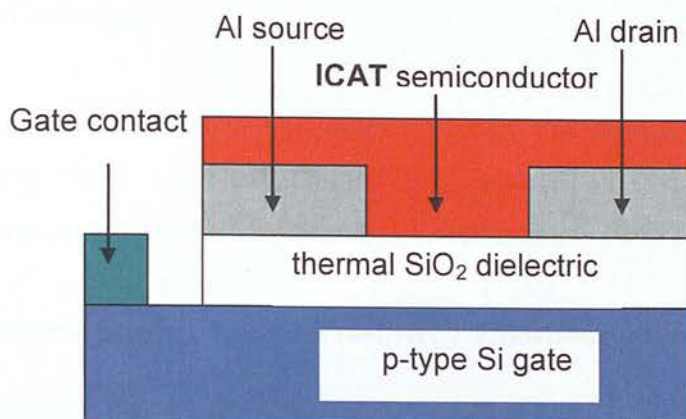


Figure 9.1: Schematic illustration of bottom-contact, back-gated OFET configuration (chip 2).

Two different FET substrates were provided by Dr Natalie Plank. One substrate (chip 2) was a back-gated high quality p-type Si wafer, with a 50 nm layer of thermal silicon dioxide, onto which aluminium source and drain electrodes of thickness 50 nm were fabricated using e-beam lithography. The backside was aluminium, and the electrode spacing was between 2 to 6  $\mu\text{m}$  dimensions, in increments of 1  $\mu\text{m}$ . The other chip (chip 1) was identical, apart from the fact that the source and drain electrodes and backside were gold. Scanning electron microscopy (Hitachi S4700) was used to check substrate quality and dimensions. All substrates were fabricated in a clean room and stored in vacuum. The source and drain electrodes formed direct ohmic contacts with the conduction channel.

### 9.2.2 Substrate cleaning procedure

Before ICAT film deposition, the substrates were cleaned as follows. This cleaning procedure took place in the clean room. The substrates were immersed in ethanol (analytical grade, Aldrich) for 5 minutes and then placed in a sonic bath in ethanol for 20 seconds and then heated on a hot plate at 100 °C. They were then exposed to oxygen plasma for 30 seconds (pressure 60mTorr, RF 100W) and placed in deionised water. They were dried under nitrogen and covered with ICAT immediately.

### 9.2.3 ICAT solutions

The solvents used to make ICAT solutions (DMF and DMSO) were analytical grade, filtered and dried (Aldrich). ICAT/DMF and ICAT/DMSO solutions, with a concentration range 0.5-3 mMol, were made immediately before use and filtered.

### 9.2.4 Micro-molding in capillaries (MIMIC) deposition

ICAT films were deposited using MIMIC (a soft lithography technique), with some developments, on the FET substrates. The technique is based on the spontaneous filling of capillaries formed between the FET substrate and the poly(dimethylsiloxane) (PDMS) stamp which has a recessed relief surface structure, by a fluid (Kim et al. 1996). The PDMS stamps were patterned on one face with parallel lines of channels, (troughs were 2  $\mu\text{m}$  deep with either 100  $\mu\text{m}$  or 1 mm widths and lengths ranging between 0.5 and 2.0 cm).

The PDMS stamps were fabricated using the standard procedure, (casting the liquid polymer precursor against a master fabricated with photolithography), (Xia et al. 1998). Before use, the PDMS stamps were immersed in ethanol and agitated for 30 minutes. They were then dried under nitrogen and exposed to oxygen plasma for 60 seconds (pressure 60 mTorr, RF 100 W). The plasma conditions were varied and these conditions were found to be optimal for reversible bonding of the PDMS stamp to the FET substrate. The stamps were then placed in deionised water and used within 10 minutes.

The soft lithography deposition procedure took place in a dark, closed container. The general procedure for MIMIC is illustrated in figure 9.2. A PDMS mold is placed on a substrate surface, in order to form a network of empty channels between them. A drop of fluid is placed at the open end of the channel and it spontaneously fills the channels by capillary action.

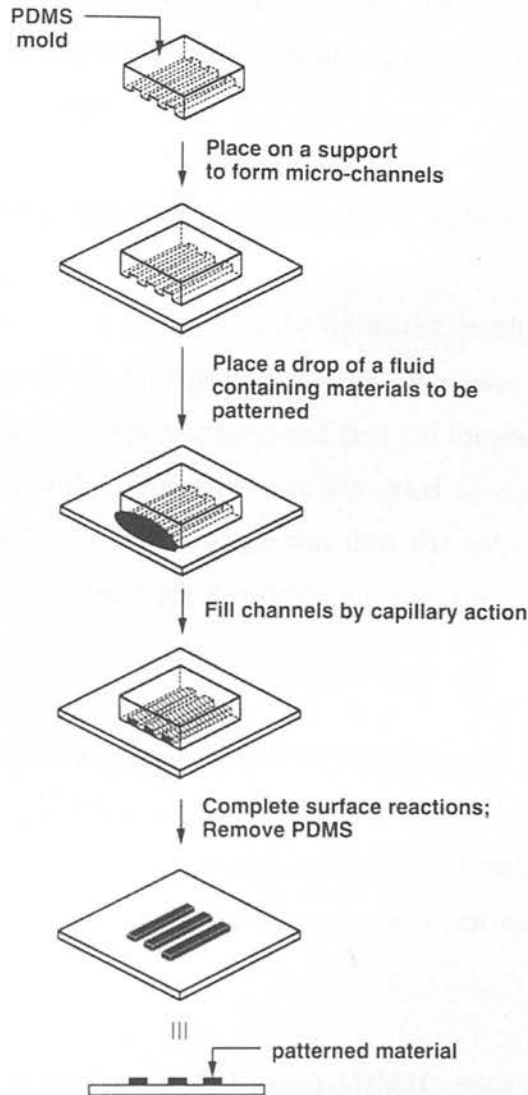


Figure 9.2: Schematic of the procedure used in MIMIC (Kim et al. 1996).

After the material in the fluid has cured, crystallized, polymerised, adsorbed or reacted with the substrate surface, the mold is removed and a pattern of the material remains on the substrate surface. Thus the pattern of the master is formed in the material on the substrate surface.

Initially the standard MIMIC procedure was copied exactly, apart from using the FET substrate rather than a glass substrate. Unfortunately, there was major leakage in

between the channels due to the uneven FET substrate topography, preventing a good seal between the PDMS and the substrate. The devices were probed and there was no measurable conduction.

#### **9.2.5 Deposition system 1: Enhanced-MIMIC at 60 °C (MIMIC at 60 °C)**

So the procedure was repeated with the following developments. The MIMIC procedure was repeated at 60° C. This procedure took place over 20 hours, and 1 ml ICAT drop was renewed 3 times (every 2 hours) and then left for another 6 hours and one more drop of solution was added. The film was not dried to completion, when the stamp was removed under DMF. The substrate was then washed in ethanol and dried in nitrogen. The substrate was heated for 2 minutes in the oven at 90° C, allowed to cool under nitrogen.

The ICAT films were probed immediately (results next chapter) and inspected under the optical microscope. They were then stored in a closed container in the dark throughout the month testing period. A thorough assessment of the film morphology and electronic properties on all areas of multiple substrates was performed. No major leakage between the channels occurred.

#### **9.2.6 Deposition system 2: Enhanced-MIMIC with applied pressure (MIMIC at room temperature)**

Another method to reduce leakage between channels, without raising the deposition temperature, was investigated. Light pressure (gentle clamping) on the PDMS stamp during the procedure was found to ensure a good seal between the PDMS and the FET substrate. (Too much pressure collapsed the channels).

The experimental procedure, as described above, was then repeated at room temperature. However, the procedure was carried out over 4 days and on the second and third day the

ICAT solution was renewed at the channel entrance. On the fourth day the stamp was removed under DMF, before the ICAT film had completely dried.

### **9.2.7 Deposition system 3: Immersion coating**

The substrate was immersed in ICAT solutions for 2, 3, 6, 10 and 21 days and then removed and washed thoroughly in DMF and ethanol. The substrate was dried under nitrogen and placed in the oven for 2 minutes at 100° C. The substrate was probed and stored as previously stated. This time however, the film morphology was inspected with the SEM. Selected substrates were functionalised with HMDS SAMs, before immersion coating (procedure in chapter 7).

### **9.2.8 Deposition system 4: Enhanced-drop casting**

The FET substrates (chip 2) were functionalised with an ICAT SAM (detailed chapter 7). Then the chip surface was covered with the ICAT/DMF solution overnight, in a closed container. 18 hours later (before the film was completely dry) the substrate was washed thoroughly with DMF and ethanol. The substrate was dried under nitrogen and another drop of ICAT solution was placed on the substrate and the process was repeated and washed, dried and tested with the standard procedure.

## **9.3 MIMIC results and discussion**

### **9.3.1 Deposition system 1: MIMIC at 60 °C results**

These devices were produced by depositing line patterns (dimensions approximately 100  $\mu\text{m}$  in width, 4 mm length, with 100  $\mu\text{m}$  gap in between the lines of film) of the ICAT film onto FET substrate one.



The active channel, (the gap between the source and drain electrodes), in the bottom contact configuration, is schematically depicted in figure 9.3. To allow charge transport in this device configuration the organic semiconductor film is required to bridge the active channel preferably with no ruptures. It is not necessary for the organic semiconductor layer however, to bridge the vertical walls of the source and drain electrodes completely, as it has been demonstrated that an organic layer which is only a few molecular layers thick will suffice (Allem et al. 1997 and Dodabalapur et al. 1995).

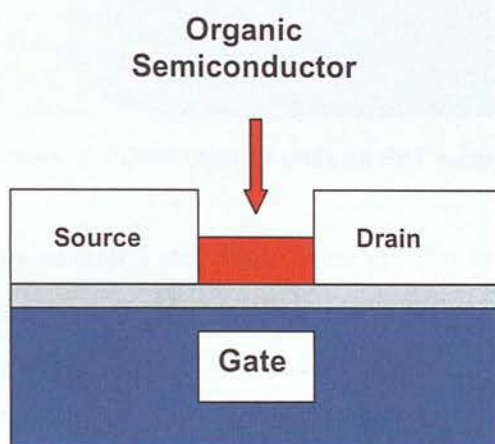


Figure 9.3: Bottom contact device configuration where the red coloured area represents the organic semiconductor deposited in the active channel. The grey coloured area is the dielectric layer.

The ICAT line pattern only spanned approximately a third of the actual PDMS channel length (length 1.5 cm) but filled the channel width (100  $\mu\text{m}$ ). The film height was not measured accurately but approximately filled the channel height (2  $\mu\text{m}$ ).

Each line of film successfully bridged the active channels (channel width between 2 and 6  $\mu\text{m}$ , in increments of 1  $\mu\text{m}$ ) of several electrode sets on each chip, so as to allow a thorough assessment of electrical properties of the ICAT film. There was a 100  $\mu\text{m}$  gap in between each line of ICAT film and there was no measurable conduction in these areas, indicating no major leakage in the patterning deposition.

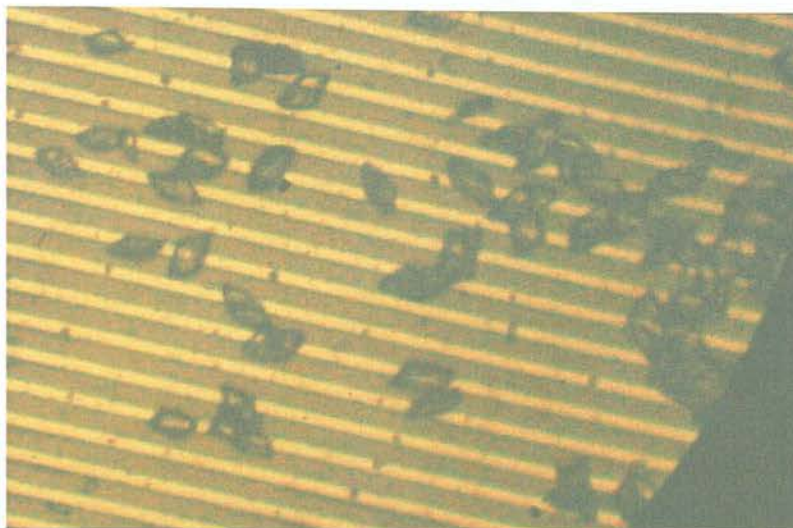


Figure 9.4: ICAT crystals at PDMS channel ends on FET substrate, (of channel width  $2\mu\text{m}$ )

Optical microscopy revealed the ICAT lines of film to be continuous, homogeneous, dark green in colour and slightly transparent. The films appeared to be polycrystalline but were so dense and dark in colour it was difficult to image the film microstructure. The films did have large indentations in but the films still bridged the electrode channels. However, at channel ends there was a deposit of material which was not densely packed which was easier to image. These deposits were ellipsoid shaped dark green crystals, which were larger than the electrode channel width ( $2\mu\text{m}$ ), as illustrated in figure 9.4. The ICAT film here was polycrystalline but the crystals bridged the electrode channel so these devices can be regarded as single crystal devices. The film patterning and morphology were reproducible.

### 9.3.2 Deposition system 2: MIMIC at room temperature results

These devices were produced by depositing line patterns of the ICAT film onto FET substrate two through MIMIC at room temperature.

The ICAT film was successfully deposited in line patterns with widths of  $1\text{mm}$ ,  $100\mu\text{m}$  and  $2.5\text{ cm}$  length. The ICAT line pattern spanned the entire PDMS stamp channel



length (approximately length 2.5 cm) with no major leakage between the PDMS channels (the areas in between the channels showed no measurable conduction). The film height was not measured accurately, but a side profile was viewed through the SEM and optical microscope, and the films did bridge the electrode channels easily (approximately 1  $\mu\text{m}$ , had a uniform thickness and they were much thinner than those deposited using MIMIC at 60°C, which had approximately filled the full channel height (2  $\mu\text{m}$ ).

Optical microscopy revealed that these films were structurally completely different to the films produced through MIMIC at 60°C, as illustrated in figure 9.5.

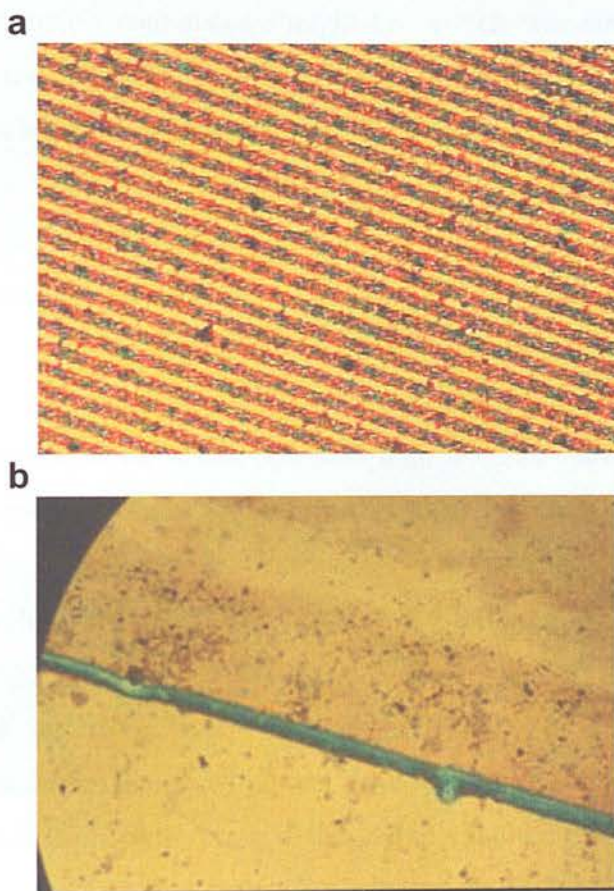


Figure 9.5: Optical microscope images showing a typical ICAT film deposited on (a) the electrodes where the active channel widths are 2  $\mu\text{m}$  and (b) the film changes when the PDMS stamp was clamped with uneven pressure during the deposition process, where the line width is approximately 130  $\mu\text{m}$ .

These films were light brown in colour, continuous in nature (no ruptures) and did not have any crystals formed at the channel ends. At higher magnification, it was observed that the brown amorphous film had tiny dark green crystalline areas dispersed throughout the active channel area, some of which, bridged the electrode channels (figure 9.5a) and some of which aligned at the aluminium electrode/gate interface. The film patterning and morphology were reproducible.

In an early experiment an interesting green crystalline edge effect occurred when uneven pressure was applied to the PDMS stamp during the deposition procedure, (raised pressure was applied parallel to the channel length), as seen in figure 9.5b. The crystalline area formed a continuous straight line which was surprisingly uniform in width and height. It would be interesting to further investigate phase control (amorphous or crystalline) as a result of applied pressure, during the MIMIC procedure on the FET substrates.

### 9.3.3 MIMIC deposition discussion

The ICAT film morphology, microstructure and substrate coverage is discussed in relation to the deposition procedure and also how it could influence device activity. Some of the science behind the actual film formation has been discussed in previous chapters. However, it is necessary to include here the basic scientific reasoning behind the deposition developments and the high quality ICAT films.

The experimental objectives were fulfilled. The two MIMIC based depositions successfully directed film growth within the PDMS channels (with widths ranging from 100  $\mu\text{m}$  to 1 mm). Both films bridged the active channel gap. The two techniques produced well controlled, reproducible continuous films with two different morphologies on the substrates. There was also a film thickness difference between the two techniques. The films produced at room temperature consistently spanned the entire length of the PDMS channel unlike those deposited at 60 °C, which only spanned

approximately a third of the channel length. The far superior control over the length of the patterned lines with the room temperature deposition is desirable when patterning microstructures on electronic substrates. The developments to the original MIMIC technique did drastically improve the film quality.

The high quality of the films is a complex matter. The solvent and concentration choice for the ICAT solution were optimised (with regards to substrate wetting and ICAT solvation), earlier in the thesis. The strong ICAT-substrate interaction and favourable solvent wetting properties with the silanol groups on  $\text{SiO}_2$  dielectric should be extremely similar to the ICAT and solvent interactions with the silanol groups on the glass substrates (chapters 7 and 8) and are discussed previously. The interfacial assembly here is expected to be similar to the well ordered (including H-bonded, directed, edge-on molecular interfacial orientation) assembly observed previously on the  $\text{SiO}_2$  (glass surfaces). The ordered interfacial alignment, (as seen in chapter 7), should maximise  $\pi$ - $\pi$  overlap between ICAT molecules and minimize traps and scattering centres (Garnier et al. 1993). Well ordered interfacial assemblies can have a positive influence on the bulk morphology and are essential in these devices, as the first couple of organic molecular layers at the gate/organic semiconductor interface can dictate OFET device output (Allem et al. 1997 and Dodabalapur et al. 1995). Finally the synthesis here produced a very pure ICAT yield which enabled single crystal devices and ordered film morphologies.

The refinements to the standard MIMIC technique included performing the procedure at two different temperatures and stamp removal under solvent before the film had dried to completion. The reasons why the enhanced-MIMIC technique worked here are as follows. The polar solvents used here had a high affinity for both the silanol covered substrate and the oxygen plasma treated-PDMS stamp, which meant that the solution tended to fill the PDMS channels. The uniform, continuous nature of the film was made possible through stamp removal before complete solvent evaporation had taken place. When dried to completion ICAT was deposited in ring patterns and along the PDMS



channel edges. Also no major leakage between patterned areas, may be partially attributed to minimised solution leakage through stamp removal under solvent. In this work, the gradual solvent evaporation rate (DMF boiling point 153° C) at both 60 °C and room temperature, which was further retarded through the PDMS channel walls and narrow openings at the channel ends, should contribute to the overall film order. The PDMS stamp needed to be clamped to the substrate at room temperature, (or major leakage occurred), but not when performed at 60 °C. The longer procedure time at room temperature meant that the reversible bond between the PDMS and silanol surface had time to reverse and weaken the seal. Also the faster evaporation rate for MIMIC at 60°C led to a more viscous liquid state in a relatively short time, which was less likely to run under the stamp during deposition.

The MIMIC deposition at 60 °C produced a polycrystalline film, which is highly sought after, as they are regarded as practically useful in devices (Katz et al. 2000). However, the crystals bridged the electrode gaps (2 µm) (figure 9.4) so the device may be regarded as a single crystal device, which tend to have superior mobilities to those of polycrystalline OFETs (Katz et al. 2004 and Podzorov et al. 2003). The large size and crystalline nature of the grains (> 2 µm) is desirable for efficient OFET charge transport, as grain boundaries and defect densities in organic films tend to act as scattering centres and charge traps (Bao et al. 1997 and Laquindanum et al. 1998). In any case the ordered polycrystalline structure and uniform continuous film microstructure should again contribute to charge mobility (minimising deep traps and enhancing oxidative stability). It has been observed previously that the smoothest and best performing organic semiconducting films as part of OFET devices were solvent cast at moderately elevated temperatures (50-60 °C) (Katz et al. 1999 and Laquindanum et al. 1998). The scientific reasoning here is not yet resolved, but it was postulated that this might be because in the absence of single crystal morphology the multiple nucleation that occurs during growth leads to a more even distribution of material at higher temperatures, especially in the first few monolayers.

MIMIC at room temperature also produced uniform, continuous films with no ruptures (again minimising deep traps and enhancing oxidative stability) but these films were amorphous, interspersed with tiny dark green crystalline areas, (some of which bridged the active channel-width  $2\text{ }\mu\text{m}$ ) (figure 9.5). The mixed phase morphology (interfaces can act as traps or scatter centres) can be detrimental to mobility. In an early experiment the crystalline edge effect (figure 9.5b), which formed a continuous perfectly straight line parallel to the channel length, as a result of applied pressure at the side of the PDMS channel was an interesting result. To my knowledge phase control, (in such a well directed manner), has not been demonstrated before with MIMIC.

## **9.4 Immersion coating and enhanced-drop casting results and discussion**

### **9.4.1 Deposition system 3: Immersion coating results**

FET substrate one was immersion coated with ICAT. Although film thickness was not accurately measured, the film profiles were inspected with the SEM. All films successfully bridged the electrode channel easily, appeared to have a smooth surface and the film thickness increased with dipping time.

These films were all amorphous (brown in colour), apart from a very limited number of dark green crystalline areas sparsely dispersed on top of the gold source and drain electrodes only. The number of crystalline domains increased with dipping time, (ranging from 12 hours to 2 weeks dipping time), but even after 2 weeks they were only very few crystalline areas, which had grown only on top of the source and drain electrodes and not in the active channel).

Figure 9.6 shows the scanning electron micrographs of the gate/gold electrode interface (substrate 1) of the blank substrate (a) and immersion coated (3 day) films deposited on

the untreated substrate (b) and on the HMDS-functionalised substrate (c). Figure 9.6 illustrates that there is an ICAT film on both substrates. The film on the untreated substrate is homogeneous, continuous, with no voids and structurally the same at the interface and in the active channel. There are crystalline areas very sparsely dispersed on top of the gold electrode. These crystalline areas however, should not interfere with charge flow, as it is the vertical wall (edge) of the gold electrode (rather than the top) adjacent to the gate that influences the charge flow in this device configuration (Katz et al. 2000).

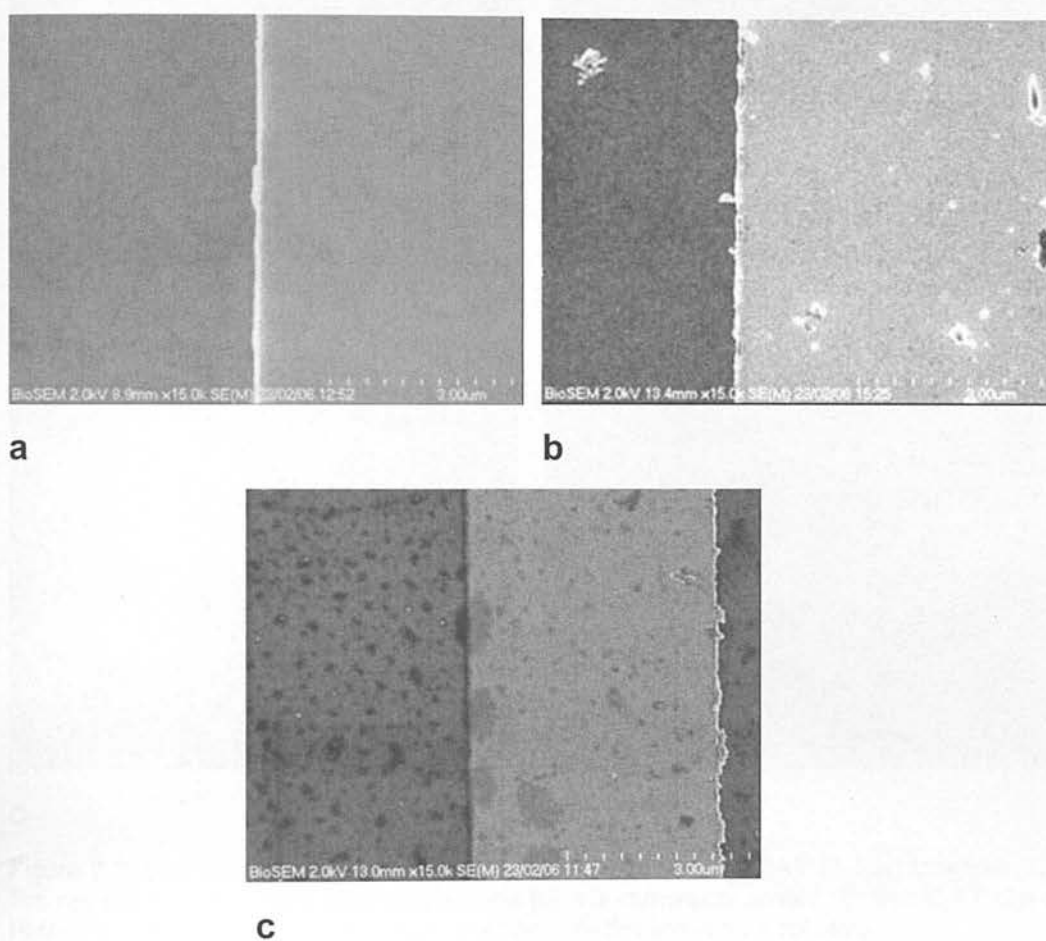


Figure 9.6: The scanning electron micrographs of the gate/gold electrode interface (substrate 1) of (a) the blank substrate and (b) the immersion coated (3 day) ICAT film on the plasma cleaned substrate and (c) the immersion coated (3 day) film on the HMDS-functionalised substrate. The darker half of each image (on the left side) is the gate and lighter half is the gold electrode. The active channel here (for b and c) is located in the dark area. (DMF was used here as the immersion solvent).

The ICAT film microstructure on the HMDS-treated substrate was quite different to that of the film on the untreated substrate. This film was full of irregular sized indentations (diameters up to several hundred nm), including holes at the gate/gold interface. It was not clear from the SEM micrographs whether these ruptures spanned the whole way through the film to leave exposed substrate or if they were just peripheral holes in the film surface. The film was homogeneous with no crystalline domains.

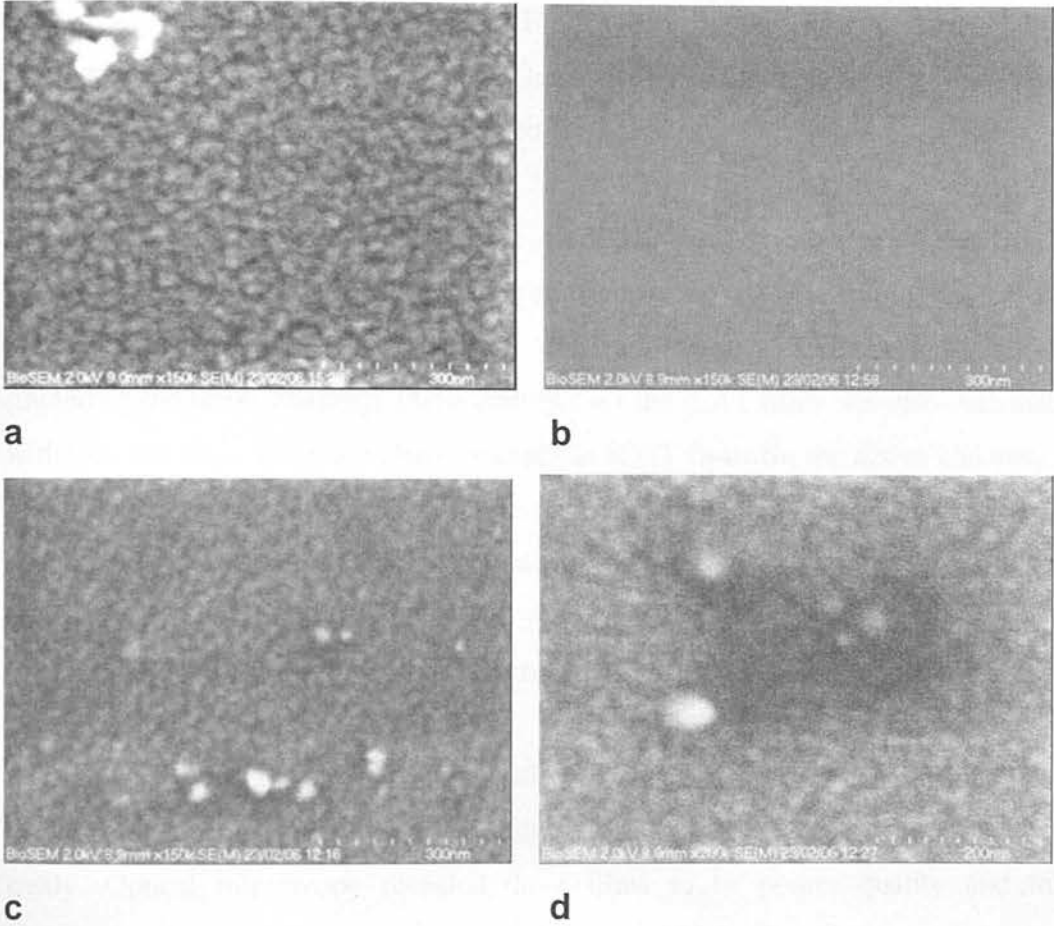


Figure 9.7: Scanning electron micrographs of the gate with (a) ICAT (3 day) immersion coated film on, (b) the blank gate and both (c) and (d) the immersion coated (3 day) ICAT film on the HMDS-functionalised gate. (DMF was used here as the immersion solvent).

The active channel ICAT morphologies were then imaged at a higher magnification with the SEM, as illustrated in figure 9.7. The film on the untreated substrate (figure 9.7a) consisted of a continuous coating of closely packed nanoparticles (with no ruptures),

with a smooth surface. The particles appeared to be narrowly dispersed, spherical in shape and approximately 30 nm in diameter. The ICAT film in the active channel was probed in several areas on each substrate and it appeared amorphous with no crystalline domains. The ICAT films on the HMDS-treated substrate (figure 9.7c and d) were also particulate, with closely packed particles of a similar size to those deposited on the untreated substrates. The particles were still roughly the same size, apart from a very limited quantity of larger sized particles (with diameters less than 80 nm) dispersed throughout the film. The voids in the film (figure 9.7d) did not penetrate all the way through the film. The film surface was less smooth (with these shallow indentations) than the ICAT film grown on the untreated substrate.

Selected substrates were immersed for elongated periods of time (up to 21 days) producing thicker ICAT films (very approximately  $1\mu\text{m}$ ), with a substantial increase in number the crystalline domains which were now dispersed all over the substrates (including the active channel). Phase control over the ICAT films was also demonstrated with this technique as single phase amorphous ICAT films (in the active channel) were produced with short and medium dipping times and crystalline domains in the active channel appeared at very long dipping times

#### **9.4.2 Deposition system 4: Enhanced drop-casting results**

These devices were produced by depositing an ICAT film onto FET substrate two through enhanced-drop casting. These films were thick enough to bridge the electrode easily. Optical microscopy revealed these films to be poorer quality and thicker (approximately  $1.5\text{-}2\mu\text{m}$ ) than the immersion coated films. The film was continuous but the surface was not smooth and the film thickness varied. (More specifically mainly one film thickness but with large areas of (deep) pits in the film (approximately 40 % of substrate covered in large pits). The film microstructure appeared to consist of single amorphous phase (no green crystalline areas). It is important to note that these films



were far superior to those prepared earlier through basic drop casting which produced random unconnected aggregates rather than a continuous film.

### 9.4.3 Immersion coating discussion

The experimental objectives were fulfilled. All films bridged the active channel gap. The immersion coating techniques produced well controlled, reproducible, continuous, smooth, single phase films with two different morphologies on the substrates (figure 9.6 and 9.7). At higher magnification it was observed that the films consisted of closely packed spherical nanoparticles with a narrow dispersity (figures 9.7). Film thickness was controlled with immersion time. Phase control was demonstrated as a function of immersion time. Short dipping times (2-10 days) consistently produced amorphous ICAT films, while prolonged dipping times (21 days) produced a mixed amorphous and crystalline morphology in the FET active channel. Enhanced drop casting produced continuous single phase films, but with a rough surface with extensive pits in. Still these films were far superior to those prepared earlier through basic drop casting which produced random unconnected aggregates rather than a continuous film.

The discussion now focuses on the superior immersion coated films. Again the continuous film microstructure and single phase morphology should enhance oxidative stability and mobility, as thermally activated trap limited transport is limited by traps at boundaries and chemical or physical defects (Chesterfield et al. 2004 and Shirota et al. 2007). The reasoning behind the ordered film assembly on SiOH terminated substrates is discussed earlier (well ordered edge-on ICAT alignment at ICAT/SiOH interface etc).

HMDS-functionlised gates have been demonstrated to improve OFET activity (Chau et al. 2005). This was attributed by some researchers to HMDS inducing favourable structural changes in the organic semiconductor film (Garnier et al. 1993 and Sirrinhaus et al. 1999) and by another researcher to HMDS not trapping electrons, like the electronegative hydroxyl groups on the untreated silanol covered gate (Chau et al. 2005).

It was established in chapter 7, that ICAT formed clusters at the HMDS-functionalised  $\text{SiO}_2$  interface which were interpreted as stacks of molecules with the ring system parallel to the substrate. Again a similar assembly is expected here, as HMDS was deposited in the same manner as chapter 7 on a  $\text{SiO}_2$  dielectric, which is structurally very similar to the chapter 7 glass substrate. Parallel alignment of the organic ring structure in the first few molecular layers to the gate surface has been demonstrated to improve OFET output, which would be interesting to test here (Garnier et al. 1993 and Sirrinhaus et al. 1999).

The HMDS-treatment altered the bulk ICAT film morphology on the devices (as compared to the ICAT film morphology on the unfunctionalised FET substrates) in the following manner (figures 9.6 and 9.7). These ICAT films still consisted of closely packed (approximately 30nm) nanoparticles (but now with slightly broader size dispersity) and the film surface was less smooth with shallow pits. The uneven surface and pits in the film can act as scattering centres and charge traps, which would increase contact resistance and reduce the oxidative stability (Chesterfield et al 2004 and Jones et al 2008). Also the slight variation in particle size could influence how reproducible the electronic properties were in the device. Despite the uneven film surface, the film quality was still far superior to that of other commonly used solution based deposition techniques (Dimitrakopoulos et al. 2001, Katz et al.2000, Katz et al. 1999, Katz et al. 1998 and Laquindanum et al. 1998).

These films consisted of closely packed nanoparticles. The particulate film microstructure is now discussed in terms how it may influence device performance. Initially there was a line of argument that devices performed better with films with larger grains, than films with a large number of small grains with many grain boundaries that form trapping sites (Horowitz et al. 2001). Studies suggested that the movement of charge carriers through a trap dense system is impeded by scattering at these traps and momentum transfer of the carriers to photons in the crystal. It was believed that this scattering, and its nonlinear relation to the electric field, accounts both for nonlinearity at

the origin in IV plots and lower effective mobility (Kymissis et al. 2001) However, researchers have since demonstrated that a highly connected, fine grain morphology results in far superior device behaviour than larger grains even with fewer boundaries, as inter-grain contact does not impose a substantial series resistance (Bao et al. 1997 and Laquindanum et al. 1998). In the limiting case of grains separated by empty space, the boundaries are catastrophic, because of the resistance of the voids. So the highly connected small (30 nm diameter) grain structure produced here is regarded as optimal for FET activity. Another major advantage of densely packed structures (particularly to n-type FETs) is that they have been shown to have far greater oxidative stability than structures with lots of voids (Bao et al 1998 and Katz et al 2000a).

## 9.5 Conclusion

The experimental objectives were fulfilled. A range of film morphologies were produced. The well controlled, reproducible, continuous film growth demonstrated with these simple, cheap, solution based techniques is far superior to that of the most commonly used solution deposition techniques (Dimitrakopoulos et al. 2002, Katz et al. 2000, Katz et al. 1999 and Laquindanum et al. 1998). The films produced here were homogeneous with no ruptures and many of them were single phase with uniform thickness. Phase control and film microstructure control were demonstrated here as a function of deposition conditions, which is again highly sought after and unusual with solution based depositions.

## **Chapter 10**

### **ICAT semiconducting properties**

## 10.1 Introduction

In chapter 9, a range of enhanced solution based deposition methods were applied to deposit ICAT onto FET substrates, resulting in films with four different morphologies. The electronic properties of these films are investigated in this chapter. The devices were probed to determine the electronic properties of the ICAT films, if the electrical outputs were consistent on different areas of the chips and how the films behaved in air. Also, through testing each device, with the four different ICAT film morphologies, it should be possible to provide insight into the semiconducting organic film morphology/property relationship. Finally, some post device production treatments were investigated to attempt to enhance device activity in ambient conditions, to determine the device suitability for chemically sensitive OFET applications and to further our understanding of these ICAT-based OFETs. Ultimately, the results should contribute towards understanding ICAT properties of which little is known, and the organic film structure/property relationship, which is complex and is not as yet understood. These results should help to determine whether the ICAT film electronic properties can be tailored through the film deposition technique and which ICAT films are suitable for organic electronic applications.

This device configuration is not ideal for use with organic semiconductors, but is commonly used for convenience sake (standard configuration, which can be applied to a wide variety of semiconductors) to investigate basic properties and determine their suitability for electronics applications. Certainly the defining step of OFET production is the organic semiconductor deposition, so once even a weak (non-ideal) reproducible semiconductor response is demonstrated with this substrate, it is easy to transfer the film to a more appropriate FET substrate to perfect device activity.



## 10.2 Experimental methodology

The OFETs chips are used from the previous chapter, so the device configuration, fabrication and thin film deposition is described there. The two chips used were identical apart from chip 1 had gold source and drain electrodes and backside, while chip 2 had aluminium source and drain electrodes and backside.

The ICAT film morphologies are briefly summarised here. Mimic at 60°C produced green polycrystalline films, with crystals that bridged the active channel, and MIMIC at room temperature produced brown amorphous films with had tiny dark green crystalline areas, dispersed throughout the active channel area. Immersion coating produced single phase films, consisting of closely packed nanoparticles, with crystalline deposits appearing at extended immersion times. Enhanced drop-casting produced amorphous films with (no green crystalline areas) and very rough film surfaces.

### 10.2.1 Electronic characterisation of ICAT films.

Devices were probed immediately after ICAT film deposition. The electronic properties of these devices were probed with a HP-4156B analyzer in the dark, at room temperature, in ambient conditions, unless otherwise stated. Blank substrates with no organic film and substrates exposed to the solvents involved in the thin film procedure were also probed. Initially the blanks and solvent exposed substrates produced no measurable conduction. After 4 weeks the substrates with gold electrodes (exposed to ethanol) started leaking pA and the device backing had become patchy. After that point all the devices were fabricated using the substrates with aluminium electrodes.

Electrical characterisation of the devices was carried out as follows. Initially a source-drain voltage ( $V_{ds}$ ) sweep was applied to the device ranging from -1.0 V to +1.0 V, at each  $V_{ds}$  a gate voltage ( $V_g$ ) ranging from -1.0 V to +1.0 V was applied in increments of 200 mV. Then a broader  $V_{ds}$  scan ranging from -5.0 V to +5.0 V with a spacing of

100 mV was applied, at each  $V_{ds}$  sweep, the  $V_g$  voltage was altered from -5.0 V to +5.0 V in increments of 1 V. The variable order was then altered with the  $V_g$  swept at 100 mV spacing from -5.0 V to +5.0 V and, at each  $V_g$  sweep, the  $V_{ds}$  from -5.0 V to +5.0 V in increments of 1.0 V.

In selected cases broader  $V_{ds}$  and  $V_g$  sweeps were performed. In these cases the initial narrow (-1.0 V to +1.0 V)  $V_{ds}$  sweep was performed before and after each broader sweep to check for damage to the device, and the device was allowed to rest for ten minutes between each reading, to allow for stray capacitance-charging effects from the previous scan. Gate bias stress was minimised through scanning for short times.

Each device was probed in all areas (covering several sets of electrodes) and scans were repeated on several devices to ensure reproducible results. All devices were probed immediately after organic film deposition and then were left in ambient conditions in the dark for a month and probed periodically.

### **10.3 Results 1: Electronic properties of films deposited with MIMIC at 60 °C**

#### **10.3.1 Electronic behaviour in ambient conditions**

All of the devices were tested in ambient conditions in the dark unless otherwise stated. The devices in section 10.3, unless otherwise stated, used substrate 1. Figure 10.1 illustrates the typical IV behaviour,  $V_{ds}$  and  $V_g$  sweep of the FET device, (channel widths between 2 and 6  $\mu\text{m}$ , in increments of 1  $\mu\text{m}$ ) when tested immediately after device production. There was not a major difference between the electronic behaviour on the films deposited on the range of channel widths but a more thorough analysis is required to comment further. Figure 10.1a is a double  $V_{ds}$  sweep, where the  $V_{ds}$  was swept between  $V_{ds} = -5.0$  V to +5.0 V at constant  $V_g$ , between  $V_g = -5.0$  V to +5.0 V in increments of 1.0 V. Figure 10.1b illustrates a single  $V_g$  sweep, where the  $V_g$  was swept

between  $V_g = -5.0\text{ V}$  to  $+5.0\text{ V}$  at constant  $V_{ds}$ , between  $V_{ds} = -5.0\text{ V}$  to  $+5.0\text{ V}$  in increments of  $1.0\text{ V}$ . The IV characteristics were consistent and the current magnitude varied within just over one order of magnitude on all film areas on several substrates, (apart from the ends of the ICAT film lines (that is the end of line furthest away from stamp entrance where the ICAT solution was deposited), which tended to have a significantly lower conductance).

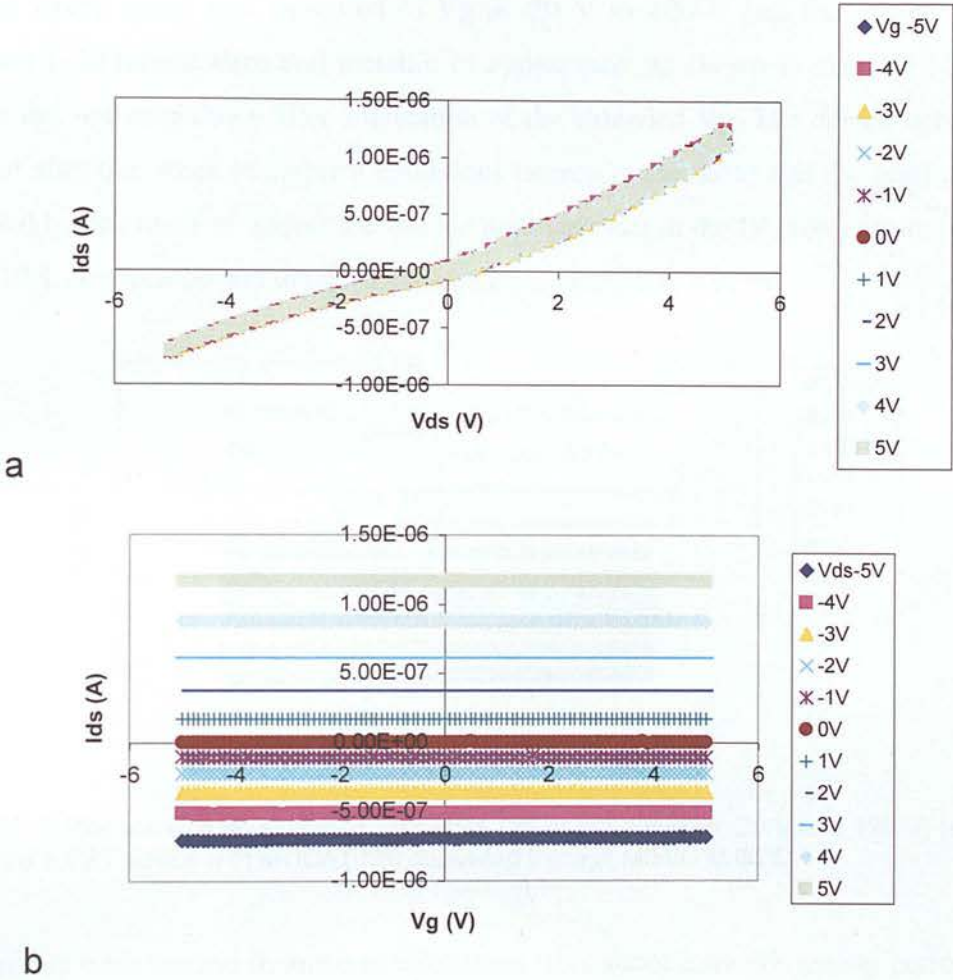


Figure 10.1: Plots showing (a) the  $I_{ds}$ - $V_{ds}$  characteristics ( $V_{ds}$  double sweep) and (b) the  $I_{ds}$ - $V_g$  ( $V_g$  sweep) characteristics of the FET device with an ICAT film deposited through MIMIC at  $60^\circ\text{C}$ .

These IV plots closely resemble that of a metal IV characteristics (nearly ohmic source-drain current ( $I_{ds}$ ) with no field effect and no current saturation) and considering the

narrow voltage probing range a high conductance (Leufgen et al. 2004) (figure 10.1). The resulting  $I_{ds}$  was greater in magnitude upon positive  $V_{ds}$  application as compared to negative  $V_{ds}$  application in all the devices. This behaviour could be attributed to a potential Schottky barrier at any of the junctions in the device or contact resistance but a larger sweep range is needed to discuss this point further.

The  $V_g$  sweep range was increased to  $V_g = -20\text{ V}$  to  $+20\text{ V}$  and the device output remained field-independent and metallic in appearance, as shown in figure 10.2. The devices did not breakdown after application of the extended  $V_g$ . The device behaviour changed after one week in ambient conditions (stored in the dark) and the conductance increased by one order of magnitude and the nonlinearities in the IV plots (asymmetry in figure 10.1 disappeared and the device appeared to operate as a metal.

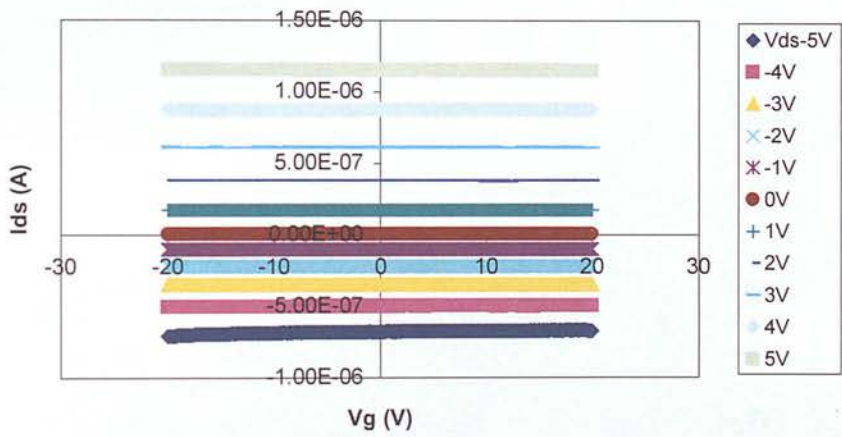


Figure 10.2: Plot showing an extended  $V_g$  sweep ( $V_g$  swept between  $-20\text{ V}$  and  $+20\text{ V}$ ) (double sweep) for a FET device with an ICAT film deposited through MIMIC at  $60^\circ\text{C}$ .

The devices were probed in ambient conditions throughout a month testing period and the IV behaviour remained unchanged after the first week.

### 10.3.2 Electronic behaviour post heat treatment

The device was heated under nitrogen, for five minutes, at  $100^\circ\text{C}$  and allowed to cool under nitrogen to room temperature and then probed and the typical  $I_{ds}$ - $V_{ds}$



characteristics are shown in figure 10.3. This  $V_{ds}$  sweep (using the standard sweep range) shows that the device behaviour changed and exhibited ohmic-like metallic characteristics (linear  $I_{ds}$  with no field dependence and no current saturation), as the previous nonlinearities in  $I_{ds}$ - $V_{ds}$  plot (before the heat treatment, figure 10.1) disappeared. In addition the device conductance was reduced dramatically ( $I_{ds}$  fell by three orders of magnitude).

After heating at 100 °C, for 15 minutes, and cooling to room temperature, under nitrogen, the  $I_{ds}$ - $V_{ds}$  behaviour changed dramatically to that of a n-type semiconductor ( $I_{ds}$  responded to positive  $V_g$ ), as illustrated in the  $V_{ds}$  sweep (with standard sweep range) in figure 10.4. Figure 10.4 illustrates a typical subthreshold n-type response, where the device is operating in unipolar electron accumulation mode (Tapponier et al. 2005).

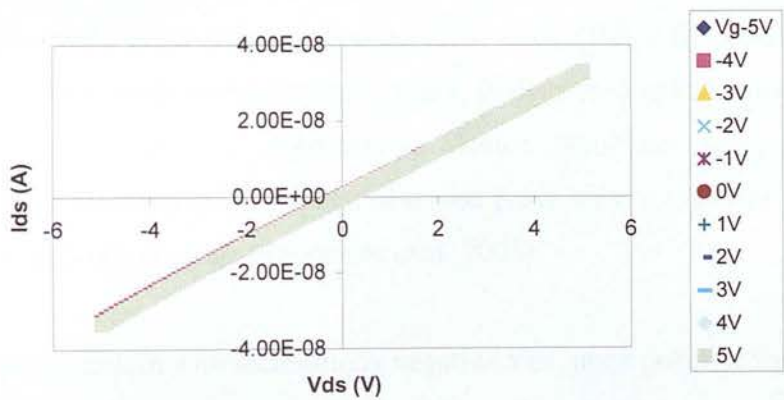


Figure 10.3: Plot showing the  $I_{ds}$ - $V_{ds}$  behaviour ( $V_{ds}$  sweep) of the FET device with an ICAT film deposited through MIMIC at 60 °C, after heating for 5 minutes (100 °C) in nitrogen, and allowing to cool to room temperature under nitrogen.



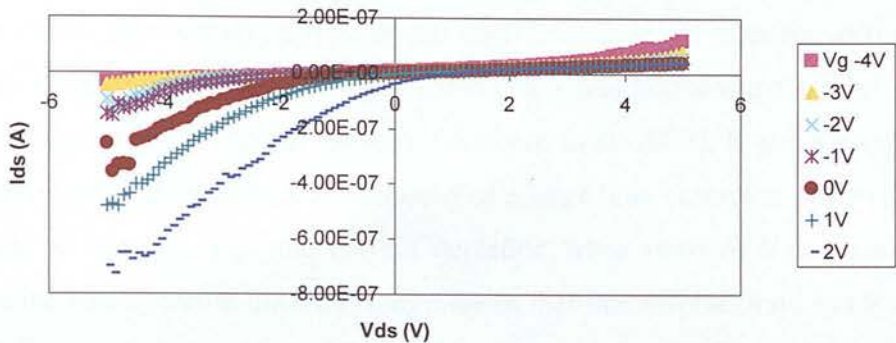


Figure 10.4 : Plot showing the  $I_{ds}$ - $V_{ds}$  behaviour ( $V_{ds}$  sweep) of the FET device with an ICAT film deposited through MIMIC at 60°C after heating for 15 minutes (100°C) and allowing to cool to room temperature in nitrogen, and then left in ambient conditions for 5 minutes.

Here the n-type  $I_{ds}$  produced when  $V_g \leq 5$  V was applied was not great enough to overcome channel resistance. (Thus  $V_g = 5$  V is below the threshold voltage). The combination of the nonlinear IV characteristics with very small currents, no current saturation and no field dependence in forward drain mode ( $V_{ds} > 0$ ) (Deen et al. 2004) and the reverse drain mode features (where  $V_{ds} < 0$ , discussed in following paragraph) observed here are typical of subthreshold device behaviour and very similar subthreshold IV characteristics have been observed previously in a n-type OFET when probed at a similar voltage range (Tapponier et al. 2005).

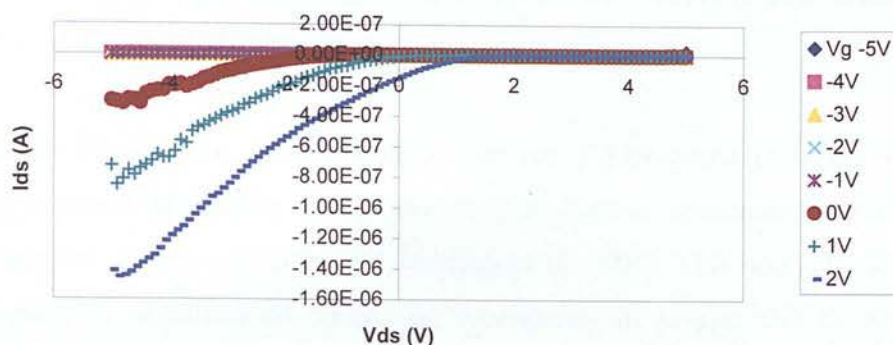
A large increase in current with increasingly negative  $V_{ds}$ , upon positive  $V_g$  application, is observed in the reverse drain mode. This has been observed before in unipolar n-type systems and was attributed to positive  $V_g$ s always inducing electron injection from both the source and negative drain electrode, which resulted in an apparent large increase in the absolute value of the current with negative  $V_{ds}$  (Tapponier et al. 2005).

The fact that no hole injection took place here is confirmed by the current depletion when negative  $V_g$ s were applied (Tapponier et al. 2005 and Tada et al. 2000). This is because when negative  $V_g$ s are applied electron injection at the source electrode is

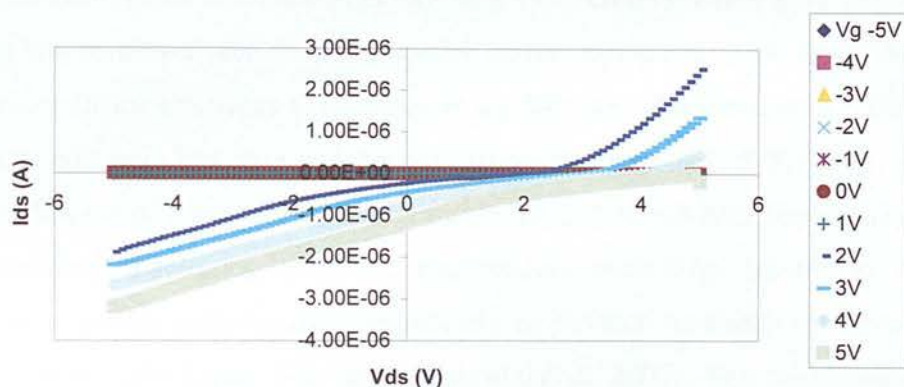
reduced and electrons are depleted from the channel. Negative  $V_{gs}$  are often applied to deliberately deplete the  $I_{ds}$ , to reduce the off currents if the device is operating in n-type depletion mode. Interestingly, a very similar reverse drain mode response to that of this OFET was produced when a p-type OFET based on nickel phthalocyanine was heated to  $100^{\circ}\text{C}$  in vacuum and probed in vacuum (Chaabane et al. 2003). It was a p-type OFET so the reverse drain mode response consisted of a large hole current at positive  $V_{ds}$ , on application of negative  $V_{gs}$  and current depletion when positive  $V_{gs}$  were applied. However, the interpretation differed from mine in that this reverse drain mode response was regarded as evidence of the existence of both n and p-conduction.

The increasing deviation from zero current at  $V_{ds} = 0\text{ V}$ , as a function of increasing gate voltage, may be attributed to leakage currents through the dielectric layer (gate leakage) (Chen et al. 2001). These leakage currents occur frequently in OFETs and typically originate through leakage through the dielectric layer, as a result of pinholes and defects mediated by conduction through a non-patterned semiconductor or gate (Bao et al. 1999a and Unni et al. 2006). This leakage current starts from the gate and passes through the insulator and comes back to the grounded source via the drain. It forms a current that flows from the drain to the source, even at zero  $V_d$ . That is why the sign of the leakage current here is opposite to that of the normal  $I_d$ . This leakage current can be minimized through proper patterning of the gate and/or the semiconducting layer or with a better quality dielectric.

After 10 minutes exposure to ambient conditions the device behaviour had developed further. Figure 10.5a illustrates the  $V_{ds}$  sweep (with standard sweep range) after 10 minutes air exposure. The  $I_{ds}$  depletion response to negative  $V_g$  had substantially diminished in magnitude (by three orders of magnitude), as compared to figure 10.4. Also the reverse drain mode  $I_{ds}$  response to positive  $V_g$  increased and there was a minor increase in gate leakage.



a



b

Figure 10.5: Plots showing the  $I_{ds}$ - $V_{ds}$  behaviour ( $V_{ds}$  sweep) of the FET device with an ICAT film deposited through MIMIC at 60°C, after heating for 15 minutes (100 °C), and allowing to cool to room temperature in nitrogen and then (a) left in air for 10 minutes and (b) 30 minutes.

Figure 10.5b shows the device behaviour after thirty minutes exposure to ambient conditions. The device behaviour had developed significantly since the previous reading. Now at constant  $V_g$  ranging from -5 V to +1 V (in increments of 1 V) all  $V_{ds}$  sweeps yielded an identical, (within 0.2 nA error due to cumulative scanning-capacitance charging effects), extremely small (maximum 0.2 nA)  $I_{ds}$  response, where the device behaved as a resistor (no field effect here). However, the most profound change is that that now a positive  $V_g$  application from  $V_g = +2.0$  V to +5.0 V induced a very pronounced n-type field effect with a very strong positive  $I_{ds}$  response for  $V_{ds} > 0$  V

(forward drain mode). The strong  $I_{ds}$  response to positive  $V_g$  with increasingly positive x-intercepts, in figure 10.5b, is typical of OFET behaviour with some gate leakage (Katz et al. 1998 and Katz et al. 2000a).

The nonlinear electron  $I_{ds}$ , at low  $V_{ds}$ , at positive  $V_g$  observed in figure 10.5b, is incredibly common in OFETs and is attributed to contact resistance and/or contact Schottky barriers (Chen et al. 2004 and Stallinga et al. 2006). This nonlinear  $I_{ds}$  at low  $V_{ds}$  is typical of subthreshold conditions (commonly in n-type OFETs there is a substantial quantity of deep electron traps which have to be filled before the channel can conduct) and tends to rectify when probed at higher  $V_g$ s (Tapponier et al. 2005). Also Schottky characteristics feature commonly in n-type OFETs when gold source/drain electrodes are employed due to the potential barrier against electron injection at the metal/semiconductor interfaces (Takahashi et al. 2005 and Takjenbu et al. 2007). It is important to note here that the nonlinear  $I_{ds}$  feature observed up to 2.5 V  $V_{ds}$ , in figure 10.5b, is indicative of a very small contact resistance and/or Schottky barrier. The use of gold source/drain electrodes in OFETs can produce such large barriers to electron injection as to inhibit n-type activity completely or produce nonlinear  $I_{ds}$  features that expand to significantly higher  $V_{ds}$  values (Takenbu et al. 2007). Also this dielectric type and atmospheric contaminants can push the threshold voltage in some n-type OFETs, so that little or no  $I_{ds}$  is observed below  $V_g = 90$  V (Malefant et al. 2002 and Newman et al. 2004).

These positive  $I_{ds}$  values are very high, considering the applied voltages are below 30 V, which is a very good indication of favourable n-type transport properties (Leufgen et al. 2004, Malefant et al. 2002 and Newman et al. 2004). Despite the gate leakage, these OFETs still presented IV characteristics with linear  $I_{ds}$  (above  $V_{ds} = 3$  V). Obviously an expanded voltage probing range and transferral of ICAT to a more appropriate chip would be necessary here to characterize the IV behaviour fully (typically in n-type OFETs a  $V_{ds}$  sweep range up to 100 V at set  $V_g$  from  $V_g = 0$  V to 100 V in increments of 10 V).



This experiment has demonstrated that the device response is sensitive to heating time under nitrogen. Post heat treatment it was also demonstrated that the device was sensitive to air exposure time. Within 30 minutes of air exposure a negative shift in threshold voltage, (as electron  $I_{ds}$  increased from effectively 0V to around  $1 \times 10^{-6}$  A in the forward drain mode), is observed indicating the atmospheric contaminants are n-doping the device. Interestingly within the 30 minutes air exposure time the initial current depletion response to negative  $V_g$  and the current carried when  $V_g = 0$  V diminished to effectively zero  $I_{ds}$ . Also the heat treatment triggered some gate leakage in the device.

The post-heat treatment device behaviour was totally reversible, when left in ambient conditions. The next day the device exhibited the metallic like behaviour it had exhibited before the treatment, although with increased  $I_{ds}$  magnitude as shown in figure 8.10. This change to metallic behaviour seems logical as the day before a negative shift in the threshold voltage was observed suggesting that the atmospheric contaminants were doping the device.

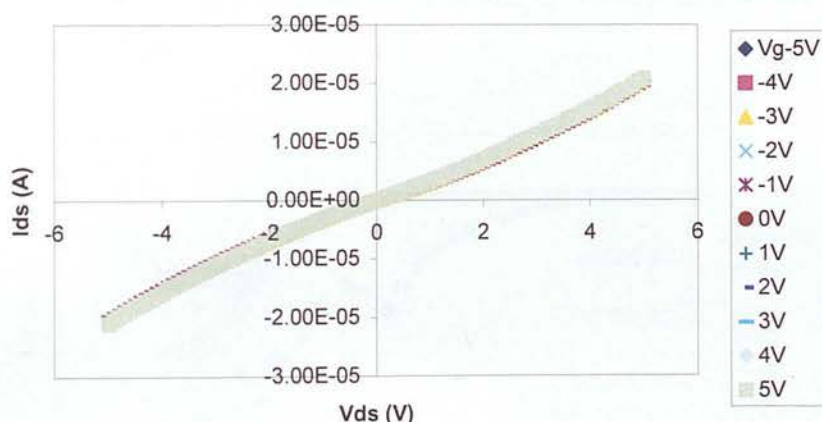


Figure 10.6: Plot showing the  $I_{ds}$ - $V_{ds}$  ( $V_{ds}$  sweep) behaviour of the FET device with an ICAT film deposited through MIMIC at  $60^{\circ}\text{C}$  after heating for 15 minutes and allowing to cool to room temperature in nitrogen and then left in air overnight.

Thus it may be deduced that the device and the ICAT film were not damaged by this heat treatment and that atmospheric doping is reversible with heat treatment.



After one month the blank substrates (substrate 1) were found to be leaking current through the gate, of the order of pA, and so from that point onwards substrate 2 was used.

10.3.3 Electronic behaviour post ethanol treatment

If the metallic device behaviour (figure 10.1) was attributed to the intrinsic conductivity of ICAT, ICAT film morphology, device structure or covalently bonded impurities (deep traps) it would not be expected to respond to ethanol treatment. However, if the metallic nature of the device was due to physisorbed dopants (shallow traps), which would be removed easily with ethanol, then the device should be responsive to the ethanol treatment. The ethanol washing will also remove dust, which would hinder charge transport in the devices. It is important to note here that the device components and ICAT are insoluble in ethanol and it has a low boiling point so it easy to remove.

Figure 10.7 shows a typical  $V_{ds}$  sweep (standard sweep range) of the device after rinsing in ethanol. The behaviour changed from that of a metal to a p-type OFET ( $I_{ds}$  response to negative  $V_g$ ).

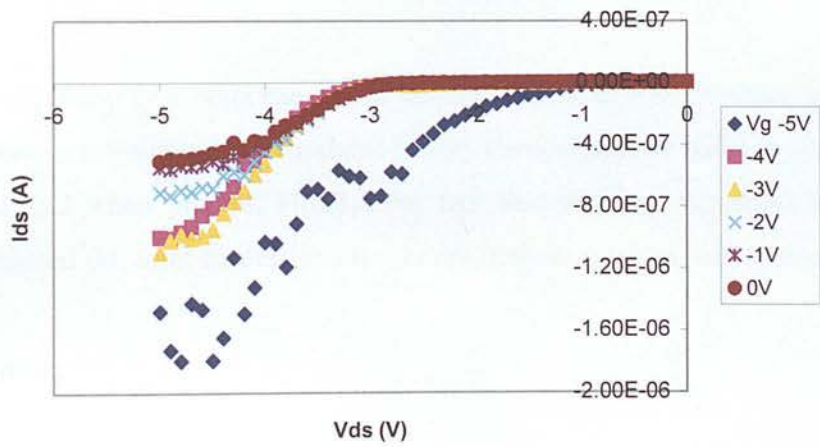


Figure 10.7: Plot showing the  $I_{ds}$ - $V_{ds}$  ( $V_{ds}$  sweep) behaviour of the FET device with an ICAT film deposited through MIMIC at 60°C after rinsing in ethanol.

Unipolar hole (p-type) activity in ambient conditions is observed. The large  $I_{ds}$  output at this limited  $V_g$  range and the fact that the current has a pronounced linear and saturation regime (apart from the nonlinear  $I_{ds}$  feature at very low  $V_{d,s}$  (which is greatly reduced when  $V_g = -5$  V), is indicative of very favourable device transport properties.

The nonlinearities below  $V_d = -3$  V are unlikely to be due to a Schottky barrier at the gold/organic interface, as the gold work function tends to be well matched with the organic semiconductor HOMO, so the feature may be attributed to channel resistance (typically surface states or impurities adsorbed during junction formation or possible reactions between materials contacted). This is a comparatively minute channel resistance feature (here effectively 0 A  $I_{ds}$  up to  $V_{ds} = 3$  V but can extend to  $V_{ds} = 30$  V in other working p-type OFETs) and would be expected to disappear completely at a slightly larger  $V_g$  ( $> 5$  V) (above threshold voltage which is usually relatively small in p-type OFETs), as it greatly diminished upon application of  $V_g = 5$  V (Chang et al. 2000 and Takahashi et al. 2006).

Note the sizable  $I_{ds}$  produced when  $V_g = 0$  V, this infers that the device could operate in depletion mode (Hong et al. 2001). However, this  $I_{ds}$  was reduced substantially through careful control of sweep rate and direction and resting time between scans.

The strong unipolar p-type response in ambient conditions, at a low voltage testing range after the ethanol treatment is a formidable result. Particularly, as these devices were up to one week old when probed. Finally, the fact that the heat treatment and ethanol treatment induced different carrier type responses in these devices is very interesting.

#### 10.3.4 Summary

Before heat treatment the device exhibited metallic-like behaviour, between  $V_g = -20$  V to  $+20$  V, in ambient conditions. The device conductance increased by an order of

magnitude after the first week in ambient conditions and then remained unchanged throughout the rest of the month testing period.

The device was sensitive to heating time and after 15 minutes of heating at 100 °C in nitrogen and subsequent cooling to room temperature the device output changed to that of unipolar enhancement mode n-type behaviour (with gate leakage). The n-type activity was unstable in ambient conditions and the device behaviour reversed overnight back to that of a metal.

After rinsing in ethanol the metallic like device properties changed to that of a p-type, unipolar OFET. This is the first time washing an aged FET chip, (stored in ambient conditions in the dark), in a solvent has been demonstrated to initiate device activity. This result is also exciting as it could lead to the tuning of semiconductor type in OFETs with a facile ethanol treatment. The real breakthrough here is that different carrier type semiconductor device activity (p-type) was realized through this treatment to that of heating (n-type). Although further investigation is required, (n and p activity require different treatments to induce them) ambipolar activity has been demonstrated in this single component device in air at a low voltage probing range which is very rare indeed (Cornil et al. 2007).

## **10.4 Results 2: Electronic properties of films deposited with MIMIC at room temperature**

### **10.4.1 Electronic behaviour in ambient conditions**

The electronic behaviour did not vary significantly with channel width (between 2 and 6  $\mu\text{m}$ ). A more thorough analysis would be required here to comment further. The blank substrates and solvent soaked substrates showed no measurable conduction throughout the month testing period. The devices were sensitive to both scan rate and scan number.

Figure 10.8 illustrates the typical  $V_{ds}$  sweep behaviour, where the  $V_{ds}$  was swept between  $V_{ds} = -5.0$  V to  $+5.0$  V at constant  $V_g$ , between  $V_g = -5.0$  V to  $+5.0$  V in increments of 1.0 V, when tested immediately after device production.

The device output from all the ICAT patterned areas on several substrates was identical ( $I_{ds}$  varied  $\ll$  one order of magnitude). p-type activity ( $I_{ds}$  response to negative  $V_g$ ) is observed and there was no  $I_{ds}$  response on application of positive  $V_g$ . Thus the device is operating in unipolar p-type mode. The hole current ( $I_{ds}$  at negative  $V_g$ s) is relatively large in magnitude, considering the low  $V_g$  and narrow  $V_{ds}$  sweep range (Leufgen et al. 2004). This strong  $I_{ds}$ , clear linear regime  $> -2.5$  V  $V_{ds}$  and distinct field effect at this narrow voltage testing range is indicative of favourable transport properties.

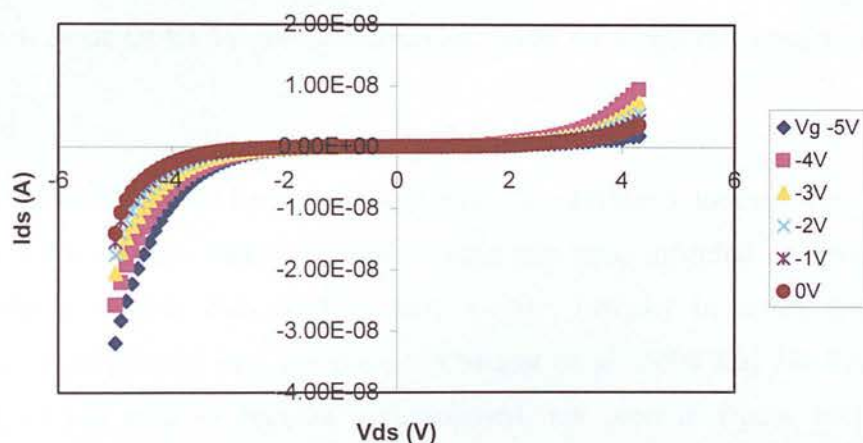


Figure 10.8: plot showing the single scan  $V_{ds}$  sweep  $I_{ds}$ - $V_{ds}$  characteristics of the FET device with an ICAT film deposited through MIMIC at room temperature (day 1).

The nonlinearities at very low  $V_{ds}$  (curve crowding round the origin) is indicative of either a Schottky barrier or contact resistance (Chwang et al. 2000, Leufgen et al. 2004 and Stallinga et al. 2006).

The most probable explanation here for the nonlinearities at very low  $V_{ds}$  is that the low work function aluminium electrodes are forming a potential barrier against hole injection at the metal/semiconductor interfaces. Again it is important to note here that the



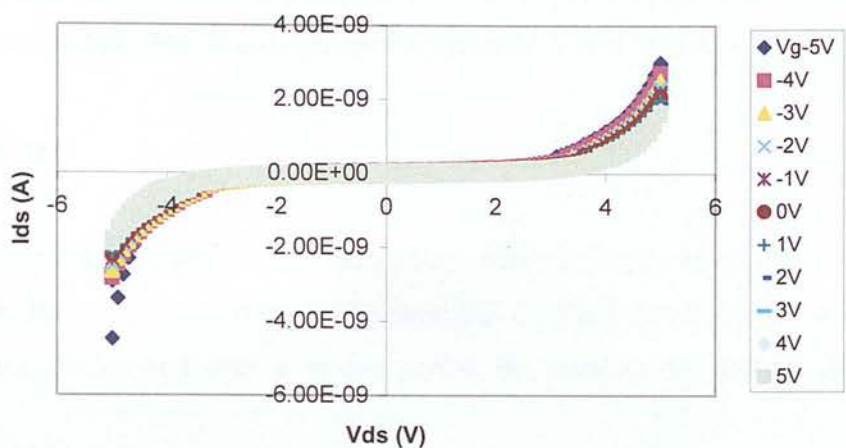
nonlinear  $I_{ds}$  feature at the origin ( $< -3$  V  $V_{ds}$ ) is indicative of a very small contact resistance and/or Schottky barrier. Again this nonlinear  $I_{ds}$  behaviour at low  $V_{ds}$  is typically observed in the subthreshold regime and tends to rectify when probed at higher set  $V_g$ . Note the sizable  $I_{ds}$  produced when  $V_g = 0$  V. This  $I_{ds}$  when  $V_g = 0$  V was reduced substantially through careful control of sweep rate and direction and resting time between scans.

The devices were tested over a month period in ambient conditions. The field effect remained only for one week. Figure 10.9 shows the  $V_{ds}$  sweep characteristics (standard sweep range) after (a) 2 weeks and (b) one month in ambient conditions. The double  $V_{ds}$  scan after 2 weeks air exposure shows slight hysteresis and resembles the IV characteristics of back to back diodes (with a very subtle field effect). In fact nonlinear back to back diode OFET IV characteristics like these are frequently observed (Kudo et al. 1998).

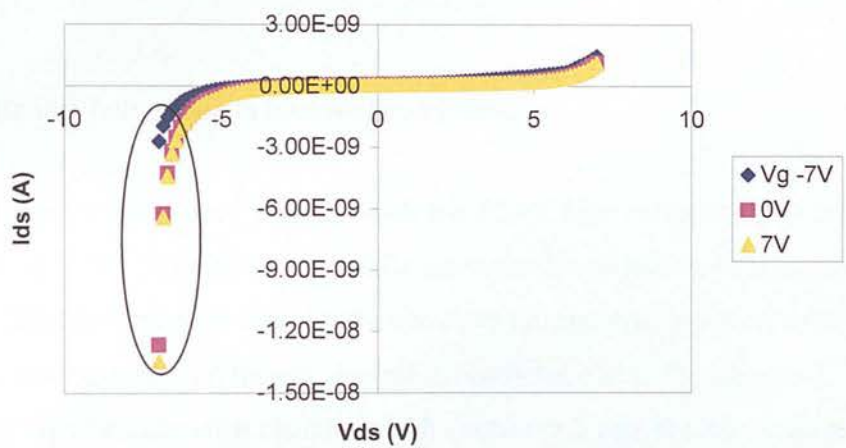
The back to back diode-like output here may be attributed to the two Al/organic interfaces in the device. OFET electrical output has been modeled successfully with standard OFET models with back to back diodes, (usually in series with contact resistances), incorporated into the circuit (Chwang et al. 2000 and Necliudov et al. 2000). IV curves tend to become superimposed, (as seen in figure 10.10a), with increasing contact resistance (Satallinga et al 2006). The formation of aluminium oxide (and the gate oxide increase to a lesser extent) in air will be the major contributor to the increased contact resistance.

Figure 10.9b illustrates the  $V_{ds}$  sweep behaviour, where the  $V_{ds}$  was swept between  $V_{ds} = -7.0$  V to  $+7.0$  V at constant  $V_g$ , between  $V_g = -7.0$  V to  $+7.0$  V in increments of 1.0 V, after 1 month air exposure, which has a very sharp diode-like increase in  $I_{ds}$  at large negative  $V_{ds}$  (tail effect marked by an oval).





a



b

Figure 10.9 plots showing the  $V_{ds}$  sweep  $I_{ds}$ - $V_{ds}$  characteristics the FET device with an ICAT film deposited through MIMIC at room temperature after (a) two weeks in ambient conditions (double scan) and (b) a single scan after 1 month in ambient conditions. The oval (figure 10.9b) marks the tail effect, which was the product of stray capacitance-charging effects from cumulative scanning.

This is the product of stray capacitance-charging effects from cumulative scanning, as when a double scan was performed this tail effect disappeared and the plot looked more symmetrical again like the IV characteristics of back to back diodes (with no field effect

this time despite the expanded  $V_g$  range). Finally there was a decrease in conductance over the month testing period (one order of magnitude over a month).

#### **10.4.2 Summary**

For the first week a strong p-type field effect was observed. After the first week in ambient conditions the field effect disappeared and the  $I_{ds}$ - $V_{ds}$  curves resembled that of back to back diodes and over a month period the conductance fell by an order of magnitude.

### **10.5 Results 3: Electronic properties of films deposited with immersion coating**

#### **10.5.1 Electronic behaviour in ambient conditions**

Substrate 1 was either coated directly with the ICAT film or functionalised first with HMDS, before ICAT film deposition, while substrate 2 was just directly coated with the ICAT film. The devices were found to be sensitive to scan rate and scan number (single and double scans exhibited different electronic characteristics). The electronic behaviour did not vary significantly with channel width (between 2 and 6  $\mu\text{m}$ ). A more thorough analysis would be required here to comment further.

The OFETs (3, 6 and 10 day immersion) were probed all over and the  $I_{ds}$  output that varied <<less than an order of magnitude. The typical electronic OFET output ( $V_{ds}$  sweep), when tested immediately after device production, is shown in figure 10.10. The  $I_{ds}$ - $V_{ds}$  characteristics revealed these devices to behave like resistors with extremely high resistances (approximately 200  $\text{M}\Omega$ ) and no field effect ( $V_{ds}$  swept from  $V_{ds} = -5$  V to +5 V with  $V_g = -5$  V to + 5 V in increments of 1 V). The HMDS-functionalized devices consistently had a resistance of one order of magnitude higher than that of the

devices with no HMDS layer. The devices which were coated in ICAT/DMSO solution also had resistances which were one order of magnitude higher than that of the devices that were coated in ICAT/DMF solution.

When the  $V_{ds}$  was scanned in one direction (standard sweep range) the device appeared to be behaving like a diode with a sharp  $I_{ds}$  increase at  $V_{ds} = -10$  V

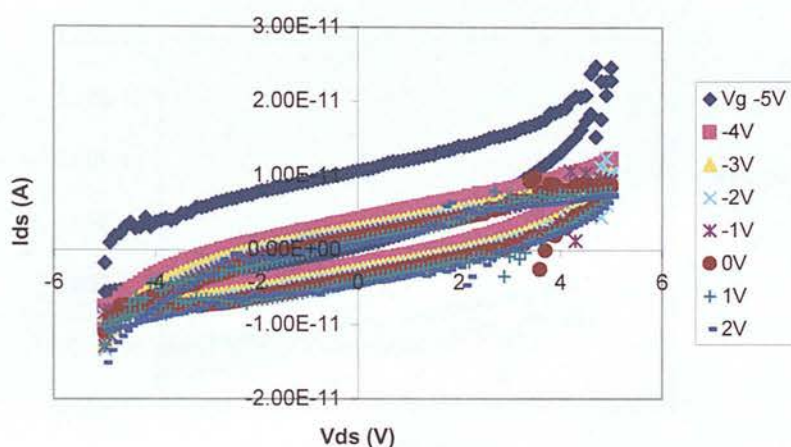


Figure 10.10: plot showing the double  $V_{ds}$  sweep for the 3 day immersion coated OFET (ICAT/DMSO solution) (substrate 1).

but this was not the case and the  $I_{ds}$  tail effect was the product of stray capacitance-charging effects from cumulative scanning. The evidence for this is as follows: the tail-effect moved along the  $I_{ds}$  axis depending on where the  $I_{ds}$  scan started, when the  $V_g$  was held at a fixed potential (between  $V_g = -5$  V to  $+5$  V) and the  $V_{ds}$  was swept in one direction initially there was no  $I_{ds}$  tail-effect and then a tail-effect appeared and increased in magnitude as a result of cumulative scanning and finally when the  $V_{ds}$  was swept in both directions (double sweeps) the tail disappeared, as illustrated in figure 10.10. Figure 10.10 shows a double  $V_{ds}$ -sweep illustrating hysteresis, and after the first scan ( $V_g = -5V$ ) where there is an initial slightly raised  $I_{ds}$  (shallow trapping effects), all the  $V_{ds}$ -scans at the other  $V_g$ s ( $V_g = -4$  V to  $+2$  V) were identical (allowing for



cumulative scanning charging effects). These IV characteristics (high resistance and no field effect) are typical of a trap rich device or subthreshold OFET behaviour.

The devices with the thickest ICAT films with crystalline domains in the active channel deposited (using elongated immersion times) were then investigated. When probed in air immediately after device production these devices exhibited n-type activity, as seen in the  $V_{ds}$  sweep (standard sweep range) in figure 10.11.

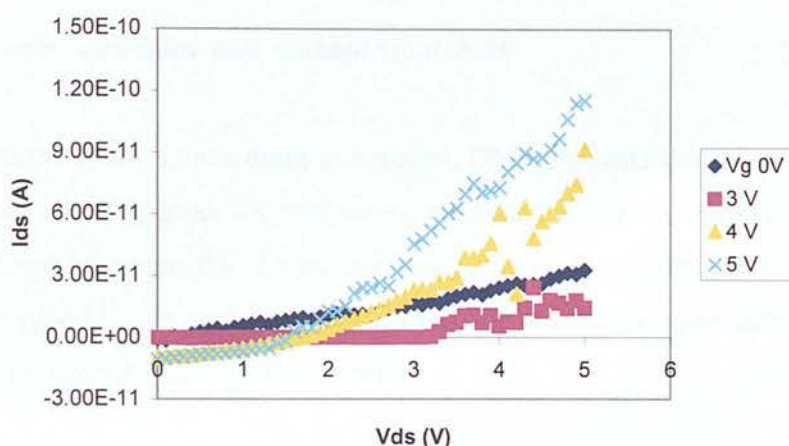


Figure 10.11: plot showing the single  $V_{ds}$  sweep  $I_{ds}$ - $V_{ds}$  characteristics for the 21 day immersion coated OFET (ICAT/DMF solution) (Substrate 2).

When negative  $V_g$ s were applied the current was depleted, which is commonly regarded as confirmation that no hole injection takes place (Tada et al. 2000 and Tapponier et al. 2005). Thus the device is operating in unipolar n-type mode. This clear linear regime  $> -2.0$  V  $V_{ds}$  and distinct field effect at this narrow voltage testing range is indicative of favourable transport properties in these devices. There are some minor leakage currents through the dielectric layer (Chen et al. 2001).

By the second day the device behaviour had changed to the resistor like behaviour, similar to that of the other devices with thinner ICAT films on. The resistance was reduced by a couple of orders of magnitude and the cumulative scanning charge  $I_{ds}$ -tail effect was reduced in size as compared to the devices with thinner ICAT films. Also the

double scans showed no hysteresis, unlike those produced by the shorter dipped ICAT films. The electronic properties were consistent on all areas of the chips.

The devices were tested over a month period and the electronic characteristics remained constant (with the exception of the device described above). The devices made using substrate 1 however, began to show gate leakage (pA range) after 4 weeks thus were then discarded.

### 10.5.2 Electronic behaviour post ethanol treatment

The 3 day coated (gold source/drain electrodes, DMF solvent) device was washed in ethanol. Figure 10.12 illustrates a  $V_{ds}$  sweep (standard voltage testing range) after the ethanol treatment, showing the device behaviour changed significantly from that of a resistor to a p-type FET device. The resistance of the devices dropped substantially (the  $I_{ds}$  increased by several orders of magnitude).

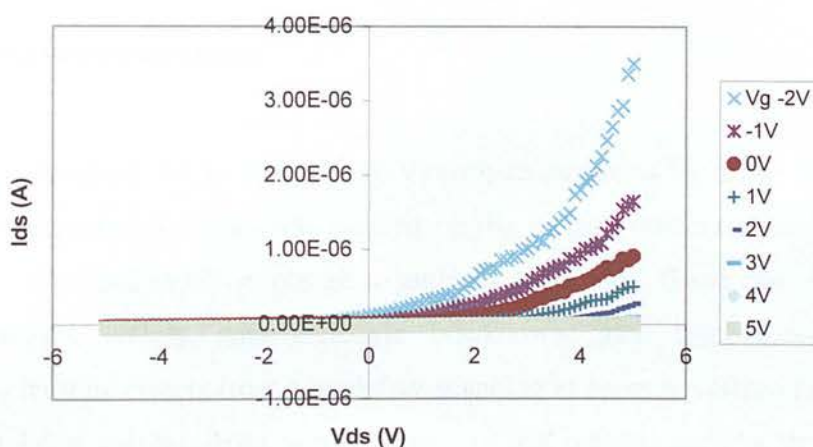


Figure 10.12: plot showing the  $V_{ds}$  sweep  $I_{ds}$ - $V_{ds}$  for the 3 day immersion coated OFETs (substrate with gold electrodes) after rinsing in ethanol.

This appears to be a subthreshold, unipolar, p-type response. In the reverse drain mode (where  $V_{ds} > 0$ ), the negative gate voltages induce large  $I_{ds}$  with increasing  $V_{ds}$  with no saturation and a there is strong  $I_{ds}$  depletion upon application of positive  $V_g$ , which



confirms that no electron injection takes place (Tada et al. 2000). These reverse drain mode characteristics are commonly observed in OFETs (Deen et al. 2004, Tada et al. 2000 and Tapponier et al. 2005). Tapponier and co-workers attributed these characteristics to the maximum potential difference over the active channel is in this case  $|V_{ds}| + |V_g|$  at the drain electrode, which limits the maximum gate voltages that can be applied. The quadratic type increase in the absolute value of  $I_{ds}$  with negative  $V_{ds}$  in reverse drain mode is attributed to the hole injection at the drain electrode that increases with  $|V_{ds}| + |V_g|$  (Tapponier et al. 2005).

Nonlinear (supralinear) IV characteristics with very small currents, no current saturation and no field dependence ( $V_{ds} < 0$ ) were observed in the forward drain mode ( $V_{ds} < 0$  V), which are typical of a sub threshold p-type response (Deen et al. 2004 and Tapponier et al. 2005). This is a narrow voltage testing range so a sub threshold response is common under these conditions, particularly in air without extensive vacuum/annealing treatment.

### 10.5.3 Expanded probing range

A broader  $V_{ds}$  sweep ( $V_{ds} = -30$  V to  $+30$  V) with an increased  $V_g$  range ( $V_g = -30$  V to  $+30$  V in increments of 10 V) was applied on the longest immersion coated devices (substrate 2), after one month exposure to ambient conditions. Great care was taken to minimize heating effects, gate dielectric breakdown, gate bias stress and stray capacitance-charging effects from cumulative scanning at broader voltage ranges. There appeared to be a sub-threshold n-type response but unfortunately with major gate leakage (deviation from zero current at zero  $V_{ds}$  as a function of increasing  $V_g$ ). Also the FET IV plots exhibited some hysteresis as scan time increased.

### 10.5.4 Summary

The electrical output in the OFETs was sensitive to the immersion solvent and to functionalizing the gate with HMDS. When limited voltage range  $V_{ds}$  sweeps were performed all the devices behaved as resistors with very high resistance and no field effect. The  $I_{ds}$ - $V_{ds}$  plots showed hysteresis. The IV behaviour was identical on all areas of the several devices.

The devices were sensitive to ethanol treatment which initiated a p-type (unipolar) response in ambient conditions. The devices with the thickest ICAT films with crystalline domains in the active channel, when probed in air immediately after device production exhibited n-type activity (figure 10.11).

## 10.6 Results 4: Electronic properties of films deposited with enhanced-drop casting.

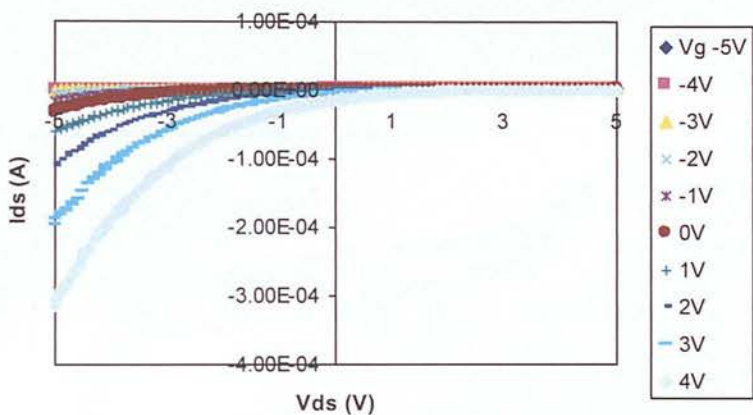
### 10.6.1 Electronic behaviour in ambient conditions

Figure 10.13 illustrates a typical  $V_{ds}$  sweep (standard range), when tested immediately after device production. These IV characteristics were reproducible on all the areas of the substrate apart from the pit areas ( $I_{ds}$  varied within one order of magnitude). These IV characteristics are typical of an n-type subthreshold unipolar response at low  $V_{gs}$ , ( $I_{ds}$  response to +  $V_g$  and current depletion with - $V_g$ ) with some gate leakage, (figure 10.13a) (Tapponier et al. 2005).

Very similar reverse drain mode characteristics have been observed previously in figure 10.12, where a detailed interpretation is provided. Figure 10.13b illustrates the device behaviour in forward drain mode (+  $V_{ds}$ ), where there is a very large current for  $V_g = 0$  V (off current), so the device would be expected to operate in depletion mode here, or

the film thickness (1.5-2  $\mu\text{m}$ ), which nearly fills the active channel gap, is leading to cross talk between devices (Hong et al. 2001). This forward drain mode electron  $I_{\text{ds}}$  response is different from previous experiments (at the same voltage probing range), where the  $I_{\text{ds}}$  was extremely small in magnitude had no field effect. The supralinear, but relatively large  $I_{\text{ds}}$  response (with field effect) here are typical of sub threshold regime with gate leakage at low  $V_{\text{ds}}$  (Katz et al. 2000a and Katz et al. 1998). It is still clear that the devices with thick ICAT film coverage give an n-type response at a narrow voltage testing range in ambient conditions.

**a**



**b**

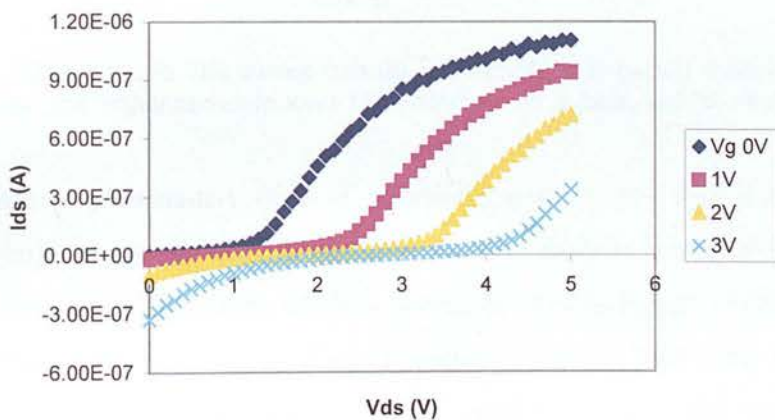


Figure 10.13: (a) is a double  $V_{\text{ds}}$  sweep and (b) a single  $V_{\text{ds}}$  sweep showing the  $I_{\text{ds}}$ - $V_{\text{ds}}$  characteristics for the enhanced-drop cast FET devices with a thick ICAT coating.

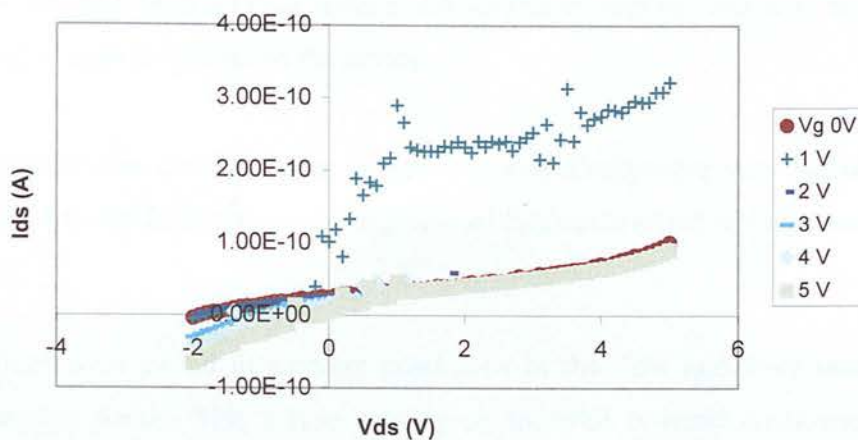
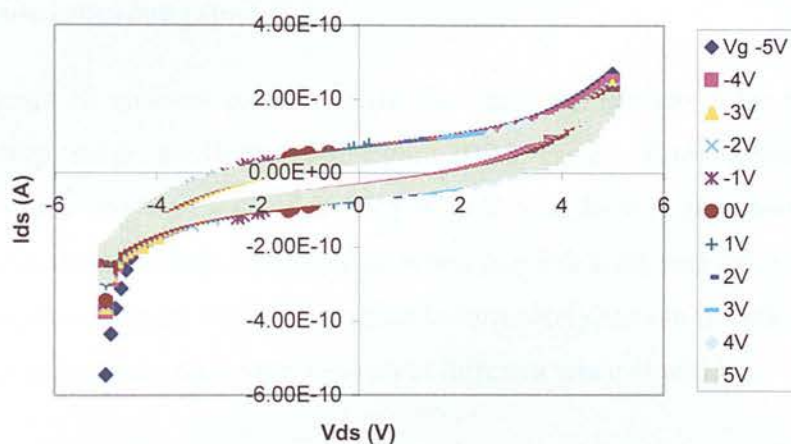
**a****b**

Figure 10.14: (a) is a single  $V_{ds}$  sweep and (b) is a double  $V_{ds}$  sweep showing the  $I_{ds}$ - $V_{ds}$  characteristics for the enhanced-drop cast FET device on a less well covered area of the substrate.

The other areas (approximately 40% of substrate) with visibly less ICAT coverage, (described as large pits in the film) behaved as resistors with no field activity (with very high resistances). The  $V_{ds}$  sweeps of these areas, as seen in figure 10.14b, exhibit IV features very similar to back to back diodes but with hysteresis. The blank substrates and solvent soaked substrates showed no measurable conduction. The  $V_{ds}$  sweep in figure 10.14a illustrates the fact that there was an initial active n-type response in these less well covered areas but it was highly unstable (few minutes in ambient conditions)

(shallow trapping effects). There was an electron  $I_{ds}$  response of small magnitude to very low  $+V_g$  with both a linear regime and saturation regime, which is indicative of favourable transport properties in the device.

However, in ambient conditions the n-type response disappeared very rapidly (during scan) and the  $I_{ds}$  curves became superimposed with no field effect which is indicative of trapping.

These devices were stored in ambient conditions in the dark and were tested over a fortnight testing period. This n-type activity on the well covered areas was constant throughout the testing period.

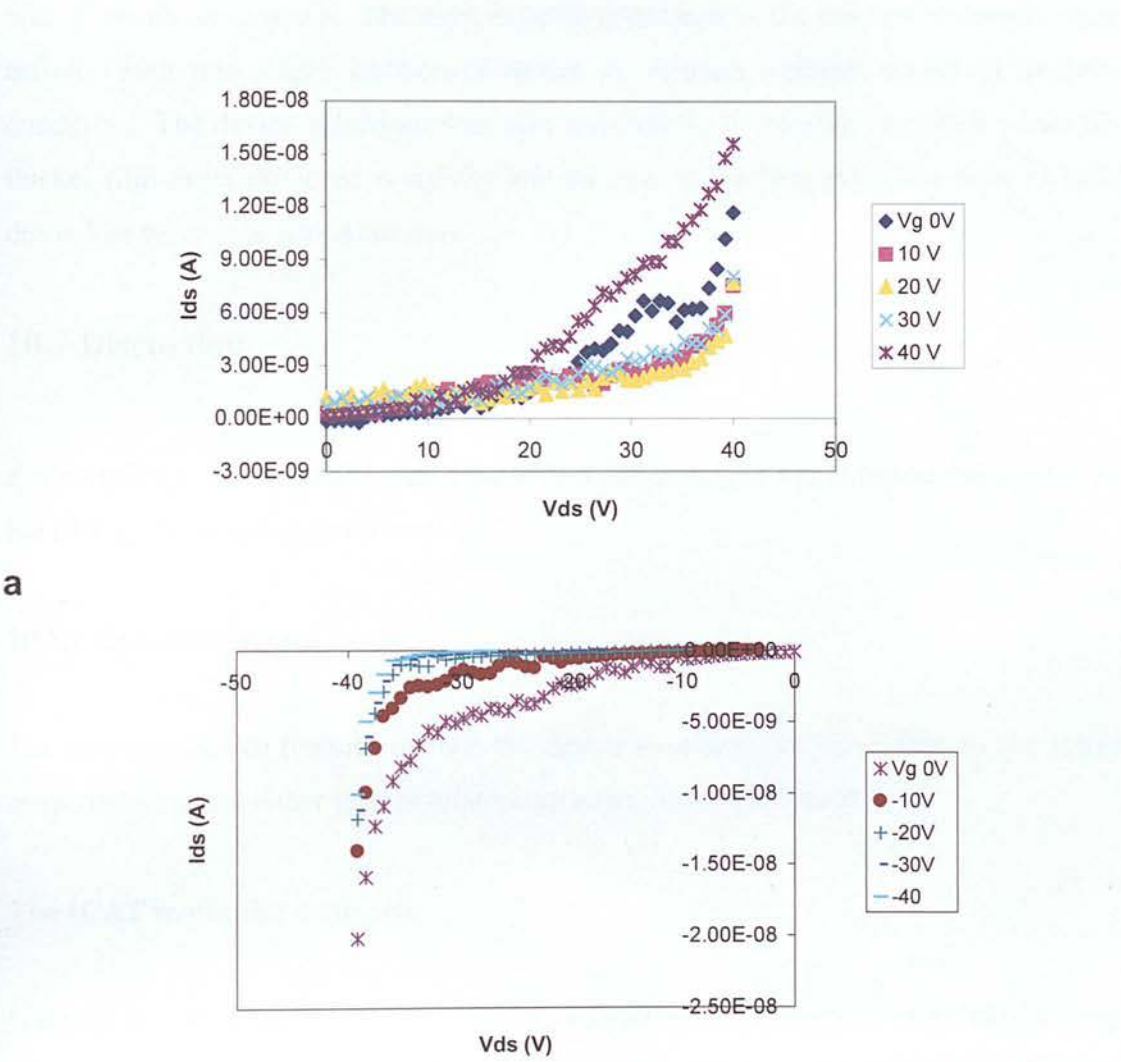
### 10.6.2 Expanded probing range

After one month in ambient conditions (in the dark) the devices were probed at an expanded voltage range, as illustrated in figure 10.15. Figure 10.15 illustrates a typical  $V_{ds}$  sweep ( $V_{ds} = -40\text{ V}$  to  $+40\text{ V}$  and  $V_g = -40\text{ V}$  to  $+40\text{ V}$  in increments of  $10\text{ V}$ ). These IV characteristics were reproducible when one substrate was probed on several areas with the same channel width ( $4\mu\text{m}$ ) (but unfortunately ran out of time to perform a thorough error assessment on several devices at different channel widths).

Here we observe a field effect and  $I_{ds}$  response (medium in magnitude) to both positive and negative applied  $V_g$ s. There is a purely diode-like hole  $I_{ds}$  response with a field effect when negative  $V_g$  is applied and the same type of electron  $I_{ds}$  response when  $V_g < 40\text{ V}$  is applied. Diode-like responses with a field effect are commonly observed in OFETs (Bao et al. 1999a, Leugen et al. 2004, Narasimhan et al. 1998 and Yasuda et al. 2004). More specifically though here, there is a superlinear current increase at low  $V_g$  and high  $V_{ds}$ , which is typical of ambipolar activity due to the injection of the opposite carrier (Cho et al. 2006, Takahashi et al. 2006 and Zaumseil et al. 2007). Most significantly there is strong linear electron  $I_{ds}$  response ( $> 15\text{ V } V_{ds}$ ) to  $V_g = +40\text{ V}$  (rather than a diode like response) (figure 10.15a), which provides further evidence for



the ambipolar theory as typically at higher  $V_g$  in ambipolar devices the true n-type (and p-type) appears as the electron current (and hole current) dominates. The fact that there is only diode-like hole  $I_{ds}$  ( $-V_g$ ) at this range is very common in these devices as charge injection is almost never balanced (Takahashi et al. 2006 and Takenbu et al. 2007). Commonly much higher voltage probing ranges are required to observe both n and p activity in ambipolar devices (up to  $V_g = 200\text{ V}$ ,  $V_{ds} = 200\text{ V}$ ) (Takenbu et al. 2007).



**b**

Figure 10.15: single  $V_{ds}$  sweeps at (a) positive  $V_g$ s and (b) negative  $V_g$ s for the enhanced-drop cast FET device with a thick ICAT coating after one month in ambient conditions.

It is also worth noting the fact that there is no gate leakage here despite the broad voltage testing range (substrate 2 had higher quality gates than substrate 1). Plus these chips were not exposed to solvent for a long period of time.

### **10.6.3 Summary**

n-type activity was demonstrated in ambient conditions, at an extended probing range, after 1 month air exposure. The most exciting result here is the onset of ambipolar type activity with this single component device at medium voltage ranges in ambient conditions. The device behaviour was very sensitive to ICAT film thickness where the thicker film areas produced n-activity and the pits in the film produced back to back diode-like behaviour with hysteresis.

## **10.7 Discussion**

For simplicity, the section commences with a discussion of the common factors for all the FET systems investigated here.

### **10.7.1 Common factors**

The common device features include the device structure, the ICAT film as the active semiconductor and either gold or aluminium source/drain electrodes.

#### **The ICAT molecular structure**

Unipolar n- and p-type activity and (what appeared to be the onset of) ambipolar activity was observed in these OFETs. Organic molecules that have demonstrated ambipolar activity tend to follow the chemistry design rules to favour n-type behaviour (Anthopoulos et al. 2004). A high electron affinity is necessary ( $> 0.3$  eV) (Newman et

al. 2004) but not higher than 0.4 eV, or the molecule is doped in air and a narrow band gap can help achieve n-type activity (Meijer et al. 2003). Structurally ICAT is an aromatic nitrogen-containing heterocycle, which are typically electron deficient, tend to have low band gaps and have been demonstrated to be particularly effective as electron-transporting materials (Laquindanum et al, 1996). The ICAT molecule has 3 carboxylic acid groups per molecule, each group having a high electron affinity, which should draw electrons away from the extremely unstable carbanion centre (which react rapidly with water and oxygen in the environment), and help stabilize it. Also, these electron withdrawing groups tend to lower the molecule LUMO, which make it more accessible to environmentally stable electrodes, such as gold. The ICAT structure therefore lends its self towards n-activity and thus ambipolar activity should be possible. p-type activity is usually readily achievable with most organic semiconductors, although it has been postulated that carboxylic acid groups may trap positive charge carriers and so may hinder p-type activity (Bao et al. 1999).

Semiconductor activity featuring strong current outputs of relatively high magnitude at narrow voltage probing ranges were observed in the ICAT-based FETs (sections 8.1 to 8.4) (Leufgen et al 2004). Charge transport in oligomeric films tends to obey a multiple thermal trapping mechanism and thus is only dependent on the trap density whereas the conductivity is dependent on the doping level. Therefore very pure and highly ordered oligomeric materials allow FETs to achieve high mobilities and low conductivities which meet the requirements for efficient devices (Dimitrakopoulos et al 2001, Garnier et al 1996 and Shirota et al 2007). Thus the high purity of the ICAT molecule synthesized here combined with the well ordered interfacial and bulk assemblies directed by interICAT and ICAT/substrate supramolecular interactions (detailed where appropriate) will contribute strongly towards effective charge transport.

## Source and drain electrodes

Gold has a relatively high work function (typically 5.0 to 5.2 eV) and is thus expected to facilitate hole injection (p-type activity) and to form a barrier to electron injection (Mott-Schottky rule) (Takenobu et al. 2007 and Zaumseil et al. 2007). While aluminium, possessing a low work function (typically 4.3 eV), should favour electron injection (n-type activity). Ambipolar activity is commonly limited by the metal source/drain electrodes and finding a suitable electrode material that allows electron and hole injection is difficult (Zameseil et al. 2007).

However, both n-type and p-type activity was observed here with single work function aluminium and gold source/drain electrodes. Ambipolar activity has been observed in a very limited number of FETs with metal single work function source/drain electrodes (including gold), and the low function metal aluminium can sometimes be outperformed by the higher work function metal gold in n-channel FETs (Anthopoulos et al. 2004, Takahashi et al. 2006 and Tapponnier et al. 2005). Aluminium oxidises very easily in air and can also form reactive complexes with organic semiconductors which can introduce gap states (Cho et al. 2006 and Kymissis et al. 2001). These chemical reactions change the local band structure at the organic/metal interface. Gold is not as reactive as aluminium but when gold is coated with organic films, the apparent work function of the metal can change by up to 1 eV (Zehner et al. 1999). The contact properties at the gold/semiconductor interface can be improved by any treatment that induces a favourable voltage drop, by inducing charge carrier drift or band bending between the metal and semiconductor, such as good semiconductor adhesion or a particular molecular orientation (Katz et al. 2000a). Finally, it has been demonstrated that interface vacuum level shift may be caused by gap states in the semiconductor interface resulting from the physical proximity of the continuum of metallic states to the semiconductor energy gap (Wan et al. 2005).

## Device Structure

The coplanar bottom contact/bottom gate geometry was selected for convenience sake to assess the ICAT film structure property relationship and is necessary in some testing and circuit applications (Katz et al. 2000). The position of the injecting electrode with respect to the gate electrode and contact between the organic layer and the source/drain electrode, which may be limited to a fraction of the vertical wall of the electrodes, both contribute to the contact resistance in the device (Katz et al. 2000). It is important to note here that some researchers experienced problems with bottom contact OFET devices with both gold and aluminium source/drain electrodes, which were found to diminish/inhibit n-activity (Katz et al. 2000a).

OFET active channel dimensions can be a major influence on electrical output. The drain current is proportional to mobility/channel length ( $\mu/L$ ) so by reducing  $L$ , a higher  $I_{ds}$  is obtainable but reducing  $L$  also tends to increase the contact resistance between the source and drain electrodes and the organic layer (Leufgen et al. 2004). So channel lengths were varied in these devices between 2 and  $6\mu\text{m}$ .

The gate dielectric  $\text{SiO}_2$  was selected here for convenience sake and because of the ordered ICAT/  $\text{SiO}_2$  interfacial alignment observed in previous chapters and this dielectric is easy to functionalise. However, this dielectric commonly shields n-type activity in OFETs, due to the high interface trap density, attributed to polar silanol groups ( $\text{Si-OH}$ ) and adsorbed water in ambient conditions (Chau et al. 2005, Guillaud et al. 1998 and Olthgius et al. 1992). Selected devices were functionalised with HMDS SAMs to alleviate this problem. However, n-activity was still observed here in ambient conditions using devices with this dielectric. This may be partially attributed to the  $\text{COOH}$  groups on the ICAT molecule H-bonding with dielectric surface, blocking water molecule physisorption. Also the H-bonded  $\text{COOH}$  groups may help stabilise the electron trapping silanol groups on the surface. It was demonstrated that the activity in OFETs with n-type organic semiconductors with low lying LUMOs and narrow band



gaps (e.g., hexadecafluorocopperphthalocyanine) was not hindered by this particular dielectric (Yoon et al. 2006).

Film morphology, thickness, Substrate type	Initial properties in air	IV consistency	Properties over 1 month in air	Heat treatment 100°C	ethanol
MIMIC at 60°  Polycrystalline  Thickness-2µm  Chip 1	Close to metal IV characteristics	IV consistent  I output varied within just over one order of magnitude	After 1 week-true metallic output and I increased by one order of magnitude.  Then remained unchanged.	Subthreshold n-type response.  30 minutes in air pronounced, strong n-type field effect.  Reversible after 1 day-metallic again	Strong p-activity
MIMIC at room temperature  Amorphous, crystalline areas dispersed  Thickness-1µm  Chip 2	Strong p-activity	IV consistent  I output varied << one order of magnitude	Strong p-activity lasted 1 week  Then back to back diode output		

Table 10.1: MIMIC films results summary

### 10.7.2 ICAT-based OFET properties

The electronic properties of each device with the four different ICAT assemblies are discussed in turn. The section closes with a discussion of some of the major achievements in this work. The results from the MIMIC deposited films are presented in table 10.1.

### System 1: MIMIC at 60°C film properties

The basic experimental objectives were fulfilled. n and p-type activity were observed with these devices. The IV characteristics were consistent, and the current magnitude varied within just over one order of magnitude, on all film areas on several substrates. The films were polycrystalline, but the crystals bridged the electrode gaps so the device may be regarded as a single crystal device.

When probed in ambient conditions (in the dark) there was a consistent strong metallic-like current response (figures 10.1 and 10.2). There was slight asymmetry in the electrical output, which is indicative of a Schottky barrier and/or contact resistance which are frequently observed in these devices (Chen et al. 2004 and Leufgen et al. 2004). Contact resistances arise from potential barriers at all junctions in the device due to surface states, impurities adsorbed during junction formation, and possible chemical reactions between the materials contacted. Schottky barriers are formed when the organic semiconductor and the metal are in contact usually a depletion layer is formed at the interface (Stalinga et al. 2006 and Zaumseil et al. 2007). When their respective work functions are different a Schottky barrier results that limits charge carrier injection.

The metallic-like behaviour could originate from doping contaminants and/or the intrinsic conductivity of the organic semiconductor, particularly as this molecule can potentially self-dope (Abdou et al. 1997 and Bao et al. 1999a). However, the gentle heat and ethanol treatments would not be expected to reverse the metallic-like behaviour if the intrinsic molecular conductivity was responsible for the metallic properties and these treatments were found to initiate semiconductor activity. Therefore this metallic-like behaviour in air is most likely due to doping atmospheric impurities.

This large parasitic conduction (large OFF currents in these devices, figure 10.1) experienced here, has been previously attributed to oxygen doping the organic film and chemisorbed water at the gate/organic interface (Abdou et al. 1997, Chen et al. 2004 and

Hoshino et al. 2004). Similar IV properties were also shown to be a result of atmospheric humidity and were thought to be attributed to water's large dipole moment generating holes in the vicinity of the semiconducting active layer surface through adsorption (Hoshino et al. 2004). These IV characteristics may also be partially attributed to positive charge trapping by the carboxylic acid side groups on the organic semiconductor (Bao et al. 1999a). As a result of these atmospheric impurities threshold voltages can be extremely high (in particular n-type OFETs can have threshold voltages of  $> 90$  V) (Katz et al. 2000, Malefant et al. 2002 and Newman et al. 2004). So OFET activity could be masked at this voltage probing range.

This metallic-like IV response maybe also partially attributed to the heating process during ICAT deposition. The difference between the coefficients of thermal expansion between the silicon substrates and organic layer can lead to microcrack formation, which inhibits charge transport and increases exposure to atmospheric contaminants in the device (Torsi et al. 1995). Also the large voids between the crystals increase the organic layer's exposure to atmospheric dopants and can also increase the contact resistance in the device (Bao et al. 1998, Katz et al. 2000a and Laquindanum et al. 1998). Finally the large  $I_{ds}$  at  $V_g = 0$  V maybe partially attributed to the thickness of the ICAT film used here and the lack of precise patterning of the gate and/or the ICAT layer.

### **Post heat treatment properties**

The OFETs were heated at  $100^\circ\text{C}$  and cooled under nitrogen to determine the origin of the metallic behaviour, to attempt to initiate semiconductor activity and to gain insight into ICAT properties.

The first point of interest is that on heating for 5 minutes, in nitrogen, at  $100^\circ\text{C}$  the device conductance dropped dramatically and the IV output took on ohmic behaviour (figure 10.3). The post heat treatment ohmic IV behaviour may also be attributed to

improved contact between the electrodes and the organic layer after physisorbed impurities at the interface have been removed (Cho et al. 2006).

A dramatic change to n-type activity occurred after heating at 100 °C for 15 minutes and cooling to room temperature under nitrogen (figure 10.5 and 10.6). This is impressive as n-type OFETs are still rare and the overwhelming majority will only operate in vacuum or nitrogen (post 48 hour heat treatment under vacuum) and tend to have extremely high threshold voltages (e.g., 75 V) (Kobayashi et al. 2003, Malefant et al. 2001 and Newman et al. 2004). Also the polar SiO<sub>2</sub> dielectric and gold source/drain electrodes used here typically suppress n-type activity in OFETs. The post heat treatment conductance drop (figure 10.3) and eventual change from metallic to n-type behaviour revealed that the contaminants removed with this treatment were doping the device (figure 10.4). This fact is confirmed by the change in IV behaviour which is indicative of the negative shift in the threshold voltage observed after 30 minutes air exposure post heat treatment (figure 10.5b) and the return to metallic behaviour overnight in air (figure 10.6).

There are two schools of thought behind n-type organic semiconductor instability in air. One opinion is that the main problem is that most semiconducting organic anions can reduce or complex very easily with oxygen or water that has diffused in the film (charge transfer complex formation) (De Leeuw et al. 1997). Others attributed the n-instability to physisorbed oxygen and water at grain boundaries causing electron trapping (Chesterfield et al. 2004 and Katz et al. 2000a). The gentle heat treatment applied here would be expected to remove physisorbed contaminants and not have any effect on covalently bonded ICAT-water/oxygen charge transfer complexes. Therefore this treatment IV response is suggestive of physisorbed contaminants trapping electrons at the grain boundaries (Yoon et al. 2006).

Oxygen could be responsible for the metallic output, as it is known to cause large parasitic conduction and can be easily removed from devices (Abdou et al. 1997 and Tagmouti et al. 1997). Absorbed water vapour and chemisorbed water at the

gate/organic interface are also removed by annealing at this temperature however they require much longer heating times (up to several days as compared to 15 minutes) (Chen et al. 2004 and Tagmouti et al. 1997).

Despite the narrow voltage testing range in ambient conditions, short annealing time, the non ideal device structure, the high work function gold source/drain electrodes, SiO<sub>2</sub> gate there was still a n-type response. This result may be partially attributed to ICAT molecular structure favouring a narrow gap, as only OFETs with narrow band gap semiconductors tend to be operational with this dielectric and high work function electrodes (Yoon et al. 2006). Also good semiconductor adhesion or increased proximity to the gold surface after the heat treatment could induce a favourable voltage drop. The film thickness could be contributing to the n-activity observed in air, as the outer molecules in the film could be acting as a protective barrier to water and oxygen penetration in the first few molecular layers at the organic/dielectric interface. Finally, the highly ordered molecular structure in the single crystals (large crystals bridge active channel) allows efficient charge transport and good stability in ambient conditions in these devices (Bao et al. 1997, Katz et al. 2004 and Podzorov et al. 2003).

### **Post ethanol treatment properties**

A strong unipolar p-type response in air at a low voltage probing range was demonstrated here (figure 8.7). The relatively large hole current with pronounced linear and saturation regimes at low voltage probing ranges is indicative of favourable transport in the devices (Leufgen et al. 2004). It is interesting that the carboxylic acid side groups are not trapping positive charge carriers, as previously suggested by Bao and co-workers (Bao et al. 1999). The easy removal of the doping contaminants with ethanol again points to physisorbed contaminants (Chesterfield et al. 2004, Katz et al. 2000a and Yoon et al. 2006).



Ethanol initiated p-activity (figure 10.7) and the heat treatment induced n-type activity (figure 10.4 and 10.5). Thus it appears that the treatments remove different contaminants or that ethanol may be chemically reacting with ICAT. The polar solvent could physisorb/H-bond with ICAT inducing gap states, changing the threshold voltage (Torsi et al. 2001). It might be expected that the physical action of the ethanol rinsing with agitation, would remove all physisorbed contaminants while there is more contaminant selectivity as a function of the heating time and temperature (even at 100°C) with the heat treatment. Finally one might postulate that if ICAT did form charge transfer complexes with oxygen/water that the enhanced solubility of these complexes would allow them to be removed by ethanol.

## **System 2: MIMIC at room temperature film properties**

The basic experimental objectives were fulfilled. Strong p-type activity in ambient conditions (with no heat/ethanol treatment) was observed. MIMIC at room temperature also produced uniform, continuous films with no ruptures (again minimising deep traps and enhancing oxidative stability) but these films were amorphous, interspersed with tiny dark green crystalline areas, (some of which bridged the active channel width). The IV characteristics were consistent and the current magnitude varied  $\ll$  one order of magnitude on all film areas on several substrates. The strong semiconductor activity, with consistent IV characteristics is partially attributed to the single crystal morphology (some crystals bridged the active channel) (Katz et al. 2004 and Podzorov et al. 2003).

When probed in ambient conditions (in the dark) this device exhibited a strong unipolar p-type response at a low voltage probing range (figure 10.8). The strong hole current, clear linear regime  $> -2.5$  V  $V_{ds}$  and distinct field effect in the  $I_{ds}$ - $V_{ds}$  curves at this narrow voltage testing range, are indicative of favourable transport properties in these devices. The nonlinearities in the  $I_{ds}$ - $V_{ds}$  characteristics are only at very low  $V_{ds}$ , under a very limited  $V_g$  testing range. This result is promising as the device was not subjected

to prolonged annealing or vacuum treatments prior to testing, which is necessary for the majority of p-type OFETs to operate (Abdou et al. 1997 and Hoshino et al. 2004).

The nonlinearities around the origin (at extremely low  $V_{ds}$ ) in the  $I_{ds}$ - $V_{ds}$  curves were most likely attributed to a Schottky contact at the low work function aluminium/ICAT interface. Aluminium could potentially block p-type activity so it is interesting here that there are strong hole currents at very low voltages with only a slight barrier feature. The fact that aluminium did not block p-type activity here could be attributed to it forming reactive complexes with ICAT or to ICAT potentially having a narrow band gap (Cho et al. 2006 and Kyminis et al. 2001). The nonlinear charge conduction may also be attributed to the trap barrier formation, at the crystalline/amorphous domain interface (Kyminis et al. 2001).

This relatively stable p-type activity in ambient conditions, with no prior annealing, maybe partially attributed to the oxidative stability of the continuous ICAT film microstructure (amorphous with sparsely dispersed crystalline areas) with no ruptures. It is interesting to compare this result with the metallic-like behaviour of the OFETs produced with MIMIC at 60 °C (figure 10.1). The film thickness difference between the two devices (1  $\mu\text{m}$  for MIMIC at room temperature and 2  $\mu\text{m}$  for MIMIC at 60°C) could account for the large parasitic conduction in MIMIC at 60°C films from cross talk between devices on chip. Also the polycrystalline films produced with MIMIC at 60 °C, had sizable voids between the large crystals (open to contaminants) and possible microcrack formation in the first few molecular layers of the ICAT film due to the heating process. Another significant difference is that the  $I_{ds}$  output varied less in magnitude between devices with ICAT deposited with MIMIC at room temperature, as compared to that of ICAT deposited at 60 °C (discussed at end of section).

Over the month testing period in ambient conditions, there was a drop in conductance (approximately one order of magnitude), and the strong p-type response had disappeared completely after a fortnight, after which the IV curves resembled that of back to back

diodes (figure 10.9a). The OFET lifetime in ambient conditions is limited here by the aging of the aluminium electrodes in air, through the formation of aluminium oxide, which increases over time and increases the contact resistance. Most low work function metals suffer from this problem but are easily replaced by polymer or calcium electrodes that are more stable in ambient conditions or high work function electrodes.

### **System 3: Immersion coated film properties**

The results from the immersion coated and enhanced drop cast films are presented in table 10.2. The basic experimental objectives were fulfilled. Strong n-type activity in ambient conditions, (with no heat/ethanol treatment) was observed. The IV characteristics were consistent and the current magnitude varied  $\ll$  one order of magnitude on all film areas on several substrates. Immersion coating produced single phase films, consisting of closely packed nanoparticles, with a very small proportion of crystalline deposits appearing at extended immersion times.

### **Amorphous ICAT properties**

The following discussion considers the immersion coated ICAT films, which had an amorphous morphology in the active channel (immersed time 2-10 days) (both substrate types used). These films were not measured accurately but were substantially thinner than those deposited through MIMIC ( $< 1 \mu\text{m}$  thickness). (Since this experiment was performed the immersion time has been decreased to less than 24 hours).

When tested immediately after production in ambient conditions, (in the dark), within a narrow  $V_{ds}$  scan range, all of the devices (except the devices which had been immersed over a very long time (21 days) behaved as resistors with extremely high resistances (approximately  $200 \text{ M}\Omega$ ) and no field effect (figure 10.10). The HMDS-functionalized devices consistently had a resistance of one order of magnitude higher than that of the devices with no HMDS layer.

Film morphology, Thickness, substrate type	Initial properties in air	IV consistency	Properties over 1 month in air	Properties after 1 month Extended probing	Ethanol treatment
Immersion coating  Amorphous close packed nanoparticles,  Long immersion-crystals dispersed  Thickness $\ll 1\mu\text{m}$  Chip 1 standard and HMDS-substrate  Chip 2 just standard immersion	Resistors with extremely high resistances.  HMDS- higher R (1 order mag) than standard film  Long immersion film strong n-activity response (Chip 2)	IV consistent  I output varied $\ll$ less than an order of magnitude	Thin films remained same.  Thick films n-activity lasted 2 days		Thin film p-response Sub threshold  Chip 2
Enhanced drop casting  Amorphous  Thickness 1.5-2 $\mu\text{m}$  Chip 2	Sub threshold n-activity, v high I output  Film pits n-active	Thick area IV consistent (Ids varied within one order of magnitude.  IV consistent within pits	Thick area stable  In pits n-activity lasts <hour Then back to back diodes	Strong n-active response and onset of ambipolar like behaviour	

Table 10.2: Immersion coated and enhanced drop-cast films results summary

The devices which were immersion coated using ICAT /DMSO solution also had resistances which were one order of magnitude higher than that of the devices that were coated using ICAT/DMF solution. These devices exhibited major hysteresis when tested in air immediately after production and the electrical output remained constant throughout the month testing period. Devices which exhibit air stable hysteresis can be

applied in memory devices so these devices could be useful here and should be investigated further.

This IV behaviour is dramatically different to the metallic output in ambient conditions, by those films prepared with MIMIC at 60° C (figure 10.1). This IV output resembled that of the film prepared through MIMIC at room temperature when aged in air. The film thicknesses from this deposition and MIMIC at room temperature were both substantially thinner ( $< 1\mu\text{m}$ ) than the film produced with MIMIC at C° ( $2\mu\text{m}$ ), which filled the active channel gap. The resistor-like behaviour from the thinner coating again reaffirms that the metallic behaviour from the MIMIC at 60°C film is attributed to cross talk between devices on the chip, associated with the thicker film.

This IV behaviour is typical of subthreshold behaviour in OFETs (Deen et al. 2004 and Malefant et al. 2001). The films behaved as resistors with both the low and high work function electrodes, which suggested that the source/drain electrodes are not limiting charge injection. If the high resistance was caused by trapping electronegative hydroxyl groups on the polar dielectric then the HMDS SAM would be expected to alleviate this problem (Chau et al. 2005). The HMDS-layer actually increased the device resistance by an order of magnitude which infers that the electronegative hydroxyl groups on the gate were not blocking device activity here (although an expanded voltage probing range is needed to clarify this). The increased resistance may be attributed to the uneven film surface and pits, (which are not present in the standard immersion films) acting as scattering centres and charge traps, which would increase contact resistance (Chesterfield et al. 2004 and Jones et al. 2008). The films on the standard and HMDS-functionalised substrates were both high quality (closely packed nanoparticles, single phase) so the high resistance is not associated with a disordered film morphology and/or microstructure. Trapping atmospheric contamination is therefore the most probable cause for this IV behaviour.



### **Long immersion time ICAT properties**

Extended immersion times were applied resulting in an increased film thickness, while the bulk film morphology remained the same apart from a sparse quantity of crystalline domains in the active channel. When probed immediately after production in ambient conditions (in the dark) the devices exhibited n-type activity (aluminium source/drain electrodes). The strong  $I_{ds}$  (mid-range in magnitude), clear linear regime  $> 2.0$  V  $V_{ds}$  and distinct field effect at this narrow voltage testing range is indicative of favourable transport properties (figure 10.11) (Leufgen et al. 2004). The n-activity here could be associated with the increased film thickness (by several hundred nm) so the outer ICAT layers could be acting as a protective barrier against water and oxygen diffusing into the inner layers in the film and/or the enhanced charge mobility associated in the newly formed crystalline domains (Horowitz et al. 2001 and Zeis et al. 2005).

n-Activity at this low voltage probing range (particularly with a polar dielectric and a non ideal device structure), in ambient conditions with no prior annealing is a striking result (Kobayashi et al. 2003, Malefant et al. 2001 and Newman et al. 2004). These devices were n-active for 24 hours before the behaviour changed to that of a resistor. This n-activity is associated with the close packed nanoparticle morphology and continuous uniform microstructure (Dodabalapur et al. 1995 and Garnier et al. 1993). These assemblies have minimal charge trap and scatter centres and the continuous microstructure and closely packed nature of the nanoparticles should allow for oxidative stability (Bao et al. 1998 and Katz et al. 2000a).

### **Post ethanol treatment properties**

The devices were sensitive to the ethanol treatment. The device behaviour changed from that of a resistor (figure 10.10) to a (sub threshold IV response) p-type OFET in ambient conditions (figure 10.12). It is interesting to note here that the ethanol treatment applied to the devices with ICAT films prepared through MIMIC at  $60^{\circ}\text{C}$  also induced a

p-type response (both devices used substrate with gold electrodes) (figure 10.7). As discussed earlier, the ethanol could be rinsing physisorbed impurities out of the film or reacting with the ICAT forming gap states. The fact that p-type activity was initiated both times in devices, with very different morphologies and microstructures, which were susceptible to different atmospheric contaminants, with very different IV behaviour in ambient conditions, points to ethanol chemically (probably H-bonding) reacting with ICAT.

#### **System 4: Enhanced-drop cast properties**

The basic experimental objectives were fulfilled. Strong n-type activity was demonstrated in ambient conditions, at an extended probing range, after 1 month air exposure (figure 10.15). The most exciting result here is the onset of ambipolar type activity, with this single component device, at medium voltage ranges, in ambient conditions. There was a clear relation between the n-activity lifetime and film thickness, where the n-activity in thinner coated areas lasted less than an hour and much longer on the thicker coated areas (weeks). It appears that the thicker films have superior oxidative stability than the thinner films. As explained earlier n-activity is quite an achievement in ambient conditions with these substrates and is associated with the favourable film morphology and/or poetically a narrow ICAT band gap.

These films were amorphous, with no crystalline domains and a more disordered microstructure than that of the immersion coated films. These film surfaces were not smooth and were substantially thicker than the immersion coated films. However, these films were initially briefly immersion coated, before drop casting, so a well ordered interfacial assembly on the SiOH terminated substrate is predicted (discussed in previous chapter, well ordered edge-on ICAT alignment at ICAT/SiOH interface). A strong n-type response was demonstrated in ambient conditions, with an amorphous film morphology and disordered microstructure. Thus it appears that the well ordered ICAT/dielectric interfacial alignment might play a key role in effective charge transport

in these devices (Dodabalapur et al. 1995 and Garnier et al. 1993). This result concurs with the fact that current flow in an OFET is thought to be mainly confined to the first 50 Å of the organic semiconductor layer at the semiconductor/dielectric interface (Allem et al. 1997 and Dodabalapur et al. 1995).

This n-activity (figures 10.13-10.15) is particularly fascinating as p-type activity was observed previously on substrate two with ICAT deposited through MIMIC at room temperature under the same probing conditions (figure 10.8). Here we have demonstrated the carrier type in the OFET is dependent on ICAT film morphology and deposition technique. Thus it is possible to make ICAT OFETs with a particular carrier type to order. It is interesting to note the amorphous morphology here and the immersion coated amorphous morphology (apart from a very very sparse quantity of crystals dispersed) produced n-activity in ambient conditions. While, p-activity was produced in ambient conditions with MIMIC at room temperature films, which were amorphous but with a medium coverage of crystals dispersed in the channel, some of which bridged the active channel. It is known that the orientation of the molecules to each other and the associated electron transfer integrals can dictate the carrier type outcome and mobility (Yoon et al. 2006a). The observation of both p and n-type unipolar behaviour, at a narrow voltage probing range, on identical FET substrates, with a single molecule is still extremely rare as most molecules are intrinsically either p or n-type and carrier type is usually limited by the source/drain and gate materials (Horlet et al. 2011 and Usta et al. 2011). The carrier type dependence on morphology has been observed previously in a few cases (Schuster et al. 2009 and Usta et al. 2011). Intermolecular LUMO-LUMO overlap may be more efficient in these amorphous films, while HOMO-HOMO intermolecular overlap may be favoured in the crystalline domains deposited with MIMIC at room temperature. The film microstructures could also have different hole and electron trap densities for example at the grain boundaries which differed in the two morphologies (Horlet et al. 2011, Jin et al. 2006 and Kraus et al. 2011).

### Expanded voltage probing range

After one month in ambient conditions (in the dark) these devices were probed at an expanded voltage range, where the onset of ambipolar activity was observed (figure 10.15). This is a real breakthrough in ambient conditions and the scientific merit of this result is discussed at the end of the section.

There was a stronger n-type current ( $V_g < +40$  V produced a diode-like response and a strong linear  $I_{ds}$  response when  $V_{ds} > +20$  V to  $V_g = +40$  V) in these devices than p-type current (just a diode like  $I_{ds}$  response up to  $V_g = -40$  V). This is to be expected in a device with aluminium source/drain electrodes, which would facilitate electron injection and this is still a comparatively narrow voltage probing range (Takenbu et al. 2007). Certainly single component ambipolar OFETs do not have balanced charge injection (Horlet et al. 2011, Takahashi et al. 2006, Takenbu et al. 2007 and Yasuda et al. 2004). This is a very promising result and it is very easy to transfer these ICAT films to a more appropriate FET substrate. The reasons why this morphology favours n-activity with enhanced oxidative stability is discussed in the previous section. The organic semiconductors that display ambipolar device activity tend to be those with molecular structures that follow the design rules for n-activity, with which the ICAT molecule complies with (Anthopoulos et al. 2004)

There was a significant drop in the current output after one month in ambient conditions (figures 8.13 and 8.21). This is to be expected as the device oxide layer, aluminium oxide layer and atmospheric contaminants concentration in the organic semiconducting film will have all have increased substantially after one month in ambient conditions. Again the intrinsic conductivity of the ICAT appeared not to influence the electrical output. Also there was no gate leakage in this device unlike the enhanced-dip coated device when it was probed at an expanded voltage range (8.20). This may be because the other chip was exposed to solvent for a much longer period of time during the deposition process than here.

## 10.8 Conclusion

Here n and p-type unipolar activity and the onset of ambipolar activity in ambient conditions at low voltage probing ranges were observed. Carrier type dependence on film morphology was demonstrated here. The film deposition technique can be selected to tailor the device carrier type. Solution based deposition methods were developed here that produced consistent IV characteristics within  $\ll$  one order of magnitude.

These results are valuable achievements for the following reasons. The development of good n-type and ambipolar materials is crucial for understanding the fundamental science in this area and fabrication of bipolar transistors, p-n junctions and light-emitting FET devices (Fachettii et al. 2006 and Zaumseil et al. 2007). Air stable ambipolar activity is particularly unusual and sought after (Anthopoulos et al. 2006). Ambipolar activity from single molecule FETs is still very rare and usually blends and bilayers combined with a special device setup (with trap free gate dielectrics, asymmetric work function electrodes and staggered geometry device configuration) are required to produce ambipolar activity (Anthopoulos et al. 2006, Horlet et al. 2011, Kraus et al. 2011, Meijer et al. 2003 Singh et al. 2005, Takenobu et al. 2007 and Yasuda et al. 2004). So both n and p-activity (in ambient conditions) with both gold and aluminium S/D electrodes, in a non ideal FET substrate (high contact resistance bottom contact/bottom gate structure, a polar gate dielectric and single work function source/drain electrodes) is a particularly strong result.

The common solution based deposition techniques typically yield films that are non-uniform in thickness, morphology and electrical properties (Dimitrakopoulos et al. 2002 and Katz et al. 2000). Thus the fact that all the enhanced-solution based deposition techniques used here produced high quality ICAT films with reproducible electrical output is a major improvement. This is an especially good result as there is still opportunity for improvement as these techniques are at the early stages of development.



The immersion coating technique, in particular, is very promising as it is facile and very versatile as it worked well with different solvents and different substrates. The range of morphologies produced here should make a contribution to the organic electronics area as each organic semiconductor film morphology offers different advantages to device properties (Kaafarani et al. 2005, Katz et al. 2004, Podzorov et al. 2003 and Saragi et al. 2005).

The organic semiconductor film structure/activity relationship established here should contribute towards the fundamental science behind charge transportation in these devices and organic electronics in general, of which little is known.

Carrier type was dependent on ICAT film morphology, which is a rare achievement and could be insightful with some more work (Schuster et al. 2009 and Usta et al. 2011). The film (deposited with MIMIC at room temperature) with a large proportion of crystals, some of which bridged the active channel, dispersed in an amorphous film was p-active in ambient conditions. While the amorphous (enhanced drop coated) film and the amorphous, apart from a very small quantity of crystalline domains (smaller than active channel), (immersion coated) film were both n-active. Intermolecular LUMO-LUMO overlap may be more efficient in the amorphous films, while HOMO-HOMO intermolecular overlap may be favoured in the crystals. The film microstructures could also have different hole and electron trap densities, for example, at the grain boundaries which differed in the two morphologies (Horlet et al. 2011, Jin et al. 2006 and Kraus et al. 2011).

The n-activity lifetime was dependent on film thickness and the extended lifetime with the thicker films was attributed to the outer layers in the thicker films, acting as protective oxidative shields. If the film thickness was similar to the active channel height ( $2\mu\text{m}$ ), then the activity was masked by parasitic currents from cross talk with other devices. If the film was too thin ( $\ll 1\mu\text{m}$ ) then the lifetime was extremely short/ or the

film just behaved as a resistor. Films with 1-1.5  $\mu\text{m}$  thickness range demonstrated activity in ambient conditions.

Despite a disordered microstructure and uneven topography, strong n-activity was observed in the enhanced drop-cast films, after one month in ambient conditions. The evidence points to the first few molecular layers at the ICAT/gate interface being the determining factor for activity, which concurs with other researchers findings (Allem et al. 1997 and Dodabalapur et al. 1995).

Two different devices, which were inactive in ambient conditions, when treated with ethanol displayed p-type activity. Torsi and co-workers used polar solvent treatments previously to alter OFETs threshold voltages. The fact that p-type activity was initiated both times in devices with very different IV behaviour in ambient conditions, and very different morphologies and microstructures, which were susceptible to different atmospheric contaminants, points to ethanol chemically (probably H-bonding) reacting with ICAT, creating gap states. This device response to alcohol demonstrates the ICAT potential as the active component in a chemically sensitive OFET (defined as an OFET, which has a gate and/or semiconducting layer with chemical sensitivity) (Torsi et al. 2003). The ICAT molecular structure allows potential for multiple H-bonding and covalent interactions, which makes it ideal for these applications. Organic based sensing systems are currently inadequate for real applications due to extremely poor organic semiconductor film morphologies so these reproducible homogenous ICAT morphologies makes them ideal candidates (de Lacy Costello et al. 2000 and Torsi et al. 2003). Also some devices here exhibited air stable hysteresis, which can be applied in memory devices (Guo et al. 2010).

All the experimental evidence points to a narrow band gap molecule, which is structurally probable. The favourable device activity here is also attributed to the high quality of the organic semiconductor films.

## 11 Conclusion

The key results are discussed in terms of delivering the experimental objectives and contributing towards the requirements in this field of research.

Firstly, a chemical synthesis was developed to produce the pure ICAT molecule, which is capable of forming multiple highly directional H-bonds with ICAT molecules, solvents and surfaces, and thus a good candidate for supramolecular assembly. The planar structure also allows for potential liquid crystal formation and  $\pi$ - $\pi$  stacking in solution to form 1D assemblies. Finally, the ICAT electron deficient, nitrogen containing, heterocyclic structure lends its self towards n-activity (Newman et al. 2004).

Through simple self-assembly of ICAT in solution, a high quality yield of narrowly dispersed discotic nanoparticles was produced that are stable in solution, transferable between surfaces. In chapter 7, extremely high quality bulk and nanoparticle thin films at both the nanoscale and the macroscale were produced, which is a rare achievement are perfect for application purposes. It was interesting to observe an example of what appeared to be the multiple highly directional ICAT H-bonding interactions dictating the assembly process at the hydroxyl functionalised solid/solution interface. Immersing the hydroxyl-functionalised glass substrate in ICAT solution, resulted in a bulk molecular film with a thickness (1.5 nm), which was consistent with a monolayer of ICAT molecules, in an edge-on configuration, with their aromatic core perpendicular to the substrate. This conformation allowed two of the carboxylic acid side groups to H-bonds with the OH surface, and is stabilized though the intermolecular  $\pi$ - $\pi$  interactions (Fraxedas et al. 1999, Fraxedas et al. 1998, Gonzalez-Rodriguez et al. 2011 and Hoebe et al. 2005).

Chapter 8 provided an elegant example, of highly ordered 1D ICAT assemblies on 2 different surfaces, where the nanostructure size and shapes were tailored by the experimental conditions. This is the first time vertically aligned nanorod arrays have been fabricated with small organic functional molecules, through a solution based technique (non-template). These 1D organic nanostructures should be particularly

effective in electronic applications, as according to theoretical modelling these organic small semiconductor structures predominantly self-assemble along the  $\pi$ - $\pi$  stacking direction, which favours high charge-carrier mobilities, as a result of the strong intermolecular coupling between the packed molecules (Curtis et al. 2004, Lemaire et al. 2004 and Rocherfort et al. 2002). There is now some experimental evidence verifying this theory and it would be interesting to resolve the particle structure and apply these nanorods in devices in the future (Che et al. 2007a and Dautel et al. 2008). Indeed  $\pi$ -stacking with ICAT has already been observed in the nanoparticles (J-stacking) produced in chapter 6. The aligned nanorod arrays, in particular, are actually highly applicable, as electroactive and chemically active, orientated, open structures are highly desirable for applications in chemical and biological sensing and diagnosis. The growth process for the immersion based nanorod deposition was interpreted in terms of heterogeneous nucleation and subsequent growth. It was interesting to note similarities between the assembly process here with that of the seeded nanostructure growth in inorganic (metal oxide) systems, and a conducting polymer orientated growth system (Aizenberg et al. 1999, Liu et al. 2003, and Sounart et al. 2006).

The FET chips produced here had consistent, reproducible current/voltage (IV) outputs that varied within  $\ll$  one order of magnitude, when probed on all areas. This is a particularly good result, as OFETs fabricated with common solution based deposition methods tend to produce electronic properties ranging from non-operational to extremely favourable within a single device (Briseno et al. 2007 and Tang et al. 2006). The devices produced n and p-type unipolar activity and the onset of ambipolar activity in ambient conditions, at low voltage probing ranges. Both n and p-activity (in ambient conditions) with both gold and aluminium source/drain electrodes, in a non-ideal FET substrate (high contact resistance bottom contact/bottom gate structure, a polar gate dielectric and single work function source/drain electrodes) is a particularly strong result. This result is attributed to the combination of high quality film morphologies and the ICAT structure, which favours n-activity (Newman et al. 2004). Ambipolar activity is typically observed in structures that favour n-activity. These ICAT films should be



applied to appropriate FET substrates, to maximize the device activity in the future, as the development of good n-type and ambipolar materials is crucial for understanding the fundamental science in this area and fabrication of bipolar transistors, p-n junctions and light-emitting FET devices (Fachetti et al. 2006 and Zaumseil et al. 2007). Also some devices here exhibited air stable hysteresis, which can be applied in memory devices (Guo et al. 2010). In future the 1D nanostructures produced here should be applied to FET devices, as molecular packing, which favours efficient directional charge transport is predicted and the structures are easily aligned with device interfaces, and favourable carrier mobilities have been obtained by a couple of researchers using organic 1D nanostructures (Briseno et al. 2007, Moon et al. 2004, Tang et al. 2006 and Xiao et al. 2007).

The morphology/activity relationship revealed some interesting behaviour. In the OFETs analysed in chapter 10, carrier type was dependent on ICAT film morphology, which is a rare achievement and could be insightful with some more work (Schuster et al. 2009 and Usta et al. 2011). It was postulated that intermolecular LUMO-LUMO overlap may be more efficient in the ICAT amorphous films, while HOMO-HOMO intermolecular overlap may be favoured in the ICAT crystals. The film microstructures could also have different hole and electron trap densities, for example, at the grain boundaries which differed in the two morphologies (Horlet et al. 2011, Jin et al. 2006 and Kraus et al. 2011). The n-activity lifetime was dependent on film thickness and the extended lifetime with the thicker films was attributed to the outer layers in the thicker films, acting as protective oxidative shields. Despite a disordered microstructure and uneven topography, strong n-activity was observed in the enhanced drop-cast films, after one month in ambient conditions. The evidence points to the first few molecular layers at the ICAT/gate interface being the determining factor for activity, which concurs with other researchers findings (Allem et al. 1997 and Dodabalapur et al. 1995).

To conclude, narrowly dispersed discotic ICAT nanoparticles and a range of 1D ICAT nanostructures were fabricated here in solution or at the solid/solution interface. High

quality ICAT films, with well ordered bulk and particulate assemblies, were produced here. Both n and p-type activity were demonstrated in the OFET devices, which is highly sought after and very unusual. ICAT, the molecule and its assemblies have great potential in optoelectronics and electronics today.

## Bibliography

### **Abdallah et al. 2000**

Abdallah D.J. and Weiss R.G., 2000. Organogels and low molecular mass organic gelators. *Advanced Materials* **12**, 1237.

### **Abdou et al. 1997**

Abdou M.S.A., Orfino F.P., Son Y., Holdcroft S., 1997. Interaction of oxygen with conjugated polymers: Charge transfer complex formation with poly(3-alkylthiopenes). *Journal of the American Chemical Society* **119**, 4518.

### **Abthagir et al. 1998**

Abthagir P.S., Dhanalakshmi K. and Saraswathi R., 1998. Thermal studies on polyindole and polycarbazole. *Synthetic Metals* **93**, 1.

### **Aizenberg et al. 1999**

Aizenburg J., Black A.J. and Whitesides G.M., 1999. Control of crystal nucleation by patterned self-assembled monolayers. *Letters to Nature* **398** 495.

### **Alivisatos et al. 1996**

Alivisatos A.P., 1996. Semiconductor clusters, nanocrystals and quantum dots. *Science* **271**, 5251.

### **Allem et al. 1997**

Allem M.A., Dodabalapur A. and Pinto M.R., 1997. A two-dimensional simulation of organic transistors. *IEEE Transactiona on Electron Devices* **44**, 8, 1332.

### **An et al. 2009**

An A.B.K., Gihm S.H., Chung J.W.M, Park C.R., Kwon S.K. and Park S.Y., 2009. Colour-tuned highly fluorescent organic nanowires/nanofabrics: easy massive fabrication and molecular structural origin. *Journal of the American Chemical Society* **131**, 3950.

### **An et al. 2004**

An B.K., Lee D.S., Lee J.S., Park Y.S., Song H.S. and Park S.Y., 2004. Strongly fluorescent organogel system comprising fibrillar self-assembly of a trifluoromethyl-based cyanostilbene derivative. *Journal of the American Chemical Society* **126**, 10232.

### **An et al. 2002**

An B.K., Kwon S.K., Jung S.D. and Park S.Y., 2002. Enhanced emission and its switching in fluorescent organic nanoparticles. *Journal of American Chemical Society* **124**, 14410.

### **Anthopoulos et al. 2006**

Anthopoulos T.D., Setayesh S., Smits E., Colle M., Cantatore E., de Boer B., Blom P.W.M. and de Leeuw D.M., 2006. Air-stable complimentary-like circuits based on organic ambipolar transistors. *Advanced Materials* **18**, 1900.

### **Anthopoulos et al. 2004**

Anthopoulos T.D., Tanase C., Setayesh S., Meijer E.J., Hummelen J.C., Blom P.W.M. and de Leeuw D.M., 2004. Ambipolar field effect transistors based on a solution processed methanofullerene. *Advanced Materials* **16**, 2174.

### **Aoki et al. 2002**

Aoki K., Nakagawa M., Seki T. and Ichimura K., 2002. Solvent effect on morphology of self-assembled fibrous materials derived from an azopyridine carboxylic acid. *Chemistry Letters* **378**.

**Aoki et al. 2000**

Aoki K., Nakagawa M. and Ichimura K., 2000. Self-assembly of amphoteric azopyridine carboxylic acids: organized structures and macroscopic organized morphology influenced by heat, Ph change and light. *Journal of the American Chemical Society* **122**, 10997.

**Arnaud et al. 2004**

Arnaud A., Belleney J., Boue F., Bouteiller L., Carrot G. and Wintgens V., 2004. Aqueous supramolecular polymer formed from amphiphilic perylene derivate. *Angewandte Chemie International Edition* **43**, 1718.

**Ashkenasky et al. 2002**

Ashkenasky G., Cahen D., Cohen R., Shanzer A. and Vilan A., 2002. Molecular engineering of semiconductor surfaces and devices. *Accounts of Chemical Research* **35**, 121.

**Attard et al. 1996**

Attard P., 1996. Solvent depletion and other effects on linear aggregation. *Molecular Physics* **89**, 691.

**Ayyappanpillai et al. 2006**

Ayyappanpillai A., Varghese R., Praveen V.K. and Mahesh S., 2006. Evolution of nano-to micro-sized spherical assemblies of a short oligo(p-phenylene-ethylene) into superstructured organogels. *Angewandte Chemie International Edition* **45**, 3261.

**Balakrishnan et al. 2006**

Balakrishnan K., Datar A., Zhang W., Yang X., Naddo T., Huang J., Zuo J., Yen M., Moore J.S. and Xang J.S., 2006. Nanofibril self assembly of an arylene ethylene macrocycle. *Journal of the American Chemical Society* **128**, 6576.

**Balakrishnan et al. 2006a**

Balakrishnan K., Datar A., Naddo T., Huang J., Otiker R., Yen M., Zhao J. and Zang L., 2006. Effect of side-chain substituents on self-assembly of perylene diimide molecules: morphology control. *Journal of the American Chemical Society* **128**, 7390.

**Balakrishnan et al. 2005**

Balakrishnan K., Datar A., Otiker R., Chen H., Zuo J. and Zang L., 2005. Nanobelt self-assembly from an organic n-type semiconductor: propoxyethyl-PTCDI. *Journal of the American Chemical Society* **127**, 10496.

**Ball et al. 1992**

Ball L. and Garwin P., 1992. Science at an atomic scale. *Nature* **355**, 761.

**Bao et al. 2006**

Bao C., Lu R., Jin M., Xue P., Tan C., Xu T., Liu G. and Zhao Y., 2006. Helical stacking tuned by alkoxy side chains in  $\pi$ -conjugated triphenylbenzene discotic derivatives. *Chemistry A European Journal* **12**, 3287.

**Bao et al. 1999**

Bao Z., Rogers J.A. and Howard E.K., 1999. Printable organic and polymeric semiconducting materials and devices. *Journal of materials chemistry* **9**, 1895.

**Bao et al. 1999a**

Bao Z. and Lovinger A.J., 1999. Soluble regioregular polythiophene derivatives as semiconducting materials for field-effect transistors. *Chemistry of Materials* **11**, 2607.

**Bao et al. 1998**

Bao Z.A., Lovinger A.J. and Brown J., 1998. New air stable n-type organic thin film field effect transistors. *Journal of the American Chemical Society* **120**, 207.

**Bao et al. 1997**

Bao Z., Dodabalapur A. and Lovinger A.J., 1997. Highly ordered vacuum deposited thin films of metallophthalocyanines and applications in field effect transistors. *Advanced Materials* **9**, 1, 42.

**Bao et al. 1996**

Bao Z., Dodabalapur A. and Lovinger A.J., 1996. Soluble and processable regioregular poly(3-hexylthiophene) for thin film field effect transistor applications with high mobility. *Applied Physics Letters* **69**, 4108.

**Barth et al. 2003**

Barth J.V., Weckesser J., Lin N., Dmitriev A. and Kern K., 2003. Supramolecular architectures and nanostructures at metal interfaces. *Applied Physics A* **76**, 645.

**Bartlett et al. 1992**

Bartlett P.N., Dawson D.H. and Farrington F., 1992. Electrochemically polymerised films of 5-carboxyindole. *Faraday Transactions* **88**, 18, 2685.

**Baude et al. 2003**

Baude P.F., Ender D.A., Haase M.A., Kelley T.W., Muyres D.V. and Theiss S.D., 2003. Pentacene-based radio frequency identification circuitry. *Applied Physics Letters* **82**, 3964.

**Baughman 1996**

Baughman R.H., 1996. Conducting polymer artificial muscles. *Synthetic Metals* **78**, 339.

**Becerril et al. 2005**

Becerril H.A., Stoltenberg R.M., Wheeler D.R., Davis R.C., Harb J.N. and Woolley A.T., 2005. DNA-templated three branched nanostructure for nanoelectronics devices. *Journal of the American Chemical Society* **127**, 9, 2828.

**Berdichevsky et al. 2006**

Berdichevsky Y. and Lo Y.H., 2006. Polypyrrole nanowire actuators. *Advanced Materials* **18**, 122.

**Berry et al. 1996**

Berry A.D., Tonucci R.J. and Fatemi M., 1996. Fabrication of GaAs and InAs wires in nanochannel glass. *Applied Physics Letters* **69** (19) 2846.

**Bertini et al. 2002**

Bertini I., Luchinat C. and Parigi G., 2002. Magnetic susceptibility in paramagnetic NMR. *Progress in Paramagnetic Nuclear Magnetic Resonance Spectroscopy* **40**, 249.

**Bieganski et al. 2005**

Bieganski A.T., Michota A., Bukowska J. and Jackowska K., 2005. Immobilization of tyrosinase on poly(indole-5-carboxylic acid) evidenced by electrochemical and spectroscopic methods. *Biochemistry* **69**, 41.

**Billaud et al. 2003**

Billaud D., Humbert B., Thevenot L., Thomas P. and Talbi H. Electrochemical properties and Fourier transform-infrared spectroscopic investigations of the redox



behaviour of poly(indole-5-carboxylic acid) in  $\text{LiClO}_4$ -acetonitrile solutions. *Spectrochimica Acta Part A* **59**, 163.

**Billaud et al. 1995**

Billaud D., Maarouf E.B. and Hannecart E., 1995. Chemical oxidation and polymerization of indole. *Synthetic Metals* **69**, 571.

**Bining et al. 1986**

Bining G., Quate C.F. and Gerber Ch., 1986. Atomic Force Microscope. *Physical Review Letters* **56**, 9, 930.

**Bocchi et al. 1986**

Bocchi V. and Pala G., 1986. Synthesis and characterization of new indole trimers and tetramers. *Tetrahedron* **42**, 18, 5019.

**Brant et al. 2005**

Brant J., Lecoanet H.J., Hotze M. and Wiesner M., 2005. Comparison of electrokinetic properties of colloidal fullerenes (n-C60) formed using two procedures. *Environmental Science and Technology* **39**, 6343.

**Bredas et al. 2002**

Bredas J.L., Calbert J.P., da Silva Filho D.A. and Cornhill J., 2002. Organic semiconductors: a theoretical characterization of the basic parameters governing charge. *Proceedings of National Academy of Sciences* **99**, 9, 5804.

**Briseno et al. 2007**

Briseno A.L., Mansfield S.C.B., Reese C., Hancock J.M., Xiong Y., Jenekhe S.J., Bao Z. and Xia Y., 2007. Perylene diimide nanowires and their use in fabricating field effect-transistors and complementary invertors. *Nanoletters* **7**, 9, 2847.

**Briseno et al. 2005**

Briseno A.L., Aizenberg J., Han Y.K., Penkala R.A., Moon H., Lovinger A.J., Kloc C. and Bao Z., 2005. Patterned growth of large orientated organic semiconductor single crystals and self-assembled monolayer templates. *Journal of the American Chemical Society* **127**, 12164.

**Brown et al. 1995**

Brown A.R., Pomp A., Hart C.M. and Deleeuw D.M., 1995. Logic gates made from polymer transistors. *Science* **270**, 972.

**Brown et al. 1987**

Brown A.R., Jarrett C.P., deLeeuw D.M. and Matters M., 1987. Field-effect transistors made from solution processed organic semiconductors. *Synthetic Metals* **88**, 37.

**Burroughes et al. 1990**

Burroughes J.H., Bradley D.D.C., Brown A.R., Marks R.N., McKay K., Friend R.H., Burns P.L. and Holmes A.B., 1990. Light-emitting diodes based on conjugated polymers. *Nature* **347**, 539.

**Callis et al. 1991**

Callis P.R., 1991. Molecular orbital theory of the  $^1\text{L}_b$  and  $^1\text{L}_a$  states of indole. *The journal of Chemical Physics* **95**, 4230.

**Cassagneau et al. 1998**

Cassagneau T., Mallouk T.E. and Fendler J.H., 1998. Layer-by-layer assembly of thin film of Zener diodes from conducting polymers and CdSe nanoparticles. *Journal of American Chemical Society* **120**, 7848.

**Castle et al. 1997**

Castle J.E. and Zhdan P.A., 1997. Characterization of surface topography by SEM and SFM: problems and solutions. *Journal of Physics D: Applied Physics* **30** 722.

**Chaabane et al. 2003**

Chaabane R.B., Ltaief A., Dridi C., Rahmouni H., Bouazizi A. and Ben Ouada, 2003. Study of organic thin film transistors based on nickel phthalocyanine: effect of annealing. *Thin Solid Films* **427**, 371.

**Chang et al. 2004**

Chang J., Sun B., Briebly D., Nielson M., Solling T., Giles M., McCulloch I. and Sirringhaus H., 2004. Enhanced mobility of poly(3-hexylthiophene) transistors by spin coating from high-boiling point solvents. *Chemistry Materials* **16**, 4772.

**Chang et al. 2000**

Chang A.B. and Frisbie C.D., 2000. Field effect transport measurements on single grains of sexithiophene: Role of the contacts. *Journal of Physical Chemistry B* **104**, 12202.

**Chau et al. 2005**

Chau L.L. Zaumseil J., Chang J.F., Ou E.C., Ho P.K., Sirringhaus H. and Friend R.H., 2005. General observation of n-type field-effect behaviour in organic semiconductors. *Nature Letters* **434**, 194.

**Chaubey et al. 2000**

Chaubey A., Pande K.K., Singh V.S. and Malhotra B.D., 2000. Co-mobization of lactate oxidase and lactate dehydrogenase on conducting polyaniline films. *Analytica Chimica Acta* **407**, 97.

**Chaudhuri et al. 2011**

Chaudhuri D., Li D., Che Y., Shafran E., Gerton J.M. and Lupton J.M., 2011. Enhancing long-range exciton guiding in molecular nanowires by H-aggregation lifetime engineering. *Nanoletters* **11**, 488.

**Che et al. 2007**

Che Y., Datar A., Balakrishnan K. and Zang L., 2007. Ultralong nanobelts self-assembled from an asymmetric perylene tetracarboxylic diimide. *Journal of the American Chemical Society* **129**, 7234.

**Che et al. 2007a**

Che Y., Datar A., Yang X., Naddo T., Zhao J. and Zang L., 2007. Enhancing one-dimensional charge transport through intermolecular  $\pi$ -electron delocalization: conductivity improvement for organic nanobelts. *Journal of the American Chemistry Society* **129**, 6354.

**Chen et al. 2011**

Chen J.T. and Hsu C.S., 2011. Conjugated polymer nanostructures for organic solar cell applications. *Polymer Chemistry Review* **2**, 2707.

**Chen et al. 2004**

Chen H., Josowicz M. and Janata J., 2004. Chemical effects in organic electronics. *Chemistry Materials* **16**, 4728.

**Chen et al. 2004a**

Chen J., Xu B., Ouyang X., Tang B.Z. and Cao Y., 2004. Aggregation-induced emission of cis,cis-1,2,3,4-tetraphenylbutadiene from restricted intermolecular rotation. *Journal of Physical Chemistry A* **108**, 7522

**Chen et al. 2001**

Chen X.L., Lovinger A.J., Bao Z. and Sapjeta J., 2001. Morphological and transistor studies of organic molecular semiconductors with anisotropic electrical characteristics. *Chemistry Materials* **13**, 1341.

**Chen et al. 2001a**

Chen L.C., Chang S.W., Chang C.S., Wen C.J., Wu J. J., Chen Y. F., Huang Y. S. and Chen K.H., 2001. Catalyst-free and controllable growth of  $\text{SiC}_x\text{N}_y$  nanorods. *Journal of Physics and Chemistry of Solids* **62**, 1567.

**Chen et al. 1990**

Chen Y., Rich R.L., Gai F. and Petrich J.W., 1990. Fluorescent species of 7-azaindole and 7-azatryptophan in water. *Journal of Physical Chemistry* **97**, 1770.

**Chescoe et al. 1990**

Chescoe P.J., and Goodhew P.J., 1990. The operation of transmission and scanning electron microscopes, Oxford University Press.

**Chesterfield et al. 2004**

Chesterfield R.J., McKeen J.C., Newman C.R., Ewbank P.C., Da Silvo Filho D.A., Bredas J.L., Miller L.L., Mann K.R. and Frisbie C.D., 2004. Organic thin film transistors based on N-Alkyl Perylene Diimides: Charge transport kinetics as a function of gate voltage and temperature. *Journal of Physical Chemistry B* **108**, 19281.

**Chiang et al. 1977**

Chiang C.K., Fincher C.R., Park Y.W., Heeger A.J., Shirakawa H., Louis E.J. and MacDiarmid A.G., 1977. Electrical conductivity of doped polyacetylene. *Physical Review Letters* **39**, 17, 1098.

**Cho et al. 2006**

Cho S., Yuen J., Kim J.Y., Lee K. and Heeger A.J., 2006. Ambipolar organic field-effect transistors fabricated using a composite of semiconducting polymer and soluble fullerene. *Applied physics letters* **89**, 153505.

**Clemens et al. 2004**

Clemens W., Fix I., Ficker J., Knobloch A. and Ullmann A., 2004. From polymer transistors toward printed electronics. *Journal of Material Research* **19**, 1963.

**Crone et al. 2001**

Crone B., Dodabapalapur A., Gelperin A., Torsi L., Katz H.E., Lovinger A.J. and Bao Z., 2001. Electronic sensing of vapours with organic transistors. *Applied Physics Letters* **78**, 2229.

**Cui et al. 2012**

Cui S., Zhao Y.S. and Yao J., 2012. Photonic applications of one dimensional organic single-crystalline nanostructures: optical waveguides and optically pumped lasers. *Journal of Materials Chemistry* **22**, 4136.

**Cui et al. 2008**

Cui S., Liu H., Gan L., Li Y. and Zhu D., 2008. Fabrication of low dimension nanostructures based on organic conjugated molecules. *Advanced Materials* **20**, 2918.

**Curtis et al. 2004**

Curtis M.D., Cao J. and Kampf J.W., 2004. Solid-state packing of conjugated oligomers: from  $\pi$ -stacks to the herringbone structure. *Journal of the American Chemistry Society* **126**, 4318.

**Dautel et al. 2008**

Dautel O.J., Robitzer M., Flores J.C., Tondelier D., Serein-Spirau F., Lere-Porte J.P., Guerin D., Lenfant S., Tillard M., Vuillaume D. and Moreau D., 2008. Electroactive nanorods and nanorings designed by supramolecular association of  $\pi$ -conjugated oligomers. *Chemistry a European Journal* **14**, 4201.

**De Boer et al. 2005**

de Boer R.W.I., Stassen A.F., Craciun M.F., Mulder C.L., Molinari A., Rogge S., and Morpurgo A.F., 2005. Ambipolar Cu- and Fe-phthalocyanine single-crystal field-effect transistors. *Applied Physics Letters* **86**, 262109.

**DeCupere et al. 2006**

Decupere V., Tant J., Vivelle P., Lazzaroni R., Osikowicz W., Salaneck W.R. and Geerts Y.H., 2006. Effect of interfaces on the alignment of a discotic liquid crystalline phthalocyanine. *Langmuir* **22**, 7798.

**Deegan et al. 1997**

Deegan R.D., Bakajin O., Dupont T.F., Huber G., Nagel S.R. and Witten T.A., 1997. Capillary flow as the cause of ring stains from dried liquid drops. *Nature* **389**, 827.

**Deen et al. 2004**

Deen M.J., Kazemeini M.H., Haddara Y.M., Yu J., Vamvounis G., Holdcroft S. and Woods W., 2004. Electrical characterization of polymer-based FETs fabricated by spin-coating poly(3-alkylthiophene)s. *IEEE Transactions on Electronic Devices* **51**, 11, 1892.

**de Lacy Costello et al. 2000**

de Lacy Costello B.P.J., Evans P., Guernion N., Ratcliffe N.M., Sivanand P.S. and Teare G.C., 2000. The synthesis of a number of 3-alkyl and 3-carboxy substituted pyrroles: their chemical polymerisation onto poly(vinylidene fluoride) membranes, and their use as gas-sensitive resistors. *Synthetic Metals* **114**, 181.

**De Leeuw et al. 1997**

De Leeuw D.M., Simenon M.M.J., Brown A.R. and Einerhand R.E.F., 1997. Stability of n-type doped conducting polymers and consequences for polymeric microelectronic devices. *Synthetic Metals* **87**, 53.

**Dholakia et al. 2006**

Dholakia G.R., Meyyapan M., Facchetti A. and Marks T., 2006. Monolayer to multistructural growth transition in n-type oligothiophenes on Au (111) and implications for organic field-effect transistor performance. *Nano letters* **6**, 11, 2447.

**Dimitrakopoulos et al. 2002**

Dimitrakopoulos C. and Malenfant P., 2002. Organic thin film transistors for large area electronics. *Advanced Materials* **14**, 2, 99.

**Dimitrakopoulos et al. 2001**

Dimitrakopoulos C.D and Masearo D.J., 2001. Organic thin-film transistors: A review of recent advances. *IBM journal of Research and Development* **45**, 2001.

**Djurisic et al. 2008**

Djurisic A.B., Ng A.M.C., Cheung K.Y., Fung M.K. and Chan W.K., 2008. Small molecule organic nanostructures-fabrication and properties. *Journal of Materials Science and Technology* **24**, 4, 563.

**Dong et al. 2007**

Dong Y., Lam J., Qin A., Sun J., Liu J., LEE Z., Sun J., Sung H., Williams I., Kwok H. and Tang B., 2007. Aggregation induced and crystallisation enhanced emissions of 1,2-diphenyl-3,4-bis(diphenylmethlene)-1-cyclobutene. *Chemical Communications* **31**, 3255.

**Dodabalapur et al. 1995**

Dodabalapur A., Torsi L. and Katz H.E., 1995. Organic Transistors: Two dimensional transport and improved electrical characteristics. *Science* **268**, 270.

**Dost et al. 2007**

Dost R., Das A. and Grell M., 2007. A novel characterization scheme for organic field effect transistors. *Journal of Physics D: Applied Physics* **40**, 3563.

**Drain et al. 2002**

Drain C.M., Batteas J.D., Flynn W., Milic T., Chi N., Yablon D.G. and Sommers H., 2002. Designing supramolecular porphyrin attays that self-organize into nanoscale optical and magnetic materials. *Proceedings of the National Academy of Sciences of the United Sates of America* **99**, 6498.

**Drain et al. 1998**

Drain C.M., Nifiatis F., Vasenko A. and Batteas J.D., 1998. Porphyrin tessellation by design: metal-mediated self assembly of large arrays and tapes. *Angewandte Chemie International Edition* **37**, 2344.

**Drury et al. 1998**

Drury C.J., Mutsaers C.M.J., Hart C.M., Matters M. and de Leeuw D.M., 1998. Low-cost all-polymer integrated circuits. *Applied Physics letters* **73**, 1, 108.

**Duan et al. 1995**

Duan C. and Meyerhoff M.E., 1995. Immobilization of proteins on gold coated porous membranes via an activatd self-assembled monolayer of thioctic acid. *Microchimica Acta* **117**, 195.

**Dunlap et al. 1997**

Dunlap M. and Adaskaveg J.E., 1997. Introduction to the scanning electron microscope. Theory, practice and procedures. *Presentation for the facility for advanced instrumentation*.

**Duzhko et al. 2006**

Duzhko V., Shi H., Singer K.D., Semyonov A.N. and Twieg R.J., 2006. Controlled self-assembly of triphenylene-based molecular nanostructures. *Langmuir* **22**, 7947.

**Ebisawa et al. 1983**

Ebisawa E., Kurokawa T. and Nara S., 1983. Electrical properties of polyacetylene/polysilxane interface. *Journal of Applied Physics*, **54**, 3255.

**Elemans et al. 2003**

Elemans J.A.A.W., Rowan A.E., Nolte J.M., 2003. Mastering molecular matter: supramolecular architecture by hierarchical self-assembly. *Journal of Material Chemistry* **13**, 2661.

**Elsenbaumer et al. 1986**

Elsenbaumer R.L., Jen K.Y. and Oboodi R., 1986. Processible and environmentally stable conducting polymers. *Synthetic Metals* **15**, 2-3, 169.

**Foster et al. 2005**



Foster E.J., Lavigne C., Ke Y.C. and Williams V.E., 2005. Self-assembly of hydrogen bonded molecules: discotic and elliptical mesogens. *Journal of Materials Chemistry* **15**, 4062.

**Fu et al. 2001**

Fu H.B. and Yao J.N., 2001. Size effects on the optical properties of organic nanoparticles. *Journal of American Chemical Society* **123**, 1434.

**Fu et al. 2003**

Fu H., Xiao D., Yao J. and Yang G., 2003. Nanofibers of 1,3-diphenyl-2-pyrazole induced by cetyltrimethylammonium bromide micelles. *Angewandte Chemie International Edition* **42**, 2883.

**Gallant et al. 1991**

Gallant M., Viet M. and Wuest J.D., 1991. Use of hydrogen bonds to control molecular aggregation. Association of dipyrindones joined by flexible spacers. *Journal of Organic Chemistry* **56**, 2284.

**Garcia et al. 2002**

Garcia R. and Perez R., 2002. Dynamic atomic force microscopy methods. *Surface Science Reports* **47**, 197.

**Garcia-Parajo et al. 1997**

Garcia-Parajo M., Longo C., Servat J., Gorostiza P. and Stanz F., 1997. Nanotribological properties of octadecyltrichlorosilane self-assembled ultrathin films studied by atomic force microscopy: contact and tapping modes. *Langmuir* **13**, 233.

**Garcia-Tellado et al. 1990**

Garcia-Tellado F., Goswami S., Chang S.K., Geib S.J. and Hamilton A.D., 1990. Molecular Recognition: A remarkably simple receptor for the selective complexation of dicarboxylic acids. *Journal of the American Chemical Society* **112**, 7393.

**Garjonyte et al. 2000**

Garjonyte R. and Malinauskas A., 2000. Amperometric glucose biosensors based on Prussian blue-and polyaniline-glucose oxidase modified electrodes. *Biosensors, Bioelectronics* **15**, 445.

**Garnier et al. 1996**

Garnier F., Horowitz G., Fichou D. and Yassar A., 1996. Molecular order in organic-based field effect transistors. *Synthetic Metals* **81**, 163.

**Garnier et al. 1993**

Garnier F., Yassar A., Hajloui R., Horowitz G., Deloffre F., Servet B., Ries S. and Alnot P., 1993. Molecular engineering of organic semiconductors: design of self assembly properties in conjugated thiophene oligomers. *Journal of American Chemistry Society* **115**, 8716.

**Geim et al. 2007**

Geim A.K. and Novoselov K.S., 2007. The rise of graphene. *Nature Materials* **6** 183.

**Gesquiere et al. 2007**

Gesquiere A., Jonkheijm P., Hoeben F.J.M., Schenning A.P.H.J., De Feyter S., Schryver F.C. and Meijer E.W., 2007. 2D structures of quadruple hydrogen bonded oligo(p-phenylenevinylene)s on graphite: self-assembly behaviour and expression of chirality. *Nanoletters* **4**, 7, 1175.

**Giessibl et al. 2003**

Giessibl F.J., 2003. Advanced in atomic force microscopy. *Reviews of Modern Physics* **75**, 949.

**Goldstein et al. 1992**

Goldstein A.N., Echer C.M. and Alvistatos A.,P., 1992. Melting in semiconductor nanocrystals. *Science* **256**, 1425.

**Gong et al. 2002**

Gong X., Milic T., Xu C., Batteas J.D. and Drain C.M., 2002. Preparation and characterization of porphyrin nanoparticles. *Journal of American Chemical Society* **124**, 14290.

**Gonzalez-Rodriguez et al. 2011**

Gonzalez-Rodriguez D. and Schenning A. P.H.J., 2011. Hydrogen bonded supramolecular  $\pi$ -functional materials. *Chemistry of Materials Review* **23**, 310.

**Goto et al. 2008**

Goto H., Yoneyama H., Togashi F., Ohta R., Tsujimoto A., Kita, Oshima K. and Rosenberg D., 2008. Preparation of conducting polymers by electrochemical methods and demonstration of a polymer battery. *Journal of Chemistry Education* **85**, 8, 167.

**Grose et al. 1992**

Grose K.R. and Bjeldanes, 1992. Oligomerization of indole-3-carbinol in aqueous acid. *Chemical Research in Toxicology* **5**, 188.

**Guillaud et al. 1998**

Guillaud G., Simon J. and Germain J.P., 1998. Metallophthalocyanines gas sensors, resistors and field-effect transistors. *Coordination Chemistry Reviews* **178**, 1433.

**Gundlach et al. 2002**

Gundlach D.J., Nichols J.A., Zhou L. and Jackson T.N., 2002. Thin-film transistors based on well ordered thermally evaporated naphthalene films. *Applied Physics Letters* **80**, 16, 2925.

**Gundlach et al. 1997**

Gundlach D.J., Lin Y.Y. and Jackson T.N., 1997. Oligophenyl-based organic thin film transistors. *Applied Physics Letters* **71**, 26, 3853.

**Gunther et al. 2001**

Gunther J. and Stupp S., 2001. Surface patterns of supramolecular materials. *Langmuir* **17**, 6530.

**Gutmann et al. 1967**

Gutmann F. and Lyons F.E., 1967. Organic semiconductors. *John Wiley and Sons, Inc.*

**Haberkorn et al. 2009**

Haberkorn N., Gutmann J.S. and Theato P., 2009. Template-assisted fabrication of free-standing nanorods arrays of a hole-conducting cross-linked triphenylamine derivative: toward ordered bulk-heterojunction solar cells. *ACS Nano* **3**, 6, 1415.

**Haddon et al. 1995**

Haddon R.C., Perel A.S., Morris A.C., Palstra T.T.M., Hebard A.F. and Flemming R.M., 1995. C<sub>60</sub> thin film transistors. *Applied physics letters* **67**, 121.

**Hamadani et al. 2005**

Hamdani B.H. and Natelson D., 2005. Extracting contact effects in organic FETs. *Proceedings of the IEEE* **93**, 7, 1306.

**Han et al. 2000**

- Han S.W., Joo S.W., Ha T.W., Kim Y. and Kim K., 2000. Adsorption characteristics of anthraquinone-2-carboxylic acid on gold. *Journal of Physical Chemistry B* **104**, 11987.
- Hartgerink et al. 2001**  
Hartgerink J.D., Zubarev E.R. and Stupp S.I., 2001. Supramolecular one-dimensional objects. *Current Opinion in Solid State and Materials Science* **5**, 355.
- Heeger et al. 2010**  
Heeger A.J., 2001. Semiconducting polymers: the third generation, 2010. *Chemical Society Reviews* **39**, 2354.
- Heeger et al. 2001**  
Heeger A.J., 2001. Semiconducting and metallic polymers: the fourth generation of polymeric materials. *Angewandte Chemie International Edition* **40**, 2591.
- Hirano et al. 2004**  
Hirano S., Masuya K. and Kuwaba M., 2004. Multi-nucleation-based formation of orientated zinc oxide microcrystals and films in aqueous solutions. *Journal of Physical Chemistry B* **108**, 4576.
- Hiremath et al. 2004**  
Hiremath R., Varney S.W. and Swift J.A., 2004. Orientated Crystal growth of 4-iodo-4'-nitrobiphenyl on polar self-assembled monolayer templates; a case of chemical epitaxy. *Chemistry of Materials* **16**, 4948.
- Hoeben et al. 2005**  
Hoeben F.J.M., Jonkheijm P., Meijer E.W. and Schenning A.P.H.J., 2005. About supramolecular assemblies of  $\pi$ -conjugated systems. *Chemistry Reviews* **105**, 1491.
- Hoffmann et al. 1991**  
Hoffmann R., Janiac C. and Kollmar C., 1991. A chemical approach to the orbitals of organic polymers. *Macromolecules* **24**, 13, 3725.
- Horlet et al. 2011**  
Horlet M., Kraus M., Brutting W. and Opiz A., 2011. Diiindenoperylene as ambipolar semiconductor: Influence of electrode materials and mobility asymmetry in organic field effect transistors. *Applied Physics letters* **98**, 233304.
- Horowitz et al. 2001**  
Horowitz G. and Hajlaoui M.E., 2001. Charge transport in polycrystalline oligothiophene thin film transistors. *Synthetic Metals* **121**, 1349.
- Horowitz et al. 1998**  
Horowitz G., 1998. Organic field effect transistors. *Advanced Materials* **10**, 5, 365.
- Hoshino et al. 2004**  
Hoshino S., Yoshida M., Uemura S., Kodzasa T., Takada N., Kamata T. and Yasa K., 2004. Influence of moisture on device characteristics of polythiophene based field-effect transistors. *Journal of Applied Physics* **95**, 9, 5088.
- Huang et al. 2009**  
Huang Y., Quan B., Wei Z., Liu G. and Sun L., 2009. Self-assembled organic functional nanotubes and nanorods and their sensory properties. *The Journal of Physical Chemistry C* **113**, 3929.
- Hunter et al. 1990**  
Hunter C.A. and Saunders J.K.M., 1990. The nature of  $\pi$ - $\pi$  interactions. *Journal of American Chemical Society* **112**, 5525.

**Ishii et al. 1998**

Ishii H., Murakami K., Sakurada E., Hosoya K. and Murakami Y., 1998. Polymerization of indole. Part 2. A new indole trimer. *Journal of Chemical Society Perkin Transactions* **1**, 2377.

**Ishii et al. 1998a**

Ishii H., Murakami K. and Sakurada E., 1998. Polymerization of indole. Part 3. Two indolylquinolines, an indole tetramer, and the dihydro derivative of the indole dimer. *Journal of Chemical Society Perkin Transactions* **1**, 2387.

**Ito et al. 1974**

Ito T., Shirakawa H. and Ikeda S., 1974. Simultaneous polymerization and formation of polyacetylene films on the surface of concentrated soluble Ziegler-type catalyst solution. *Journal of Polymer Science Polymer Chemistry Edition* **12**, 1,11.

**Jang et al. 2002**

Jang J., Oh J.H. and Stucky G.D., 2002. Fabrication of ultrafine conducting polymer and graphite nanoparticles. *Angewandte Chemie International Edition* **41**, 21, 4016.

**Jennings et al. 1997**

Jennings P., Jones A.C., Mount A.R. and Thompson A.D., 1997. Electrooxidation of 5-substituted indoles. *Faraday Transactions* **93**, 3791.

**Jennings et al. 1998**

Jennings P., Jones A. and Mount A., 1998. Fluorescence properties of 5-substituted indoles in solution. *Journal of Chemistry Society Faraday Transactions* **94**, 3619.

**Jensen et al. 2004**

Jensen B.W. and West K., 2004. Vapour-phase polymerisation of 3,4-ethylenedioxythiophene: a route to highly conducting polymer surface layers. *Macromolecules* **37**, 12, 4538.

**JEOL Ltd.**

JEOL publications ltd, 2006. A guide to scanning microscope observation.

**Jiang et al. 2008**

Jiang L., Fu Y., Li H. and Hu W., 2008. Single-Crystalline, size and orientation controllable nanowires and ultralong microwires of organic semiconductor with strong photoswitching property. *Journal of the American Chemical Society* **130**, 3937.

**Jin 2008**

Jin M.H.C., 2008. The thin-film deposition of conjugated molecules for organic electronics. *Journal of Minerals, Metals and Materials society* **60**, 6, 81.

**Jones et al. 2008**

Jones B. A., Facchetti A., Wasielewski M.R. and Marks T.J., 2008. Effects of aylene diimide thin film growth conditions on n-channel OFET performance. *Advanced Functional Materials* **18**, 1329.

**Jonkheijm et al. 2003**

Jonkheijm P., Hoeben F.J.M., Kleppinger R., van Herrikhuyzen J., Schenning A.P.H.J. and Meijer E.W., 2003. Transfer of  $\pi$ -conjugated columnar stacks from solution to surfaces. *Journal of the American Chemical Society* **125**, 15941.

**Jorgensen et al. 1990**

Jorgenses W.L. and Pranata J., 1990. Importnace of secondary interactions in triply hydrogen bonded complexes: Guanine-cytosine vs uracil-2,6-diaminopyridine. *Journal of the American Chemical Society* **112**, 2008.

**Kafaraani et al. 2005**

Kafarrani B.R., Kondo T., Yu J., Zhang Q., Dattilo D., Risko C., Jones S.C., Barlow S., Domercq B., Amy F., Kahn A., Bredas J.L., Kippelen B. and Marder S.R., 2005. High charge carrier mobility in an amorphous hexaazatrinaphthylene derivative. *Journal of American Chemical Society Communications* **127**, 16358.

**Kaneko 1981**

Kaneko T., 1981. Reactions of indole with hydroxyl radicals and X-ray crystal structure of a novel indole trimer, 14-diacetyldiindole [2,3-a:2'3'c] carbazole. *Chemical and Pharmaceutical Bulletin* **29**, 12, 3499.

**Kano et al. 2000**

Kano K., Fukuda K., Wakami H., Nishiyabu R. and Pasternack R., 2000. Factors influencing self-aggregation tendencies of cationic porphyrins in aqueous solution. *Journal of the American Chemical Society* **122**, 7494.

**Kasai et al. 1997**

Kasai H., Kamatani H., Yoshikawa Y., Okada S., Oikawa H., Nakanishi H., Watanabe A., Ito O. and Nakanishi H., 1997. Crystal size dependence of emission from perylene microcrystals. *Chemistry Letters* **26**, 11, 1181.

**Kasha et al. 1965**

Kasha M., Rawls H.R. and EL-Bayoumi M.A., 1965. The exciton model in molecular spectroscopy. *Pure and Applied Chemistry* **11**, 371.

**Kasha et al. 1963**

Kasha M., 1963. Energy transfer mechanisms and the molecular exciton model for molecular aggregates. *Radiation Research* **20**, 55.

**Katz 2004**

Katz H.E., 2004. Chemically sensitive field effect transistors and chemiresistors: new materials and device structures. *Electroanalysis* **16**, 22, 1837.

**Katz 2004a**

Katz H.E., 2004A. Recent advances in semiconductor performance and printing processes for organic transistor-based electronics. *Chemistry Materials* **16**, 4748.

**Katz et al. 2000**

Katz H.E., Lovinger A.J., Johnson J., Kloc C., Siergist, Li W., Lin Y.Y. and Dodabalapur A., 2000. A soluble and air-stable organic semiconductor with high electron mobility. *Nature* **404**, 478.

**Katz et al. 2000a**

Katz H.E., Lovinger A.J., Johnson J. and Li W., 2000. Naphthalenetertacarboxylic diimide-based n-channel transistor semiconductors: Structural variation and thiol-enhanced gold contacts. *Journal of the American Chemical Society* **122**, 7787.

**Katz et al. 1999**

Katz H.E., Li W., Lovinger A.J. and Laquindanum J., 1999. Solution-phase deposition of oligomeric TFT semiconductors. *Synthetic Metals* **102**, 897.

**Katz et al. 1998**



Katz H.E., Lovinger A.J. and Laquindanum J., 1998. Synthesis, solubility, and field-effect mobility of elongated and oxa-substituted  $\alpha,\omega$ -dialkyl thiophene oligomers. Extension of "polar intermediate" synthetic strategy and solution deposition on transistor substrates. *Chemistry of Materials* **10**, 633.

**Kim et al. 2011**

Kim F., Ren G. and Jenekhe S., 2011. One-dimensional nanostructures of  $\pi$ -conjugated molecular systems: Assembly, properties and applications from photovoltaics, sensors and nanophotonics to nanoelectronics. *Chemistry of Materials Review* **23**, 682.

**Kim et al. 2003**

Kim T., Park I. and Ryoo R., 2003. A synthetic route to ordered mesoporous carbon materials with graphitic pore walls. *Angewandte Chemie International Edition* **42**, 4375.

**Kim et al. 1996**

Kim E., Xia Y. and Whitesides G.M., 1996. Micromolding in Capillaries: Applications in Materials Science. *Journal of American Chemical Society* **118**, 5722.

**Kline et al. 2005**

Kline R.J., McGehee M.D., Kadnikova E.N., Liu J., Frechet J.M. and Toney M.F., 2005. Dependence of regioregular poly(3-hexylthiophene) film morphology and field-effect mobility on molecular weight. *Macromolecules* **38**, 3312.

**Kline et al. 2003**

Kline R.J., McGehee M.D., Kadnikova E.N., Liu J.S. and Frechet J.M.J., 2003. Molecular engineering of peripherally and axially modified phthalocyanines for optical limiting and nonlinear optics. *Advanced Materials* **15**, 19.

**Kobayashi et al. 2004**

Kobayashi S., Nishikawa T., Takenbu T., Mori S., Shimoda T., Mitani T., Shimotani H., Yoshimoto N., Ogawa S. and Iwasa Y., 2004. Control of carrier density by self-assembled monolayers in organic field-effect transistors. *Nature* **3**, 317.

**Kobayashi et al. 2003**

Kobayashi S., Takenobu T., Mori S., Fujiwara A., Isawasa Y., 2003. Fabrication and characterisation of C<sub>60</sub> thin film transistors with high field effect mobility. *Applied Physics Letters* **82**, 4581.

**Kraus et al. 2011**

Kraus M., Haug S., Brutting W. and Opiz A., 2011. Achievement of balanced electron and hole mobility in copper-phthalocyanine field-effect transistors by using a crystalline aliphatic passivation layer. *Organic Electronics* **12**, 731.

**Kumaran et al. 2010**

Kumaran N., Veneman P., Minch A., Mudalige A., Pemberton J., O'Brien D. and Armstrong N., 2010. Self-organized thin films of hydrogen bonded phthalocyanines: characterisation of the structure and electrical properties on nanometer length scales. *Chemistry of Materials* **22**, 2491.

**Kymissis et al. 2001**

Kymissis I., Dimitrakopoulos C.D. and Pushothman S., 2001. High performance bottom electrode organic thin film transistors. *IEEE Transactions on Electron Devices* **45**, 6, 1060.

**Lahiri et al. 2000**

Lahirir S., Thompson J.L. and Moore J.S., 2000. Solvophobicity driven  $\pi$ -stacking of phenylene ethylene macrocycles and oligomers. *Journal of the American Chemical Society* **122**, 11315.

**Lami et al. 1986**

Lami H. and Glasser N., 1985. Indole's solvachromatism revisited. *Journal of Chemical Physics* **84**, 597.

**Laquindanum et al. 1998**

Laquindanum J.G., Katz H.E. and Lovinger A.J., 1998. Synthesis, Morphology and field-effect mobility of anthradithiopenes. *Journal of the American Chemical Society* **120**, 664.

**Laquindanum et al. 1997**

Laquindanum J.G., Katz H.E., Lovinger A.J. and Dodabalapur A., 1997. Benzodithiophene rings as semiconductor building blocks. *Advanced Materials* **9**, 36.

**Laquindanum et al. 1996**

Laquindanum J.G., Katz H.E., Dodabalapur A. and Lovinger A.J., 1998. n-channel organic transistor materials based on naphthalene frameworks. *Journal of American Chemical Society* **118**, 11331.

**Latterini et al. 2006**

Latterini L., Roscini C., Carlotti B., Aloisi G.G. and Elisei F., 2006. Synthesis and characterization of perylene nanoparticles. *Physica status solidi* **203**, 6, 1470.

**Leclerc et al. 2004**

Leclerc P., Surin M., Viville P., Lazzaroni R., Kilbinger A.F.M., Henze O., Feast W.J., Cavallini M., Biscarni F., Schenning A.P.H.J. and Meijer E.W., 2004. About oligothiophene self-assembly: from aggregation in solution to solid-state nanostructures. *Chemistry of Materials* **16**, 4452.

**Lee et al. 2007**

Lee Y., Park S-Y., Kim K.B. and Lee J.K., 2007. Fabrication of hierarchical structures on a polymer surface to mimic natural superhydrophobic surfaces. *Advanced Materials* **19**, 2330.

**Lee et al. 2002**

Lee J.K., Koh W.K., Chaeb W.S. and Kim Y.R., 2002. Novel synthesis of organic nanowires and their optical properties. *Chemical Communications* 138.

**Lemaur et al. 2004**

Lemaur V., da Silva Filho D. A., Coropceanu V., Lehmann M., Geerts Y., Pirirs J., Debije M.G., van der Craats A.M., Senthikumar K., Siebbeles L.D., Warman J.M., Bredas J.L. and Cornil J., 2004. Charge Transport properties in discotic liquid crystals: a quantum-chemical insight into structure-property relationships. *Journal of the American Chemical Society* **126**, 3271.

**Leufgen et al. 2004**

Leufgen M. Bass U., Muck T., Borzenco T., Schmidt G., Geurts J., Wagner V. and Molenkamp L.W., 2006. Optimized sub-micron organic thin-film transistors: the influence of contacts and oxide thickness. *Synthetic Metals* **146**, 341.

**Lewis et al. 1997**

Lewis T.W. and Wallace G.G., 1997. Communicative polymers: the basis for development for intelligent materials. *Journal of Chemical Education* **74**, 6, 703.

**Li et al. 2004**

Li S., He L., Xiong F., Li Y. and Wang G., 2004. Enhanced fluorescent emission of organic nanoparticles of an intramolecular proton transfer compound and spontaneous formation of one-dimensional nanostructures. *Journal of Physical Chemistry B* **108**, 10887.

**Li et al. 2003**

Li L.S. and Alivisatos P., 2003. Semiconductor nanorod liquid crystals and their assembly on a substrate. *Advanced Materials* **15**, 5, 408.

**Li et al. 2003a**

Li G., Wang T., Bhosale S., Zhang Y. and Fuhrhop J.H., 2003. Completely reversible aggregation of nanoparticles by varying the pH. *Colloid and Polymer Science short communication* **281**, 1099.

**Lim et al. 2009**

Lim J.A., Lee H.S., Lee W.H. and Cho K., 2009. Control of the morphology and structural development of solution-processed functionalized acenes for high performance organic transistors. *Advanced Functional Materials* **19**, 1515.

**Lim et al. 2004**

Lim S.J., An B.K., Jung S.D., Chung M.A. and Park S.Y., 2004. Photoswitchable organic nanoparticles and a polymer film employing multifunctional molecules with enhanced fluorescence emission and bistable photochromism. *Angewandte Chemie International Edition* **43**, 6346.

**Lin et al. 1997**

Lin Y.Y., Gundlach D.J., Nelson S.F. and Jackson T.N., 1997. Stacked pentacene layer organic thin-film transistors with improved characteristics. *IEEE Electron Device Letters* **18**, 12, 606.

**Ling et al. 2004**

Ling M.M. and Bao Z., 2004. Thin film deposition, patterning and printing in thin film transistors. *Chemistry of Materials* **16**, 4824.

**Liu et al. 2009**

Liu N., Zhou Y., Wang L., Peng J., Wang J., Pei J. and Cao Y., 2009. In situ growing and patterning of aligned organic nanowire arrays via dip coating. *Langmuir* **25**, 665.

**Liu et al. 2004**

Liu H., Li Y.J., Jiang L., Gn H.Y., Liu H.B., Li Y.L., Zhuang J.P., Lu F.S. and Zhu D.B., 2004. Assembly and characterization of novel hydrogen-bond-induced nanoscale rods. *Journal of Organic Chemistry* **69**, 9049.

**Liu et al. 2003**

Liu J., Lin Y., Liang L., Voigt J.A., Huber D.L., Tian Z.R., Coker E., McKenzie B. and McDermott M.J., 2003. Templateless assembly of molecularly aligned conductive polymer nanowires: a new approach for orientated nanostructures. *Chemistry A European Journal* **9**, 3, 605.

**Liu et al. 2003a**

Liu H., Li Y., Xiao S., Gan H., Jiu T., Li H., Jiang L., Zhu D., Yu D. and Xiang B., 2003. Synthesis of organic one-dimensional nanomaterials by solid-phase reaction. *Journal of the American Chemistry Society* **125**, 10794.

**Lockilin et al. 2006**

Locklin J. and Bao S., 2006. Effect of morphology on organic thin film transistor sensors. *Analytical and Bioanalytical Chemistry* **384**, 336.

**MacDiarmid et al. 2001**

MacDiarmid A., 2001. "Synthetic metals": A novel role for organic polymers (Nobel lecture). *Angewandte Chemie International Edition* **40**, 2581.

**Macdonald et al. 1991**

Macdonald B.F., Cole R.J. and Koutsos V., 2004. The formation of dewetting structures after evaporation of n-dodecane on graphite studied by atomic force microscopy. *Surface Science* **548**, 41.

**MacInnes Jr. et al. 1981**

MacInnes Jr. D., Druy M.A., Nigrey P.J., Nairns D.P., MacDiarmid A.J. and Heeger A.J., 1981. Organic batteries: reversible n- and p-type electrochemical doping of polyecetylene. *Journal of Chemical Society: Chemical Communications* **317**.

**Mackintosh et al. 1995**

Mackintosh J.G., Redpath C.R., Jones A.C., Langridge-Smith P.R.R. and Mount A.R., 1995. The electropolymerization and characterization of 5-cyanoindole. *Journal of Electroanalytical chemistry* **388**, 179.

**Mackintosh et al. 1994**

Mackintosh J.G., Redpath C.R., Jones A.C., Langridge-Smith P.R.R., Reed D.R. and Mount A.R., 1994. Determination of the structure of the electropolymerized indole-5-carboxylic acid. *Journal of Electroanalytical chemistry* **375**, 163.

**Mackintosh et al. 1994a**

Mackintosh J.G. and Mount A.R., 1994. Electropolymerisation of indole-5-carboxylic acid. *Journal of the Chemical Society, Faraday Transactions* **90**, 8, 1121.

**Maeda et al. 2006**

Maeda S., Momose F., Saitoh Y. and Saitoh T., 2006. Method for producing timer of indole derivative, and trimer of indole derivative and laminated structure thereof. *United States Patent* US7585981B2.

**Maeda et al. 1996**

Maeda H., 1996. Atomic force microscopy studies for investigating the smectic structures of colloidal crystals of  $\beta$ -FeOOH. *Langmuir* **12**, 1446.

**Malefant et al. 2002**

Malefant P.R.L., Dimitrakopoulos C.D., Gelorme J.D., Kosbar L.L. and Graham T.O., 2002. n-type organic thin-film transistor with high field-effect mobility based on a N,N'-dialkyl-3,4,9,10-perylene tetracarboxylic diimide derivative. *Applied Physics Letters* **80**, 14, 2517.

**March et al. 1992**

March J., 1992. *Advanced organic chemistry: reactions, mechanisms and structure*. John Wiley and sons inc., 1992.

**Martin et al. 1999**

Martin R.E., Diederich F., 1999. Linear monodisperse  $\pi$ -conjugated oligomers. *Angewandte Chemie International Edition* **38**, 1350.

**Meijer et al. 2003**

Meijer E.J., 2003. Solution-processed ambipolar organic field effect transistors and invertors. *Nature Materials* **2**, 678.

**Meijer et al. 2003a**

Meijer E.J., Detcheverry C., Baesjou P.J., van Veenendaal E., deLeeuw D.M. and Klapwijk T.M., 2003. Dopant density determination in disordered organic field effect transistors. *Journal of Applied Physics* **93**, 4831.

**Meijer et al. 2002**

Meijer E.J., Tanasse C., Blom P.W.M., van Veenendaal E., Huisman B.H., deLeeuw D.M. and Klapwijk T.M., 2003. Switch-on voltage from disordered organic field-effect transistors. *Applied Physics letters* **80**, 3838.

**Minelli et al. 2005**

Minelli C., Hinderling C., Heinzelmann H., Pugin R., Liley M., 2005. Micrometer-long gold nanowires fabricated using block copolymer templates. *Langmuir* **21**, 7080.

**Moon et al. 2004**

Moon H., Zeis R., Borkent E.J., Besnard C., Lovinger A.J., Siegrist T., Kloc C. and Bao Z., 2004. Synthesis, crystal structure and transistor performance of tetracene derivatives. *Journal of American Chemistry Society* **126**, 15322.

**Mount et al. 1994**

Mount A. and Thomson A., 1994. Electrooxidation of N-methylindole. *Journal of Chemical Society, Faraday Transactions* **94**, 553

**Murphy et al. 2005**

Murphy A.R., Chang P.R., VanDyke P., Liu J., Frechet J.M., Subramanian V., DeLongchamp D., Sambasivan S., Fischer D. and Lin E., 2005. Self-assembly, molecular ordering, and charge mobility in solution-processed ultra-thin oligothiophene films. *Chemistry of Materials* **17**, 6033.

**Murray et al. 1992**

Murray T.J. and Zimmerman S.C., 1992. New triply hydrogen bonded complexes with highly variable stabilities. *Journal of the American Chemical Society* **114**, 4010.

**Nakanishi et al. 1998**

Nakanishi H. and Katagi H., 1998. Microcrystals of polydiacetylene derivatives and their linear and nonlinear optical properties. *Supramolecular Science*. **5**, 289.

**Narasimhan et al. 1998**

Narasimhan M., Hagler M. Cammarata V. and Thakur M., 1998. Junction devices based on sulfonated polyaniline. *Applied Physics Letters* **72**, 9, 1998.

**Nath et al. 1998**

Nath S., Pal H., Palit D.K., Sapre A.V. and Mittal J.P., 1998. Aggregation of fullerene, C60 in benzonitrile. *Journal of Physical Chemistry B* **102**, 10158.

**Necliudov et al. 2000**

Necliudov P.V. and Shur M.S., 2000. Modelling of organic thin film transistors of different designs. *Journal of Applied Physics* **88**, 11, 6594.

**Newman et al. 2004**

Newman C.R., Frisbie C.D., Fihlo D.A., Bredas J.L., Ewbank P.C. and Mann K.R., 2004. Introduction to organic thin film transistors and design of n-channel organic semiconductors. *Chemistry Materials* **16**, 4436.

**Nguyen et al. 2007**



Nguyen T.Q., Martel R., Bushely M., Avouris P., Carlsen A., Nuckolls C. and Brus L., 2007. Self-assembly of 1-D organic semiconductor nanostructures. *Physical Chemistry Chemical Physics* **9**, 1515.

**Nguyen et al. 2004**

Nguyen T.Q., Martel R., Avouris P., Bushely M., Brus L. and Nuckolls C., 2004. Molecularly interactions in one-dimensional organic nanostructures. *Journal of the American Chemical Society* **126**, 5234.

**Nguyen et al. 2002**

Nguyen T.Q., Bushey M.L., Brus L.E. and Nuckolls, 2002. Tuning intermolecular attraction to create polar order and one-dimensional nanostructures on surface. *Journal of the American Chemical Society* **124**, 15051.

**Nigrey et al. 1979**

Nigrey P.J., MacDiarmid A.G. and Heeger A.J., 1979. Electrochemistry of polyacetylene: electrochemical doping of polyacetylene films to the metallic state. *Journal of Chemical Society: Chemical Communications* **594**.

**Njikang et al. 2008**

Njikang G.N., Cao L. and Gauthier M., 2008. Self-assembly of arborescent polystyrene-graft-poly(ethylene oxide) copolymers at the air/water interface. *Macromolecular Chemistry and Physics* **209**, 9, 907.

**O'Carroll et al. 2007**

O'Carroll D., Lieberwirth I. and Redmond G., 2007. Melt-processed polyfluorene nanowires as active waveguides. *Small* **3**, 7, 1178.

**Okada et al. 2003**

Okada S. and Segawa H., 2003. Substituent-control exciton in J-aggregates of protonated water-insoluble porphyrins. *Journal of the American Chemical Society* **125**, 2792.

**Ong et al. 2005**

Ong B.S., Wu Y., Liu P. and Gardner S., 2005. Structurally ordered polythiophene nanoparticles for high performance organic thin film transistors. *Advanced Materials* **17**, 1141.

**MacDiarmid et al. 1980**

MacDiarmid A.G. and Heeger A.J., 1980. Organic metals and semiconductors: the chemistry of polyacetylene and its derivatives. *Synthetic Metals* **1**, 101.

**MacDiarmid et al. 1987**

MacDiarmid A.G., Chiang A.C. and Richter A.F., 1987. Polyaniline: a new concept in conducting polymers. *Synthetic Metals* **18**, 285.

**MacDiarmid et al. 2001**

MacDiarmid A., 2001. "Synthetic metals": A novel role for organic polymers (Nobel lecture). *Angewandte Chemie International Edition* **40**, 2581.

**Maeda et al. 1996**

Maeda H., 1996. Atomic force microscopy studies for investigating the smectic structures of colloidal crystals of  $\beta$ -FeOOH. *Langmuir* **12**, 1446.

**Maiti et al. 1998**

Maiti N., Mazamudar S. and Periasamy N., 1998. J and H-aggregates of porphyrin-surfactant complexes: time resolved fluorescence and other spectroscopic studies. *Journal of Physical Chemistry B* **102**, 1528.

**Maiti et al. 1995**

Maiti N., Ravikanth M., Mazamudar S. and Periasamy N., 1995. Fluorescence dynamics of noncovalently linked porphyrin dimers and aggregates. *Journal of Physical Chemistry* **99**, 17192.

**Marmur et al. 2000**

Marmur A., 2000. Dissolution and self-assembly: The solvophobic/hydrophobic effect. *Journal of the American Chemical Society* **122**, 2120.

**Mas-Torrent et al. 2004**

Mas-Torrent M., Hadley P., Bromley S., Ribas X., Tarres J., Mas M., Molins E., Vaciana J. and Rovira C., 2004. Correlation between crystal structure and mobility in organic field-effect transistors based on single crystals of terathiafulvalene derivatives. *Journal of the American Chemical Society* **126**, 8546.

**Mataga et al. 1956**

Mataga N. and Kaifu Y. and Koizumi M., 1956. Solvent effects upon fluorescence spectra and the dipole moments of excited molecules. *Bulletin of the Chemical Society of Japan* **29**, 4, 465.

**Metwalli et al. 2006**

Metwalli E., Haines D., Becker O., Conzone S. and Pantano C.G., 2006. Surface characterizations of mono-, di-, and tri-aminosilane treated glass substrates. *Journal of Colloid and Interface Science* **298**, 825.

**Miao et al. 2009**

Miao X., Gao A., Li Z., Hiroto S., Shinokubo, Osuka A. and Deng W., 2009. First self-assembly study of large  $\pi$ -conjugated corrole dimers on solid substrates. *Applied Surface Science* **255**, 5885.

**Milic et al. 2002**

Milic T.N., Chi N., Yablon D.G., Flynn G.W., Batteas J.D. and Drain C.M., 2002. Controlled hierarchical self-assembly and deposition of nanoscale photonic materials. *Angewandte Chemie International Edition* **41**, 2117.

**Monti et al. 2004**

Monto D., Venanzi M., Russo M., Bussetti G., Goletti C., Montalti M., Zaccheroni N., Prodi L., Rella R., Manera M.G., Mancini G., Di Ntale C. and Paolesse R., 2004. Spontaneous deposition of amphiphilic porphyrin films on glass. *The New Journal of Chemistry* **28**, 1123.

**Padmaker et al. 1999**

Padmaker A.s., Kargupta K. and Sharma A., 1999. Instability and dewetting of evaporating thin films on partially and completely wettable substrates. *Journal of Chemical Physics* **110**, 3, 1735.

**Pandey et al. 1998**

Pandey P.C. and Prakash R., 1998. Characterization of electropolymerized polyindole. *Journal of the Electrochemical Society* **145**, 12, 4103.

**Pandey et al. 1998a**

Pandey P.C. and Prakash R., 1998. Electrochemical synthesis of polyindole and its evaluation for rechargeable battery applications. *Journal of the Electrochemical Society* **145**, 3, 999.

**Pandey 1999**

Pandey P.C., 1999. Copper (II) ion sensor based on electropolymerized undoped-polyindole modified electrode. *Sensors and Actuators B* **54**, 210.

**Pandey et al. 1998b**

Pandey P.C. and Prakash R., 1998. Polyindole modified potassium ion-sensor using 18-crown-6 mediated PVC matrix membrane. *Sensors and Actuators B* **46**, 61.

**Park et al. 2007**

Park Y.D., Lim J.A., Lee H.S. and Cho K., 2007. Interface engineering in organic transistors. *Materials Today* **10**, 3, 46.

**Peng et al. 1999**

Peng Z., Xu B., Zhang J. and Pan Y., 1999. Synthesis and optical properties of water soluble poly(p-phenylenevinylene)s. *Chemical Communications* 1855.

**Philip et al. 1996**

Philip D. and Stoddart J.F., 1996. Self assembly in natural and unnatural systems. *Angewandte Chemie International Edition* **35**, 1154.

**Piok et al. 2003**

Piok T., Gamerith S., Gadermaier C., Plank H., Wenzl P., Patil S., 2003. Organic light-emitting device fabrication from semiconducting nanospheres. *Advanced Materials* **15**, 10, 800.

**Podzorov et al. 2003**

Podzorov V., Pudalov V.M. and Gershenson M.E., 2003. Field-effect transistors on rubene single crystals with parylene gate insulator. *Applied Physics Letters* **82**, 1739.

**Pramanik et al. 2006**

Pramanik S., Bandyopadhyay S., Garre K. and Cahay M., 2006. Normal and inverse spin-valve effect in organic semiconducting nanowires and the background monotonic magnetoresistance. *Physical Review B* **74**, 235329.

**Prins et al. 2001**

Prins L.J., Reinhoudt D.N. and Timmerman P., 2001. Noncovalent synthesis using hydrogen bonding. *Angewandte Chemie International edition* **40**, 2383.

**Pron et al. 2010**

Pron A., Garhys Zagorska M., Djurado D. and Demadrille R., 2010. Electroactive materials for organic electronics; preparation strategies, structural aspects and characterisation techniques. *Chemical Society Reviews* **39**, 2577

**Reed et al. 1989**

Reed M.A., Frensley W.R., Matyi R.J., Randall J.A. and Seabaugh A.C., 1989. Realization of a three terminal resonant tunnelling device: The bipolar quantum resonant tunnelling transistor. *Applied Physics Letters* **54**, 1034.

**Reichardt et al. 2003**

Reichardt C., 2003. Solvents and solvent effects in organic chemistry. Wiley-VCH, Weinheim.

**Riby et al. 2000**

Riby J.E., Feng C., Chang Y., Schaldach M., Firestone G.L. and Bjeldanes L.F., 2000. The major cyclic trimeric product of indole-3-carbinol is a strong agonist of the estrogen receptor signalling pathway. *Biochemistry* **39**, 910.

**Richardson et al. 2000**

Richardson T. H., 2000. Functional organic and polymeric materials. John Wiley and sons, ltd, Chichester.

**Rocherfort et al. 2002**

Rocherfort A., Martel R. and Avouris P., 2002. Electrical switching in  $\pi$ -resonant 1D intermolecular channels. *Nano Letters* **2**, 8, 877.

**Rogers et al. 1998**

Rogers J.A., Bao Z. and Raju V.R., 1998. Nonphotolithographic fabrication of organic transistors with micron feature sizes. *Applied Physics Letters* **72**, 2716.

**Roncali et al. 1997**

Roncali J., 1997. Synthetic principles for band gap control in linear  $\pi$ -conjugated systems. *Chemical Reviews* **97**, 1, 173.

**Samori et al. 2001**

Samori P., Keil M., Friedlein R., Birgerson J., Watson M., Mullen K., Salaneck W.R. and Rabe J.P., 2001. Growth of ordered hexakis-dodecyl-hexabenzocoronene layers from solution: A SFM and ARUPS study. *Journal of Physical Chemistry B* **105**, 11114.

**Samori et al. 1998**

Samori P., Francke V., Mangel T., Mullen and Rabe J.P., 1998. Poly-para-phenylene assemblies for a potential molecular nanowire: an SFM study. *Optical Materials* **9**, 390.

**Samori et al. 1998a**

Samori P., Francke V., Mullen K. and Rabe J.P., 1998. Growth of solution cast macromolecular  $\pi$ -conjugated nanoribbons on mica. *Thin Solid Films* **336**, 13.

**Saragi et al. 2005**

Saragi T.P.I., Fuhrmann-Lieker T. and Salbeck J., 2005. High ON/OFF ratios and stability of amorphous organic field-effect transistors based on spiro-linked compounds. *Synthetic Materials* **148**, 267.

**Saragi et al. 2004**

Saragi T.P.I., 2004. PhD thesis, University of Kassel.

**Saxena et al. 2003**

Saxena V. and Malhotra B.D., 2003. Prospects of conducting polymers in molecular electronics. *Current Applied Physics* **3**, 293.

**Schenning et al. 2005**

Schenning A. and Meijer E., 2005. Supramolecular electronics; nanowires from self-assembled  $\pi$ -conjugated systems. *Chemistry Communications* 3245.

**Schlenker et al. 2007**

Schlenker E., Bakin A., Schmid H., Mader W., Sievers S., Albrecht M., Ronning C., Muller S., Al-Suleiman M., Postels B., Wehmann H.H., Siegner U. and Waag A., 2007. Properties of V-implanted ZnO nanorods. *Nanotechnology* **18**, 125609.

**Schon et al. 2001**

Schon J.H., Dodabalapur A., Bao Z., Kloc C., Schenker O. and Battlog B., 2001. Gate-induced superconductivity in a solution-processed organic polymer thin film. *Nature* **410**, 189.

**Schoonbeek et al. 1999**

Schoonbeek F.S., van Esch J.H., Wegewijs B., Rep D.B.A., de Haas M.P., Klapwijk T.M., Kellog R.M. and Feringa B.L., 1999. Efficient intermolecular charge transport in self assembled fibers of mono- and bithiophene bisurea compounds. *Angewandte Chemie International Edition* **38**, 10, 1393.

**Schwab et al. 2003**

Schwab A.D., Smith D.E., Rich C.R., Young E.R., Smith W.F. and dePaula J.C., 2003. Porphyrin nanorods. *Journal of Physical Chemistry B* **107**, 11339.

**Seeman et al. 2001**

Seeman R., Herminghaus S. and Jacobs K., 2001. Gaining control of pattern formation of dewetting liquid films. *Journal of Physics Condensed Matter* **13**, 4925.

**Seo et al. 2006**

Seo S.H., Tew G.N. and Chang J.Y., 2006. Lyotropic columnar liquid crystals based on polycatenar 1H-imidazole amphiphilics and their assembly into bundles at the surface of silicon. *Soft Matter* **2**, 886.

**Seo et al. 2006a**

Seo S., Park S.B.N. and Evans P.G., 2006. Ambipolar rubrene thin film transistors. *Applied Physics Letters* **88**, 232114.

**Shao et al. 2011**

Shao W., Dong H., Jiang L. and Hu W., 2011. Morphology control for high performance organic thin film transistors. *Chemical Science* **2**, 590.

**Shipway et al. 2000**

Shipway A.N., Katz E. And Willner I., 2000. Nanoparticle arrays on surfaces for electronic, optical and sensor applications. *Chemphyschem* **1**, 18.

**Shaw et al. 2001**

Shaw J.M. and Seidler P.F., 2001. Organic electronics: introduction. *IBM Journal of Research and Development* **45**, 3.

**Shea et al. 2007**

Shea P.B., Pattison L.R., Kawano M., Chen C., Chen J., Petroff P., Martin D.C., Yamada H., Ono N. and Kanicki J., 2007. Solution-processed polycrystalline copper tetrabenzoporphyrin thin-film transistors. *Synthetic Metals* **157**, 190.

**Shea et al. 2006**

Shea P.B. and Kanicki J., 2006. Solution-processed nickel tetrabenzoporphyrin thin-film transistors. *Journal of Applied Physics* **100**, 34502.

**Shirakawa 2001**

Shirakawa H., 2001. The discovery of polyacetylene film: the dawning of an era of conducting polymers. *Angewandte Chemie International Edition* **40**, 2574.

**Shirakawa et al. 1977**

Shirakawa H., Louis F.J., MacDiarmid A.G., Chiang C.K. and Heeger A.J., 1977. Synthesis of electrically conducting organic polymers: halogen derivatives of polyacetylene. *Journal of Chemistry Society: Chemical Communications* **578**.

**Shirota et al. 2007**

Shirota Y. and Kageyama H., 2007. Charge carrier transporting molecular materials and their applications in devices. *Chemistry Reviews* **107**, 953.

**Sijbesma et al. 2003**



Sibjesma R.P. and Meijer E.W., 2003. Quadrupole hydrogen bonded systems. *Chemistry Communications* 5

**Simkiene et al. 2006**

Simkiene I., Sabataityte J., Babonas G.J., Reza A. and Beinoras J., 2006. Self-organization of porphyrin structures on Si. *Materials Science and Engineering C* **26**, 1007.

**Simson et al. 2004**

Simson C.D., Wu J.S., Watson M.D. and Mullen K., 2004. From graphite molecules to columnar superstructures-an exercise in nanoscience.. *Journal of Materials Chemistry* **14**, 494.

**Singh et al. 2006**

Singh T.B., Erten S., Gunes S., Zafer C., Turkmen G., Kuban B., Teoman Y., Sariciftci N.S. and Icli S., 2006. Soluble derivatives of perylene and naphthalene diimide for n-channel organic field-effect transistors. *Organic Electronics* **7**, 480.

**Singh et al. 2006a**

Singh T.B., Senkarabacak P. and Sariciftci N.S., 2006. Organic inverter circuits employing ambipolar pentacene field-effect transistors. *Applied Physics letters* **89**, 33512.

**Singh et al. 2005**

Singh T.B., Meghdadi F., Gunes S., Marjanovic N., Horowitz G., Lang P., Bauer S. and Sariciftci N.S., 2005. High performance ambipolar pentacene organic field effect transistors on poly(vinyl alcohol) organic gate dielectric. *Advanced Materials* **17**, 2315.

**Sirringhaus 2005**

Sirringhaus H., 2005. Device physics of solution processed organic field effect transistors. *Advanced Materials* **17**, 2411.

**Sirrinhaus et al. 1999**

Sirrinhaus H., Brown P.J., Friend R.H., Nielson M.M., Bechgaard K., Langeveld V., Spiering A.J.H., Jannsesn R.A.J., Meijer E. W., Herwig P. and de Leeuw. Two-dimensional charge transport in self-organized, high-mobility conjugate polymers. *Nature* **401**, 685.

**Siiringhaus et al. 1998**

Sirringhaus H., Tessler N. and Friend R.H., 1998. Integrated optoelectronic devices based on conjugated polymers. *Science* **280**, 1741.

**Sivakkumar et al. 2005**

Sivakkumar S.R., Angulakshmi N. and Saraswathi R., 2005. Characterization of Poly(indole-5-carboxylic acid) in aqueous rechargeable cells. *Journal of Applied Polymer Science* **98**, 917.

**Snitka et al. 2005**

Snitka V., Rackaitis M. and Rodaite R., 2005. Assemblies of TPPS<sub>4</sub> porphyrin investigated by TEM, SPM and UV-vis spectroscopy. *Sensors and Actuators B* **109**, 159.

**So et al. 1992**

So F. and Forest S.R., 1992. Evidence for exciton confinement in crystalline organic multiple quantum wells. *Physical review letters* **66**, 2649.

**Soberanis et al. 2009**

Soberanis C.R., Bonilla R.A.L., Estrada H., Manzano C.V., Rodriguez L. and Can A.C., 2009. Microstructure formation in polymer composites prepared with polypropylene and a polyaniline complex. *Polymer International* **58**, 817.

**Sounart et al. 2006**

Sounart T.L., Liu J., Voigt J.A., Hsu J.W.P., Spoerke E.D., Tian Z. and Jiang Y., 2006. Sequential nucleation and growth of complex nanostructured films. *Advanced Functional Materials* **16**, 335.

**Stallinga et al. 2006**

Stallinga P. and Gomes H.L., 2006. Modeling electrical characteristics of thin-film field-effect transistors 1. Trap-free materials. *Synthetic Metals* **156**, 1305.

**Stathos et al. 1997**

Stathos E., Lianos P., Del Monte F., Levy D. and Tsiourvas D., 1997. Formation of TiO<sub>2</sub> nanoparticles in reverse micelles and their deposition as thin films on glass substrates. *Langmuir* **13**, 16, 4295.

**Steen et al. 1974**

Steen H.B., 1974. Wavelength dependence of the quantum yield of fluorescence and photoionization of indoles. *Journal of Chemical Physics* **61**, 10 397.

**Sun et al. 2010**

Sun X., Di C. and Liu Y., 2010. Engineering of the dielectric-semiconductor interface in organic field effect transistors. *Journal of Materials Chemistry* **20**, 2599.

**Sun et al. 1989**

Sun B., Jones J.J., Burford R.P. and Skylas K. Stability and mechanical properties of electrochemically prepared conducting polypyrrole films. *Journal of Materials Science* **24**, 4024.

**Surin et al. 2004**

Surin M., Lazzaroni R., Feast W.J., Schenning A.P.H.J., Meijer E.W. and Leclerc Ph. Oligothiophene-based nanostructures from solution to solid-state aggregates. *Synthetic Metals* **147**, 67.

**Tada et al. 2000**

Tada H., Touda H., Takada M. and Matsushige K., 2000. Quasi-intrinsic semiconducting state of titanyl-phthalocyanine films obtained under ultrahigh vacuum conditions. *Applied Physics Letters* **76**, 7, 873.

**Tagmouti et al. 1997**

Tagmouti S., Oueriaagli A., Outzourhit A., Khaidar M., Amezziane E.L., Yassar A., Youssioufi H.G. and Garnire F., 1997. Effect of water vapour on poly(3-methylthiophene)/Mo Schottky diodes. *Synthetic Metals* **88**, 109.

**Takahashi et al. 2006**

Takahashi Y., Hasegawa T., Abe Y., Tookura Y. and Saito G., 2006. Organic metal electrodes for controlled p- and n-type carrier injections in organic field transistors. *Applied Physics Letters* **88**, 73504.

**Takahashi et al. 2005**

Takahashi Y., Hasegawa T., Abe Y., Tookura Y., Nishimura K. and Saito G., 2005. Tuning of electron injection for n-type organic transistor based on charge-transfer compounds. *Applied Physics Letters* **86**, 63504.

**Takazawa et al. 2007**

Takazawa K., 2007. Waveguiding properties of fiber-shaped aggregates self-assembled from thiacyanine dye molecules. *Journal of Physical Chemistry C* **111**, 8671.

**Takazawa et al. 2005**

Takazawa K., Kitahama Y., Kimura Y. and Kido G., 2005. Optical waveguide self-assembled from organic dye molecules in solution. *Nano letters* **5**, 1293.

**Takenobu et al. 2007**

Takenobu T., Takahashi T., 2007. Effect of metal electrodes on rubrene single-crystal transistors. *Applied Physics Letters* **90**, 13507.

**Talbi et al. 1998**

Talbi H. and Bilaud D., 1997. Oxidative electropolymerization of 5-nitroindole. *Synthetic Metals* **97**, 239.

**Talbi et al. 1998a**

Talbi H., Monard J., Loos M. and Bilaud D., 1998. Theoretical study of indole polymerization. *Journal of Molecular Structure (Theochem)* **434**, 129.

**Talbi et al. 1998b**

Talbi H. and Bilaud D., 1998. Electrochemical properties of polyindole and poly(5-cyanoindole) in  $\text{LiClO}_4$ -acetonitrile and in HCl and  $\text{HClO}_4$  solutions. *Synthetic Metals* **93**, 105.

**Talbi et al. 1997**

Talbi H., Humbert B. and Bilaud D., 1997. Polyindole and poly(5-cyanoindole): electrochemical and FT-IR spectroscopic comparative studies. *Synthetic Metals* **84**, 875.

**Tanaka et al. 2005**

Tanaka S., Shirakawa M., Kaneko K., Takeuchi M. and Shinkai S., 2005. Porphyrin-based organogels: control of the aggregation mode by a pyridine-carboxylic acid interaction. *Langmuir* **21**, 2163.

**Tang et al. 2006**

Tang Q., Li H., He M., Hu W., Liu C., Chen J., Wang C., Liu Y. and Zhu D., 2006. Low threshold voltage transistors based on individual single-crystalline submicrometer-sized ribbons of copper phthalocyanine. *Advanced Materials* **18**, 65.

**Tang et al. 1988**

Tang C.W., and Van Slyke S.A., 1998. Organic Electroluminescent diodes. *Applied Physics Letters* **51**, 913.

**Tapponier et al. 2005**

Tapponier A., Biaggio I. And Gunter P., 2005. Ultrapure C60 field-effect transistors and the effects of oxygen exposure. *Applied Physics Letters* **86**, 112114.

**Tautz et al. 2007**

Tautz F.S., 2007. Structure and bonding of large aromatic molecules on noble metal surfaces: the example of PTCDA. *Progress in Surface Science* **82**, 479.

**Tatischeff et al. 1978**

Tatischeff I., Klein R., Zemb T. and Duquesne M., 1977. Solvent interactions with the indole chromophore. *Chemical Physics letters* **54**, 2, 394.

**Taurz et al. 2007**

Tautz F.S., 2007. Structure and bonding of large aromatic molecules on noble metal surfaces: the example of PTCDA. *Progress in Surface Science* **82**, 479.

**Templeton et al. 1999**

Templeton A.C., Chen S., Gross S.M. and Murray R.W., 1999. Water soluble gold clusters protected by tiopronin and coenzyme A monolayers. *Langmuir* **15**, 66.

**Tessler et al. 2009**

Tessler N., Preezant Y., Rappaport N. and Roichman Y., 2009. Charge transport in disordered organic materials and its relevance to thin film devices- a tutorial review. *Advanced Materials* **21**, 2741.

**Tian et al. 2004**

Tian Z., Chen Y., Yang W., Yao J., Zhu L. and Shuai Z., 2004. Low-dimensional aggregates from stilbazolium-like dyes. *Angewandte Chemie International Edition* **43**, 4060.

**Tistra et al. 1990**

Tilstra L., Sattler M.C., Cherry W.R. and Barkley M.D., 1990. Fluorescence of rotationally constrained tryptophan derivative: 3-carboxy-1,2,3,4-tetrahydro-2-carboline. *Journal of American Chemical Society* **112**, 9176.

**Tong et al. 2007**

Tong H., Hong Y., Dong Y., Ren Y., Wong K. and Tang B., 2007. Colour tunable aggregation induced emission of a butterfly shaped molecule comprising of a pyran skeleton and two cholestral wings. *Journal of Physical Chemistry B* **111**, 2000.

**Tong et al. 2006**

Tong H., Hong Y., Dong Y., Ren Y., Wong K., Lam J., Yu X., Williams I., Kwok H. and Tang, Z., 2007. Aggregation induced emission: effects of molecular structure, solid state conformation, and morphological packing arrangements on light emitting behaviours of diphenyldibenzofulvene derivatives. *Journal of Physical Chemistry C* **111**, 2287

**Torsi et al. 2003**

Torsi L., Tanese M.C., Cioffi N., Gallazzi M.C., Sabbatini M.C., Zamboni P.G., Raos G., Meille S.V., and Giangregorio M.M., 2003. Side-chain role in chemical sensing conducting polymer field-effect transistors. *Journal of Physical Chemistry B* **107**, 7589.

**Torsi et al. 2001**

Torsi L., Cioffi N., Franco C., Sabbatini L., Zamboni P.G. and Bleve-Zacheo T., 2001. Organic thin film transistors: from active materials to novel applications. *Solid State Electronics* **45**, 1479.

**Torsi et al. 1995**

Torsi L., Dodabalapur A., Lovinger A.J., Katz H.E., Ruel R., Davis D.D. and Baldwin K.W., 1995. Rapid thermal processing of  $\alpha$ -hexathienylene thin film transistors. *Chemistry Materials* **7**, 2247.

**Tourillon et al. 1982**

Tourillon G. and Garnier F., 1982. New electrochemically generated conducting polymers. *Journal of Electroanalytical chemistry* **135**, 173.

**Tran et al. 2009**

Tran H.D., Li D. and Kaner R.B., 2009. One-dimensional conducting polymer nanostructures: bulk synthesis and applications. *Advanced Materials* **21**, 1487.

**Treossi et al. 2009**

Treossi E., Liscio A., Feng X., Palermo V., Mullen K. and Samori P., 2009. Temperature-enhanced solvent vapour annealing of a C<sub>3</sub> symmetric hexa-peri-

hexabenzocoronene: controlling the self assembly from nano- to macroscale. *Small* **5**, 1, 112.

**Ren et al. 1998**

Ren Z.F., Huang Z.P., Xu J.W., Wang J.H., Bush P., Siegel M.P. and Provencio P.N., 1998. Synthesis of large arrays of well-aligned carbon nanotubes on glass. *Science* **282**, 1105.

**Unni et al. 2006**

Unni K.N.N., Dabos-Seignon S. and Nunzi J.M., 2006. Influence of the polymer dielectric characteristics on the performance of a quaterthiophene organic field effect transistor. *Journal of Materials Science* **41**, 317.

**Usta et al. 2011**

Usta H., Fachetti A. and Marks T., 2011. n-Channel semiconductor materials design for organic complementary circuits. *Accounts of Chemical Research* **44**, 7, 501.

**Van Nostrum et al. 1995**

Van Nostrum C.F., Picken S.J., Schouten A.J. and Nolte R.J.M., 1995. Synthesis and supramolecular chemistry of novel liquid crystalline crown ether-substituted phthalaocyanines: toward molecular wires and molecular ionoelectronics. *Journal of American Chemical Society* **117**, 9957.

**Vayssieres et al. 2003**

Vaysierres L., 2003. Growth of arrayed nanorods and nanowires of ZnO from aqueous solution. *Advanced Materials* **15**, 5, 464.

**Veres et al. 2004**

Veres J., Ogier S. and Lloyd G., 2004. Gate insulators in organic field-effect transistors. *Chemical Materials* **16**, 4543.

**Walker et al. 1967**

Walker M.S., Bednar T.W. and Lumry R., 1967. Exciplex studies. 11. Indole and indole derivatives. *Journal of Chemical Physics* **47**, 3, 4020.

**Waltman et al. 1984**

Waltman R.J., Diaz A.F. and Bargon J., 1984. Substituent effects in the electropolymerization of aromatic heterocyclic compounds. *Journal of Physical Chemistry* **88**, 4343.

**Wan et al. 2005**

Wan A., Hwang H., Amy F. and Kahn A., 2005. Impact of electrode contamination on the  $\alpha$ -NPD/Au hole injection barrier. *Organic Electronics* **6**, 47.

**Wan et al. 2001**

Wan F., Liang L., Wan X. and Xue G., 2001. Modification of polyindole by the incorporation of pyrrole unit. *Journal of Applied Polymer Science* **85**, 814.

**Wang et al. 2011**

Wang Z., Bao R., Zhang X., Ou X., Lee C., Chang J. and Zhang X., 2011. One step self assembly, alignment and patterning of organic semiconductor nanowires by controlled evaporation on microfluidics. *Angewandte Chemie Int. Ed.* **50**, 2811.

**Wang et al. 2007**

Wang Y., Fu H., Peng A., Zhao Y., Ma J., Ma Y. and Yao J., 2007. Distinct nanostructures from isomeric molecules of bis(iminopyrrole) benzenes: effects of molecular structures on nanostructural morphologies. *Chemical Communications* 1623.



**Wang et al. 2006**

Wang A., Kyymissis I., Bulovic V. and Ibitayo A. I., 2006. Engineering density of semiconductor-dielectric interface states to modulate threshold voltage in OFETs. *IEEE Transactions on Electron Devices* **53**, 9.

**Wang et al. 2005**

Wang F., Han M.Y., Mya K.H., Wang Y. and Lai Y.H., 2005, Aggregation-driven growth of size-tunable organic nanoparticles using electronically altered conjugated polymers. *Journal of American Chemical Society* **127**, 10350.

**Wang et al. 2004**

Wang Z., Qian X., Yin J. and Zhu Z., 2004. Large scale fabrication of tower-like, flower like and tube-like ZnO arrays by a simple chemical solution route. *Langmuir* **20**, 3441.

**Wen et al. 2010**

Wen Y. and Liu Y., 2010. Recent progress in n-channel organic thin-film transistors. *Advanced Materials* **22**, 1331.

**Winiarz et al. 1999**

Winiarz J.G., Zhang L.M., Lal M., Friend C.S. and Paras P.N., 1999. Observation of the photorefractive effect in a hybrid organic-inorganic nanocomposite. *Journal of American Chemical Society* **121**, 5287.

**Wisnieff. 1998**

Wisnieff, 1998. Printing screens. *Nature* **394**, 225.

**Wurthner et al. 2011**

Wurthner F., Kaiser T.E. and Saha-Moller C.R., 2011. J-aggregates: from serendipitous discovery to supramolecular engineering of functional dye materials. *Angewandte Chemie International edition* **50** 3376

**Xia et al. 2003**

Xia Y., Yang P., Sun Y., Wu Y., Mayers B., Gates Y., Yin Y., Kim F. and Yan H., 2003. One-dimensional nanostructures: synthesis, characterisation and applications. *Advanced Materials* **15**, 353.

**Xia et al. 1998**

Xia W. and Whitesides G.M., 1998. Soft Lithography. *Angewandte Chemie Review International edition* **37**, 5, 550.

**Xiao et al. 2007**

Xiao K., Tao J., Pan Z., Puretzky A.A., Ivaanov I.N., Pennycook S.J. and Geohagan D.B., 2007. Single-crystal organic nanowires of copper-tetracyanoquino-dimethane: synthesis, patterning, characterization, and device applications. *Angewandte Chemie International Edition* **46**, 2650.

**Xiao et al. 2004**

Xiao D. Xi L. Yang W., Yao J., Yang X. and Shuai Z., 2004. Size-dependent exciton chirality in R-(+) 1,1-Bi-2-naphthol dimethyl ether nanoparticles. *Journal of the American Chemical Society* **126**, 15439.

**Xiao et al. 2003**

Xiao D. Xi L. Yang W., Fu F., Shuai Z., Fang Y. and Yao J., 2003. Size tunable emission from 1,3-diphenyl-5-(2-anthryl)-2-pyrazoline nanoparticles. *Journal of the American Chemical Society* **125**, 6740.

**Yan et al. 2008**

Yan H., Zheng Y., Blache R., Newman C., Lu S., Woerle J. and Facchetti A., 2005. Solution processed top-gate n channel transistors and complementary circuits on plastics operating in ambient conditions. *Advanced Materials* **20**, 3393.

**Yang et al. 2008**

Yang X., Xu X. and Ji H.F., 2008. Solvent effect on the self-assembled structure of an amphiphilic perylene diimide derivative. *Journal of Physical Chemistry B* **112**, 7196.

**Yang et al. 2005**

Yang M., Wang W., Yuan F., Zhang X., Li J., Liang F., He B., Minch B. and Wegner G., 2005. Soft vesicles formed from diblock codendrimers of poly(benzylether) and poly(methallyl dichloride). *Journal of the American Chemical Society* **127**, 1507.

**Yang et al. 2005a**

Yang H., Shin T.J., Ling M.M., Cho K., Ryu C.Y. and Bao Z., 2005. Conducting AFM and 2D GIXD studies of pentacene thin films. *Journal of American Chemical Society Communications* **127**, 11542.

**Yang et al. 2005b**

Yang S., Shin K. and Park C., 2005. The effect of gate dielectric surface energy on pentacene morphology and OTFET characteristics. *Advanced Functional Materials* **15**, 1806.

**Yang et al. 2005c**

Yang F., Shtein M. and Forrest S.R., 2005. Controlled growth of a molecular bulk heterojunction photovoltaic cell. *Nature Materials* **4**, 37.

**Yang et al. 2005d**

Yang H., Shin T.J., Yang L., Cho K., Chang Y. and Bao Z., 2005. Effect of mesoscale crystalline structure on the field effect mobility of regioregular poly(3-hexylthiophene) in thin film transistors. *Advanced Functional Materials* **15**, 4, 671.

**Yasuda et al. 2004**

Yasuda T., Goto T., Fujita K. and Tsutsui T., 2004. Ambipolar pentacene field-effect transistors with calcium source-drain electrodes. *Applied Physics Letters* **85**, 11, 2098.

**Yin et al. 2004**

Yin Y. and Alivisatos P., Colloidal nanocrystal synthesis and the organic-ionorganic interface. *Nature* **437**, 4664.

**Yoon et al. 2006**

Yoon M.H., Kim C., Facchetti A. and Marks T.J., 2006. Gate dielectric chemical structure-organic field-effect transistor performance correlations for electron, hole and ambipolar organic semiconductors. *Journal of the American Chemical Society* **128**, 12851.

**Yoon et al. 2006a**

Yoon M.H., Kim C., Facchetti A., Stern C.E. and Marks T.J., 2006. Fluorocarbon modified organic semiconductors: Molecular architecture, electronic and crystal structure tuning of arene versus fluorarene-thiophene oligomer thin film properties. *Journal of the American Chemical Society* **128**, 5792.

**Young et al. 2008**

Young R.J., Templeton T., Roussel L.Y., Gestmann I., Veen G., Van Dingle T. and Henstra S., 2008. Extreme High Resolution SEM; a paradigm shift. *Microscopy Today* **16**, 4, 24.

**Zang et al. 2008**

Zang X., Zhang X., Wang B., Zhang C., Chang J.C., Lee C.S. and Lee S.T., 2008. One or semi-two-dimensional organic nanocrystals induced by directional supramolecular interactions. *Journal of Physical Chemistry C* **112**, 162264.

**Zang et al. 2008b**

Zang L., Che Y. and Moore J.S., 2008. One-dimensional self-assembly of planar  $\pi$ -conjugated molecules: adaptable building blocks for organic nanodevices. *Accounts of chemical research*.

**Zaumseil et al. 2007**

Zaumseil J. and Sirringhaus H., 2007. Electron and ambipolar transport in organic field effect transistors. *Chemistry Reviews* **107**, 1296.

**Zaumseil et al. 2006**

Zaumseil J., Donley C.L., Kim J.S., Friend R.H. and Sirringhaus H., 2006. Efficient top-gate, ambipolar, light-emitting field-effect transistors based on a green-light-emitting polyfluorene. *Advanced Materials* **18**, 2708.

**Zehner et al. 1999**

Zehner R.W., Parsons B.F., Hsung R.P. and Sita L.R., 1999. Tuning the work function of gold with self assembled monolayers derived from  $X-[C_6H_4-C\equiv C-]_n C_6H_4SH$  ( $n = 0, 1, 2$ ;  $X = H, F, CH_3, CF_3$  AND  $OCH_3$ )

**Zeis et al. 2005**

Zeis R., Siegrist T. and Kloc C., 2005. Single-crystal field effect transistors based on copper phthalocyanine. *Applied Physics letters* **86**, 22103

**Zhang et al. 2008**

Zhang X., Yuan G., Li Q., Wang B., Zhang X., Zhang R., Chang J., Lee C. and Lee S., 2008. Single-crystal 9,10-diphenylanthracene nanoribbons and nanorods. *Chemistry of Materials* **20**, 6945.

**Zhang et al. 2004**

Zhang F. and Srinivasan M.P., 2004. Self-assembled molecular films of aminosilanes and their immobilization capacities. *Langmuir* **20**, 2309.

**Zhao et al. 2010**

Zhao Y.S., Wu J. and Huang J., 2010. Vertical organic nanowire arrays: controlled synthesis and chemical sensors. *Journal of American Chemical Society Communications* **131**, 3158.

**Zhao et al. 2009**

Zhao Y.S., Wu J. and Huang J., 2009. Vertical organic nanowire arrays: controlled synthesis and chemical sensors. *Journal of the American Chemical Society* **131**, 3158.

**Zhao et al. 2008**

Zhao Y.S., Fu H., Peng A., Ma Y., Xiao D. and Yao J., 2008. Low-dimensional nanomaterials based on small organic molecules: preparation and optoelectronic properties. *Advanced Materials* **9999**, 1.

**Zhao et al. 2008a**

Zhao Y.S., Peng A., Fu H., Ma Y. and Yao J., 2008. Nanowire waveguides and ultraviolet lasers based on small organic molecules. *Advanced Materials* **20**, 1661.

**Zhao et al. 2007**

Zhao Y.S., Fu H., Hu F., Peng A. and Yao J., 2007. Multicolour emission from ordered assemblies of organic 1D nomaterials. *Advanced Materials* **19**, 3554.

**Zhao et al. 2006**

Zhao Y.S., Wang W. and Yao J., 2006. Organic nanocrystals with tunable morphologies and optical properties prepared through a sonication technique. *Physical Chemistry Chemical Physics*. **8**, 3300.

**Zhao et al. 2006a**

Zhao Y.S., Xiao D., Yang W., Peng A. and Yao J., 2006. 2,4,5-Triphenylimidazole nanowires and fluorescent narrowing spectra prepared through the adsorbent-assisted physical vapour deposition method. *Chemistry Materials* **18**, 2302.

**Zhao et al. 2005**

Zhao Y.S., Yang W., Xiao D., Sheng X., Yang X., Shuai Z., Luo Y. and Yao J., 2005. Single crystalline submicrotubes from small organic molecules. *Chemistry of Materials* **17**, 6430.

**Zhao et al. 2005a**

Zhao L., Yang W., Luo Y., Zhai T., Zhang G. and Yao J., 2005. Nanotubes from isomeric bibenzoylmethane molecules. *Chemistry a European Journal* **11**, 3773.

**Zhijiang et al. 2005**

Zhijiang C., 2005. Study on a novel polymer-based secondary battery system. *Journal of Polymer Research* **13**, 207.

**Zhong et al. 1993**

Zhong G., 1993. Fractures polymer/silica fiber surface studied by tapping mode atomic force microscopy. *Surface Science letters* **290**, L688.

**Zotti et al. 1994**

Zotti G., Zecchin S., Shiavon G., Seraglia R., Berlin A. and Canavesi A., 1994. Structure of polyindoles from anodic coupling of indoles: an electrochemical approach. *Chemistry Materials* **6**, 1742.